Collective Quantum Dynamics for Large Ensembles of Clock Atoms in Optical Cavities

Dissertation
zur Erlangung des akademischen Grades
Doctor of Philosophy

eingereicht an der
Fakultät für Mathematik, Informatik und Physik
der Leopold-Franzens-Universität Innsbruck

von
Christoph Hotter, M.Sc.

Betreuung der Dissertation:
Univ.-Prof. Dr. Helmut Ritsch
Institut für Theoretische Physik
Universität Innsbruck

Innsbruck, Februar 2023

Zusammenfassung

Optische Übergänge mit langlebigen angeregten Zuständen sind die Basis von Atomuhren, die genausten Messapparate der Menschheit. In diesen Uhren wird die Frequenz eines Lasers auf den schmalbandigen atomaren Übergang stabilisiert. Da die Atome selbst kein Frequenzsignal erzeugen, sondern lediglich als Referenz dienen, spricht man von passiven Atomuhren. Die Gewinnung von schmalbandigem Licht direkt aus dem sogenannten Uhrenübergang ist eine vielversprechende Idee, die theoretisch die Genauigkeit der aktuell besten Uhr übertreffen sollte. Das Konzept eines solchen Apparats entspricht dem eines Lasers, jedoch in einem ungewöhnlichen Regime. Die Verstärkungsbandbreite des aktiven Mediums ist viel schmaler als die Linienbreite des Resonators, was dazu führt, dass das Laserlicht der atomaren Übergangsfrequenz und nicht der Resonatorfrequenz folgt. Dadurch sind thermische Fluktuationen in den Resonatorspiegeln, welche momentan die Frequenzstabilität der besten Laser limitieren, irrelevant.

Natürlich bringt der Aufbau eines solchen sogenannten Superradianten Lasers auch Schwierigkeiten mit sich. Das Hauptproblem besteht darin, kontinuierliche Inversion im atomaren Ensemble zu erzeugen, ohne den Laserübergang zu stören oder die Atome aufzuheizen. Im ersten Teil dieser Arbeit beschäftigen wir uns mit möglichen Realisierungen von solch einem Anregungsprozess. Zu diesem Zweck untersuchen wir ein verblüffendes Phänomen in einem V-Level Atom, bei dem durch kohärentes Treiben beider Übergänge Inversion im Langlebigeren erreicht werden kann. Dabei wurden Parameterbereiche gefunden, in denen simultanes Kühlen während des Laserbetriebs möglich ist. Allerdings wird bei dem Pumpprozess der Laserübergang stark verbreitert, sodass eine schmale Linienbreite lediglich im normalen Good-Cavity Regime erreicht werden kann. In einem anderen Ansatz betrachten wir ein Pumpschema für ein Viel-Niveau Atom entsprechend der Levelstruktur vom Uhrenatom Strontium-88. Wir konnten zeigen, dass durch eine geeignete Wahl der Parameter eine ausreichende Inversion bei gleichzeitig nur minimalen Störungen erreicht werden kann.

Neben der Anwendung als aktive Atomuhr haben wir weitere dynamische Eigenschaften dieses Systems, bestehend aus einem Ensemble von langlebigen Atomen in einem Resonator, untersucht. Dabei haben wir einen Übergang von resonatorvermittelter Sub- zu Superradianz entdeckt, welcher für kohärent bestrahlte Atome bei halber Anregung auftritt. Zusätzlich schlagen wir vor, diesen Übergang zur Verbesserung von passiven Atomuhren zu verwenden. Diese theoretisch beschriebenen Phänomene konnten experimentell verifiziert werden.

Um die oben genannten großen offenen Quantensysteme zu beschreiben, müssen wir eine Näherung durchführen. Eine Methode, die sich für solche Systeme bewährt hat, ist die Kumulantenentwicklung. Dieser Ansatz hat jedoch den Nachteil, dass die Gleichungen zunächst mühsam analytisch hergeleitet werden müssen. Um diesen fehleranfälligen und

aufwendigen Prozess zu vereinfachen, haben wir ein Computeralgebrasystem entwickelt, das die gewünschten Gleichungen aus einem benutzerdefinierten Modell automatisch erzeugt und numerisch implementiert. Dieses Programm kann nicht nur zur Beschreibung des Superradianten Lasers verwendet werden, sondern auch für viele andere Quantensysteme.

Abstract

Optical transitions with long-lived excited states are the basis of atomic clocks, the most accurate man-made devices. In such clocks, the frequency of a laser is stabilized relative to a narrow-band atomic transition. Since the atoms themselves here do not generate a frequency signal but merely serve as a reference, those are referred to as passive atomic clocks. Obtaining narrow-band light directly from the so-called clock transition is a promising idea that is predicted to surpass the accuracy of the current best clock. The concept of such an apparatus corresponds to that of a laser but in an unusual regime. The gain bandwidth of the active medium is much narrower than the linewidth of the resonator, which results in the laser light following the atomic transition frequency instead of the cavity resonance frequency. This makes fluctuations in the resonator mirrors irrelevant, which currently limit the frequency stability of the best lasers.

Of course, the construction of such a so-called superradiant laser also comes with challenges. The main problem is to find a mechanism to produce continuous inversion in the atomic ensemble without disturbing the laser transition or heating the atoms. In the first part of this work we deal with possible realizations of such a process. To this end, we investigate a very counterintuitive process in a V-level atom, where coherent driving of both transitions can result in inversion for the longer-lived one. We found parameter ranges in which simultaneous cooling during laser operation is possible. However, the laser transition is broadened due to the pumping process, thus a narrow linewidth can only be achieved in the conventional good-cavity regime. In another approach, we study a pumping scheme in a multilevel atom corresponding to the level structure of the clock atom strontium-88. We were able to show that an appropriate choice of parameters can achieve a sufficient inversion with only minimal perturbations at the same time.

In addition to its application as an active atomic clock, we have further investigated dynamical properties of an ensemble of long-lived atoms in a resonator. We discovered a transition from cavity mediated sub- to superradiance, which occurs for a transversely driven atomic ensemble at the point of half excitation. We propose to use this transition to improve the readout of passive atomic clocks. Several of these theoretically observed phenomena have been demonstrated experimentally.

To describe the large open quantum systems mentioned already above, we need to make approximations. One method that has proven successful for such systems is the cumulant expansion. This approach requires that first the equations are laboriously derived analytically. To simplify this error-prone and cumbersome process, we developed a symbolic algebra framework that automatically generates and numerically implements the desired equations from a user-defined model. This program can be used not only to describe the superradiant laser but also for many other quantum systems.

Danksagung

Zuallererst bedanke ich mich bei Helmut Ritsch für die hervorragende Betreuung. Seine Expertise, großartige physikalische Intuition und unzähligen Ideen waren ausschlaggebend für diese Arbeit. Zudem schuf er durch seine freundliche und hilfsbereite Art ein wunderbares Arbeitsklima.

In diesem Zuge möchte ich allen ehemaligen und aktuellen Mitgliedern der Ritsch Gruppe danken: Anna Bychek, Elvia Colella, Martin Fasser, Karol Gietka, Raphael Holzinger, Daniela Holzmann, Arkadiusz Kosior, Natalia Masalaeva, Farokh Mivehvar, Mariona Moreno-Cardoner, Julian Moser, Wolfgang Niedenzu, Laurin Ostermann, Stefan Ostermann, David Plankensteiner, Verena Scheil, Matthias Sonnleitner, Elias Starchl, Valentin Torggler, sowie meinem langjährigen Studienkollegen Alexander Eberharter. Ganz besonders bedanke ich mich nochmals bei David Plankensteiner, der einen Großteil meiner Arbeit mitbetreute.

Weiters bedanke ich mich bei Nicole Jorda, Birgit Laimer, Jade Meysami-Hörtnagl, Katharina Renz und Elke Stenico für die stets schnellen und unkomplizierten administrativen Arbeiten am Institut.

Auf privater Seite bedanke ich mich natürlich bei meinen Freunden auf die immer Verlass ist, besonder bei Alexander, Bernhard, Hannes K., Hannes L. und Mario. Selbstverständlich gilt auch ein großer Dank meiner Familie, die mich stets unterstützt hat, speziell meinen Eltern Claudia und Christian sowie meinen Geschwistern Elias und Manuel.

Zuletzt danke ich aufrichtig der liebevollen Frau an meiner Seite, ohne die die letzten Jahre nicht mal halb so schön gewesen wären. Danke, Sarah.

Contents

1 Introduction

The invention of the laser led to a revolution in science and substantially impacts modern life. This makes it probably the prime application of cavity quantum electrodynamics (CQED), the physics of atoms inside a resonator. The LASER, an acronym for *Light Amplification by Stimulated Emission of Radiation*, relies, as the name suggests, on stimulated emission of light. This process has been described already in 1917 by Albert Einstein in his groundbreaking work *Zur Quantentheorie der Strahlung* [1.1], where he describes it as the inverse mechanism to absorption, which, together with spontaneous emission are the three fundamental processes describing the interactions of matter with electromagnetic radiation. To achieve steady state lasing, a mechanism to continuously recreate inversion in the atomic ensemble is required, i.e., the upper state of the lasing transition needs to be populated more than the lower one. Unfortunately, this is not possible by considering two atomic levels only. Even though Einstein described already in 1917 all constituents for such a repumping process, it was only proposed more than three decades later [1.2]. The first realization of a radiation amplification device was achieved by Charles Townes in 1953 [1.3], emitting microwave radiation, the so-called maser. Soon afterwards the optical maser, operating on a much shorter wavelength, was introduced [1.4], which was later on called *laser*. Eventually, in 1960 the first laser [1.5], the ruby laser, was built. Since then many types of lasers, based on different technologies and targeting different properties have been developed [1.6, 1.7]. The number of applications is almost countless, ranging from everyday objects such as bar code scanners to industrial cutting machines and precision instruments in research laboratories. A maybe not obvious, but particularly important and interesting scientific use case is its function as a time keeping device. Stabilizing the frequency of a laser on a narrow transition of an atom is the underlying basis of the best clocks, the so-called atomic clocks [1.8].

1.1 Passive atomic clocks

Every apparatus with a repeating periodic signal can, in principle, be used as a clock. The precision of a clock is usually determined by the time it is off after a given duration. For an oscillator we can describe it equivalently by its relative frequency error, which is given by the ratio between the frequency uncertainty Δf and the frequency of the signal itself f. Therefore, to obtain a small relative error $\Delta f/f \ll 1$ one aims for large frequencies with small inaccuracies. This can be achieved with atomic transitions, e.g., in Cesium clocks the laser frequency is stabilized on a microwave transition in the hyperfine structure of the atomic ground state, with a frequency of around 9 GHz. Since 1967 this transition still defines the second as the duration of 9.192.631.770 periods [1.9]. The

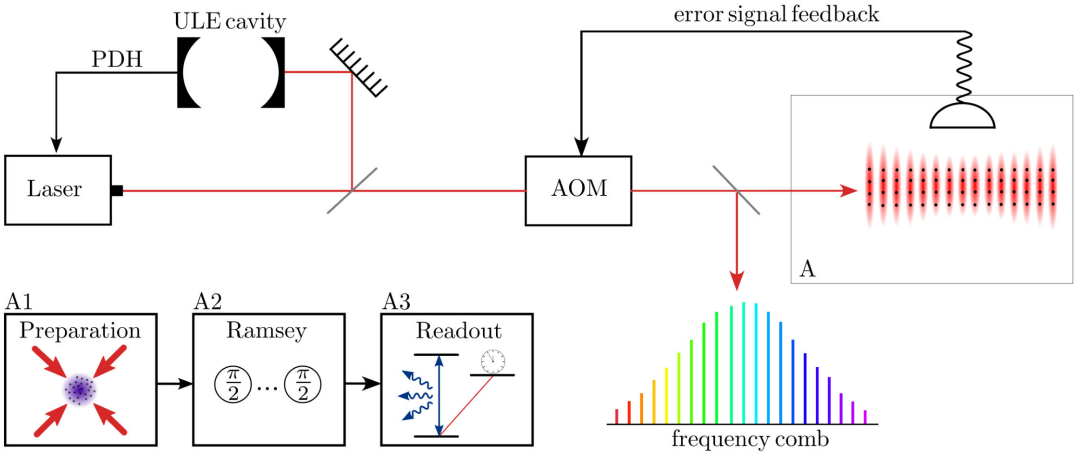

Figure 1.1: *Schematic illustration of an atomic lattice clock.* A laser is locked on a ULE cavity and then stabilized on a narrow atomic transition. To electronically measure the optical frequency, the signal is mapped to, e.g., a radio frequency with a frequency comb.

best Cesium clocks reach a precision of 10^{-16} [1.10], which corresponds to an inaccuracy of only one second in 300 million years. However, using an optical transition instead of a microwave transition features a more than four magnitudes larger frequency with several hundred THz. Optical lattice clocks [1.11], where the atoms are trapped in a magic wavelength optical lattice [1.12], achieve a precision at the level of 10^{-19} [1.13–1.15]. Such a clock is off by less than a second at the age of the universe.

The basic operational scheme of an optical lattice clock [1.8, 1.11, 1.16] is shown in Fig. 1.1: A laser is locked with the Pound-Drever-Hall technique (PDH) [1.17] on to the resonance frequency of an ultra low expansion (ULE) cavity. This frequency stabilization sets the short term stability of the laser. The frequency of the laser is then changed by, e.g., an acousto-optic modulator (AOM), according to the error signal from the clock measurement. To convert the huge optical frequency into a measurable electronic signal, a frequency comb [1.18] is used. The clock measurement usually looks as follows: First, of course, the atomic ensemble needs to be prepared, the atoms need to be cooled [1.19], trapped in the optical lattice and prepared in the (desired) ground state. Afterwards one tries to excite the atoms with the clock laser in a Ramsey measurement sequence [1.20, 1.21]. In the simplest case this means a $\pi/2$-pulse on the atoms is followed by another $\pi/2$-pulse after some free evolution time τ. The inverse of the free evolution time $1/\tau$ defines the width of the Ramsey fringes, which in turn determines the precision of the frequency measurement. Of course, the free evolution time can not be longer than the excited state lifetime, therefore an atomic transition with a long lived upper state is used, a so-called *clock transition*. In the end a readout, to determine the fraction of excited atoms, needs to be performed. There are many different ways to do this, however, a very common one is the electron-shelving technique [1.8, 1.22]. For this method one drives a strong dipole transition with a fast decay channel into

the ground state and measures the number of emitted photons. Detecting almost no fluorescence photons indicates that most atoms have been excited to the upper clock state, which means the clock laser has the correct frequency. If many photons are detected, it means that the laser frequency is not perfectly resonant and needs to be changed. The obtained measurement signal is processed and sent to the AOM to adapt the laser frequency. This results in a feedback loop stabilizing the laser on the atomic clock transition.

Due to the many scattered photons the atoms will be strongly heated. For such destructive measurements the atomic ensemble needs to be prepared for every cycle. This undesired dead time limits the long-term stability of the clock, which refers to the Dick effect [1.8, 1.23]. Therefore the dead time should be reduced as far as possible, with the ultimate goal of a continuous measurement. A feasible step in this direction are non-destructive readout methods [1.8]. However, another, more profound, limiting factor stems from the precision of the clock laser. As mentioned before, the laser is stabilized on the resonance frequency of a ULE cavity. Thermal noise in the mirrors of this cavity [1.24] induces tiny fluctuations on the resonator length, which lead to changes of the resonance frequency. The resulting clock laser frequency fluctuations are currently the main constraint for the performance of optical atomic clocks.

A proposed device, which is theoretically capable to overcome all of these obstacles, is the so-called superradiant laser [1.25, 1.26], an active optical atomic clock.

1.2 Active atomic clocks

The atomic clocks described in the previous section are passive since the atoms are merely used as a reference to stabilize the laser. The idea of an active atomic clock is to directly extract narrow bandwidth light from the clock transition. In the microwave regime a similar device already exists for decades in the form of the hydrogen maser [1.27]. This is a well working device, but it can not reach the precision of current atomic clocks. In the optical domain a continuous operation has not been achieved so far, due to various difficulties:

First of all, it is hard to obtain a decent radiation power from a narrow clock transition with a decay rate below one Hertz. The solution to this problem is to utilize superradiance [1.28], the enhanced collective light emission of a large ensemble. A particular way to achieve this for a dilute atomic cloud is within a cavity, which enables long range interaction between the atoms. Cavity enhanced emission of a superradiant pulse from a narrow optical transition has already been demonstrated in several experiments [1.29–1.31]. The more involved challenge is to preserve the superradiance for continuous output. One promising approach is to create a beam of excited atoms, which transversely passes the cavity [1.32], similar to the working principle of the hydrogen maser. The main obstacle here is to obtain the necessary atomic flux, but this seems technically feasible [1.33]. Another possible realization is to trap the atoms inside the cavity and repump them incoherently on the clock transition [1.25]. The main problems here are that the clock transition gets disturbed

and the atoms are heated by the repumping process.

Anyway, from a basic inspection of the system, continuous light emission from inverted atoms inside a cavity resembles very much a laser. So why should this realization be any better, in terms of frequency stability, than a 'normal' laser? As mentioned in section 1.1, the main limitation for passive clocks are the length fluctuations of the ULE cavity. For 'normal' lasers, with a narrow cavity linewidth and a broad gain medium bandwidth, usually referred to as the good cavity regime, the same applies. In this case, the frequency of the emitted photons is governed by the resonance frequency of the cavity, which in turn is determined by the cavity length. In contrast, the laser described in this section is in a completely different regime. The linewidth of the gain medium - the clock transition, is several orders of magnitudes narrower than the cavity linewidth. Deep in this so-called bad cavity regime, the frequency of the emitted photons is set by the atomic transition frequency instead of the cavity resonance frequency. The phase information of the laser is mainly stored in the collective dipole of the atoms [1.26], this makes the device largely insensitive to cavity length fluctuations, the current main limitation. Such a laser is predicted to achieve a linewidth at the millihertz level [1.25, 1.32].

1.3 Outline of this thesis

The focus of this thesis is on the simulation of large atomic ensembles in optical cavities. In particular, we are interested in the collective cavity induced atomic behavior, but also in the various excitation possibilities and their consequences for the atoms inside the resonator.

In chapter 2 we introduce the necessary fundamental tools and phenomena used for the publications in the following chapters.

Coherently driving both transitions of a V-level atom with very different decay rates can surprisingly yield almost perfect steady state inversion on the narrower transition. In chapter 3 we showed a possible realization of a laser utilizing this repumping process, where we additionally identified regimes with simultaneous cooling.

A well established method to describe large atomic ensembles in cavities is the cumulant expansion. This approach makes it possible to describe realistic system sizes. However, deriving the equations and implementing them can be a cumbersome and error-prone task. To this end, we developed a toolbox which does this automatically. Some theoretical background, the working principle and many examples of this package are described in chapter 4.

A still missing piece to achieve continuous operation of a superradiant laser is a practical repumping mechanism. First of all the process needs to provide the necessary gain, but it should also not perturb the clock transition and heat the atoms significantly. In chapter 5 we investigated a realistic multi-level repumping scheme according to the level structure of strontium-88. We found parameter regimes for a sufficiently large repumping rate with simultaneously small perturbations and acceptable heating.

In chapter 6 we studied a system similar to a superradiant laser, where basically the

incoherent pump is replaced by a coherent transverse drive. We discovered a transition from cavity sub- to superradiance at 50% excitation in the atomic ensemble, due to an overall vanishing phase between the atoms and the cavity. Additionally, we proposed a cavity enhanced Ramsey scheme, utilizing this feature. The transition from cavity sub- to superradiance, as well as a proof of principle for the Ramsey scheme, are verified experimentally. Preliminary results from the collaboration between theory and experiment are shown in chapter 7.

The conclusions in chapter 8 are followed by additional publications completed during the thesis period: The publication presented in chapter 9 considers motion in a toy model of a bad cavity laser, where we found regimes for simultaneous lasing, cooling and trapping. In chapter 10 we focused on imperfections of a superradiant laser, such as inhomogeneous broadening and varying cavity couplings. Although this publication would conceptionally fit into the main part, we mention it as additional material, since the contributions from the author of this thesis were mainly discussions, support and minor calculations.

2 Theoretical background

The purpose of this chapter is to introduce the fundamental theoretical concepts underlying the physical results of this thesis. We start by briefly describing the very basics of quantum optics, i.e., atoms, photons and their interaction. After this, we deal with open quantum systems, where we characterize the relevant dissipative processes. To handle realistic system sizes we specify the cumulant expansion method with a practical implementation. Then, a more detailed introduction to the calculation of the emission spectrum is given and we explain the concept of cavity mediated superradiance. In the final section we utilize almost all of these tools to analyze the properties of a superradiant laser.

2.1 Building blocks of quantum optics

Quantum optics describes the interaction between atoms and light on the quantum level. Although the considered systems can be arbitrarily complicated, the elemental building blocks are simple [2.1, 2.2]. Atoms are condensed to their relevant transitions as multi-level systems with discrete energies and photons are described as excitations of quantum harmonic oscillators. Of course, not all systems can be expressed in terms of multiple levels and harmonic oscillators. However, a large number of problems in quantum optics are covered by these two concepts or can be reduced to them.

2.1.1 Multi-level atoms

The simplest form of a multi-level atom is a two-level system with a dipole transition [2.1–2.3]. With the two states $|1\rangle$ and $|2\rangle$, the transition dipole moment operator can be written as

$$\mathbf{d} = \mathbf{d}_{21}|2\rangle\langle 1| + \mathbf{d}_{21}^{*}|1\rangle\langle 2|, \tag{2.1}$$

where $\mathbf{d}_{21}$ is the dipole matrix element. Without loss of generality $\mathbf{d}_{21}$ is assumed to be real and we introduce the transition operator $\sigma^{ij} = |i\rangle\langle j|$ to express the dipole operator as

$$\mathbf{d} = \mathbf{d}_{21}(\sigma^{21} + \sigma^{12}). \tag{2.2}$$

Extending this to multi-level atoms is straightforward, by dealing with one transition at a time. The transition operator $\sigma^{ij} = |i\rangle\langle j|$ transfers an atom from state $|j\rangle$ to $|i\rangle$ and for i equal to j it represents the projector on the state $|i\rangle$. Using the orthonormality between two distinct states leads to the simple algebraic rule

$$\sigma^{ij}\sigma^{kl} = |i\rangle\langle j|k\rangle\langle l| = \delta_{jk}\sigma^{il}, \tag{2.3}$$

with δ_{jk} the Kronecker delta. Each state $|i\rangle$ of a multi-level atom has a corresponding energy $E_i = \hbar\omega_i$. For ω_i the transition frequency between state $|1\rangle$ and $|i\rangle$, the energy of such a free N-level atom can be expressed with the Hamiltonian

$$H_\mathrm{a} = \sum_{i=2}^{N} \hbar\omega_i \sigma^{ii}, \tag{2.4}$$

where we set the energy of the state $|1\rangle$ equal to 0 without loss of generality.

2.1.2 Photons

The quantized electromagnetic field, derived from Maxwell's equations without source, is described by quantum harmonic oscillators. In particular, one obtains a position $\mathbf{r}$ and time t dependent electric field operator [2.4]

$$\mathbf{E}(\mathbf{r},t) = i\sum_{\mathbf{k},\lambda} E_k \left(a_{\mathbf{k},\lambda}(t) f_{\mathbf{k},\lambda}(\mathbf{r}) - a^\dagger_{\mathbf{k},\lambda}(t) f^*_{\mathbf{k},\lambda}(\mathbf{r}) \right) \mathbf{e}_{\mathbf{k},\lambda}, \tag{2.5}$$

with the sum over all possible wave vectors $\mathbf{k}$ and two orthogonal polarizations λ. The field amplitude E_k for each mode is given by the frequency $\omega_k = c|\mathbf{k}|$ and the chosen volume in space V according to $E_k = \sqrt{\hbar\omega_k/(2\epsilon_0 V)}$, which corresponds to the electric field of one photon. Boundary conditions determine the spatial dependence of the mode described by the normalized function $f_{\mathbf{k},\lambda}$. The polarization direction $\mathbf{e}_{\mathbf{k},\lambda}$ is orthogonal to the propagation direction given by the wave vector $\mathbf{k}$. The bosonic creation ($a^\dagger_{\mathbf{k},\lambda}$) and annihilation ($a_{\mathbf{k},\lambda}$) operators obey the canonical commutation relation

$$\left[a_{\mathbf{k},\lambda}, a^\dagger_{\mathbf{k}',\lambda'} \right] = \delta_{\mathbf{k},\mathbf{k}'}\delta_{\lambda,\lambda'}\mathbb{1}. \tag{2.6}$$

An excitation of the harmonic oscillator described by $a^\dagger_{\mathbf{k},\lambda}$ and $a_{\mathbf{k},\lambda}$ corresponds to a photon with frequency ω_k and polarization λ. The number of photons in each mode is given by the operator $a^\dagger_{\mathbf{k},\lambda} a_{\mathbf{k},\lambda}$, therefore we can intuitively express the energy of the electromagnetic field as

$$H_\mathrm{f} = \sum_{\mathbf{k},\lambda} \hbar\omega_{\mathbf{k},\lambda} a^\dagger_{\mathbf{k},\lambda} a_{\mathbf{k},\lambda}. \tag{2.7}$$

A rigorous derivation of the energy for the electromagnetic field [2.4] leads to an additional term $\hbar\omega_{\mathbf{k},\lambda}/2$, which is usually referred to as the energy of the electromagnetic vacuum. However, it can be neglected, since it is irrelevant for the dynamics of the system.

The mode function of a running plane wave in free space is given by $f(\mathbf{r}) = e^{i\mathbf{kr}}$. For a resonator the electric field needs to vanish at the surface of the mirrors. These boundary conditions lead to standing waves along the axis of a linear cavity. The corresponding mode function is $f(\mathbf{r}) = \cos(\mathbf{kr})$, where merely wave vectors fulfilling the condition $|\mathbf{k}| = n\pi/L$, with n an integer and L the distance between the mirrors, are allowed [2.5].

If only a single mode of the cavity is relevant, the Hamiltonian (2.7) simplifies to

$$H_\mathrm{f} = \hbar\omega_\mathrm{f} a^\dagger a, \tag{2.8}$$

where ω_f is the resonance frequency of the single-mode cavity and we omitted the wave vector and polarization subscripts.

2.2 Atom-light interaction

The interaction of a two-level atom with a light field in the dipole approximation is described by the interaction Hamiltonian [2.1]

$$H_\mathrm{int} = -\mathbf{d}\cdot\mathbf{E}. \tag{2.9}$$

Inserting the expression for the dipole operator (2.2) and the quantized electric field (2.5) results in

$$H_\mathrm{int} = i\hbar \sum_{\mathbf{k},\lambda} g_{\mathbf{k},\lambda} \left(\sigma^{21} + \sigma^{12}\right) \left(a_{\mathbf{k},\lambda} f(\mathbf{r}) - a^\dagger_{\mathbf{k},\lambda} f^*(\mathbf{r})\right), \tag{2.10}$$

with $g_{\mathbf{k},\lambda} = -\sqrt{\hbar\omega_\mathbf{k}/(2\epsilon_0 V)}\mathbf{d}_{21}\mathbf{e}_{\mathbf{k},\lambda}/\hbar$. Considering only a single mode of the electromagnetic field with frequency ω_f results in the quantum Rabi model [2.6]

$$H_\mathrm{R} = \hbar\omega_\mathrm{a}\sigma^{22} + \hbar\omega_\mathrm{f} a^\dagger a + i\hbar g \left(\sigma^{21} + \sigma^{12}\right) \left(a f(\mathbf{r}) - a^\dagger f^*(\mathbf{r})\right). \tag{2.11}$$

From the free Hamiltonian $H_0 = \hbar\omega_\mathrm{a}\sigma^{22} + \hbar\omega_\mathrm{f} a^\dagger a$ we obtain the following time dependence for the operators of the uncoupled atom-field system in the Heisenberg picture:

$$a(t) = a(0)e^{-i\omega_\mathrm{f} t}, \qquad \sigma^{12}(t) = \sigma^{12} e^{-i\omega_\mathrm{a} t}. \tag{2.12}$$

Thus, one finds that the operator products $\sigma^{21}a$ and $\sigma^{12}a^\dagger$ rotate at a frequency $|\omega_\mathrm{a} - \omega_\mathrm{f}|$, whereas $\sigma^{21}a^\dagger$ and $\sigma^{12}a$ rotate at $\omega_\mathrm{a} + \omega_\mathrm{f}$. For a resonant field $\omega_\mathrm{a} \approx \omega_\mathrm{f}$ the latter two terms oscillate much faster, which means they quickly average to zero. Neglecting those terms amounts to the application of the rotating wave approximation (RWA) [2.2, 2.3, 2.7], which is valid if the condition $\omega_\mathrm{a} + \omega_\mathrm{f} \gg |\omega_\mathrm{a} - \omega_\mathrm{f}|, g$ is fulfilled. This leads to the well-known Jaynes-Cummings model [2.8]

$$H_\mathrm{JC} = \hbar\omega_\mathrm{a}\sigma^{22} + \hbar\omega_\mathrm{f} a^\dagger a + i\hbar g \left(\sigma^{21} a f(\mathbf{r}) - \sigma^{12} a^\dagger f^*(\mathbf{r})\right). \tag{2.13}$$

An extension of this model to N two-level atoms is straightforward and results in the Tavis-Cummings Hamiltonian [2.9]

$$H_\mathrm{TC} = \sum_j \hbar\omega_j \sigma_j^{22} + \hbar\omega_\mathrm{f} a^\dagger a + i\hbar \sum_j g_j \left(\sigma_j^{21} a f(\mathbf{r}_j) - \sigma_j^{12} a^\dagger f^*(\mathbf{r}_j)\right), \tag{2.14}$$

with ω_j the transition frequency of the j-th atom.

For classical monochromatic light described by an electric field

$$\mathbf{E}(\mathbf{r},t) = i\mathcal{E}_0\left(f(\mathbf{r})e^{-i\omega_\mathrm{f}t} - f^*(\mathbf{r})e^{i\omega_\mathrm{f}t}\right), \tag{2.15}$$

the atom-light interaction Hamiltonian within the rotating wave approximation results in

$$H_\mathrm{d} = \hbar\omega_\mathrm{a}\sigma^{22} + i\hbar\frac{\Omega}{2}\left(\sigma^{21}e^{-i\omega_\mathrm{f}t}f(\mathbf{r}) - \sigma^{12}e^{i\omega_\mathrm{f}t}f^*(\mathbf{r})\right), \tag{2.16}$$

where $\Omega = -2\mathbf{d}_{21}\mathcal{E}_0/\hbar$ is called the Rabi-frequency [2.1, 2.2]. Assuming classical light corresponds to describing the field by its mean value, this approximation is valid for coherent light [2.10, 2.11].

2.3 Open quantum systems

In the previous section we introduced the coherent interaction between atoms and light, where we implicitly assumed a closed system. The time evolution of the state vector $|\psi(t)\rangle$ for a closed quantum system is governed by the time-dependent Schrödinger equation

$$i\hbar\frac{d}{dt}|\psi\rangle = H|\psi\rangle. \tag{2.17}$$

However, quantum systems are sometimes, or usually, not perfectly closed, which means they interact with the environment. This might be undesired if one aims at optimal control, but it can also be necessary, as the leakage of photons through the mirrors of a laser cavity. In any case, we need to describe it to predict the correct behavior of the system. The dynamics of an open quantum system can be calculated by the quantum master equation [2.12, 2.13]

$$\frac{d}{dt}\rho = -i[H,\rho] + \mathcal{L}[\rho], \tag{2.18}$$

for the density matrix ρ, where the Hamiltonian term describes the coherent system dynamics and the Liouvillian super-operator $\mathcal{L}$ keeps track of the dissipative processes. In the Born-Markov approximation [2.12, 2.13] we can express the Liouvillian in standard Lindblad form

$$\mathcal{L}[\rho] = \frac{1}{2}\sum_j R_j(2J_j\rho J_j^\dagger - J_j^\dagger J_j\rho - \rho J_j^\dagger J_j), \tag{2.19}$$

where R_j represents the rate of the dissipative process described by the jump operator J_j. In the following we introduce the dissipative processes used in the publications of this thesis, namely atomic and cavity decay, incoherent repumping as well as atomic and cavity dephasing, see Fig. 2.1.

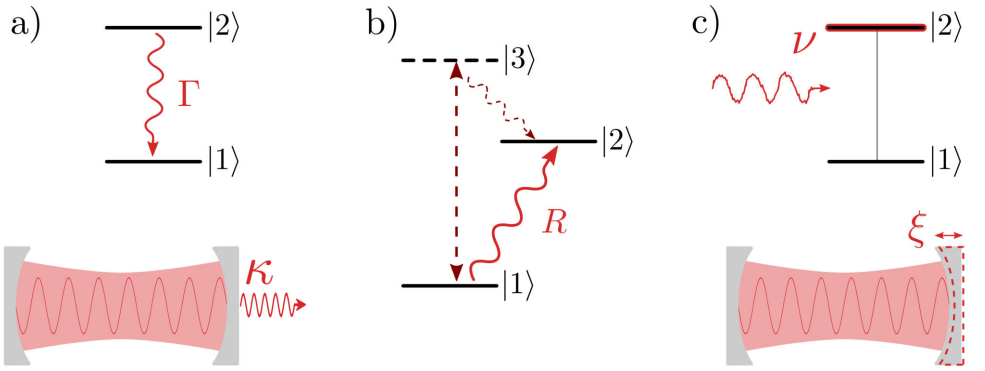

Figure 2.1: *Dissipative processes.* Schematic illustration of the considered dissipative processes. Atomic and cavity decay is depicted in a), incoherent repumping in b) and c) indicates the origin of atomic and photon dephasing.

2.3.1 Decay

The origin of decay, the spontaneous emission of a photon from an excited atom or the loss of a photon through the cavity mirrors, is the interaction of the system with the environment. The system couples to a bath of oscillators of the electromagnetic field with infinitely many degrees of freedom, as described in section 2.2. In the case of a two-level atom the Hamiltonian describing the system and the environment within the RWA is

$$H = \hbar\omega_\mathrm{a}\sigma^{22} + \sum_{\mathbf{k},\lambda}\hbar\omega_{\mathbf{k},\lambda}a^\dagger_{\mathbf{k},\lambda}a_{\mathbf{k},\lambda} + i\hbar\sum_{\mathbf{k},\lambda}g_{\mathbf{k},\lambda}\left(\sigma^{21}a_{\mathbf{k},\lambda}f(\mathbf{r}) - \sigma^{12}a^\dagger_{\mathbf{k},\lambda}f^*(\mathbf{r})\right). \tag{2.20}$$

Eliminating the bath degrees of freedom by performing the partial trace on the environment and considering Markovian processes [2.12, 2.13], which means that there is no back-action onto the system from the bath, leads to a Liouvillian term in Lindblad form (2.19) with a jump operator σ^{12} and rate Γ corresponding to the atomic excited state decay rate. A detailed derivation can for example be found in [2.1]. The interpretation of the jump operator σ^{12} is very intuitive: It acts on the atom in the excited state $|2\rangle$ and transverses it to the lower state $|1\rangle$. The decay of the cavity field can be derived in the same way, which results in a jump operator a and a rate κ which determines the loss rate of the photons. The atomic [2.14] and cavity [2.15] decay rates are given by

$$\Gamma = \frac{\omega_\mathrm{a}^3\mu^2}{3\pi\epsilon_0 c^3} \quad \text{and} \quad \kappa = 2\pi\frac{\mathrm{FSR}}{\mathcal{F}}, \tag{2.21}$$

where μ is the atomic transition dipole, $\mathrm{FSR} = c/2L$ the free spectral range of the cavity with length L and $\mathcal{F}$ the cavity finesse. Note that we assumed for these two dissipative processes that the bath is in the vacuum state, i.e., at zero temperature without any photons. For an optical frequency ω at room temperature T this is valid since the relevant

modes of the bath have a vanishing small occupation $\bar{n} = (e^{\hbar\omega/k_\mathrm{B}T})^{-1} \ll 1$ [2.1, 2.13].

2.3.2 Repumping

To achieve steady state lasing it is necessary to maintain the inversion in the atomic ensemble in order to provide gain for the stimulated emission. Unfortunately, this is not possible with only a coherent drive. We can excite the atoms once by applying a π-pulse on them, but this does not allow for continuous output. A common way to create inversion is to utilize decay processes in multi-level atoms. The simplest model considers a three-level atom with suitable transitions, see Fig. 2.1 b: A transition from the lower lasing state $|1\rangle$ to an upper auxiliary state $|3\rangle$ is coherently driven and the state $|3\rangle$ decays fast into the upper lasing state $|2\rangle$. If the decay rate of state $|3\rangle$ is much larger than the one of state $|2\rangle$, we can adiabatically eliminate state $|3\rangle$. This results in a dissipative process with jump operator σ^{21} and corresponding rate R depending on the coherent drive strength, the decay rates and the laser detuning. Additionally, the repumping process induces a dephasing on the lasing transition and for a not perfectly resonant drive laser we obtain a frequency shift [2.7, 2.16] on the lower lasing state. A detailed calculation is shown in the appendix of chapter 5. This publication also includes a more complicated repumping scheme involving a six-level atom where we introduce a numerical approach to adiabatically eliminate the auxiliary levels.

2.3.3 Dephasing

External perturbations on the system can lead to fluctuations of the resonance frequency. Concerning atoms these might originate from varying electric or magnetic fields, resulting in an effective Hamiltonian for a two-level atom of $H_\mathrm{a} = \hbar(\omega_\mathrm{a} + \xi(t))\sigma^{22}$, with a time-dependent frequency fluctuation $\xi(t)$. For cavities they can, e.g., stem from thermal fluctuations affecting the cavity length, described by the Hamiltonian $H_\mathrm{c} = \hbar(\omega_\mathrm{c} + \xi(t))a^\dagger a$. Therefore, besides the usual deterministic part H_D a stochastic part $\xi(t)H_\mathrm{S}$ appears in the Hamiltonian. For white noise frequency fluctuations, obeying the two-time correlation function [2.13]

$$\langle \xi(t)\xi(t')\rangle = \nu\delta(t-t'), \tag{2.22}$$

with the Dirac delta function δ and ν the characteristic frequency of the noise, we can write the Heisenberg equation for a system operator $\mathcal{O}$ for such a Hamiltonian as

$$\text{(S)} \qquad \frac{d}{dt}\mathcal{O} = L_\mathrm{D}[\mathcal{O}] + \xi(t)L_\mathrm{S}[\mathcal{O}]. \tag{2.23}$$

Here $L_\mathrm{D}[\mathcal{O}] = i[H_\mathrm{D}, \mathcal{O}]$ and $L_\mathrm{S}[\mathcal{O}] = i[H_\mathrm{S}, \mathcal{O}]$. However, we need to interpret Eq. (2.23) as Stratonovich stochastic differential equation, indicated by (S), and transform it into Itô form [2.1, 2.13]

$$\text{(I)} \qquad \frac{d}{dt}\mathcal{O} = L_\mathrm{D}[\mathcal{O}] + \frac{1}{2}\nu L_\mathrm{S}^2[\mathcal{O}] + \xi(t)L_\mathrm{S}[\mathcal{O}]. \tag{2.24}$$

For a stochastic average of Eq. (2.24), indicated by $\langle\cdot\rangle_\mathrm{s}$, the white noise part vanishes and we are left with

$$\frac{d}{dt}\langle\mathcal{O}\rangle_\mathrm{s} = \langle L_\mathrm{D}[\mathcal{O}]\rangle_\mathrm{s} + \frac{1}{2}\nu\langle L_\mathrm{S}^2[\mathcal{O}]\rangle_\mathrm{s}. \tag{2.25}$$

The first term in Eq. (2.25) describes the usual time evolution due to the deterministic part of the Hamiltonian and from the stochastic part we obtain a contribution proportional to $L_\mathrm{S}^2[\mathcal{O}]$, called the Itô correction [2.1, 2.13]. Evaluating this term leads to

$$L_\mathrm{S}^2[\mathcal{O}] = -[H_\mathrm{S},[H_\mathrm{S},\mathcal{O}]] = 2H_\mathrm{S}\mathcal{O}H_\mathrm{S} - \mathcal{O}H_\mathrm{S}H_\mathrm{S} - H_\mathrm{S}H_\mathrm{S}\mathcal{O}. \tag{2.26}$$

For white noise frequency fluctuations of a two-level atom this corresponds to a Liouvillian with jump operator σ^{22} and for a single mode cavity we obtain the jump operator $a^\dagger a$. The corresponding rate is determined by the frequency ν characterizing the noise.

2.3.4 Drive laser phase noise

Such an effective dephasing process can also stem from a fluctuating phase of a laser. Adding laser phase fluctuations $\phi(t)$ to the Hamiltonian of a driven two-level atom (2.16) leads to

$$H = \hbar\omega_\mathrm{a}\sigma^{22} + i\frac{\Omega}{2}\left(\sigma^{21}e^{-i(\omega_\mathrm{l}t+\phi(t))} - \sigma^{12}e^{i(\omega_\mathrm{l}t+\phi(t))}\right), \tag{2.27}$$

where we chose $f(\mathbf{r}) = 1$. Transforming into the (instantaneous) frame of the fluctuating laser frequency with the unitary transformation

$$U(t) = e^{i(\omega_\mathrm{l}t+\phi(t))\sigma^{22}}, \tag{2.28}$$

according to

$$H' = i\hbar\dot{U}(t)U^\dagger(t) + U(t)H(t)U^\dagger(t), \tag{2.29}$$

results in

$$H_\mathrm{I} = \hbar(\omega_\mathrm{a}-\omega_\mathrm{l})\sigma^{22} + i\hbar\frac{\Omega}{2}\left(\sigma^{21}-\sigma^{12}\right) - \dot{\phi}(t)\sigma^{22}. \tag{2.30}$$

This Hamiltonian has the same structure, with a deterministic and stochastic part, as described in the previous section. For white noise frequency fluctuations, fulfilling $\langle\dot{\phi}(t)\dot{\phi}(t')\rangle = \nu\delta(t-t')$, we will again obtain an effective dephasing process with jump operator σ^{22} and corresponding rate ν.

2.4 Cumulant expansion

The master equation (2.18) fully describes the time evolution of an open quantum system, nevertheless, solving this equation analytically is usually not possible and exact numerical approaches are limited by the size of the Hilbert space. For example, the density matrix of a composite quantum system with N two-level atoms has a size of 2^{2N}. This exponential scaling with the constituents restricts full quantum calculations

to rather small systems. However, very often one is only interested in some specific operator expectation values. From the master equation (2.18) we can derive the time evolution of an operator expectation value $\langle\mathcal{O}\rangle$ as follows: The time derivative of a not explicitly time-dependent operator can be written as

$$\frac{d}{dt}\langle\mathcal{O}\rangle = \frac{d}{dt}\mathrm{tr}\{\mathcal{O}\rho\} = \mathrm{tr}\{\mathcal{O}\frac{d}{dt}\rho\}. \tag{2.31}$$

Inserting the master equation (2.18) with the Liouvillian term in Lindblad form (2.19) we obtain

$$\frac{d}{dt}\langle\mathcal{O}\rangle = -i\,\mathrm{tr}\{\mathcal{O}[H,\rho]\} + \frac{1}{2}\sum_j R_j\Big(2\,\mathrm{tr}\{\mathcal{O}J_j\rho J_j^\dagger\} - \mathrm{tr}\{\mathcal{O}J_j^\dagger J_j\rho\} - \mathrm{tr}\{\mathcal{O}\rho J_j^\dagger J_j\}\Big). \tag{2.32}$$

Using the cyclic permutation property of the trace we find

$$\frac{d}{dt}\langle\mathcal{O}\rangle = i\,\langle[H,\mathcal{O}]\rangle + \frac{1}{2}\sum_j R_j\Big(2\langle J_j^\dagger\mathcal{O}J_j\rangle - \langle\mathcal{O}J_j^\dagger J_j\rangle - \langle J_j^\dagger J_j\mathcal{O}\rangle\Big). \tag{2.33}$$

Equivalently this equation can be derived from the average of the quantum Langevin equation [2.13, 2.17].

Using Eq. (2.33) we can directly derive the time evolution for a desired expectation value. But, one will immediately encounter the problem that this equation depends on other expectation values, potentially including multiple operators. To be able to calculate the dynamics, a closed set of equations for all appearing expectation values would need to be derived. For most systems this procedure leads to an infinite, or at least huge, set of coupled differential equations. In this straightforward approach we would again capture the full quantum description, reflecting the master equation. However, there is a variety of systems featuring only a limited amount of quantum correlations, which do not require a full quantum model. A measure for the quantum correlations in a product of n operators $\mathcal{O}_1\mathcal{O}_2...\mathcal{O}_n$ is the joint cumulant [2.18]

$$\langle\mathcal{O}_1\mathcal{O}_2...\mathcal{O}_n\rangle_c = \sum_{p\in P(\mathcal{I})}(|p|-1)!(-1)^{|p|-1}\prod_{B\in p}\langle\prod_{i\in B}\mathcal{O}_i\rangle\,, \tag{2.34}$$

with $\mathcal{I}=\{1,2,...,n\}$, $P(\mathcal{I})$ the set of all partitions of $\mathcal{I}$, $|p|$ denotes the length of the partition p, and B runs over the blocks of each partition. A vanishing joint cumulant indicates that at least one operator in the product is independent of the others. To make this abstract expression tangible we write it down explicitly for the two cases $n=2$ and $n=3$

$$\langle\mathcal{O}_1\mathcal{O}_2\rangle_c = \langle\mathcal{O}_1\mathcal{O}_2\rangle - \langle\mathcal{O}_1\rangle\langle\mathcal{O}_2\rangle \tag{2.35a}$$

$$\begin{aligned}\langle\mathcal{O}_1\mathcal{O}_2\mathcal{O}_3\rangle_c = {}& \langle\mathcal{O}_1\mathcal{O}_2\mathcal{O}_3\rangle - \langle\mathcal{O}_1\mathcal{O}_2\rangle\langle\mathcal{O}_3\rangle - \langle\mathcal{O}_1\rangle\langle\mathcal{O}_2\mathcal{O}_3\rangle \\ & - \langle\mathcal{O}_1\mathcal{O}_3\rangle\langle\mathcal{O}_2\rangle + 2\langle\mathcal{O}_1\rangle\langle\mathcal{O}_2\rangle\langle\mathcal{O}_3\rangle.\end{aligned} \tag{2.35b}$$

In general, the joint cumulant of order n, i.e., for the product of n operators, represents

the difference between the average of order n and lower orders. Hence, if the n-th order cumulant is equal to zero, we can express the corresponding n-th order average by averages of order $n-1$ and below. From Eq. (2.34) we derive

$$\langle \mathcal{O}_1 \mathcal{O}_2 ... \mathcal{O}_n \rangle = \sum_{p \in P(\mathcal{I}) \setminus \mathcal{I}} (|p|-1)!(-1)^{|p|} \prod_{B \in p} \langle \prod_{i \in B} \mathcal{O}_i \rangle \,, \tag{2.36}$$

where the sum runs over all partitions of $\mathcal{I}$ not including $\mathcal{I}$ itself. For the two examples in Eq. (2.35) we obtain

$$\langle \mathcal{O}_1 \mathcal{O}_2 \rangle = \langle \mathcal{O}_1 \rangle \langle \mathcal{O}_2 \rangle \tag{2.37a}$$

$$\langle \mathcal{O}_1 \mathcal{O}_2 \mathcal{O}_3 \rangle = \langle \mathcal{O}_1 \mathcal{O}_2 \rangle \langle \mathcal{O}_3 \rangle + \langle \mathcal{O}_1 \rangle \langle \mathcal{O}_2 \mathcal{O}_3 \rangle + \langle \mathcal{O}_1 \mathcal{O}_3 \rangle \langle \mathcal{O}_2 \rangle - 2 \langle \mathcal{O}_1 \rangle \langle \mathcal{O}_2 \rangle \langle \mathcal{O}_3 \rangle. \tag{2.37b}$$

Rewriting an average according to Eq. (2.36) is only exact if the corresponding joint cumulant vanishes. We can also do it if this is not the case, though, it will be an approximation then, which neglects quantum correlations or equivalently assumes that the joint cumulant of the operator product is zero. The resulting inaccuracy of this approximation in the cumulant expansion method is determined by the joint cumulant. Keeping averages of the product for n operators and approximating all above is called the n-th order cumulant expansion. Using the cumulant expansion method to approximate averages to a desired order always leads to a closed set of equations. For a system of N particles in the n-th order cumulant expansion, the number of equations scales as N^n.

In section 2.5.1 and 2.7 we apply the second order cumulant expansion in two particular examples. Furthermore, the method has been used in all publications of this thesis, except for the one in chapter 9.

2.4.1 Practical implementation

The cumulant expansion method is well suited for large systems with moderate quantum correlations. Examples are cavity QED systems [2.19] as lasers [2.20] and optomechanical systems in specific regimes [2.21], but also dipole interacting atomic arrays [2.22, 2.23] or coupled harmonic oscillator systems [2.24]. This expansion was and still is used successfully to approximate specific systems, but there is one obstacle to its practicality: In order to solve the equations of motion one needs to derive them first. This might be a straightforward task, obtaining them from Eq. (2.33) by using operator commutation relations and then applying the cumulant expansion (2.36) to some desired order, however, for non-trivial systems it is usually very tedious and error-prone. In many cases it is not possible in a feasible amount of time. To this end, we created the toolbox *QuantumCumulants.jl* [2.17, 2.25], which automatically derives the symbolic equations and additionally implements them numerically. The underlying concept of the program is actually quite simple:

The equation of motion for an operator average $\langle \mathcal{O} \rangle$ of an open quantum system is implemented according to Eq. (2.33), where the user only needs to specify the operator (product) $\mathcal{O}$, the Hamiltonian H of the system and a list of jump operators J with their corresponding rates. To define the Hamiltonian and dissipative processes, it is possible to create symbolic parameters and the fundamental operators of quantum

optics, described in section 2.1, are predefined with their commutation relations. These commutation relations are applied to the operators via the following rules: From the commutation relation of the bosonic creation and annihilation operator (2.6) we obtain the rule

$$aa^\dagger \to a^\dagger a + 1, \tag{2.38}$$

which is immediately applied if the expression $aa^\dagger$ is found in the equations. This means these terms are forced to normal ordering. For multi-level atoms the orthonormality (2.4) between two states is used. Therefore, a product of transition operators is simplified as

$$\sigma^{ij}\sigma^{kl} \to \delta_{jk}\sigma^{il}. \tag{2.39}$$

Hence, it either results in another transition operator or vanishes. After the simplification on the operator level, the cumulant expansion to a desired order is performed according to Eq. (2.36). To expand a higher order term by several orders, the cumulant expansion is applied successively.

A more detailed description of the toolbox's working principle can be found in chapter 4 and on the official documentation [2.26].

Choice of rules and operators

The above described rules for the operators have some arbitrariness to them, which is important to be aware of. For example, we choose normal ordering for the bosonic operators. To describe photons this seems to be the natural choice to interpret the mean photon number $a^\dagger a$ correctly, however, there might be other systems where anti-normal ($aa^\dagger$) or symmetric ($(a^\dagger a + aa^\dagger)/2$) ordering is the better choice.

In the case of transition operators we simplify the expression as far as possible. Thus, there will be at maximum one transition operator per atom in an operator product. The resulting transition operator can also be a projector, this implies that we keep the discrete energy structure, which already implies some quantumness. Therefore, it is not possible to derive fully classical equations for interacting dipoles with the implemented rule. The related question if, e.g., $\langle\sigma^{22}\rangle = \langle\sigma^{21}\sigma^{12}\rangle$ is a first or second order term arose several times. The simple answer to it is that it is just a matter of definition and in any case one needs to choose the order of the approximation such that it is reasonable for the investigated system. For many quantum optics systems it has proven advantageous to consider the above term as a first order one, therefore we choose this convention.

Symbolic sums and indices

A new key extension we have added to the toolbox [2.25] after the publication in chapter 4 are symbolic sums and indices [2.26]. This allows us to define and solve systems with multiple elements of the same kind very efficiently. A particular example is the Tavis-Cummings Hamiltonian (2.14) introduced in section 2.2. Instead of deriving the equation for each atom individually, we can now derive the equation for the i-th atom, specified with a symbolic index i. In the end, we can then either evaluate the

equations for a specific number of atoms or if we assume that all atoms behave identically we can scale up the system, which can reduce the number of equations enormously. With the latter approach it is possible to describe realistic system sizes since the particle number merely enters as a numerical factor. For this and other new features we refer to the documentation of the toolbox [2.26].

2.5 Spectrum

A fascinating feature of lasers that distinguishes them from other light sources is their narrow frequency spectrum [2.27]. For a stationary field the spectrum is given by the Fourier transform of the two-time correlation function [2.1, 2.28]

$$S(\omega) = \mathrm{Re}\left[\int_0^\infty e^{i\omega\tau}\langle a^\dagger(t+\tau)a(t)\rangle d\tau\right], \tag{2.40}$$

where t is some fixed time at which the system is in the steady state. Therefore, in order to calculate the spectrum of the laser, we first need to determine the two-time correlation function of the field $\langle a^\dagger(t+\tau)a(t)\rangle$. To this end, we use the quantum regression theorem [2.1, 2.29], which states that the expectation value of an operator product evaluated at different times $\langle \mathcal{O}_1(t+\tau)\mathcal{O}_2(t)\rangle$ follows the same equation as $\langle \mathcal{O}_1(t+\tau)\rangle$, with respect to τ. For the time evolution of the two-time correlation function $\langle a^\dagger(t+\tau)a(t)\rangle$ this means, that we can derive the equation for $\langle a^\dagger(t+\tau)\rangle$ and complement all averages with $a(t)$. The equation for $\langle a^\dagger(t+\tau)a(t)\rangle$ might depend on other two-time correlation functions and time-dependent expectation values. For the correlation functions we derive the equations for the additional ones. The time-dependent expectation values can be treated as constants since we demand to be in a steady state. To obtain a closed set of equations we use the cumulant expansion. In section 2.7 we derive the equations for a superradiant laser in a second order cumulant expansion.

To evaluate the Fourier transformation in Eq. (2.40) we can follow different approaches. The straightforward way is to calculate the time evolution of the correlation function and then take the Fourier transform of this. Another possibility is to calculate the Laplace transform of the correlation function, this is usually much more efficient. Since $a(t)$ can appear at most once in each operator product, we can in general express the correlation function equations for a system in steady state as

$$\frac{d}{d\tau}\mathbf{g}(\tau) = \mathbf{M}\mathbf{g}(\tau) + \mathbf{c}, \tag{2.41}$$

where $\mathbf{g}(\tau)$ is the vector of two-time correlation functions, $\mathbf{M}$ a matrix of parameters and steady state values and $\mathbf{c}$ a possible constant inhomogeneity of the differential equation set. The Laplace transform $\tilde{\mathbf{g}}(s) = \mathcal{L}\{\mathbf{g}(\tau)\}$ corresponds to the Fourier transform in Eq. (2.40) for $s = i\omega$. Applying the Laplace transform on Eq. (2.41) leads to

$$s\tilde{\mathbf{g}}(s) - \mathbf{g}(0) = \mathbf{M}\tilde{\mathbf{g}}(s) + \frac{\mathbf{c}}{s}. \tag{2.42}$$

Rewriting this expression we obtain an equation of the form $\mathbf{A}\tilde{\mathbf{g}}(s) = \mathbf{b}$, where $\mathbf{A} = s\mathbb{1} - \mathbf{M}$ and $\mathbf{b} = \mathbf{g}(0) + \mathbf{c}/s$. Solving this system of linear equations as

$$\tilde{\mathbf{g}}(s) = \mathbf{A}^{-1}\mathbf{b}, \tag{2.43}$$

which essentially corresponds to inverting the matrix A, can be very efficient and is usually much faster than the straightforward time evolution approach. In some cases it can even be solved analytically [2.20].

2.5.1 Drive laser phase noise

To numerically treat quantum optic systems we usually transform into a suitable rotating frame. In many cases this allows us to eliminate the explicit time dependence in the Hamiltonian, as in section 2.3.4. Furthermore, we can get rid of the huge optical frequencies, which are usually orders of magnitude larger than the other frequencies of the system. Dealing numerically with very small and large numbers at the same time is disadvantageous, therefore one tries to describe the system in terms of frequency differences. Calculating the spectrum in a fixed (coherent) reference frame does not lead to any trouble, all results are simply shifted by the constant frequency of the reference frame. However, transforming the system into a fluctuating (instantaneous) rotating frame as we did in section 2.3.4, does not allow for a straightforward calculation of the spectrum, since there is no constant reference frequency [2.30]. Obtaining the correct spectrum in that case requires a more careful derivation for the set of correlation functions:

If avoidable, one does not want to deal with a time-dependent or stochastic Hamiltonian. Therefore, we describe the system in the instantaneous rotating frame with the Hamiltonian H_I. Let's assume that we have already calculate the steady state of the system in this frame. As mentioned before, we can not use the instantaneous frame to calculate the spectrum, a rotating frame with constant frequency is required. To make it more descriptive, we consider the example of a two-level atom inside a cavity, driven by a noisy laser. This system is described by the Jaynes-Cummings Hamiltonian (2.13) with an additional classical atomic drive term including phase fluctuations (2.27). In the laboratory frame we obtain the Hamiltonian ($\hbar = 1$)

$$H_\mathrm{lab} = \omega_\mathrm{a}\sigma^{22} + \omega_\mathrm{f} a^\dagger a + g\left(\sigma^{21}a + \sigma^{12}a^\dagger\right) + i\frac{\Omega}{2}\left(\sigma^{21}e^{-i(\omega_\mathrm{l}t+\phi(t))} - \sigma^{12}e^{i(\omega_\mathrm{l}t+\phi(t))}\right). \tag{2.44}$$

Furthermore, we assume atomic and cavity decay as described in section 2.3.1. Transforming (2.29) the Hamiltonian into the instantaneous frame of the fluctuating laser with the unitary $U_\mathrm{I}(t) = e^{i(\omega_\mathrm{l}t+\phi(t))(a^\dagger a+\sigma^{22})}$ yields

$$H_\mathrm{I} = -\Delta_\mathrm{a}\sigma^{22} - \Delta_\mathrm{f} a^\dagger a + g\left(\sigma^{21}a + \sigma^{12}a^\dagger\right) + i\frac{\Omega}{2}\left(\sigma^{21} - \sigma^{12}\right) - \dot{\phi}(t)\left(a^\dagger a + \sigma^{22}\right). \tag{2.45}$$

We introduced here the atomic $\Delta_\mathrm{a} = \omega_\mathrm{a} - \omega_\mathrm{l}$ and cavity detuning $\Delta_\mathrm{f} = \omega_\mathrm{f} - \omega_\mathrm{l}$. Following the procedure in section 2.3.3 we can rewrite the stochastic part as a dephasing process

with jump operator $a^\dagger a + \sigma^{22}$, which allows us to solve the dynamics of the system with a time independent Hamiltonian. As discussed before, to obtain the correct spectrum we need to go into a rotating frame with a fixed frequency. Therefore, we transform the Hamiltonian H_{lab} into the coherent frame of the laser (without the noise term) by the unitary transformation $U_{\text{c}}(t) = e^{i\omega_{\text{l}} t(a^\dagger a + \sigma^{22})}$. We end up with the (time-dependent) Hamiltonian

$$H_{\text{C}} = -\Delta_{\text{a}}\sigma^{22} - \Delta_{\text{f}} a^\dagger a + g\left(\sigma^{21} a + \sigma_j^{12} a^\dagger\right) + i\frac{\Omega}{2}\left(\sigma^{21} e^{-i\phi(t)} - \sigma^{12} e^{i\phi(t)}\right). \tag{2.46}$$

Deriving the equation of the two-time correlation function for the field with this Hamiltonian, as described in section 2.5, leads to

$$\frac{d}{d\tau}\langle \tilde{a}^\dagger \tilde{a}_0\rangle = -\left(i\Delta_{\text{f}} + \frac{\kappa}{2}\right)\langle \tilde{a}^\dagger \tilde{a}_0\rangle + ig\langle \tilde{\sigma}^{21}\tilde{a}_0\rangle. \tag{2.47}$$

The tilde indicates the coherent rotating frame, we omit the time dependence (τ) and use the notation $\tilde{a}_0 = \tilde{a}(0)$ for readability, where we set $t = 0$. Next, we derive the equation for $\langle \tilde{\sigma}^{21}\tilde{a}_0\rangle$

$$\frac{d}{d\tau}\langle \tilde{\sigma}^{21}\tilde{a}_0\rangle = -\frac{\Gamma}{2}\langle \tilde{\sigma}^{21}\tilde{a}_0\rangle + \Omega\langle \tilde{\sigma}^{22}\tilde{a}_0\rangle e^{i\phi(t)} - \frac{\Omega}{2}\langle \tilde{a}_0\rangle e^{i\phi(t)} + ig\langle \tilde{a}^\dagger \tilde{a}_0\rangle - 2ig\langle \tilde{a}^\dagger \tilde{\sigma}^{22}\tilde{a}_0\rangle. \tag{2.48}$$

Assuming we want to treat the system in second order, we expand the third order term $\langle \tilde{a}^\dagger \tilde{\sigma}^{22}\tilde{a}_0\rangle$ as usual. Furthermore, undesired terms proportional to $e^{i\phi(t)}$ appear in Eq. (2.48). To deal with them we use the following properties: Averages not depending on two different times are steady state values. Additionally, we can transform them from the coherent to the instantaneous frame with the unitary transformation $U_{\text{C}\to\text{I}}(t) = e^{i\phi(t)(a^\dagger a + \sigma^{22})}$. Thereby we can use the steady state values from the instantaneous frame. Performing the cumulant expansion to second order and transforming all steady state values with the unitary leads to

$$\begin{aligned}\frac{d}{d\tau}\langle \tilde{\sigma}^{21}\tilde{a}_0\rangle = &-\frac{\Gamma}{2}\langle \tilde{\sigma}^{21}\tilde{a}_0\rangle + \Omega\langle \tilde{\sigma}^{22}\tilde{a}_0\rangle e^{i\phi(t)} - \frac{\Omega}{2}\langle a\rangle + ig\langle \tilde{a}^\dagger \tilde{a}_0\rangle \\ &- 2ig\left(\langle a^\dagger\rangle\langle \tilde{\sigma}^{22}\tilde{a}_0\rangle e^{i\phi(t)} + \langle a\rangle\langle a^\dagger \sigma^{22}\rangle + \langle \sigma^{22}\rangle\langle \tilde{a}^\dagger \tilde{a}_0\rangle - 2\langle a^\dagger\rangle\langle a\rangle\langle \sigma^{22}\rangle\right).\end{aligned} \tag{2.49}$$

Note that we got rid of the factor $e^{i\phi(t)}$ in the steady state field term, but we gained the same factor from the steady state value of $\langle a^\dagger\rangle$. However, we find in Eq. (2.49) that the unknown two-time correlation function $\langle \tilde{\sigma}^{22}\tilde{a}_0\rangle$ solely appears in combination with $e^{i\phi(t)}$. Therefore, we simply derive the equation for $\langle \tilde{\sigma}^{22}\tilde{a}_0\rangle e^{i\phi(t)}$. From the product rule of the derivative we obtain

$$\text{(S)} \qquad \frac{d}{d\tau}\langle \tilde{\sigma}^{22}\tilde{a}_0\rangle e^{i\phi(t)} = i\dot{\phi}(\tau)\langle \tilde{\sigma}^{22}\tilde{a}_0\rangle e^{i\phi(\tau)} + \frac{d}{d\tau}\left(\langle \tilde{\sigma}^{22}\tilde{a}_0\rangle\right) e^{i\phi(t)}. \tag{2.50}$$

As described in section 2.3.3 we need to transform this stochastic equation from Stratonovich to Itô form. For white noise frequency fluctuations, obeying $\langle \dot{\phi}(t)\dot{\phi}(t')\rangle =$

$\nu\delta(t-t')$, this leads to [2.1, 2.13]

$$\text{(I)} \qquad \frac{d}{d\tau}\langle\tilde{\sigma}^{22}\tilde{a}_0\rangle e^{i\phi(t)} = -\frac{\nu}{2}\langle\tilde{\sigma}^{22}\tilde{a}_0\rangle e^{i\phi(\tau)} + \frac{d}{d\tau}\left(\langle\tilde{\sigma}^{22}\tilde{a}_0\rangle\right) e^{i\phi(t)}. \tag{2.51}$$

Evaluating the second term, applying the cumulant expansion and the steady state transformation procedure as described above, we will find other two-time correlation functions for which the equations need to be derived. They might also be combined with a factor of the form $e^{\pm in\phi(\tau)}$, where n is an integer. Including these factors in the derivation and performing the Itô correction as in Eq. (2.51) leads to the following closed of set equations:

$$\frac{d}{d\tau}\langle\tilde{a}^\dagger\tilde{a}_0\rangle = -\left(i\Delta_\mathrm{f} + \frac{\kappa}{2}\right)\langle\tilde{a}^\dagger\tilde{a}_0\rangle + ig\langle\tilde{\sigma}^{21}\tilde{a}_0\rangle \tag{2.52a}$$

$$\begin{aligned}\frac{d}{d\tau}\langle\tilde{\sigma}^{21}\tilde{a}_0\rangle = &-\frac{\Gamma}{2}\langle\tilde{\sigma}^{21}\tilde{a}_0\rangle + \Omega\langle\tilde{\sigma}^{22}\tilde{a}_0\rangle e^{i\phi(t)} - \frac{\Omega}{2}\langle a\rangle + ig\langle\tilde{a}^\dagger\tilde{a}_0\rangle \\ &-2ig\Big(\langle a^\dagger\rangle\langle\tilde{\sigma}^{22}\tilde{a}_0\rangle e^{i\phi(t)} + \langle a\rangle\langle a^\dagger\sigma^{22}\rangle + \langle\sigma^{22}\rangle\langle\tilde{a}^\dagger\tilde{a}_0\rangle - 2\langle a^\dagger\rangle\langle a\rangle\langle\sigma^{22}\rangle\Big)\end{aligned} \tag{2.52b}$$

$$\begin{aligned}\frac{d}{d\tau}\langle\tilde{\sigma}^{22}\tilde{a}_0\rangle e^{i\phi(t)} = &-\frac{\nu}{2}\langle\tilde{\sigma}^{22}\tilde{a}_0\rangle e^{i\phi(\tau)} - \Gamma\langle\tilde{\sigma}^{22}\tilde{a}_0\rangle - \frac{\Omega}{2}\Big(\langle\tilde{\sigma}^{21}\tilde{a}_0\rangle + \langle\tilde{\sigma}^{12}\tilde{a}_0\rangle\Big) \\ &-ig\Big(\langle\sigma^{21}\rangle\langle\tilde{a}\tilde{a}_0\rangle e^{2i\phi(\tau)} + \langle a\rangle\langle a\sigma^{21}\rangle + \langle a\rangle\langle\tilde{\sigma}^{21}\tilde{a}_0\rangle - 2\langle a\rangle\langle a\rangle\langle\sigma^{21}\rangle\Big) \\ &+ig\Big(\langle a\rangle\langle a^\dagger\sigma^{12}\rangle + \langle\sigma^{12}\rangle\langle\tilde{a}^\dagger\tilde{a}_0\rangle + \langle a^\dagger\rangle\langle\tilde{\sigma}^{12}\tilde{a}_0\rangle e^{2i\phi(\tau)} - 2\langle a^\dagger\rangle\langle a\rangle\langle\sigma^{12}\rangle\Big)\end{aligned} \tag{2.52c}$$

$$\frac{d}{d\tau}\langle\tilde{a}\tilde{a}_0\rangle e^{2i\phi(\tau)} = \Big(-2\nu + i\Delta - \frac{\kappa}{2}\Big)\langle\tilde{a}\tilde{a}_0\rangle e^{2i\phi(\tau)} - ig\langle\tilde{\sigma}^{12}\tilde{a}_0\rangle e^{2i\phi(\tau)} \tag{2.52d}$$

$$\begin{aligned}\frac{d}{d\tau}\langle\tilde{\sigma}^{12}\tilde{a}_0\rangle e^{2i\phi(\tau)} = &-2\nu\langle\tilde{\sigma}^{12}\tilde{a}_0\rangle e^{2i\phi(\tau)} - \frac{\Gamma}{2}\langle\tilde{\sigma}^{12}\tilde{a}_0\rangle e^{2i\phi(\tau)} + \Omega\langle\tilde{\sigma}^{22}\tilde{a}_0\rangle e^{i\phi(\tau)} \\ &+2ig\Big(\langle a\rangle\langle a\sigma^{22}\rangle + \langle\sigma^{22}\rangle\langle\tilde{a}\tilde{a}_0\rangle e^{2i\phi(\tau)} + \langle a\rangle\langle\tilde{\sigma}^{22}\tilde{a}_0\rangle e^{i\phi(\tau)} - 2\langle a\rangle\langle a\rangle\langle\sigma^{22}\rangle\Big) \\ &-\frac{\Omega}{2}\langle a\rangle - ig\langle\tilde{a}\tilde{a}_0\rangle e^{2i\phi(\tau)}\end{aligned} \tag{2.52e}$$

2.5.2 Filter cavities

An intuitive and straightforward method to calculate the cavity emission spectrum is to simulate the measurement with frequency filters. This can be implemented by a back action free weak coupling of filter cavities with different resonance frequencies to the main cavity [2.31, 2.32]. The distribution of the photon number in the filter cavities depicts the frequency spectrum. A system described by a Hamiltonian H_sys can be extend by N_fc filter cavities as

$$H = H_\mathrm{sys} + \sum_j^{N_\mathrm{fc}} \omega_\mathrm{fc}^j f_j^\dagger f_j + g_\mathrm{fc}\sum_j^{N_\mathrm{fc}}\left(f_j^\dagger a + f_j a^\dagger\right), \tag{2.53}$$

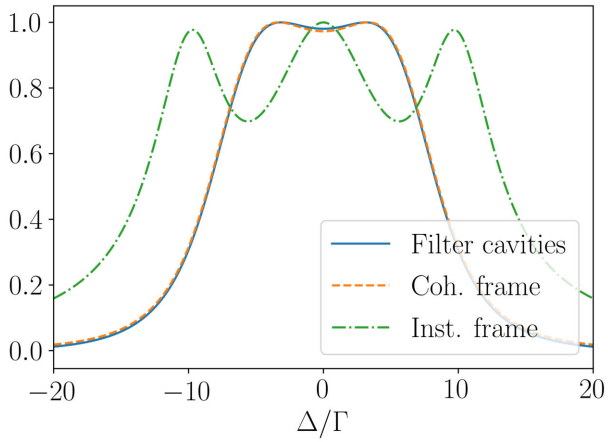

Figure 2.2: *Spectrum methods comparison.* The spectrum calculated in the coherent frame matches the filter cavity method. The spectrum calculated in the instantaneous frame yields a wrong result. The parameters are $\Delta_a = \Delta_f = 0\Gamma$, $g = \Gamma/2$, $\kappa = 200\Gamma$, $\Omega = 10\Gamma$, $\nu = 10\Gamma$ and $\kappa_{fc} = g_{fc} = \Gamma/50$.

with $f_j^\dagger$ (f_j) the photon creation (annihilation) operator of the j-th filter cavity, ω_{fc}^j the resonance frequency and g_{fc} the coupling strength of the filter cavities to the main cavity. For the dissipative processes we need to add the decay of the filter cavities described by the jump operators f^j with photon loss rate κ_{fc} equal for all of them. The bandwidth of the filter cavities κ_{fc} sets the frequency resolution and the coupling g_{fc} is required to be so weak that back action on the system is negligible. This (brute-force) approach is usually rather computationally intense, however, it has the advantage that the spectrum can be calculated straightforwardly within an ordinary time evolution. Additionally, difficulties as in the previous section due to the (instantaneous) rotating frame do not arise, since the photon numbers in the filter cavities correspond to the absolute frequencies ω_{fc}^j. Therefore, in principle, it always yields the correct spectrum, which can be convenient to check the results of more complicated systems [2.33].

In figure 2.2 we compare the spectrum obtained by the filter cavity method with the Fourier transform, for the example of the atom coupled to the cavity driven by a noisy laser, described in section 2.5.1. We see that the filter cavity spectrum (blue solid line) agrees well with the spectrum calculated in the coherent frame (orange dashed). The small difference stems from the inaccuracy of the filter cavity method, due to the small but finite values of g_f and κ_f. In contrast, the spectrum calculated in the instantaneous frame of the fluctuating drive laser (green dashed-dotted line) is completely different.

2.6 Cavity mediated superradiance

In section 2.3.1 we introduced the free space decay of a single excited (two-level) atom, originating from the interaction with the electromagnetic vacuum modes. For a dilute

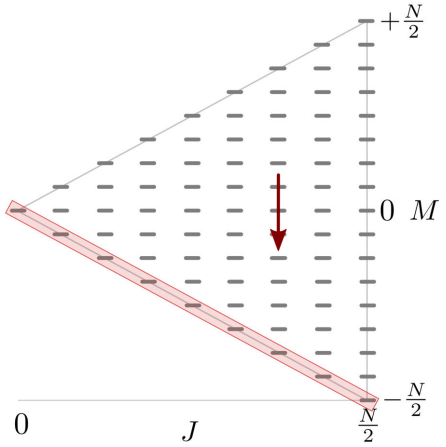

Figure 2.3: *Dicke states.* The Dicke states for $N = 16$ are shown. The red arrow indicates the action of collective decay. States at $M = -J$ (labeled red) can not decay collectively.

cloud of emitters we can still describe each atom individually, as long as the spacing between them is sufficiently large. However, the behavior of an excited atomic ensemble changes drastically, if the distance between the atoms is at the order of the atomic transition wavelength. In this limit collective emission from fully excited atoms occurs, which results in a strong and short light pulse with a peak intensity proportional to the square of the atom number [2.34]. This phenomenon, called superradiance, essentially stems from the interaction of multiple emitters with a common electromagnetic (vacuum) mode [2.35].

Achieving superradiance in free space is typically very challenging, due to the required confinement in the small volume. A convenient way to circumvent this problem is to use a cavity. Instead of the electromagnetic vacuum modes in free space, the interaction between the atoms is mediated by a cavity field mode. The crucial advantage is that the atoms can be widely distributed, due to the periodic long-range interaction of the standing wave along the cavity axis [2.5].

In the bad cavity regime, where photons inside the cavity are lost immediately such that reabsorption by the atoms is highly unlikely, we can adiabatically eliminate the cavity mode. The resulting equations feature conceptionally the same collective decay process as the optimal free space case described by the jump operator $J^- = \sum_{j=1}^{N} \sigma^{12}$ [2.36–2.38]. In free space the corresponding dissipative rate is the single atom decay rate Γ, whereas for the cavity mediated case we obtain the rate $C\Gamma$, which corresponds to the single atom photon emission rate into the cavity, with the cooperativity parameter $C = \frac{4g^2}{\kappa\Gamma}$. Note that the N^2 emission enhancement originates from the sum over all atoms in the jump operator.

2.6.1 Dicke states

A particularly useful representation to describe the collective behavior of N identical two-level atoms are the Dicke states $|J, M\rangle$ [2.34], the eigenstates of the collective spin operators

$$J^z |J, M\rangle = \frac{1}{2} \sum_j \sigma_j^z |J, M\rangle = M |J, M\rangle \tag{2.54a}$$

$$\mathbf{J}^2 |J, M\rangle = \frac{3N}{4} + \frac{1}{4} \sum_{j \neq k} \left[\sigma_j^{21} \sigma_k^{12} + \sigma_j^z \sigma_k^z \right] |J, M\rangle = J(J+1) |J, M\rangle , \tag{2.54b}$$

with $0 \leq J \leq N/2$ and $|M| \leq J$, where we use the notation of transition operators and $\sigma_j^z = \sigma_j^{22} - \sigma_j^{11}$. These states can be visualized in a plot with J on the x- and M on the y-axis, leading to a triangle shaped diagram of states [2.37, 2.39]. In figure 2.3 we show an example for $N = 16$. Investigating the action of the collective decay operator we find that it solely reduces M, but leaves J unchanged

$$J^- |J, M\rangle = \sqrt{(J - M + 1)(J + M)} |J, M - 1\rangle . \tag{2.55}$$

In the visualization of the Dicke triangle this corresponds to a vertical downward line. From this we see that a state at the lower edge of the triangle ($M = -J$) can not decay collectively. Incoherently pumping an atomic ensemble, as described in section 2.3.2, populates mostly such states with minimal J. This means a non-inverted ($M < 0$) incoherently pumped ensemble does not emit a superradiant pulse [2.23, 2.36, 2.37]. For cavity mediated superradiance a very similar behavior can occur for a transverse coherent excitation of the atoms. Here the alternating sign of the cavity coupling leads to an effective population of mainly the states, which are subradiant with respect to the collective cavity emission. Therefore, with a transverse drive, a superradiant pulse will only appear for coherent excitation which achieves inversion. A more detailed explanation can be found in the publication of chapter 6, where we showed this phenomenon theoretically. Preliminary results of an experimental verification are shown in chapter 7.

2.7 Superradiant laser

In this section we introduce the theoretical concept and show the main properties of the superradiant laser [2.20, 2.40, 2.41]. To this end, we utilize many of the tools developed so far. A minimalistic model [see figure 2.4] to describe this system features N two-level atoms coupled to a single mode cavity described by the Tavis-Cummings Hamiltonian (2.14). To gain inversion the atoms are incoherently pumped with a repumping rate R and cavity photons are lost very quickly at a decay rate κ. Besides these main constituents we include the individual decay and dephasing of the atoms with rates Γ and ν, respectively. Furthermore, we model thermal fluctuations of the cavity mirrors as white noise resonance frequency fluctuations with a cavity dephasing term specified by the rate ξ. We derive the equations of motion for this system in a second order cumulant expansion [2.17, 2.20]. The main system observable we are interested in is the

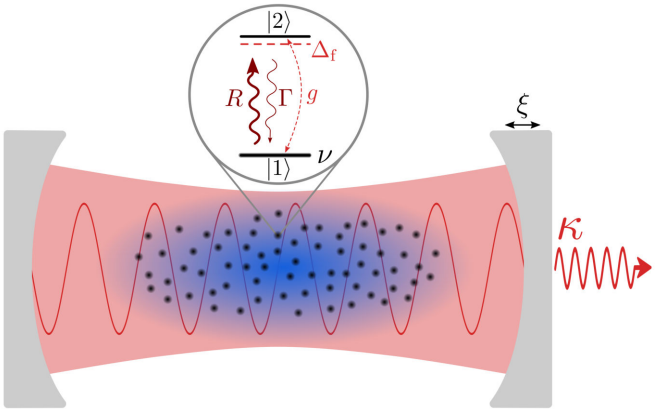

Figure 2.4: *Schematics superradiant laser.* N two-level atoms couple to a single cavity mode with strength g. The atoms are incoherently pumped, decay and dephase individually with rates R, Γ and ν, respectively. Cavity photons are lost at a rate κ and cavity dephasing is characterized by the rate ξ.

cavity photon number $\langle a^\dagger a\rangle$. Deriving the equation for this and all the other occurring averages according to Eq. (2.33) leads to the following closed set of equations

$$\frac{d}{dt}\langle a^\dagger a\rangle = i\sum_i^N g_i\langle a\sigma_i^{21}\rangle - i\sum_i^N g_i\langle a^\dagger\sigma_i^{12}\rangle - \kappa\langle a^\dagger a\rangle \tag{2.56a}$$

$$\frac{d}{dt}\langle \sigma_j^{22}\rangle = R\left(1-\langle\sigma_j^{22}\rangle\right) + ig_j\langle a^\dagger\sigma_j^{12}\rangle - ig_j\langle a\sigma_j^{21}\rangle - \Gamma\langle\sigma_j^{22}\rangle \tag{2.56b}$$

$$\begin{aligned}\frac{d}{dt}\langle a^\dagger\sigma_j^{12}\rangle =& -\left(\frac{R+\Gamma+\nu+\kappa+\xi}{2}+i\Delta_\mathrm{f}\right)\langle a^\dagger\sigma_j^{12}\rangle + ig_j\langle a^\dagger a\rangle\left(2\langle\sigma_j^{22}\rangle-1\right)\\ &+i\sum_{i\neq j}^N g_i\langle\sigma_i^{21}\sigma_j^{12}\rangle + ig_j\langle\sigma_j^{22}\rangle\end{aligned} \tag{2.56c}$$

$$\begin{aligned}\frac{d}{dt}\langle\sigma_j^{12}\sigma_k^{21}\rangle =& -\left(R+\Gamma+\nu\right)\langle\sigma_j^{12}\sigma_k^{21}\rangle + ig_j\langle a\sigma_k^{21}\rangle\left(2\langle\sigma_j^{22}\rangle-1\right)\\ &-ig_k\langle a^\dagger\sigma_j^{12}\rangle\left(2\langle\sigma_k^{22}\rangle-1\right).\end{aligned} \tag{2.56d}$$

In this derivation we used that an incoherently pumped system is phase invariant, i.e., terms as $\langle a\rangle$ and $\langle\sigma_j^{12}\rangle$ are and will remain zero for any time. In contrast, a coherently driven system inherits a prescribed phase and these terms do not vanish. Solving this system now for realistic particle numbers with millions of atoms is still not possible, since it would result in billions of equations. However, the number of equations can be massively reduced by assuming that several atoms behave identically. We deploy the most drastic reduction, where we assume that all atoms behave identically, this means $\langle\sigma_j^{22}\rangle = \langle\sigma_1^{22}\rangle$, $\langle a^\dagger\sigma_j^{12}\rangle = \langle a^\dagger\sigma_1^{12}\rangle$ and $\langle\sigma_j^{12}\sigma_k^{21}\rangle = \langle\sigma_1^{12}\sigma_2^{21}\rangle$ for all j and k. Hence, in this case, we obtain a set of only four coupled differential equations. Note that the sums in Eq. (2.56a) and (2.56c) become $\sum_i^N g_i\langle a\sigma_i^{21}\rangle \to Ng\langle a\sigma_1^{21}\rangle$ and

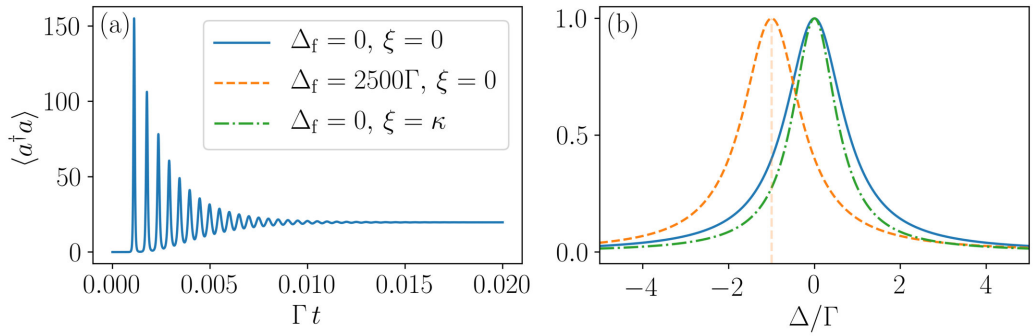

Figure 2.5: *Superradiant laser.* (a) Time evolution of the intra-cavity photon number, superradiant pulses can be observed in the transient phenomenon. (b) Emission spectrum for cavity detuning and dephasing, shows the insensitivity to cavity length fluctuations. The legend in (a) corresponds to both subfigures.

$\sum_{i\neq j}^{N} g_i \langle \sigma_i^{21} \sigma_j^{12} \rangle \to (N-1) g \langle \sigma_1^{21} \sigma_2^{12} \rangle$.

Besides the photon number we are also interested in the spectrum of the laser. To this end, we first need to obtain the equation for the two-time correlation function of the field $\langle a^\dagger a(0) \rangle$. We derive the equations as described in section 2.5, again in a second order cumulant expansion, utilizing the phase invariance of the system and assuming that all atoms behave identically. We obtain the closed set of equations for the correlation functions

$$\frac{d}{d\tau}\langle a^\dagger a(0)\rangle = -\left(\frac{\kappa+\xi}{2} + i\Delta_f\right)\langle a^\dagger a(0)\rangle + iNg\langle \sigma_1^{21} a(0)\rangle \tag{2.57a}$$

$$\frac{d}{d\tau}\langle \sigma_1^{21} a(0)\rangle = -\frac{R+\Gamma+\nu}{2}\langle \sigma_1^{21} a(0)\rangle - ig\left(2\langle \sigma_1^{22}\rangle - 1\right)\langle a^\dagger a(0)\rangle. \tag{2.57b}$$

For the system in steady state the spectrum can be calculated with the Laplace transform as described in section 2.5, we obtain

$$\begin{pmatrix} \langle a^\dagger a\rangle(s) \\ \langle \sigma_1^{21} a\rangle(s) \end{pmatrix} = \begin{pmatrix} i\Delta_f - \frac{\kappa+\xi}{2} & iNg \\ -ig(\langle \sigma_1^{22}\rangle_0 - 1) & -\frac{R+\gamma+\nu}{2} \end{pmatrix}^{-1} \begin{pmatrix} \langle a^\dagger a\rangle_0 \\ \langle \sigma_1^{21} a\rangle_0 \end{pmatrix}, \tag{2.58}$$

where the subscript 0 indicates the steady state of the averages. This leads to the analytic solution for the spectrum

$$S(\Delta) = \langle a^\dagger a\rangle(i\Delta) = \mathrm{Re}\left[\frac{\langle a^\dagger a\rangle_0\left(i\Delta + \frac{R+\Gamma+\nu}{2}\right) - igN\langle \sigma_1^{21} a\rangle_0}{\left(i\Delta + \frac{R+\Gamma+\nu}{2}\right)\left(i\Delta + \frac{\kappa+\xi}{2} - i\Delta_f\right) - g^2 N\langle \sigma_1^{22}\rangle_0}\right]. \tag{2.59}$$

Note that we are in the rotating frame of the atomic transition frequency ω_a, therefore the spectrum is also shifted by this frequency.

Figure 2.5(a) shows the dynamics of the photon number. A noticeable feature of it are the decreasing pulses, which can be explained in the Dicke triangle picture: The incoherent pump populates mainly states with minimal J at the edge of the triangle. For a non-inverted ensemble these states are subradiant with respect to the collective cavity mediated decay, however, as soon as a certain inversion is reached a superradiant pulse occurs, which deexcites the atoms. This process repeats several times until a steady state is reached. In figure 2.5(b) the spectrum is shown. Besides the narrow linewidth close to the optimal value of FWHM $= 4g^2/\kappa$, we also see the intriguing insensitivity to cavity resonance frequency changes. For a cavity detuning of $\Delta_\mathrm{f} = 2500\Gamma$ (orange dashed line) the central lasing frequency is merely changed by $\Delta = 1\Gamma$. For a 'normal' good cavity laser the peak of the spectrum would directly follow the cavity detuning. This feature is also visible for the cavity dephasing $\xi = \kappa$ (green dashed-dotted line). For a 'normal' laser the linewidth would approximately be determined by ξ, here the linewidth is almost not affected, it even becomes a little bit narrower.

We used *QuantumCumulants.jl* to derive and solve the equations, a similar example (without cavity dephasing term) can be found on the documentation of the toolbox [2.26].

3 Publication

New Journal of Physics **22**(11), 113021 (2020)

Continuous narrowband lasing with coherently driven V-level atoms[†]

C. Hotter[1], D. Plankensteiner[1] and H. Ritsch[1]

[1]*Institut für Theoretische Physik, Universität Innsbruck, Technikerstraße 21, A-6020 Innsbruck, Austria*

Simultaneous strong coherent pumping of the two transitions of a V-level atom with very different decay rates has been predicted to create almost perfect inversion on the narrower transition. Using the example of the blue and red transitions in Strontium we show that for suitable operating conditions the corresponding resonant gain can be used to continuously operate a laser on the narrow transition. In particular, for a strong detuning of the pump field with respect to the narrow transition, coherent laser emission occurs close to the bare atomic transition frequency exhibiting only a negligible contribution from coherent pump light scattered into the lasing mode. Calculations of the cavity output spectrum show that the resulting laser linewidth can get much smaller than the bandwidth of the pump light and even the natural linewidth of the narrow atomic transition. Its frequency is closely tied to the atomic transition frequency for properly chosen atom numbers. Simulations including atomic motion show Doppler cooling on the strong transition with minor motion heating on the lasing transition, so that continuous laser operation in the presence of a magneto-optical trap should be possible with current experimental technology.

doi: 10.1088/1367-2630/abc70c

[†]The author of this thesis conducted all analytical and numerical calculations in this paper. D. Plankensteiner provided helpful discussions and support, in particular on the finite laser linewidth part. Furthermore, he created an early version of the toolbox QuantumCumulants.jl, which was used for this project.

3.1 Introduction

It has been a longstanding dream of AMO physics to implement an active optical frequency standard by operating a continuous laser on a narrow atomic transition in close analogy to microwave masers [3.1–3.3]. This new class of lasers would exhibit superb accuracy, precision, and robustness against thermal noise [3.4, 3.5]. In particular, in view of the recent development and outstanding success of optical atomic clocks, worldwide efforts towards implementations of such an active optical clock have enormously grown in the past few years [3.6–3.10]. This was further fueled by the prospects of superior stability and accuracy theoretically predicted for superradiant clock lasers [3.5, 3.11–3.13]. Since in such bad-cavity lasers the phase coherence of the system is stored in the atomic gain medium, the laser setup is largely insensitive to technical fluctuations for an isolated atomic gas. In particular, thermal fluctuations of the cavity mirrors [3.14] are strongly suppressed. An important challenge that hinders the further development in this direction lies in achieving the necessary steady-state inversion of such a narrow transition: the implementation of efficient and minimally perturbative pump schemes proves extremely difficult. Thus, finding a suitable driving mechanism constitutes a central issue for the realization of highly stable active optical frequency standards [3.15].

One possible route create a continuously inverted intra-cavity gain medium is to send a sufficiently dense beam of excited atoms through a cavity [3.16, 3.17]. In this process a π-pulse is applied to the atoms just before they enter the lasing region. However, such a setup requires a cold and dense atomic beam which has to be perfectly controlled. Furthermore, the coherence can only be stored within the part of the atomic medium that is within the active lasing region, which requires a high intra-cavity atom number. Therefore, finding a mechanism to create steady-state inversion by repumping atoms within the cavity is highly desirable since this would allow straightforward continuous operation.

Unfortunately, inversion on a transition cannot simply be achieved by coherent pumping as stimulated emission always compensates absorption. However, in Ref. [3.18] a surprising mechanism leading to steady-state population inversion on the narrower transition of a V-type atom via coherent driving was shown theoretically. In the model considered therein, both transitions of the V-level atom are driven coherently and no direct decay channel between the two excited states is present, as depicted in Fig. 3.1(a). To the best of our knowledge, this scheme was so far not shown experimentally. Interestingly, lasing using a V-level system was recently observed experimentally [3.19]. While the pump mechanism for this virtual-state lasing appears very similar at first sight, it turns out that the system is operated in a distinctly different parameter regime, which leads to anti-Stokes Raman gain with no inversion on the narrow transition.

While the appearance of inversion on the narrow transition has already been theoretically shown, the usefulness of this unconventional driving scheme in a lasing setup [see Fig. 3.1(b)] remained an open question. The aim of this paper is to address precisely this point: we start by reviewing the driving scheme. Then, we show that steady-state inversion can still be achieved for pump lasers with a realistic spectral linewidth far above the natural linewidth of the narrow atomic transition. We proceed by coupling

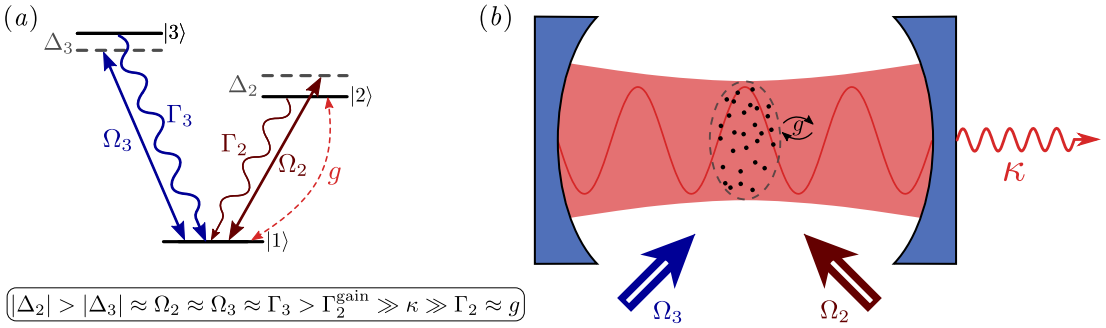

Figure 3.1: *Continuous lasing of a driving V-type atom.* In the sketch (a) we show the considered coherently pumped V-level system. Population inversion can be achieved on the narrower transition, which in our case is the transition $|1\rangle \leftrightarrow |2\rangle$ with a negative detuning on the broad transition, $\Delta_3 < 0$, and $\Delta_2 > 0$. (b) An ensemble of such atoms is then placed inside a cavity and the narrow transition is coupled to the cavity mode with coupling strength g. For later reference we show the frequency hierarchy in the parameter region needed for lasing action in (a). Note that Γ_2^{gain} denotes the power-broadened transition $|1\rangle \leftrightarrow |2\rangle$ which provides the gain for lasing.

the inverted, narrow transition to an optical cavity and show that the system behaves like a laser with a clear threshold for sufficient gain with increasing atom number. As an important feature we predict that the spectral linewidth of the output laser light can be well below that of the narrow transition and the pump light. Note, however, that even though the linewidth of the cavity we consider is much larger than the natural linewidth of the narrow transition, we do not operate in the typical low intensity bad cavity regime: due to the power broadening induced by the strong driving laser the effective linewidth of the gain medium is much larger than that of the optical resonator. Thus, the system resembles more a conventional laser than a superradiant one.

Another important aspect for stable operation of our laser is the thermal back-action of lasing on the gain medium: this includes heating due to optical pumping or photon recoil from spontaneous emission, which causes line broadening as well as particle loss via heating in the gain medium. Hence, we provide an estimate of these effects for the considered unconventional driving scheme. We show that Doppler cooling from the two pump lasers occurs. Therefore, for operating parameters that allow lasing (even though not optimal ones), we find that the kinetic energy of an atomic ensemble subjected to the driving scheme is limited to the Doppler temperature of the broad transition, which should allow stationary operation.

3.2 Steady-State Population Inversion via Coherent Driving

In this section, we provide a brief review of the driving scheme from Ref. [3.18]. Moreover, we investigate the influence of a finite pump laser linewidth and the time scale of the process. Note, that the key point is that population inversion can be achieved without

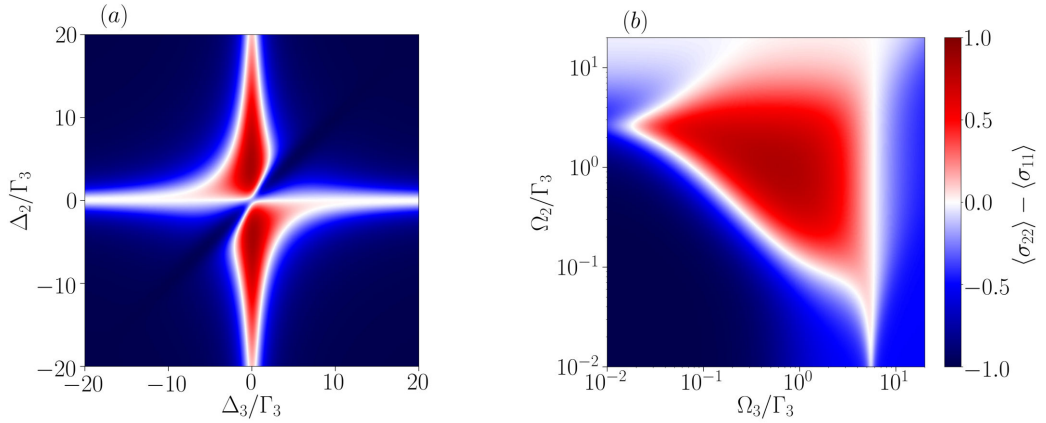

Figure 3.2: *Steady-state inversion of a V-level atom.* The figures show the population difference of the narrow transition $|1\rangle \leftrightarrow |2\rangle$ as a function of both driving laser detunings (a) and Rabi frequencies (b), respectively. Red areas indicate population inversion. The parameters when kept constant are $\Delta_2 = 5\Gamma_3$, $\Delta_3 = -1\Gamma_3$, $\Omega_2 = 0.5\Gamma_3$ and $\Omega_3 = 0.5\Gamma_3$.

a direct irreversible process that causes gain in the excited state. Rather, the scheme here is based on an indirect incoherent process [3.18].

We consider a V-level atom, which is coherently pumped on both transitions, as depicted in Fig. 3.1(a). The ground state is denoted by $|1\rangle$ and the two excited states by $|2\rangle$ and $|3\rangle$. Decay from an excited state $|i\rangle$ to the ground state $|1\rangle$ occurs at a rate Γ_i. Each transition $|1\rangle \leftrightarrow |i\rangle$ is driven coherently with the respective Rabi frequency Ω_i. The difference of the driving laser frequency $\omega_{\ell i}$ and the atomic resonance frequency of a transition ω_i is given by the detuning $\Delta_i = \omega_{\ell i} - \omega_i$. The time evolution of the density matrix ρ for this system is described by the master equation

$$\dot{\rho} = -i[H, \rho] + \mathcal{L}[\rho]. \tag{3.1}$$

In the rotating frame of both pump lasers the Hamiltonian reads

$$H = \sum_{i=\{2,3\}} -\Delta_i \sigma_{ii} + \Omega_i(\sigma_{i1} + \sigma_{1i}) \tag{3.2}$$

with the atomic operators defined by $\sigma_{ij} \coloneqq |i\rangle\langle j|$. The dissipative processes are accounted for by the Liouvillian in standard Lindblad form. For the decay from an excited state $|i\rangle$ to the ground state $|1\rangle$ the Liouvillian term reads

$$\mathcal{L}_\Gamma[\rho] = \sum_{i=\{2,3\}} \frac{\Gamma_i}{2}(2\sigma_{1i}\rho\sigma_{i1} - \sigma_{ii}\rho - \rho\sigma_{ii}) \tag{3.3}$$

Let us stress here again that there is no decay channel from $|3\rangle$ to $|2\rangle$ or vice versa.

A necessary property for the V-level atom to be able to exhibit steady-state population

inversion with this scheme, is that the atom needs to have a big ratio between the two decay rates. In our case we choose the transition $|1\rangle \leftrightarrow |2\rangle$ to be the narrower one, i.e. $\Gamma_3/\Gamma_2 \gg 1$. For example, in the case of ^{88}Sr we get a ratio of $\Gamma_3/\Gamma_2 \approx 4266$ for the transitions $|1\rangle \equiv {}^1\mathrm{S}_0$, $|2\rangle \equiv {}^1\mathrm{P}_1$, and $|3\rangle \equiv {}^3\mathrm{P}_1$, with the corresponding decay rates $\Gamma_2 = 2\pi 7.5\mathrm{kHz}$ and $\Gamma_3 = 2\pi 32\mathrm{MHz}$, respectively. For ^{174}Yb the ratio for the same transitions is approximately $\Gamma_3/\Gamma_2 \approx 160$. This is still sufficient to create population inversion, but leads to a lower maximal steady-state population inversion compared to ^{88}Sr. In general, a larger ratio of the decay rates leads to a higher maximal population inversion. Note, that through this pumping scheme steady-state population inversion can only be achieved on the narrower transition. In the following calculations, we will always use the case of ^{88}Sr, i.e. with a decay rate ratio of $\Gamma_3/\Gamma_2 = 4266$.

Using the above Hamiltonian Eq. (3.2) and Liouvillian Eq. (3.3), we compute the steady state of the system. Fig. 3.2 shows scans of the population difference $\langle\sigma_{22}\rangle - \langle\sigma_{11}\rangle$ over tunable system parameters, namely both detunings and Rabi frequencies. We can see that it is possible to achieve an inversion of almost 100% for ^{88}Sr. Note, that all parameters are in units of Γ_3. Hence, a relatively large Rabi frequency on the transition $|1\rangle \leftrightarrow |2\rangle$ ($\Omega_2 \gtrsim 0.1\Gamma_3$) is needed to achieve a significant population inversion.

Investigating the inversion when varying the detunings [Fig. 3.2(a)], we see that for a given Δ_2 the minimum is always at $\Delta_3 = \Delta_2$. The scan over different Rabi frequencies [Fig. 3.2(b)] shows that there is a threshold which the driving amplitudes have to surpass in order to achieve population inversion. Yet, there is also an upper limit: if either Rabi frequency becomes much larger than all other frequencies in the system, one simply obtains the result of a strongly driven two-level transition; i.e., the population is distributed equally between the ground state and the strongly driven upper level. If both Rabi frequencies become extremely large simultaneously, half the population accumulates in the ground state, while the excited states are populated with a quarter each.

Note also, that the symmetry in the detunings is just due to the freedom of choice zero-point energy (direction of the rotating frame; $\tilde{\Delta}_i \to -\Delta_i$).

3.2.1 Effects of Driving with a Finite Laser Linewidth

The driving term in the Hamiltonian Eq. (3.2) assumes lasers with an infinitely small linewidth. Certainly, this is not always a good assumption for real experimental setups. In particular, the linewidth of transitions in clock atoms (such as the ones considered here) can be much smaller than that of a driving laser. Thus, we study the influence of a finite pump laser linewidth on the system. A finite linewidth ν_i of the driving laser on the transition $|1\rangle \leftrightarrow |i\rangle$ can be modelled by an effective atomic decoherence process in the form of dephasing [3.20, 3.21]. The Liouvillian for such a process is

$$\mathcal{L}_{\nu_i}[\rho] = \frac{\nu_i}{2}(2\sigma_{ii}\rho\sigma_{ii} - \sigma_{ii}\rho - \rho\sigma_{ii}). \tag{3.4}$$

In Fig. 3.3(a), we see that for laser linewidths up to the order of $10\Gamma_2$ the population difference stays almost the same. This is a consequence of the Rabi frequency Ω_2 being

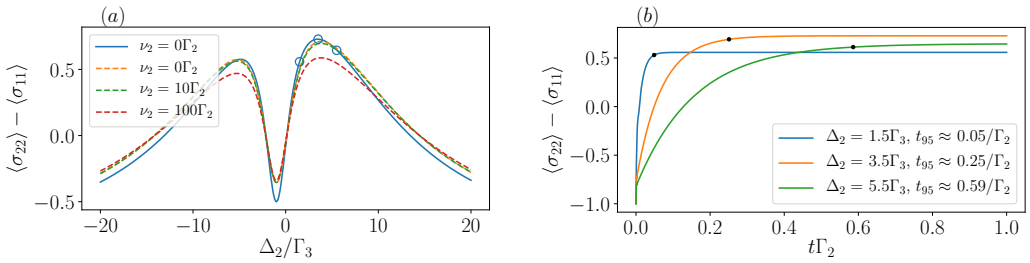

Figure 3.3: *Laser linewidth influence and process time scale.* In figure (a) we can see that for $\nu_2 = 10\Gamma_2$ the population difference $\langle\sigma_{22}\rangle - \langle\sigma_{22}\rangle$ is still almost the same. The blue solid line is for $\nu_3 = 0$ and the dashed lines are for $\nu_3 = 0.5\Gamma_3$. Since $\Gamma_3 \gg \Gamma_2$, the linewidth ν_3 can be neglected in comparison to ν_2. The parameters are $\Delta_3 = -\Gamma_3$, $\Omega_2 = 0.5\Gamma_3$, $\Omega_3 = 0.5\Gamma_3$ and the blue circles indicate the values for Δ_2 in (b). Figure (b) shows that the steady state can be reached much faster if Δ_2 is closer to zero. Here, we have $\nu_2 = \nu_3 = 0$, and the black dots indicate the t_{95} data points.

much larger than the pump laser linewidth ν_2. Only with a dephasing at the order of $100\Gamma_2$, we start to see a significant reduction of the maximal population inversion. Hence, the laser on the narrower transition does not need to be extremely narrow in order to excite the atom, which is advantageous in experimental setups. Furthermore, a linewidth of the laser on the broader transition of up to several hundred Γ_2 ($\nu_3 = 0.5\Gamma_3 \approx 2000\Gamma 2$) has almost no impact on the state population. This is expected since $\Gamma_3 \gg \Gamma_2$.

3.2.2 Time scale

For some applications it is necessary or useful to create the population inversion on a shorter timescale. In Fig. 3.3(b) the time evolution of the population difference for different values of Δ_2 is shown. First of all we can see that the timescale is determined by Γ_2 rather than Γ_3. Thus, the time needed to reach the steady-state population inversion can be quite long, e.g. for clock atoms with decay rates in the mHz-regime. Furthermore, we also see that the time strongly depends on Δ_2. The closer Δ_2 is to zero, the faster the steady state can be reached. However, this can cause a lower population inversion.

In order to quantitatively compare the times needed to reach the steady state, we introduce the variable t_{95}, which is the time at which the population inversion exceeds 95% of its steady-state value. By choosing the lowest possible value for Δ_2 we can reduce t_{95} by up to one magnitude compared to the case with the highest inversion. To further decrease t_{95} we can establish a bigger effective decay rate $\Gamma_2^{\text{eff}} > \Gamma_2$, which then determines the time scale. This can be achieved by, for example, creating an additional decay channel from $|2\rangle$ to $|1\rangle$. Since $|3\rangle$ decays into $|1\rangle$ with $\Gamma_3 \gg \Gamma_2$ we could open an additional decay channel for $|2\rangle$ if it is possible to incoherently drive the atom from $|2\rangle$ to $|3\rangle$. The corresponding rate needs to be $\Gamma_{23} \approx (M-1)/M\Gamma_2$ in order to have M-fold faster decay from $|2\rangle$. This is valid as long as $\Gamma_2^{\text{eff}} \ll \Gamma_3$ holds.

3.3 Continuous Stationary Lasing

We proceed by considering an ensemble of V-type atoms placed inside an optical resonator, as shown in Fig. 3.1(b). Since inversion on the narrow transition can be achieved using the driving scheme, the atoms act as gain for the field inside the resonator. In the following, we investigate the properties of the output light and show that we obtain continuous lasing.

Consider N V-level atoms inside a cavity, each of which couples with a rate g_j to the cavity field via the transition $|1\rangle \leftrightarrow |2\rangle$. The Hamiltonian is given by

$$H = -\Delta_\mathrm{c} a^\dagger a + \sum_{j=1}^{N} g_j (a^\dagger \sigma_{12}^j + a\sigma_{21}^j) + \sum_{i=\{2,3\}} \sum_{j=1}^{N} -\Delta_i^j \sigma_{ii}^j + \Omega_i^j (\sigma_{i1}^j + \sigma_{1i}^j), \tag{3.5}$$

where $\Delta_\mathrm{c} = \omega_{\ell 2} - \omega_\mathrm{c}$ is the detuning between the cavity resonance frequency ω_c and the laser frequency $\omega_{\ell 2}$. The cavity photon creation (annihilation) operator is denoted by $a^\dagger$ (a) and the superscript index j specifies the j-th atom. Photons leaking through the cavity mirrors at a rate 2κ give rise to an additional Liouvillian term

$$\mathcal{L}_\kappa[\rho] = \kappa(2a\rho a^\dagger - a^\dagger a\rho - \rho a^\dagger a). \tag{3.6}$$

For individually decaying atoms, the same decay process as described in Eq. (3.3) applies to each atom. Thus, we have

$$\mathcal{L}_{\mathrm{N}\Gamma}[\rho] = \sum_{i=\{2,3\}} \frac{\Gamma_i}{2} \sum_{j=1}^{N} (2\sigma_{1i}^j \rho \sigma_{i1}^j - \sigma_{ii}^j \rho - \rho \sigma_{ii}^j), \tag{3.7}$$

for the decay processes of both excited states. If we assume that all atoms are driven by the same laser, we obtain the following dissipative processes due to the finite laser linewidth (see 3.6.1 for details). On the transition $|1\rangle \leftrightarrow |3\rangle$ we get a dephasing with

$$\mathcal{L}_{N\nu_3}[\rho] = \frac{\nu_3}{2}(2S_3 \rho S_3 - S_3^2 \rho - \rho S_3^2), \tag{3.8}$$

whereas on the transition $|1\rangle \leftrightarrow |2\rangle$ we have

$$\mathcal{L}_{N\nu_2}[\rho] = \frac{\nu_2}{2}(2(a^\dagger a + S_2)\rho(a^\dagger a + S_2) - (a^\dagger a + S_2)^2 \rho - \rho(a^\dagger a + S_2)^2), \tag{3.9}$$

where $S_i = \sum_{j=1}^{N} \sigma_{ii}^j$ is the collective atomic operator. The additional term $(a^\dagger a)$ in Eq. (3.9) is due to the shared rotating frame of the atom and the cavity. The full Liouvillian for the lasing setup then reads

$$\mathcal{L}_\mathrm{laser}[\rho] = \mathcal{L}_\kappa[\rho] + \mathcal{L}_{N\Gamma}[\rho] + \mathcal{L}_{N\nu_2}[\rho] + \mathcal{L}_{N\nu_3}[\rho] \tag{3.10}$$

Solving the master equation for more than just a few atoms is an impossible task due to the exponential scaling of the Hilbert space with the atom number. Therefore,

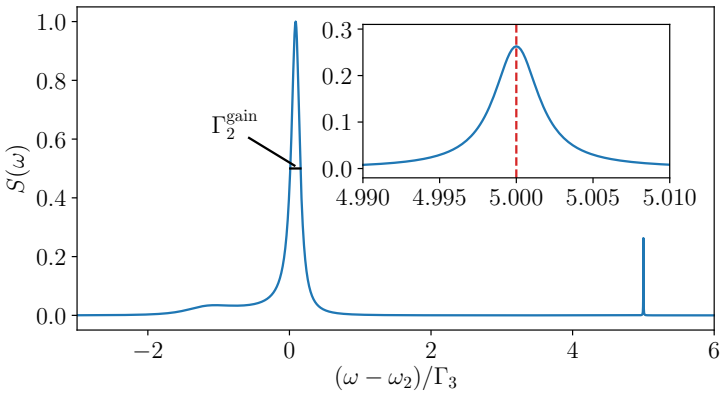

Figure 3.4: *Single atom emission spectrum.* The peak at the atomic resonance frequency ($\omega = \omega_2$) has a FWHM of approximately $\Gamma_2^{\text{gain}} = 614\Gamma_2$, and the smaller peak at the pump laser frequency ($\omega = \omega_{\ell 2} = 5\Gamma_3 + \omega_2$, see inset) of FWHM $\approx 15\Gamma_2$. The red, dashed line in the inset indicates the driving laser frequency $\omega_{\ell 2}$. The parameters are $\Delta_2 = 5\Gamma_3$, $\Delta_3 = -1\Gamma_3$, $\Omega_2 = 0.5\Gamma_3$, $\Omega_3 = 0.5\Gamma_3$ and $\nu_2 = \nu_3 = 0$. This single atom emission spectrum was calculated with a master equation approach, using the Wiener-Khinchin theorem [3.23].

we employ a second-order cumulant expansion [3.22] to calculate the time evolution of average values of interest. Furthermore, we assume that all atoms couple equally to the cavity. Exploiting the symmetry of the system renders N a constant factor, which does not change the number of equations one needs to solve. This allows us to solve the equations of motion for a large number of atoms. The most relevant second-order equations can be found in appendix 3.6.3.

3.3.1 Lasing Threshold

As a first step, we compute the normalized power spectral density $S(\omega)$ of a single atom when it is subject to the driving scheme. This gives us a general idea of what to expect for the resulting lasing output.

Due to the strong coherent driving amplitude, a considerable power broadening on the otherwise narrow transition is induced. This transforms the naturally narrow gain medium into a relatively broad one, see Fig. 3.4. Thus, with respect to the power-broadened linewidth, the resulting laser operates in the good-cavity regime ($\kappa \ll \Gamma_2^{\text{gain}}$). In general, the strong coherent drives lead to distinct energies of multiple dressed states, i.e. they induce considerable ac-Stark shifts. For example, for the parameters chosen in Fig. 3.4, we see that the laser gain peak is slightly shifted from the bare resonance frequency ω_2. Furthermore, we observe an additional small and broad peak to the left of the laser gain frequency, which is the signature of a dressed state. The other small, but narrow peak (linewidth $\sim 15\Gamma_2$) in Fig. 3.4 (see inset) is located at the frequency of the pump laser ($\omega = \omega_{\ell 2}$) and can therefore not be used for lasing. A large amount

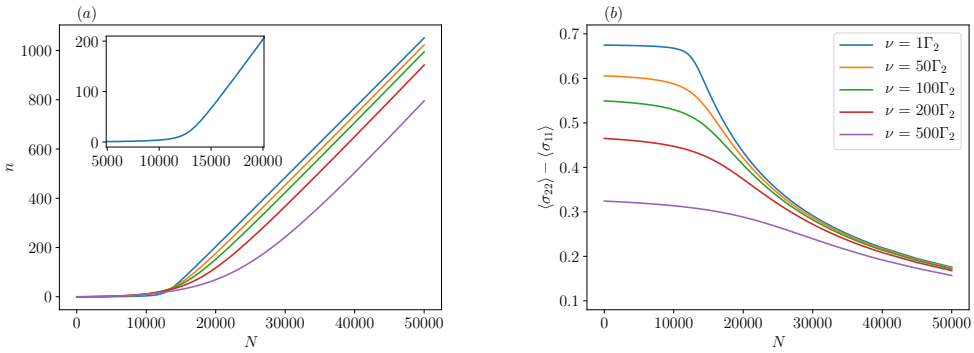

Figure 3.5: *Laser threshold behaviour.* The threshold behaviour of the cavity photon number n on the atom number N is shown in the figure (a) and the population inversion $\langle\sigma_{22}\rangle - \langle\sigma_{11}\rangle$ for the same dephasings ($\nu \equiv \nu_1 = \nu_2$) and number of atoms is shown in (b). The parameters are $\Delta_2 = 5\Gamma_3$, $\Delta_3 = -1\Gamma_3$, $\Omega_2 = 0.5\Gamma_3$, $\Omega_3 = 0.5\Gamma_3$, $\Delta_c = \Delta_2$ ($\omega_c = \omega_2$), $g = 2\Gamma_2$ and $\kappa = 50\Gamma_2$.

of photons from the pump laser would be coherently scattered into the cavity. At the same time, the largest amount of emitted power is far detuned from any driving laser. Coherent scattering of the driving laser into the cavity is therefore suppressed. This already indicates that lasing can indeed be achieved at this frequency.

Making use of the inversion scheme on the narrow transition results in a steady state of the optical cavity featuring a potentially large number of photons. Therefore, the optical resonator provides a continuous output. In Fig. 3.5 we investigate the behaviour of the system with an increasing number of atoms N. We find that the system exhibits a threshold, as can be clearly seen in Fig. 3.5(a), where we plot the steady-state photon number inside the cavity. Once the threshold is passed, the number of photons inside the cavity (and hence the lasing power) rapidly increases. The threshold atom number is approximately $N \approx 12000$ for $\nu_1 = \nu_2 = \Gamma_2$ (see inset). For stronger dephasing a larger gain medium is required in order to sustain the lasing operation. Therefore, the number of atoms needed to pass the threshold increases. This can also be seen from Fig. 3.5(b), where the population inversion per atom is depicted. For stronger dephasing, the inversion decreases and thus the gain provided by each atom is reduced. The key observation, however, is that the threshold can still be passed almost regardless of the linewidth of the driving lasers used in the inversion scheme.

In order to avoid coherent scattering of photons from the pump laser on the transition $|1\rangle \leftrightarrow |2\rangle$ into the cavity, we need to ensure that the laser is far detuned from the cavity resonance frequency. Because of this, we chose a large detuning of $\Delta_2 = 5\Gamma_3$, at which the inversion scheme also works well. Fig. 3.6(a) shows the amount of coherently scattered photons $|\langle a\rangle|^2$ in comparison to the total photon number n in the cavity as a function of Δ_2. We see, that if the detuning Δ_2 is small, a considerable amount of photons enter the cavity via coherent scattering. Moreover, we can see that the chosen value for Δ_2 is not optimal. The cavity photon number therefore is not maximal. If we change Δ_2 from $5\Gamma_3$ to e.g. $2\Gamma_3$, the photon number would in fact increase by almost

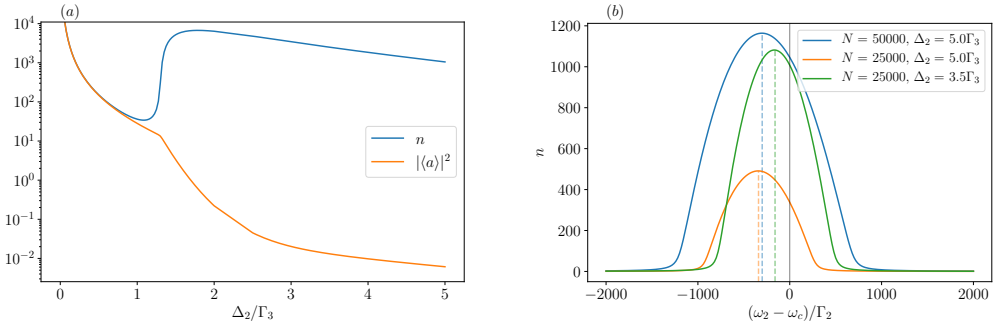

Figure 3.6: *Stimulated emission of photons.* Figure (a) shows the steady-state average photon number n and the coherent fraction of photons $|\langle a\rangle|^2$ inside the cavity as a function of the detuning Δ_2. The cavity is always on resonance with the unperturbed atomic transition frequency ($\Delta_c = \Delta_2$). If Δ_2 is small, coherent scattering of photons into the cavity is more likely to occur. In figure (b) the photon number n is plotted as a function of the detuning between the atomic transition frequency and the cavity resonance frequency $\omega_2 - \omega_c = \Delta_c - \Delta_2$. For the maximum photon number the cavity needs to be blue detuned from the atoms ($\omega_c > \omega_2$). The parameters when kept constant for both subfigures are the same as in Fig. 3.5 for $N = 50000$.

one order of magnitude, still keeping the coherently scattered photon number sufficiently low.

Fig. 3.6(b) shows that, if the cavity is blue detuned from the atomic transition frequency, the photon number can further increase. Of course, if the cavity is too far off-resonant, the photon number almost vanishes. The three different sets of parameters considered, indicate that above threshold an increasing atom number N and a decreasing pump laser detuning Δ_2 shift the optimal cavity resonance frequency towards the atomic resonance frequency.

3.3.2 Cavity Emission Spectrum

The steady-state cavity power spectral density can be calculated as the Fourier transform of the first order correlation function $g^1(\tau) = \langle a^\dagger(\tau)a(0)$

$$S(\omega) = \int_0^\infty d\tau g^1(\tau) e^{-i(\omega)\tau}. \tag{3.11}$$

Using the quantum regression theorem [3.24] we can calculate the time evolution of the correlation function $g^1(\tau)$ with a second order cumulant expansion. In appendix 3.6.1 one can see that the time evolution for the laser systems with finite pump laser linewidth have been calculated in a fluctuating rotating frame ($U(t) = e^{i(\omega_{\ell 2}t+\phi(t))(a^\dagger a+\sum_{j=1}^N \sigma_{22}^j)}$, instantaneous frame). But since we want to obtain the spectrum with respect to a stable monochromatic reference frequency we are only allowed to transform the system into a non-fluctuating rotating frame (e.g. $U(t) = e^{i\omega_{\ell 2}t(a^\dagger a+\sum_{j=1}^N \sigma_{22}^j)}$, coherent frame) [3.25].

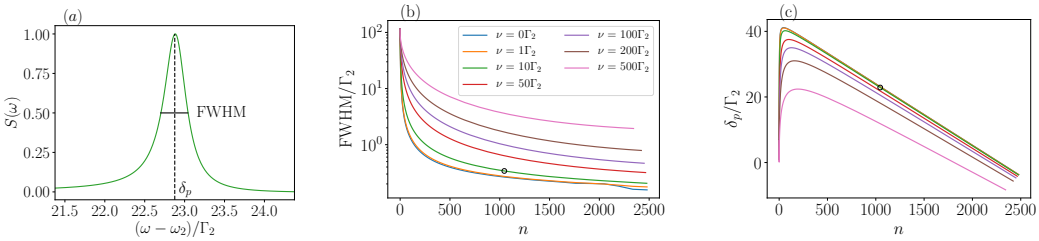

Figure 3.7: *Spectral properties of the cavity.* Figure (a) shows a typical (normalized) spectrum $S(\omega)$ above threshold, where we chose $N = 50000$ and $\nu = 10\Gamma_2$ (black circles in (b) and (c)). The FWHM ($0.35\Gamma_2$) and the peak position δ_p ($22.9\Gamma_2$) are indicated. Note that the spectrum is plotted with respect to the atomic transition frequency. The reduction of the laser linewidth with increasing cavity photon number is plotted in (b). And (c) shows the shift of the peak position due to a stark shift caused by large cavity photon numbers. The legend in (b) is for all three plots.

The set of equations to calculate the correlation function and a detailed derivation is shown in appendix 3.6.4 and 3.6.2, respectively.

The properties of the cavity emission spectrum are depicted in Fig. 3.7. The most significant result here is that a FWHM below Γ_2 can be reached, even if the linewidths of the driving lasers are above $100\Gamma_2$. Hence, a narrow bandwidth laser can be achieved with relatively broad pump lasers. Furthermore, the system does not rely on a direct decay channel into the lasing transition, as opposed to conventional laser systems. Only a V-level structure is necessary, which can be often found in rare earth atoms, commonly used in optical clocks. Let us stress here, that we assumed an ideal model with all atoms fixed at the cavity field anti-nodes.

As expected for a conventional laser, the FWHM is approximately given by the cavity linewidth 2κ for small photon numbers [see Fig. 3.7(b)]. Above threshold, where the photon number is large, it reduces with $\mathrm{FWHM}(n) \sim 1/n$. This behaviour is well-know in the case of good-cavity lasers [3.1]. In Fig. 3.7(c), we can see that the peak position shows an almost linear dependency on the photon number, if the latter is large. This is caused by an ac-Stark shift due to the cavity field. In general we find that the spectral properties are very similar to those of a conventional laser. For example, also the cavity pulling coefficient above threshold is $d\delta_p(\Delta_c)/d\Delta_c \approx 1$.

The FWHM shows an unexpected behaviour for $\nu = 0$ at high photon numbers. The most likely reason for this is that the second order cumulant expansion reaches its limits there. The fact that this happens only for $\nu = 0$ is a good indicator: the dephasing destroys the coherences and therefore makes the system more classical, i.e. the approximation is more accurate. By keeping specific third order terms as e.g. $\langle a^\dagger a \sigma_{22} \rangle$ [3.26] one may get rid of this inaccuracy. However, the equations listed in the appendix are already quite lengthy; taking third order corrections would ultimately go beyond the intended scope of this work.

3.4 Cooling

Another point of interest for the stability of continuous lasing operation is cooling of the atoms. On the one hand, this ensures that the atoms stay in the cavity as long as possible thereby providing gain. On the other hand, heating will generally cause noise and broadening of the gain medium, which will have a detrimental impact on the spectral properties of the laser.

Therefore, we consider the impact of the inversion scheme on the atomic motion in this section. To this end, effects of photon recoil from spontaneous emission events are taken into account. This allows us to estimate the temperature of the gain medium when subjected to the two driving lasers.

We employ a Monte-Carlo wave function (MCWF) approach [3.27, 3.28], where we treat the atomic motion as classical variables. In the MCWF method, the norm of the state vector decreases over time. Once the norm decreases below a certain (randomly chosen) value, a quantum jump occurs. In our approach, we include an additional momentum kick whenever a jump occurs.

In the following, we restrict the atomic motion to two spatial dimensions. The pump lasers are considered to be aligned perpendicularly, in directions determined by their respective wavevectors $\mathbf{k}_i$, respectively (i.e. $\mathbf{k}_2 \cdot \mathbf{k}_3 = 0$). Furthermore, we neglect the influence of the cavity field in these calculations. In the case of many photons inside the cavity this assumption may be far from ideal. However, note that the lasing operation is optimal (maximal output power) when the cavity is blue detuned from the atomic transition frequency, as shown in [Fig. 3.6(b)]. Therefore, the cavity would effectively provide an additional cooling mechanism [3.29, 3.30]. Thus, neglecting the cavity leads to higher final temperatures, which provides a sufficient estimate.

Since the atoms do not interact with one another, we repeatedly compute trajectories of the particle motion for a single atom only. The considered system is modeled as follows: the internal atomic structure is treated quantum mechanically, while the motional degrees of freedom are assumed to be fully described by their average values. This assumption is well justified if the momentum of the atom is large compared to the momentum of a single photon. The Hamiltonian of this system reads

$$H = \sum_{i=\{2,3\}} -\Delta_i \sigma_{ii} + \Omega_i \cos(\mathbf{k}_i \cdot \mathbf{r})(\sigma_{i1} + \sigma_{1i}), \tag{3.12}$$

where $\mathbf{r}$ is the atomic position vector in the plane spanned by the wavevectors. The atomic motion is described by the classical equations of motion for the velocity

$$\dot{\mathbf{r}} = \frac{\mathbf{p}}{m}, \tag{3.13}$$

and the forces acting on the atom

$$\dot{p}_i = k_i \Omega_i \sin(\mathbf{k}_i \cdot \mathbf{r}) 2\mathrm{R}e \langle \sigma_{1i} \rangle + \xi_i(t). \tag{3.14}$$

The terms $\xi_i(t)$ account for the momentum kicks due to the spontaneous emission of a

photon. Whenever a jump from an excited state $|j\rangle$ to the ground state occurs in the Monte Carlo trajectory, we add the recoil momentum k_j with a random direction to the particle's momentum vector. In our case, we project the three dimensional random momentum vector with length k_j along the axis determined by the lasers wavevectors. In particular, we have

$$\xi_i(t) = s_i(t) \sum_{j=\{2,3\}} k_j \delta(t - t_j^{\mathrm{rec}}), \tag{3.15}$$

where $s_i(t)$ is the i-th component of a random, three-dimensional unit vector. Furthermore, t_j^{rec} denotes any point in time at which a jump from the j-th level occurs. The dissipative processes are the same as described before in equations Eq. (3.3) and Eq. (3.4).

In Fig. 3.8 we plot the time evolution of the particle's kinetic energy and of the population inversion. For the lasing parameters used before (blue lines) we see that the pump on the lasing transition slowly heats the particles. However, the pump on the broader transition cools them quite well. The lasing transition is still inverted, but the population inversion is significantly decreased. The main reason for this is that, on average, the particle feels a much weaker pump field, since they are not always located at the field maxima. This could be circumvented by simply increasing the laser power. The second set of parameters (orange lines) shows that it is possible to achieve much better cooling on both transitions, and also a larger population inversion. Specifically, the cooling rate is much larger. Unfortunately, these parameters are not suitable for lasing: the comparably small detuning would lead to substantial coherent scattering of the driving laser into the cavity.

Additionally, for the parameters where lasing works well, we find that the finite linewidth of the driving laser rarely affects the particle motion. In the case of optimal cooling, however, the final kinetic energy as well as the cooling time scale is significantly increased. Note also, that the final temperature along the $\mathbf{k}_3$-axis is on the order of the Doppler temperature of the broader transition [$k_{\mathrm{B}}T \approx \Gamma_3/2$ (blue) and $k_{\mathrm{B}}T \approx 3\Gamma_3/10$ (orange)]. The Doppler broadening $\Delta\omega_D$ corresponding to this temperature $k_BT \approx \Gamma_3/2$ on the narrower transition is approximately

$$\Delta\omega_D = \frac{\omega_2}{c}\sqrt{\frac{8k_BTln(2)}{m}} \approx 120\Gamma_2, \tag{3.16}$$

with $\omega_2 = 2\pi \times 435\mathrm{THz}$ and $m = 87u$. Since this Doppler broadening is approximately a factor of 5 smaller than the power broadened gain ($614\Gamma_2$, see Fig. 3.4), the finite temperature does not significantly affect the lasing.

Note that $\Delta_2 < 0$ and $\Delta_3 > 0$ is required to achieve cooling. This is because the atoms are inverted on the transition $|1\rangle \leftrightarrow |2\rangle$, but not on the transition $|1\rangle \leftrightarrow |3\rangle$ [3.31]. Furthermore, we also want to mention here that for strong pumping and far blue-detuned lasers it is possible that atoms in the ground state get cooled and trapped at the field nodes (high-intensity Sisyphus cooling) [3.32]. We were able to observe this for some

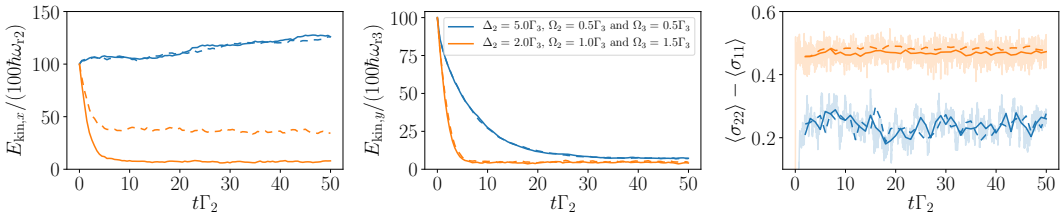

Figure 3.8: *Particle motion.* The solid lines are for $\nu = \Gamma_2$ and the dashed lines for $\nu = 10\Gamma_2$. We chose $\Delta_3 = -\Gamma_3$. For $\langle\sigma_{22}\rangle - \langle\sigma_{11}\rangle$ we averaged 50 data points to increase the visibility, the bright fast fluctuating lines are the non-averaged for $\nu = 1.0\Gamma_2$. The atom starts with a momentum of $p_i(0) = 100k_i$ at the pump field anti-nodes in the ground state. We average 500 MCWF trajectories and the legend is for all three plots.

specific parameters on the narrow transition. For the motion of ^{174}Yb, as mentioned in section 3.2, we almost always obtained heating or trapping at the field nodes.

3.5 Conclusions

We have shown that continuous lasing on a narrow atomic transition can be implemented in a V-level configuration, when a second closed broad transition sharing the same ground state is available. Using two strong and sufficiently detuned coherent driving lasers lead to almost perfect inversion on the narrow transition. The entire mechanism does not rely on a direct decay channel into the excited state with a narrow line, which makes it distinctly different from previously considered lasing setups. When the inverted transition is coupled to an optical resonator, the system starts to lase once a certain threshold number of atoms is passed. The spectral properties of the output laser light exhibit a linewidth that can be well below the natural linewidth of the narrow transition. Notice, that despite the fact that the natural linewidth of the lasing transition is smaller than the cavity linewidth by far, the power broadening induced by the strong pump light means that we are effectively in the good-cavity regime. Furthermore, we found optimal lasing for many atoms and, accordingly, many photons in the cavity. The coherence is thus stored in the cavity field rather than the atomic dipoles. Hence, the lasing setup we consider is more similar to a conventional laser rather than a superradiant one. Yet, the spectral linewidth of the laser can be extremely small and is effectively determined by the natural linewidth of the atom. Finally, we have shown that the overall promising properties of such a laser are conserved even when considering pump lasers that are broad and induce strong dephasing.

Interestingly lasing has been found recently in a closely related setup using Ytterbium atoms [3.19]. However in this case it was identified as Raman lasing [3.11, 3.33] which occurs in a very different operation regime and inherits the pump laser linewidth. While our configuration finally does not meet all criteria for a clock laser it can be seen as a major experimental step in this direction.

In order to estimate heating effects induced by the strong driving beams, we considered the motion of an atom subjected to the inversion scheme. We found that the kinetic energy is limited by the Doppler temperature of the broad transition. Therefore, we conclude that the system should not exhibit instabilities due to heating.

Acknowledgement

We thank S. Schäffer, M. Tang and G. Kazakov for helpful discussions. This project has received funding from the European Union's Horizon 2020 research and innovation programme under grant agreement No 820404 (iqClock) (C. H., D. P. and H. R.).

Numerical simulations were performed with the open source framework QuantumOptics.jl [3.34, 3.35]. The graphs were produced using the open source plotting library Matplotlib [3.36].

3.6 Appendix

3.6.1 Dephasing due to a finite pump laser linewidth

In this section we show the fundamental steps to derive the dephasing Liouvillian originating from a finite pump laser linewidth for N coherently driven two-level atoms coupled to a cavity Eq. (3.9). Using the standard phase diffusion model with a noisy phase $\phi_2(t)$ we have the following Hamiltonian written in the lab frame

$$\begin{aligned} H_{\text{lab}} = \omega_c a^\dagger a + \sum_{j=1}^{N} g_j (a^\dagger \sigma_{12}^j + a\sigma_{21}^j) + \sum_{j=1}^{N} \omega_2^j \sigma_{22}^j \\ + \sum_{j=1}^{N} \Omega_2^j \left(\sigma_{21}^j e^{-i(\omega_{\ell 2} t + \phi_2(t))} + \sigma_{12}^j e^{i(\omega_{\ell 2} t + \phi_2(t))} \right), \end{aligned} \tag{3.17}$$

where the noise statistics of $\phi_2(t)$ is determined by its derivative, which is assumed to be a white noise frequency fluctuation such that

$$\langle \dot{\phi}_2(t) \dot{\phi}_2(t') \rangle = \nu_2 \delta(t - t'). \tag{3.18}$$

Additionally, we assume here that all atoms experience the same pump laser phase (collective phase noise). We switch into the (instantaneous) rotating frame of the pump laser with the unitary transformation

$$U_I(t) = e^{i(\omega_{\ell 2} t + \phi_2(t))(a^\dagger a + \sum_{j=1}^{N} \sigma_{22}^j)}, \tag{3.19}$$

in which the Hamiltonian becomes

$$\begin{aligned} H = &-\Delta_c a^\dagger a + \sum_{j=1}^{N} g_j(a^\dagger \sigma_{12}^j + a\sigma_{21}^j) + \sum_{j=1}^{N} -\Delta_2^j \sigma_{22}^j \\ &+ \sum_{j=1}^{N} \Omega_2^j(\sigma_{21}^j + \sigma_{12}^j) - \dot{\phi}_2(t)(a^\dagger a + \sum_{j=1}^{N} \sigma_{22}^j). \end{aligned} \tag{3.20}$$

We distinguish now between the deterministic part of the Hamiltonian H_D and the stochastic part

$$H_S = -(a^\dagger a + \sum_{j=1}^{N} \sigma_{22}^j), \tag{3.21}$$

such that $H = H_D + \dot{\phi}_2(t) H_S$. The Heisenberg equation of a system operator O for this Hamiltonian can be written as

$$\text{(S)} \quad \frac{d}{dt}O = L_D[O] + \dot{\phi}_2(t) L_S[O], \tag{3.22}$$

with $L_D[O] = i[H_D, O]$ and $L_S[O] = i[H_S, O]$. Equation Eq. (3.22) needs to be interpreted as a Stratonovich stochastic differential equation [indicated by (S)] , which can be transformed into Itô form [indicated by (I)] as follows [3.37]:

$$\text{(I)} \quad \frac{d}{dt}O = L_D[O] + \frac{1}{2}\nu_2 L_S^2[O] + \dot{\phi}_2(t) L_S[O], \tag{3.23}$$

By averaging equation Eq. (3.23) the stochastic part vanishes and we get

$$\frac{d}{dt}\langle O \rangle_S = \langle L_D[O] \rangle_S + \frac{1}{2}\nu_2 \langle L_S^2[O] \rangle_S . \tag{3.24}$$

Evaluating $L_S^2[O] = -[H_S, [H_S, O]]$, we find that the fluctuating phase leads to dephasing as described in equation Eq. (3.9). Note, that $\langle \cdot \rangle_S$ indicates a stochastic average, not a quantum average as in the cumulant expansion.

3.6.2 Derivation of correlation function equations

On the one hand, we compute the steady-state expectation values in the instantaneous rotating frame (see 3.6.1). On the other hand, the correlation function for the spectrum has to be computed in a non-fluctuating (coherent) rotating frame [3.25]. In this section we show the main procedure to derive the equations. The full set of equations to obtain the correlation function is given in 3.6.4. Again, we consider N two-level atoms coupled to a cavity as in 3.6.1, including the third level is straight forward. In the coherent rotating frame with the unitary transformation

$$U_C(t) = e^{i\omega_{\ell 2} t(a^\dagger a + \sum_{j=1}^{N} \sigma_{22}^j)}, \tag{3.25}$$

we obtain the time-dependent Hamiltonian

$$\tilde{H} = -\Delta_c \tilde{a}^\dagger \tilde{a} + \sum_{j=1}^{N} g_j(\tilde{a}^\dagger \tilde{\sigma}_{12}^j + \tilde{a}\tilde{\sigma}_{21}^j) - \sum_{j=1}^{N} \Delta_2^j \tilde{\sigma}_{22}^j + \sum_{j=1}^{N} \Omega_2^j \left(\tilde{\sigma}_{21}^j e^{-i\phi_2(t)} + \tilde{\sigma}_{12}^j e^{i\phi_2(t)}\right). \tag{3.26}$$

The tilde indicates that the operator is in the coherent rotating frame. With cavity decay and individual atomic decay, described by Eq. (3.6) and Eq. (3.7), respectively, we obtain with the quantum regression theorem [3.24] the differential equation for the correlation function

$$\frac{d}{dt}\langle \tilde{a}^\dagger \tilde{a}_0\rangle = igN\langle \tilde{\sigma}_{21}^1 \tilde{a}_0\rangle - i\Delta_c\langle \tilde{a}^\dagger \tilde{a}_0\rangle - 0.5\kappa\langle \tilde{a}^\dagger \tilde{a}_0\rangle \tag{3.27}$$

Here and in the following, we use the notation $\langle \tilde{O}(t)\tilde{a}(0)\rangle = \langle \tilde{O}\tilde{a}_0\rangle$. To calculate Eq. (3.27) we also need the equation for $\langle \tilde{\sigma}_1^{21}(t)\tilde{a}(0)\rangle$ which is given by

$$\begin{aligned}\frac{d}{dt}\langle \tilde{\sigma}_{21}^1 \tilde{a}_0\rangle = &-2ig\left(\langle \tilde{a}^\dagger\rangle\langle \tilde{\sigma}_{22}^1 \tilde{a}_0\rangle + \langle \tilde{a}_0\rangle\langle \tilde{a}^\dagger \tilde{\sigma}_{22}^1\rangle + \langle \tilde{\sigma}_{22}^1\rangle\langle \tilde{a}^\dagger \tilde{a}_0\rangle - 2\langle \tilde{a}^\dagger\rangle\langle \tilde{a}_0\rangle\langle \tilde{\sigma}_{22}^1\rangle\right)\\ &+ ig\langle \tilde{a}^\dagger \tilde{a}_0\rangle - 0.5\Gamma_2\langle \tilde{\sigma}_{21}^1 \tilde{a}_0\rangle - i\Delta_2\langle \tilde{\sigma}_{21}^1 \tilde{a}_0\rangle\\ &+ i\Omega_2\langle \tilde{a}_0\rangle e^{i\phi_2(t)} - 2i\Omega_2\langle \tilde{\sigma}_{22}^1 \tilde{a}_0\rangle e^{i\phi_2(t)}.\end{aligned} \tag{3.28}$$

Equation Eq. (3.28) contains some specific averages proportional to $e^{i\phi(t)}$ ($\langle \tilde{a}\rangle$ and $\langle \tilde{\sigma}_{22}^1 \tilde{a}_0\rangle$). To solve this problem we use two properties: first, since we are in steady state, all averages that do not involve $\tilde{a}_0$ do not depend on two different times and hence can be replaced by the respective steady-state values. Second, the change of the steady-state values from the coherent to the instantaneous frame is given by the unitary transformation

$$U_{C\to I}(t) = e^{i\phi_2(t)(a^\dagger a + \sum_{j=1}^{N}\sigma_{22}^j)}. \tag{3.29}$$

We get for example $\langle \tilde{a}\rangle = \langle a\rangle\, e^{-i\phi_2(t)}$. With this we can use the steady-state values in the instantaneous frame, which we have obtained before. Replacing them, we find that all averages $\langle \tilde{\sigma}_{22}^1 \tilde{a}_0\rangle$ only occur in combination with the factor $e^{i\phi_2(t)}$. Therefore, we derive the equations of motion for $\langle \tilde{\sigma}_{22}^1 \tilde{a}_0\rangle\, e^{i\phi_2(t)}$ rather than $\langle \tilde{\sigma}_{22}^1 \tilde{a}_0\rangle$ alone. In equation Eq. (3.30) we show two examples of such differential equations for averages multiplied with a phase fluctuation term:

$$\begin{aligned}\frac{d}{dt}\langle \tilde{\sigma}_{22}^1 \tilde{a}_0\rangle e^{i\phi_2(t)} = &\, ig\Big(\langle \tilde{a}^\dagger\rangle\langle \tilde{\sigma}_{12}^1 \tilde{a}_0\rangle + \langle \tilde{a}_0\rangle\langle \tilde{a}^\dagger \tilde{\sigma}_{12}^1\rangle + \langle \tilde{\sigma}_{12}^1\rangle\langle \tilde{a}^\dagger \tilde{a}_0\rangle\\ &- 2\langle \tilde{a}^\dagger\rangle\langle \tilde{a}_0\rangle\langle \tilde{\sigma}_{12}^1\rangle - \langle \tilde{a}\rangle\langle \tilde{\sigma}_{21}^1 \tilde{a}_0\rangle - \langle \tilde{a}_0\rangle\langle \tilde{a}\tilde{\sigma}_{21}^1\rangle\\ &- \langle \tilde{\sigma}_{21}^1\rangle\langle \tilde{a}\tilde{a}_0\rangle + 2\langle \tilde{a}\rangle\langle \tilde{a}_0\rangle\langle \tilde{\sigma}_{21}^1\rangle\Big)e^{i\phi_2(t)}\\ &+ i\dot{\phi}_2\langle \tilde{\sigma}_{22}^1 \tilde{a}_0\rangle - \Gamma_2\langle \tilde{\sigma}_{22}^1 \tilde{a}_0\rangle e^{i\phi_2(t)} i\dot{\phi}_2\langle \tilde{\sigma}_{22}^1 \tilde{a}_0\rangle\\ &- i\Omega_2\langle \tilde{\sigma}_{21}^1 \tilde{a}_0\rangle + i\Omega_2\langle \tilde{\sigma}_{12}^1 \tilde{a}_0\rangle e^{2i\phi_2(t)}\end{aligned} \tag{3.30a}$$

$$\begin{aligned}\frac{d}{dt}\langle\tilde{\sigma}_{12}^{1}\tilde{a}_0\rangle e^{2i\phi_2(t)} &= 2i\dot{\phi}_2\langle\tilde{\sigma}_{12}^{1}\tilde{a}_0\rangle + 2ig\Big(\langle\tilde{a}\rangle\langle\tilde{\sigma}_{22}^{1}\tilde{a}_0\rangle + \langle\tilde{a}_0\rangle\langle\tilde{a}\tilde{\sigma}_{22}^{1}\rangle \\ &\quad + \langle\tilde{\sigma}_{22}^{1}\rangle\langle\tilde{a}\tilde{a}_0\rangle - 2\langle\tilde{a}\rangle\langle\tilde{a}_0\rangle\langle\tilde{\sigma}_{22}^{1}\rangle\Big)e^{2i\phi_2(t)} - i\Omega_2\langle\tilde{a}_0\rangle e^{i\phi_2(t)} \\ &\quad - ig\langle\tilde{a}\tilde{a}_0\rangle e^{2i\phi_2(t)} - 0.5\Gamma_2\langle\tilde{\sigma}_{12}^{1}\tilde{a}_0\rangle e^{2i\phi_2(t)} \\ &\quad + i\Delta_2\langle\tilde{\sigma}_{12}^{1}\tilde{a}_0\rangle e^{2i\phi_2(t)} + 2i\Omega_2\langle\tilde{\sigma}_{22}^{1}\tilde{a}_0\rangle e^{i\phi_2(t)}\end{aligned} \tag{3.30b}$$

In equations Eq. (3.30a) and Eq. (3.30b), terms proportional to $\dot{\phi}$ appear, namely $i\dot{\phi}\,\langle\tilde{\sigma}_{22}^{1}\tilde{a}_0\rangle$ and $2i\dot{\phi}\,\langle\tilde{\sigma}_{12}^{1}\tilde{a}_0\rangle$, respectively. Transforming these Stratonovich stochastic differential equations to Itô as in section 3.6.1 leads to a dephasing term $-0.5\nu_2\,\langle\tilde{\sigma}_{22}^{1}\tilde{a}_0\rangle$ and $-2\nu_2\,\langle\tilde{\sigma}_{22}^{1}\tilde{a}_0\rangle$, respectively. In section 3.6.4 you find the closed system of differential equations derived via this procedure.

3.6.3 Second-order cumulant expansion

In order to derive the following equations we wrote a program [3.38] that symbolically evaluates bosonic and fermionic commutation relations. Then, the generalized cumulant expansion is applied to obtain a closed set of equations featuring only first- and second-order averages. The correctness of the equations is ensured by comparing numerical results for smaller systems with a full quantum treatment for a variety of parameters.

System equations

Note, that we only show part of the derived equations in order to keep the length of the entire set at a comprehensible level. As previously mentioned, the (in total 37) equations were derived using a software tool. The tool is open source and available online [3.38].

$$\frac{d}{dt}\langle a^\dagger a\rangle = -\kappa\langle a^\dagger a\rangle + iNg\langle a\sigma_{21}^{1}\rangle - iNg\langle a^\dagger\sigma_{12}^{1}\rangle$$

$$\frac{d}{dt}\langle a\rangle = i\Delta_c\langle a\rangle - 0.5\,(\kappa+\nu_2)\,\langle a\rangle - iNg\langle\sigma_{12}^{1}\rangle$$

$$\frac{d}{dt}\langle\sigma_{22}^{1}\rangle = -\Gamma_2\langle\sigma_{22}^{1}\rangle + i\Omega_2\langle\sigma_{12}^{1}\rangle + ig\langle a^\dagger\sigma_{12}^{1}\rangle - i\Omega_2\langle\sigma_{21}^{1}\rangle - ig\langle a\sigma_{21}^{1}\rangle$$

$$\begin{aligned}\frac{d}{dt}\langle\sigma_{12}^{1}\rangle &= i\Delta_2\langle\sigma_{12}^{1}\rangle - 0.5\,(\Gamma_2+\nu_2)\,\langle\sigma_{12}^{1}\rangle + i\Omega_3\langle\sigma_{32}^{1}\rangle + i\Omega_2\left(-1+\langle\sigma_{33}^{1}\rangle\right) + ig\langle a\sigma_{33}^{1}\rangle \\ &\quad - ig\langle a\rangle + 2i\Omega_2\langle\sigma_{22}^{1}\rangle + 2ig\langle a\sigma_{22}^{1}\rangle\end{aligned}$$

$$\begin{aligned}\frac{d}{dt}\langle\sigma_{32}^{1}\rangle &= -0.5\,(\Gamma_2+\Gamma_3+\nu_2+\nu_3)\,\langle\sigma_{32}^{1}\rangle + i\Omega_3\langle\sigma_{12}^{1}\rangle + i\Delta_2\langle\sigma_{32}^{1}\rangle - i\Omega_2\langle\sigma_{31}^{1}\rangle \\ &\quad - i\Delta_3\langle\sigma_{32}^{1}\rangle - ig\langle a\sigma_{31}^{1}\rangle\end{aligned}$$

$$\frac{d}{dt}\langle\sigma_{33}^{1}\rangle = -\Gamma_3\langle\sigma_{33}^{1}\rangle + i\Omega_3\langle\sigma_{13}^{1}\rangle - i\Omega_3\langle\sigma_{31}^{1}\rangle$$

$$\frac{d}{dt}\langle a\sigma_{21}^1\rangle = i\Omega_2\langle a\rangle + ig\langle a^\dagger a\rangle + i\Delta_c\langle a\sigma_{21}^1\rangle - 0.5\Gamma_2\langle a\sigma_{21}^1\rangle - 0.5\kappa\langle a\sigma_{21}^1\rangle - ig\langle\sigma_{22}^1\rangle$$
$$- 2ig\left(\langle a^\dagger\rangle\langle a\sigma_{22}^1\rangle + \langle a\rangle\langle a^\dagger\sigma_{22}^1\rangle + \langle\sigma_{22}^1\rangle\langle a^\dagger a\rangle - 2\langle a^\dagger\rangle\langle a\rangle\langle\sigma_{22}^1\rangle\right)$$
$$- ig\left(\langle a^\dagger\rangle\langle a\sigma_{33}^1\rangle + \langle a\rangle\langle a^\dagger\sigma_{33}^1\rangle + \langle\sigma_{33}^1\rangle\langle a^\dagger a\rangle - 2\langle a^\dagger\rangle\langle a\rangle\langle\sigma_{33}^1\rangle\right)$$
$$- i\Delta_2\langle a\sigma_{21}^1\rangle - 2i\Omega_2\langle a\sigma_{22}^1\rangle - i\Omega_2\langle a\sigma_{33}^1\rangle - i\Omega_3\langle a\sigma_{23}^1\rangle - ig\left(-1+N\right)\langle\sigma_{21}^1\sigma_{12}^2\rangle$$

$$\frac{d}{dt}\langle a\sigma_{22}^1\rangle = ig\left(\langle a^\dagger\rangle\langle a\sigma_{12}^1\rangle + \langle a\rangle\langle a^\dagger\sigma_{12}^1\rangle + \langle\sigma_{12}^1\rangle\langle a^\dagger a\rangle - 2\langle a^\dagger\rangle\langle a\rangle\langle\sigma_{12}^1\rangle\right) + i\Delta_c\langle a\sigma_{22}^1\rangle$$
$$+ i\Omega_2\langle a\sigma_{12}^1\rangle - \Gamma_2\langle a\sigma_{22}^1\rangle - 0.5\kappa\langle a\sigma_{22}^1\rangle - 0.5\nu_2\langle a\sigma_{22}^1\rangle - i\Omega_2\langle a\sigma_{21}^1\rangle$$
$$- ig\left(\langle\sigma_{21}^1\rangle\langle aa\rangle + 2\langle a\rangle\langle a\sigma_{21}^1\rangle - 2\langle\sigma_{21}^1\rangle\langle a\rangle^2\right) - ig\left(-1+N\right)\langle\sigma_{22}^1\sigma_{12}^2\rangle$$

$$\frac{d}{dt}\langle\sigma_{21}^1\sigma_{12}^2\rangle = ig\left(\langle a\rangle\langle\sigma_{33}^1\sigma_{21}^2\rangle + \langle\sigma_{33}^1\rangle\langle a\sigma_{21}^1\rangle + \langle\sigma_{21}^1\rangle\langle a\sigma_{33}^1\rangle - 2\langle a\rangle\langle\sigma_{33}^1\rangle\langle\sigma_{21}^1\rangle\right)$$
$$+ i\Omega_2\langle\sigma_{12}^1\rangle + ig\langle a^\dagger\sigma_{12}^1\rangle + i\Omega_2\langle\sigma_{33}^1\sigma_{21}^2\rangle + i\Omega_3\langle\sigma_{21}^1\sigma_{32}^2\rangle - \Gamma_2\langle\sigma_{21}^1\sigma_{12}^2\rangle$$
$$- 2ig\left(\langle a^\dagger\rangle\langle\sigma_{22}^1\sigma_{12}^2\rangle + \langle\sigma_{22}^1\rangle\langle a^\dagger\sigma_{12}^1\rangle + \langle\sigma_{12}^1\rangle\langle a^\dagger\sigma_{22}^1\rangle - 2\langle a^\dagger\rangle\langle\sigma_{22}^1\rangle\langle\sigma_{12}^1\rangle\right)$$
$$- ig\left(\langle a^\dagger\rangle\langle\sigma_{33}^1\sigma_{12}^2\rangle + \langle\sigma_{33}^1\rangle\langle a^\dagger\sigma_{12}^1\rangle + \langle\sigma_{12}^1\rangle\langle a^\dagger\sigma_{33}^1\rangle - 2\langle a^\dagger\rangle\langle\sigma_{33}^1\rangle\langle\sigma_{12}^1\rangle\right)$$
$$+ 2ig\left(\langle a\rangle\langle\sigma_{22}^1\sigma_{21}^2\rangle + \langle\sigma_{22}^1\rangle\langle a\sigma_{21}^1\rangle + \langle\sigma_{21}^1\rangle\langle a\sigma_{22}^1\rangle - 2\langle a\rangle\langle\sigma_{22}^1\rangle\langle\sigma_{21}^1\rangle\right)$$
$$- i\Omega_2\langle\sigma_{21}^1\rangle - ig\langle a\sigma_{21}^1\rangle - 2i\Omega_2\langle\sigma_{22}^1\sigma_{12}^2\rangle + 2i\Omega_2\langle\sigma_{22}^1\sigma_{21}^2\rangle - i\Omega_2\langle\sigma_{33}^1\sigma_{12}^2\rangle$$
$$- i\Omega_3\langle\sigma_{12}^1\sigma_{23}^2\rangle$$

$$\frac{d}{dt}\langle\sigma_{22}^1\sigma_{22}^2\rangle = ig\left(2\langle a^\dagger\rangle\langle\sigma_{22}^1\sigma_{12}^2\rangle + 2\langle\sigma_{22}^1\rangle\langle a^\dagger\sigma_{12}^1\rangle + 2\langle\sigma_{12}^1\rangle\langle a^\dagger\sigma_{22}^1\rangle - 4\langle a^\dagger\rangle\langle\sigma_{22}^1\rangle\langle\sigma_{12}^1\rangle\right)$$
$$- 2ig\left(\langle a\rangle\langle\sigma_{22}^1\sigma_{21}^2\rangle + \langle\sigma_{22}^1\rangle\langle a\sigma_{21}^1\rangle + \langle\sigma_{21}^1\rangle\langle a\sigma_{22}^1\rangle - 2\langle a\rangle\langle\sigma_{22}^1\rangle\langle\sigma_{21}^1\rangle\right)$$
$$- 2\Gamma_2\langle\sigma_{22}^1\sigma_{22}^2\rangle + 2i\Omega_2\langle\sigma_{22}^1\sigma_{12}^2\rangle - 2i\Omega_2\langle\sigma_{22}^1\sigma_{21}^2\rangle$$

3.6.4 Correlation function equations

We omit the phase factors in these equations, since this only corresponds to a variable relabeling of some specific correlation functions.

$$\frac{d}{dt}\langle\tilde{a}^\dagger\tilde{a}_0\rangle = -i\Delta_c\langle\tilde{a}^\dagger\tilde{a}_0\rangle - 0.5\kappa\langle\tilde{a}^\dagger\tilde{a}_0\rangle + iNg\langle\tilde{\sigma}_{21}^1\tilde{a}_0\rangle$$

$$\frac{d}{dt}\langle\tilde{\sigma}_{21}^1\tilde{a}_0\rangle = -2ig\left(\langle a^\dagger\rangle\langle\tilde{\sigma}_{22}^1\tilde{a}_0\rangle + \langle a\rangle\langle a^\dagger\sigma_{22}^1\rangle + \langle\sigma_{22}^1\rangle\langle\tilde{a}^\dagger\tilde{a}_0\rangle - 2\langle a^\dagger\rangle\langle a\rangle\langle\sigma_{22}^1\rangle\right)$$
$$- ig\left(\langle a^\dagger\rangle\langle\tilde{\sigma}_{33}^1\tilde{a}_0\rangle + \langle a\rangle\langle a^\dagger\sigma_{33}^1\rangle + \langle\sigma_{33}^1\rangle\langle\tilde{a}^\dagger\tilde{a}_0\rangle - 2\langle a^\dagger\rangle\langle a\rangle\langle\sigma_{33}^1\rangle\right)$$
$$+ i\Omega_2\langle a\rangle + ig\langle\tilde{a}^\dagger\tilde{a}_0\rangle - 0.5\Gamma_2\langle\tilde{\sigma}_{21}^1\tilde{a}_0\rangle - i\Delta_2\langle\tilde{\sigma}_{21}^1\tilde{a}_0\rangle - 2i\Omega_2\langle\tilde{\sigma}_{22}^1\tilde{a}_0\rangle$$
$$- i\Omega_2\langle\tilde{\sigma}_{33}^1\tilde{a}_0\rangle - i\Omega_3\langle\tilde{\sigma}_{23}^1\tilde{a}_0\rangle$$

$$\frac{d}{dt}\langle\tilde{\sigma}_{31}^{1}\tilde{a}_0\rangle = -ig\left(\langle a^\dagger\rangle\langle\tilde{\sigma}_{32}^{1}\tilde{a}_0\rangle + \langle a\rangle\langle a^\dagger\sigma_{32}^{1}\rangle + \langle\sigma_{32}^{1}\rangle\langle\tilde{a}^\dagger\tilde{a}_0\rangle - 2\langle a^\dagger\rangle\langle a\rangle\langle\sigma_{32}^{1}\rangle\right) + i\Omega_3\langle a\rangle - 0.5\Gamma_3\langle\tilde{\sigma}_{31}^{1}\tilde{a}_0\rangle - i\Delta_3\langle\tilde{\sigma}_{31}^{1}\tilde{a}_0\rangle - i\Omega_2\langle\tilde{\sigma}_{32}^{1}\tilde{a}_0\rangle - i\Omega_3\langle\tilde{\sigma}_{22}^{1}\tilde{a}_0\rangle - 2i\Omega_3\langle\tilde{\sigma}_{33}^{1}\tilde{a}_0\rangle - 0.5\gamma_2\langle\tilde{\sigma}_{31}^{1}\tilde{a}_0\rangle - 0.5\gamma_3\langle\tilde{\sigma}_{31}^{1}\tilde{a}_0\rangle$$

$$\frac{d}{dt}\langle\tilde{\sigma}_{22}^{1}\tilde{a}_0\rangle = -ig\left(\langle a\rangle\left(\langle a\sigma_{21}^{1}\rangle + \langle\tilde{\sigma}_{21}^{1}\tilde{a}_0\rangle\right) + \langle\sigma_{21}^{1}\rangle\langle\tilde{a}\tilde{a}_0\rangle - 2\langle\sigma_{21}^{1}\rangle\langle a\rangle^2\right) + ig\left(\langle a^\dagger\rangle\langle\tilde{\sigma}_{12}^{1}\tilde{a}_0\rangle + \langle a\rangle\langle a^\dagger\sigma_{12}^{1}\rangle + \langle\sigma_{12}^{1}\rangle\langle\tilde{a}^\dagger\tilde{a}_0\rangle - 2\langle a^\dagger\rangle\langle a\rangle\langle\sigma_{12}^{1}\rangle\right) - \Gamma_2\langle\tilde{\sigma}_{22}^{1}\tilde{a}_0\rangle - i\Omega_2\langle\tilde{\sigma}_{21}^{1}\tilde{a}_0\rangle + i\Omega_2\langle\tilde{\sigma}_{12}^{1}\tilde{a}_0\rangle - 0.5\gamma_2\langle\tilde{\sigma}_{22}^{1}\tilde{a}_0\rangle$$

$$\frac{d}{dt}\langle\tilde{\sigma}_{32}^{1}\tilde{a}_0\rangle = -ig\left(\langle a\rangle\left(\langle a\sigma_{31}^{1}\rangle + \langle\tilde{\sigma}_{31}^{1}\tilde{a}_0\rangle\right) + \langle\sigma_{31}^{1}\rangle\langle\tilde{a}\tilde{a}_0\rangle - 2\langle\sigma_{31}^{1}\rangle\langle a\rangle^2\right) - 0.5\Gamma_2\langle\tilde{\sigma}_{32}^{1}\tilde{a}_0\rangle - 0.5\Gamma_3\langle\tilde{\sigma}_{32}^{1}\tilde{a}_0\rangle + i\Delta_2\langle\tilde{\sigma}_{32}^{1}\tilde{a}_0\rangle - i\Delta_3\langle\tilde{\sigma}_{32}^{1}\tilde{a}_0\rangle - i\Omega_2\langle\tilde{\sigma}_{31}^{1}\tilde{a}_0\rangle + i\Omega_3\langle\tilde{\sigma}_{12}^{1}\tilde{a}_0\rangle - 2\gamma_2\langle\tilde{\sigma}_{32}^{1}\tilde{a}_0\rangle - 0.5\gamma_3\langle\tilde{\sigma}_{32}^{1}\tilde{a}_0\rangle$$

$$\frac{d}{dt}\langle\tilde{\sigma}_{33}^{1}\tilde{a}_0\rangle = -\Gamma_3\langle\tilde{\sigma}_{33}^{1}\tilde{a}_0\rangle - i\Omega_3\langle\tilde{\sigma}_{31}^{1}\tilde{a}_0\rangle + i\Omega_3\langle\tilde{\sigma}_{13}^{1}\tilde{a}_0\rangle - 0.5\gamma_2\langle\tilde{\sigma}_{33}^{1}\tilde{a}_0\rangle$$

$$\frac{d}{dt}\langle\tilde{a}\tilde{a}_0\rangle = i\Delta_c\langle\tilde{a}\tilde{a}_0\rangle - 2\gamma_2\langle\tilde{a}\tilde{a}_0\rangle - 0.5\kappa\langle\tilde{a}\tilde{a}_0\rangle - iNg\langle\tilde{\sigma}_{12}^{1}\tilde{a}_0\rangle$$

$$\frac{d}{dt}\langle\tilde{\sigma}_{12}^{1}\tilde{a}_0\rangle = 2ig\left(\langle a\rangle\left(\langle a\sigma_{22}^{1}\rangle + \langle\tilde{\sigma}_{22}^{1}\tilde{a}_0\rangle\right) + \langle\sigma_{22}^{1}\rangle\langle\tilde{a}\tilde{a}_0\rangle - 2\langle\sigma_{22}^{1}\rangle\langle a\rangle^2\right) + ig\left(\langle a\rangle\left(\langle a\sigma_{33}^{1}\rangle + \langle\tilde{\sigma}_{33}^{1}\tilde{a}_0\rangle\right) + \langle\sigma_{33}^{1}\rangle\langle\tilde{a}\tilde{a}_0\rangle - 2\langle\sigma_{33}^{1}\rangle\langle a\rangle^2\right) - i\Omega_2\langle a\rangle - ig\langle\tilde{a}\tilde{a}_0\rangle - 0.5\Gamma_2\langle\tilde{\sigma}_{12}^{1}\tilde{a}_0\rangle + i\Delta_2\langle\tilde{\sigma}_{12}^{1}\tilde{a}_0\rangle + 2i\Omega_2\langle\tilde{\sigma}_{22}^{1}\tilde{a}_0\rangle + i\Omega_2\langle\tilde{\sigma}_{33}^{1}\tilde{a}_0\rangle + i\Omega_3\langle\tilde{\sigma}_{32}^{1}\tilde{a}_0\rangle - 2\gamma_2\langle\tilde{\sigma}_{12}^{1}\tilde{a}_0\rangle$$

$$\frac{d}{dt}\langle\tilde{\sigma}_{13}^{1}\tilde{a}_0\rangle = ig\left(\langle a\rangle\left(\langle a\sigma_{23}^{1}\rangle + \langle\tilde{\sigma}_{23}^{1}\tilde{a}_0\rangle\right) + \langle\sigma_{23}^{1}\rangle\langle\tilde{a}\tilde{a}_0\rangle - 2\langle\sigma_{23}^{1}\rangle\langle a\rangle^2\right) - i\Omega_3\langle a\rangle - 0.5\Gamma_3\langle\tilde{\sigma}_{13}^{1}\tilde{a}_0\rangle + i\Delta_3\langle\tilde{\sigma}_{13}^{1}\tilde{a}_0\rangle + i\Omega_2\langle\tilde{\sigma}_{23}^{1}\tilde{a}_0\rangle + i\Omega_3\langle\tilde{\sigma}_{22}^{1}\tilde{a}_0\rangle + 2i\Omega_3\langle\tilde{\sigma}_{33}^{1}\tilde{a}_0\rangle - 0.5\gamma_2\langle\tilde{\sigma}_{13}^{1}\tilde{a}_0\rangle - 0.5\gamma_3\langle\tilde{\sigma}_{13}^{1}\tilde{a}_0\rangle$$

$$\frac{d}{dt}\langle\tilde{\sigma}_{23}^{1}\tilde{a}_0\rangle = ig\left(\langle a^\dagger\rangle\langle\tilde{\sigma}_{13}^{1}\tilde{a}_0\rangle + \langle a\rangle\langle a^\dagger\sigma_{13}^{1}\rangle + \langle\sigma_{13}^{1}\rangle\langle\tilde{a}^\dagger\tilde{a}_0\rangle - 2\langle a^\dagger\rangle\langle a\rangle\langle\sigma_{13}^{1}\rangle\right) - 0.5\Gamma_2\langle\tilde{\sigma}_{23}^{1}\tilde{a}_0\rangle - 0.5\Gamma_3\langle\tilde{\sigma}_{23}^{1}\tilde{a}_0\rangle - i\Delta_2\langle\tilde{\sigma}_{23}^{1}\tilde{a}_0\rangle + i\Delta_3\langle\tilde{\sigma}_{23}^{1}\tilde{a}_0\rangle + i\Omega_2\langle\tilde{\sigma}_{13}^{1}\tilde{a}_0\rangle - i\Omega_3\langle\tilde{\sigma}_{21}^{1}\tilde{a}_0\rangle - 0.5\gamma_3\langle\tilde{\sigma}_{23}^{1}\tilde{a}_0\rangle$$

4 Publication

Quantum **6**, 617 (2022)

QuantumCumulants.jl: A Julia framework for generalized mean-field equations in open quantum systems[†]

D. Plankensteiner[1], C. Hotter[1] and H. Ritsch[1]

[1] *Institut für Theoretische Physik, Universität Innsbruck, Technikerstraße 21, A-6020 Innsbruck, Austria*

A full quantum mechanical treatment of open quantum systems via a Master equation is often limited by the size of the underlying Hilbert space. As an alternative, the dynamics can also be formulated in terms of systems of coupled differential equations for operators in the Heisenberg picture. This typically leads to an infinite hierarchy of equations for products of operators. A well-established approach to truncate this infinite set at the level of expectation values is to neglect quantum correlations of high order. This is systematically realized with a so-called cumulant expansion, which decomposes expectation values of operator products into products of a given lower order, leading to a closed set of equations. Here we present an open-source framework that fully automizes this approach: first, the equations of motion of operators up to a desired order are derived symbolically using predefined canonical commutation relations. Next, the resulting equations for the expectation values are expanded employing the cumulant expansion approach, where moments up to a chosen order specified by the user are included. Finally, a numerical solution can be directly obtained from the symbolic equations. After reviewing the theory we present the framework and showcase its usefulness in a few example problems.

https://github.com/qojulia/QuantumCumulants.jl

doi: 10.22331/q-2022-01-04-617

[†]D. Plankensteiner came up with the idea for the toolbox *QuantumCumulants.jl* and wrote most of its code. The contributions from the author of this thesis were discussions and support about fundamental concepts and implementations of the framework, as well as testing and writing examples. In 2022 the author of this thesis took over the responsibility for the maintenance and development of *QuantumCumulants.jl*.

4.1 Introduction

Numerical simulation of the time evolution of quantum systems has become a key method in the fields of quantum optics and quantum information as analytic approaches and solutions are only rarely available. In particular, for open systems one has to go beyond the determination of eigenenergies and eigenstates of a given Hamiltonian and look for the stationary solution of the corresponding system density matrix. To study processes like quantum annealing even solutions for time-dependent Hamiltonians are required. As there are only a finite number of building blocks for quantum optics Hamiltonians, the desire to reduce the repeated effort for implementing quite similar problem Hamiltonians and master equations has led to the development of several generic numerical frameworks and developer tools in the past decades. These simultaneously target fast coding, high memory efficiency and short execution times.

Among the most well-known frameworks are the early Quantum Optics MATLAB toolbox implemented by Sze Tan already over two decades ago [4.1] and its first open source successor, the Quantum Toolbox in Python (QuTiP) [4.2, 4.3]. Further efforts to optimize code efficiency and memory use lead to C++ based software such as C++QED [4.4]. Similar projects exist for quantum information applications and highly correlated quantum spin systems [4.5–4.8].

More recently, based on the highly efficient Julia programming language [4.9], the framework QuantumOptics.jl [4.10] was developed with the goal to implement a large class of quantum optics problems and methods. All these numerical toolboxes aim to streamline and simplify the usage of standard numerical techniques, which are generally based on the matrix representation of quantum mechanical operators in truncated Hilbert spaces. Equations of motion that govern the dynamics of quantum systems, such as the Schrödinger equation for closed systems, stochastic wavefunction simulations or the master equation for open systems then amount to solving finite sets of (stochastic) coupled differential equations.

One practical limitation here is the growing size of the matrices representing quantum mechanical operators in larger Hilbert spaces. A generic example is the exponential growth of the size of the Hilbert space describing N two-level atoms (qubits) whose state is described by a vector of a size scaling as 2^N. Correspondingly, operators in this Hilbert space are represented by matrices of the size $2^N \times 2^N$. Clearly, representing many atoms is hardly feasible in such an approach. In some specific cases this number has been pushed to several tens of spins [4.11], which is still well below the numbers nowadays available in experimental implementations.

In order to treat configurations of higher numbers of subsystems, one has to apply different techniques to reduce the problem size. One highly successful approach in the study of lattice dynamics is based on matrix product states and the density renormalization group [4.12, 4.13]. Given a state that describes a potentially large composite system one can reduce the degrees of freedom to the relevant ones to represent the state vector more efficiently thereby reducing the dimensionality of the problem. Similar restrictions to the low energy sector of a many-body Hilbert space can lead to sufficient accuracy in the low temperature or low excitation regime.

An alternative approach follows a similar idea by neglecting quantum correlations of higher order leading to a sufficiently accurate description in regimes exhibiting low correlations. The starting point are the c-number differential equations describing the dynamics of the expectation values of a given set of operators. These are generally coupled to higher order products of these operators leading to an infinite number of equations. In order to truncate the set of equations one can systematically approximate the higher-order products. To this end the concept of cumulants, originally conceived for the treatment of stochastic variables, has been generalized to operators [4.14]. The joint cumulant of a set of operators is a measure of the correlations of those operators, in that it vanishes if one (or a subset) of the operators is statistically independent of the others. Neglecting quantum correlations above a certain order is then equivalent to neglecting the joint cumulant of a set of operators.

Such order-based reductions allow for the construction of a closed set of ordinary differential equations for the averages of operators of interest. The equations of motion for the corresponding averages are obtained from the operators which appear as noncommutative variables, that obey prescribed fundamental commutation relations. These commutation relations can be used in the symbolic computation of the Heisenberg equations (for closed systems) or Quantum Langevin equations (for open systems) in operator form, from which the equations of motion for averages can be obtained. Neglecting the joint cumulants above a certain order generally leads to a complexity that scales polynomially, where the leading order is determined by the point up to which correlations are kept. In this sense a second-order treatment of N identical subsystems requires numerically solving $\mathcal{O}(N^2)$ equations.

As already discovered in the early days of quantum optics, the generalized cumulant expansion approach works well in open-system problems such as lasing [4.15, 4.16]. In the recent renewed interest in so-called superradiant lasers, where large ensembles of particles interact via a single cavity mode, the method was extensively used with notable success [4.17–4.26]. Furthermore, not only cavity QED systems have been calculated, but also ensembles of interacting free-space atoms, pointing out the importance of higher orders in specific cases [4.27–4.29].

The disadvantage of this method is that it requires the analytical computation of a large number of equations even at fairly low orders of expansions and thus lacks the conceptual simplicity of encoding the numerical solution of master equations via the toolboxes mentioned in the beginning. Higher-order treatments can quickly result in a set of equations that is too large to be manageable by hand in a reasonable amount of time. Furthermore, for each modification one wants to implement with this approach it is required to rederive the equations of motion for the operators before performing the cumulant expansion up to the desired order.

In this paper, we present a framework which aims to address these issues. We developed QuantumCumulants.jl in order to automize the derivation of equations, the cumulant expansion to an arbitrary order, as well as the final step of numerically implementing the resulting set of equations. It is written in the Julia language [4.9], combining a certain ease of use with high performance. Before presenting the framework itself, we will provide a review of the theory behind the cumulant expansion approach [4.14].

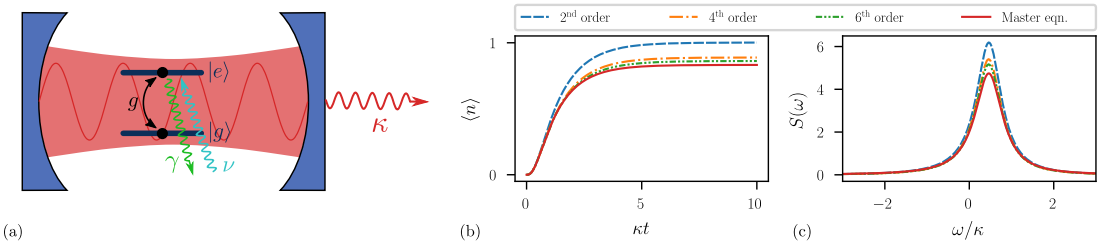

Figure 4.1: *The single-atom laser.* (a) Schematic illustration of an optical resonator containing a single atom that acts as a gain medium for the laser. (b,c) Comparison of the dynamics when treating the single-atom laser model in a second-, fourth- and sixth-order approximation, as well as in a full quantum model (master equation). In (b), we show the average photon number, and (c) shows the power density spectrum of the laser. The parameters where $\Delta = \kappa/2$, $g = 1.5\kappa$, $\gamma = 1.25\kappa$, and $\nu = 4\kappa$.

Next, we will highlight some details of the implementation. After that, we showcase the capability of the framework at the hand of some examples. Finally, we provide an overview of the framework's limitations and an outlook on possible future changes.

4.2 Theoretical background

In this section we will set the ground for the programmatic framework by providing a detailed review of the underlying theory.

4.2.1 A brief example

For didactic purposes, we will specify a model of a well-known example for which the cumulant expansion approach is known to work well. We will return to this example at each step of the approach for clarity.

Consider the simplest quantum model of a laser: a single two-level atom, acting as gain medium, is placed inside an optical cavity, cf. Fig. 4.1(a). The coherent dynamics of this system is described by the Jaynes-Cummings Hamiltonian,

$$H_{\mathrm{JC}} = \hbar\Delta a^\dagger a + \hbar g \left(a^\dagger \sigma^{ge} + a\sigma^{eg}\right). \tag{4.1}$$

Here, $\Delta = \omega_{\mathrm{c}} - \omega_{\mathrm{a}}$ is the detuning between the cavity resonance frequency ω_{c} and the atomic transition frequency ω_{a}. The coupling between the cavity and the atom is governed by the frequency g. The operators $\sigma^{ij} = |i\rangle\langle j|$ describe atomic transitions between the ground state $|g\rangle$ and its excited state $|e\rangle$, whereas the field dynamics are characterized by the photonic annihilation operator a and the creation operator $a^\dagger$.

The atom can spontaneously emit a photon at a rate γ, described by the damping operator σ^{ge}. At the same time, the cavity loses photons at a rate κ, which is included with the damping operator a. Finally, gain to the system is provided by incoherently

driving the atom from the ground to the excited state at rate ν with the "damping" operator σ^{eg} [see Fig. 4.1(a)].

Solving the Master equation of this system will yield the time dynamics of the density matrix, which contains the entire information about the system. However, if we only want to compute some specific expectation values in the end, we may not need all this information. Rather, the task is then to find equations of motion for the averages that allow us to solve for them directly. As we will see in the following, this can be achieved by approximating the full dynamics, which also reduces the numerical complexity of obtaining the average values.

4.2.2 Equations of motion in the Heisenberg picture

The starting point of any system that is to be simulated is its definition. Essentially, this means that the Hamiltonian and corresponding decay channels (if any) are specified. The time evolution of a system operator $\mathcal{O}$ is then given by

$$\dot{\mathcal{O}} = \frac{i}{\hbar}[H, \mathcal{O}] + \sum_n [c_n^\dagger, \mathcal{O}] \left(\sqrt{\gamma_n}\xi_n(t) + \frac{\gamma_n}{2} c_n \right) - \left(\sqrt{\gamma_n}\xi_n^\dagger(t) + \frac{\gamma_n}{2} c_n^\dagger \right) [c_n, \mathcal{O}]. \quad (4.2)$$

In the above, H is the Hamiltonian describing the unitary time evolution of the system. Additionally, the system features distinct decay channels with rates γ_n and corresponding collapse operators c_n. The operators ξ_n describe quantum noise. Eq. (4.2) is known as the Quantum Langevin equation [4.30].

In the following, we will assume that any noise that occurs in the systems is white noise. Then, the operators ξ_n in Eq. (4.2) do not contribute to any averages we compute. Hence, if we are only interested in averages we may drop the noise terms from Eq. (4.2) and compute

$$\dot{\mathcal{O}} = \frac{i}{\hbar}[H, \mathcal{O}] + \sum_n \frac{\gamma_n}{2} \left(2c_n^\dagger \mathcal{O} c_n - c_n^\dagger c_n \mathcal{O} - \mathcal{O} c_n^\dagger c_n \right). \quad (4.3)$$

For closed systems, i.e. $\gamma_n = 0$, we recover the Heisenberg equation. In the following, we will develop a theory that allows us to obtain a closed set of c-number equations from Eq. (4.3) by truncating the "order" of averages (or moments) of operator products.

To illustrate, take the example of a single-atom laser. Say we would like to compute the time evolution of the average of the field operator a. Using Eq. (4.2) in order to derive the corresponding operator equation of motion, we see that a depends on the atomic operators as well. Hence, we derive the equations for all occurring operators to obtain a complete set of equations, and find

$$\dot{a} = -\left(i\Delta + \frac{\kappa}{2} \right) a - ig\sigma^{ge}, \quad (4.4a)$$

$$\dot{\sigma}^{ge} = -\frac{\gamma + \nu}{2}\sigma^{ge} + iga\sigma^{ee}, \quad (4.4b)$$

$$\dot{\sigma}^{ee} = -\gamma\sigma^{ee} + \nu\left(1 - \sigma^{ee}\right) + ig\left(a^\dagger \sigma^{ge} - a\sigma^{eg} \right). \quad (4.4c)$$

The above set of equations consists of operator equations. Solving these directly is equivalent of the numerical complexity of solving a Master equation. In addition, Eq. (4.4) is incomplete: in order to obtain correct results, we need to include the quantum noise; i.e., the equations are stochastic operator differential equations, making them numerically even more expensive.

Averaging over the above equations, however, makes them more tractable. The averages of operators are simple c-numbers and we hope to obtain a set of equations that is simple to solve in the end. For the averages of Eq. (4.4), we find

$$\langle \dot{a} \rangle = -\left(i\Delta + \frac{\kappa}{2}\right) \langle a \rangle - ig \langle \sigma^{ge} \rangle , \tag{4.5a}$$

$$\langle \dot{\sigma}^{ge} \rangle = -\frac{\gamma + \nu}{2} \langle \sigma^{ge} \rangle + ig \langle a\sigma^{ee} \rangle , \tag{4.5b}$$

$$\langle \dot{\sigma}^{ee} \rangle = -\gamma \langle \sigma^{ee} \rangle + \nu \left(1 - \langle \sigma^{ee} \rangle\right) + ig \left(\langle a^\dagger \sigma^{ge} \rangle - \langle a\sigma^{eg} \rangle \right) . \tag{4.5c}$$

Now, we are confronted with another problem: averages of operator products, such as $\langle a\sigma^{ee} \rangle$ occur in Eq. (4.5), and since in general $\langle a\sigma^{ee} \rangle \neq \langle a \rangle \langle \sigma^{ee} \rangle$ the set of c-number equations is incomplete. Deriving equations of motion for those averages does not solve the problem either, since they will couple to averages of ever longer operator products. We thus converted the operator equations to c-number equations. However, this does not lead to a closed set of equations and involves contributions of any order. Hence, in order to find a full solution one would have to derive and solve infinitely many equations.

We therefore have to resort to some kind of approximation which allows for a cutoff at higher orders. The systematic approach to do this the so-called cumulant expansion [4.14] which we will review in the next section.

4.2.3 Cumulant expansion

At this point of the theoretical introduction, we will introduce the most essential part of the approach used in our simulation package QuantumCumulants.jl. To this end, we provide a short review of the generalized cumulant expansion method, which was initially introduced by R. Kubo [4.14]. The basic idea is to truncate c-number equations such as Eqs. (4.5) by expanding averages of higher-order operator products in terms of products of lower order expectation values. To clarify, we call the number of operator constituents in a product the "order" of the product; e.g., $\langle a\sigma^{ee} \rangle$ is of order 2.

The joint cumulant (which we denote by $\langle \cdot \rangle_c$) of a product of order n of the operators $\{X_1, ..., X_n\}$ is given by [4.14]

$$\langle X_1 X_2 ... X_n \rangle_c = \sum_{p \in P(\mathcal{I})} (|p| - 1)!(-1)^{|p|-1} \prod_{B \in p} \langle \prod_{i \in B} X_i \rangle . \tag{4.6}$$

In the above, $\mathcal{I} = \{1, 2, ..., n\}$, $P(\mathcal{I})$ is the set of all partitions of $\mathcal{I}$, $|p|$ denotes the length of the partition p, and B runs over the blocks of each partition. As a short

example, consider $n = 3$, where we have

$$\begin{aligned}\langle X_1X_2X_3\rangle_c = \langle X_1X_2X_3\rangle - \langle X_1X_2\rangle\langle X_3\rangle - \langle X_1X_3\rangle\langle X_2\rangle \\ - \langle X_1\rangle\langle X_2X_3\rangle + 2\langle X_1\rangle\langle X_2\rangle\langle X_3\rangle .\end{aligned} \tag{4.7}$$

Let us stress here that the cumulant of order n is given by averages of order n or lower. Furthermore, the average of order n occurs precisely once on the right-hand-side of Eq. (4.6).

The joint cumulant can be thought of as a general measure of correlation of operators. The key assumption behind the cumulant expansion approach follows from Theorem I in Ref. [4.14]. This theorem states that the joint cumulant of a set of operators is zero if any one (or any subset) of them is statistically independent of the others. The assumption we are making is to essentially invert this statement: instead of computing the joint cumulant of a given order to see if it is zero, we assume that it is. Since the average of the same order as the cumulant occurs only once in Eq. (4.6), we may rearrange the relation to arrive at an expression of an average in terms of only lower-order averages; i.e., if we assume the joint cumulant of order n to vanish, $\langle X_1X_2...X_n\rangle_c = 0$, then the average of the same order is given by

$$\langle X_1X_2...X_n\rangle = \sum_{p\in P(\mathcal{I})\backslash\mathcal{I}} (|p|-1)!(-1)^{|p|}\prod_{B\in p}\langle\prod_{i\in B} X_i\rangle , \tag{4.8}$$

where now $P(\mathcal{I})\backslash\mathcal{I}$ is the set of all partitions of $\mathcal{I}$ that does not contain $\mathcal{I}$ itself. We therefore approximate the average of order n by an expression that only involves averages of the order $n-1$ and below.

Returning to the example of $n = 3$, we see that when assuming $\langle X_1X_2X_3\rangle_c = 0$ in Eq. (4.7), we arrive at

$$\langle X_1X_2X_3\rangle = \langle X_1X_2\rangle\langle X_3\rangle + \langle X_1X_3\rangle\langle X_2\rangle + \langle X_1\rangle\langle X_2X_3\rangle - 2\langle X_1\rangle\langle X_2\rangle\langle X_3\rangle . \tag{4.9}$$

Note that the joint cumulant of order $n = 2$ is just the covariance. Neglecting this is equivalent to neglecting all quantum correlations in the system leading to the assumption that $\langle X_1X_2\rangle = \langle X_1\rangle\langle X_2\rangle$. This is the lowest-order mean-field approximation and renders the dynamics of the system under consideration classical.

The relation obtained in Eq. (4.8) can also be applied recursively, if for example one aims to express a fourth-order average as second-order terms only. Applying Eq. (4.8) once yields an expression consisting only of third-order averages and below. Upon repeated application, we can express the third-order terms as second-order ones, finally leading to an expression that has no terms above the second order.

Let us now return to our example of the single-atom laser. As we have just seen, the simplest thing we can do is a first-order cumulant expansion in which we neglect all

correlations. The set of equations from Eq. (4.5) then becomes

$$\langle \dot{a} \rangle = -\left(i\Delta + \frac{\kappa}{2}\right)\langle a \rangle - ig\langle \sigma^{ge} \rangle, \tag{4.10a}$$

$$\langle \dot{\sigma}^{ge} \rangle = -\frac{\gamma+\nu}{2}\langle \sigma^{ge} \rangle + ig\langle a \rangle \langle \sigma^{ee} \rangle, \tag{4.10b}$$

$$\langle \dot{\sigma}^{ee} \rangle = -\gamma\langle \sigma^{ee} \rangle + \nu(1 - \langle \sigma^{ee} \rangle) - 2g\mathrm{Im}\left\{\langle a^\dagger \rangle \langle \sigma^{ge} \rangle\right\}. \tag{4.10c}$$

The above system of equations is simple enough to solve using standard numerical techniques. However, it does not capture any quantum mechanical properties of the lasing setup. Furthermore, we can also see that if we consider the system to initially have zero field ($\langle a \rangle = 0$), and no coherence stored in the atom ($\langle \sigma^{ge} \rangle = 0$) we will never observe any lasing action. This is a signature of the phase invariance of the considered system: in a full quantum treatment, phase-dependent terms such as $\langle a \rangle$ are 0. Only phase-independent operators are nonzero in this example.

We proceed by employing the cumulant expansion approach to obtain a second-order treatment of the single-atom laser in hopes of a more accurate description. Just as before, we derive a set of operator equations, but this time operators such as $a^\dagger a$ are considered. Averaging over the resulting equations, we find

$$\frac{d}{dt}\langle a^\dagger a \rangle = -ig\langle a^\dagger \sigma^{ge} \rangle + ig\langle a\sigma^{eg} \rangle - \kappa\langle a^\dagger a \rangle, \tag{4.11a}$$

$$\frac{d}{dt}\langle a^\dagger \sigma^{ge} \rangle = \left(i\Delta - \frac{\gamma+\nu+\kappa}{2}\right)\langle a^\dagger \sigma^{ge} \rangle + ig\left(\langle \sigma^{ee} \rangle - \langle a^\dagger a \rangle\right) + 2ig\langle a^\dagger a \sigma^{ee} \rangle, \tag{4.11b}$$

$$\frac{d}{dt}\langle \sigma^{ee} \rangle = -\gamma\langle \sigma^{ee} \rangle + \nu(1 - \langle \sigma^{ee} \rangle) + ig\left(\langle a^\dagger \sigma^{ge} \rangle - \langle a\sigma^{eg} \rangle\right). \tag{4.11c}$$

The only term that keeps the above set of equations from being closed is $\langle a^\dagger a \sigma^{ee} \rangle$. Assuming that these operators are sufficiently uncorrelated, we employ the cumulant expansion from Eq. (4.9) to find

$$\begin{aligned}\langle a^\dagger a \sigma^{ee} \rangle &= \langle a^\dagger a \rangle \langle \sigma^{ee} \rangle + \langle a^\dagger \sigma^{ee} \rangle \langle a \rangle + \langle a^\dagger \rangle \langle a\sigma^{ee} \rangle - 2\langle a^\dagger \rangle \langle a \rangle \langle \sigma^{ee} \rangle \\ &= \langle a^\dagger a \rangle \langle \sigma^{ee} \rangle.\end{aligned} \tag{4.12}$$

In the second step we used that all phase-dependent averages vanish. Using the above completes the set of equations from Eqs. (4.11), and we can once again numerically solve it in a straightforward fashion. We find that it indeed provides a more precise description of the system, nicely approximating the full quantum model, as shown in Fig. 4.1(b) and Fig. 4.1(c).

For comparison, we also plot higher-order approximations in Fig. 4.1(b) and Fig. 4.1(c). You can see that with increasing order the approximate results converge to the full quantum description. From that we deduce that the approach based on a cumulant expansion is suitable for the description of physical systems. We note, however, that the overall accuracy of the approximations and convergence with higher orders is

strongly dependent on the chosen parameter regime. Going into a strong coupling regime (increasing the coupling g), for example, would lead to a high degree of quantum correlations between the atom and the cavity mode. Approximations in low order will fail to capture these. A sufficiently accurate approximation, however, might not be feasible since high orders lead to a large number of equations that need to be considered.

The single-atom laser considered here is already well-studied and understood. What if we wanted to adapt the model in order to describe a more realistic lasing setup? This could be done by, for example, adding multiple levels to the atom and considering a more realistic driving scheme. A laser usually features a gain medium consisting of a large number of atoms. What if we wanted to consider many atoms? The cumulant expansion approach is well suited for this as the complexity scales polynomially rather than exponentially with the number of atoms as in a full quantum treatment. However, to actually investigate any changes in the model, we would have to rederive all equations of motion, perform the cumulant expansion, complete the system of equations, and finally implement it for numerical solution. Each step involved in this procedure is both error-prone and tedious.

4.3 The framework

The entire procedure explained above can be automatically performed by QuantumCumulants.jl. To summarize, here is the step-by-step approach with which problems can be treated within the framework:

1. The Hilbert space of the system under consideration is defined. This is necessary since operators acting on different Hilbert spaces commute.

2. Fundamental operators and the corresponding Hamiltonian and dissipative processes need to be defined.

3. Equations of motion for a given set of operators are derived.

4. These equations are averaged and expanded in terms of cumulants up to a specified order.

5. A numerical solution can be obtained directly from the symbolic set of equations.

In this section we will provide a detailed description of the basic concepts QuantumCumulants.jl uses to perform these steps. For more extensive instructions on the usage of the framework, we refer the reader to the documentation that is available online [4.31]. The source code is also publicly accessible and hosted on GitHub [4.32].

We note that the noncommutative algebra and the symbolic rewriting using commutation relations is directly implemented in QuantumCumulants.jl. Standard simplifications are performed with the Symbolics.jl [4.33] library. In the final step, the modeling framework ModelingToolkit.jl [4.34] is employed to generate fast numerical code that can be used to obtain a numerical solution with the DifferentialEquations.jl [4.35] package.

4.3.1 Hilbert spaces and operators

The first thing one has to specify when treating a system is the Hilbert space that describes this system. There are currently two Hilbert spaces implemented: one that represents the quantum harmonic oscillator, a Hilbert space of infinite dimension, called `FockSpace`. The other one describes a finite set of discrete energy levels (such as atoms) and is called `NLevelSpace` as it allows for arbitrarily many energy levels. Note that there is no principal limitation that prevents the implementation of other kinds of Hilbert spaces, but these fundamental two cover a large number of problems already (see also Sec. 4.5.2).

A Hilbert space is a complete vector space. Choosing a basis in such a vector space allows one to represent operators as matrices. This is commonly used in order to solve Master equations. On a more abstract level, however, one can omit the choice of a basis, denoting operators as noncommutative elements of the Hilbert space rather than as matrices. This latter approach is used by QuantumCumulants.jl: operators are defined as noncommutative variables on a specified Hilbert space. Algebraic combinations of operators (such as addition and multiplication) are only possible if the combined operators are defined on the same Hilbert space. To treat composite systems, one needs to consider the product of the respective Hilbert spaces. Consider, for example, the Jaynes-Cummings model. Let $\mathcal{H}_\mathrm{c}$ be the Hilbert space of the cavity, and $\mathcal{H}_\mathrm{a}$ the Hilbert space of the atom, respectively. The operators in the Jaynes-Cummings model are then defined as elements of the Hilbert space $\mathcal{H}_\mathrm{c} \otimes \mathcal{H}_\mathrm{a}$. Strictly speaking, we would have to define

$$a \equiv a_0 \otimes \mathbb{1}_\mathrm{a}, \tag{4.13}$$

$$\sigma^{ij} \equiv \mathbb{1}_\mathrm{c} \otimes \sigma_0^{ij}, \tag{4.14}$$

where $\mathbb{1}_i$ is the identity operator on the Hilbert space $\mathcal{H}_i$. Technically, a_0 is the photonic annihilation operator, and a is only its extension on the product space. This is necessary since, e.g. the product $a_0\sigma_0^{eg}$, is not defined, yet the product $a\sigma^{eg}$ is.

This rigorous distinction is usually omitted since the action of a on the atomic Hilbert space is trivial (and vice-versa for σ). However, we have to take this into account when implementing algebra necessary for operators: while they are noncommutative in general, they commute if they act trivially on disjunct subspaces. Therefore, QuantumCumulants.jl stores the information on which subspace each operator acts nontrivially and uses it to swap operators where it is allowed to do so. In that sense, the operators of Eq. (4.13) are stored as, e.g. $a \in \mathcal{H}_\mathrm{c} \otimes \mathcal{H}_\mathrm{a}$ acting nontrivially on 1 (the first subspace) and $\sigma \in \mathcal{H}_\mathrm{c} \otimes \mathcal{H}_\mathrm{a}$ acting nontrivially on 2.

```julia
# Load the package
using QuantumCumulants

# Define Hilbert spaces and product space
hc = FockSpace(:cavity)
ha = NLevelSpace(:atom,(:g,:e))
h = hc ⊗ ha

# Define the operators
a = Destroy(h,:a)
σge = Transition(h,:σ,:g,:e)
```

Code sample 1: *Defining the Hilbert space and the fundamental operators of the Jaynes-Cummings model.*

In order to treat any system in the framework, one therefore has to specify the respective Hilbert spaces and then the operators. Note, that QuantumCumulants.jl infers the spaces on which an operator acts nontrivially if the choice is unambiguous. In the case of the Jaynes-Cummings model, the photonic annihilation operator can only be defined on the first Hilbert space, as the other one is not a space representing a quantum harmonic oscillator. If there are multiple Hilbert spaces of the same type in a composite system, however, the space on which an operator acts nontrivially must be explicitly specified on construction (see for example code sample 5).

4.3.2 Application of commutation relations

The basic simplification in the framework uses a few fundamental commutation relations which are immediately applied in any calculation involving operators. On top of that, standard algebraic simplification is performed using the Symbolics.jl [4.33] framework. In the following, we detail which commutation relations are used. Note that we rewrite terms such that the result adheres to normal ordering. The bosonic annihilation and creation operators fulfil the canonical commutation relation

$$[a, a^\dagger] = 1, \tag{4.15}$$

which is implemented such that all occurrences of the product $aa^\dagger$ are replaced by $a^\dagger a + 1$. Products of operators describing transitions between discrete energy levels are computed as

$$\sigma^{ij}\sigma^{kl} = \delta_{jk}\sigma^{il}, \tag{4.16}$$

which either vanishes or results in another transition operator. An additional property of these operators is that the sum over all projectors is conserved and equal to unity. I.e, considering n levels, we have

$$\sum_{i=1}^{n} \sigma^{ii} = 1. \tag{4.17}$$

This property is used to reduce the number of equations by replacing one of the projectors. By default, the projector of the first level specified is replaced in the framework.

As mentioned above, the commutation relations are applied as soon as operators are combined in a multiplication. This is a deliberate design choice since it is imperative that all possible commutation relations are applied prior to the cumulant expansion. For example, if we were to perform a first-order cumulant expansion on the term $aa^\dagger$, we would have

$$\langle aa^\dagger \rangle = \langle a^\dagger a \rangle + 1 \approx |\langle a \rangle|^2 + 1. \tag{4.18}$$

If the commutation relations were not applied at some point, the cumulant expansion would instead yield

$$\langle aa^\dagger \rangle \approx |\langle a \rangle|^2. \tag{4.19}$$

Obviously, this is incorrect as it would imply that $\langle aa^\dagger \rangle = \langle a^\dagger a \rangle$.

4.3.3 Averaging and cumulant expansion

On the one hand, computing the average of an operator is straightforward: it is simply converted to a complex number. The same is done for products of operators. For constants involved in the product, as well as for addition, the linearity is used. For example,

$$\langle \lambda_1 ab + \lambda_2 c \rangle = \lambda_1 \langle ab \rangle + \lambda_2 \langle c \rangle, \tag{4.20}$$

where a, b, and c are operators and $\lambda_i \in \mathbb{C}$.

On the other hand, the cumulant expansion is more involved, as has been described in Sec. 4.2. The framework implements the expansion using a programmatic version of Eq. (4.8). To this end, standard combinatoric functions from the mathematical Combinatorics.jl library are employed [4.36].

4.3.4 Additional features

Here, we will provide a brief overview of some convenient features that QuantumCumulants.jl offers.

Automatic completion of systems

So far, we have dealt only with the single-atom laser. In second-order, this led to a comparatively small number of equations. It was thus easy to see which equations of motion were necessary in order to arrive at a complete set of equations. However, when dealing with many equations, this might no longer be so simple. Even for small systems, though, we would like to avoid the iterative work of looking for averages that are missing from the equations, and adding them to the set.

The framework offers an automized version of this procedure: using the `complete` function, it will look for any averages that occur on the right-hand-side in a system of equations and check whether the equations of motion are already there. If not, it will derive the necessary equations and add them to the set. Essentially, this means that the only thing the user needs to provide is a starting point, namely the equation for at least one average of interest, and the order at which the equations should be truncated.

An additional noteworthy feature in this automatic completion is that the user can provide a custom filter function, which specifies whether an average should be included. This can be very useful if certain averages should be excluded from the completion algorithm since it can significantly speed up the program as symbolic rewriting operations are reduced. For example, you can use this to neglect phase-dependent terms that are actually zero in a laser model (cf. code sample 4).

Two-time correlation functions

As the name suggests, this type of correlation function depends on two different time parameters. For example, in order to compute the spectrum shown in Fig. 4.1(c), we need to consider the correlation function defined by

$$g(t,\tau) = \langle a^\dagger(t+\tau)a(t)\rangle \,. \tag{4.21}$$

The spectrum is then determined by taking the Fourier transform of Eq. (4.21). This correlation function depends not only on the time t but also on the delay τ. The detailed method with which the correlation functions and spectra are computed is rather extensive, and we refer to Appendix 4.7.1 for details.

The basic idea is that the equation of motion for a two-time correlation function such as the one in Eq. (4.21) is determined by the equation of motion of the operator that depends on the delay τ, which is also known as the quantum regression theorem. Deriving this equation will usually lead to couplings with other two-time correlation functions. Ultimately, one obtains a system of equations involving correlation functions, whose initial values are determined by the state of the original system under consideration at time t. For example, at $\tau = 0$, the correlation function in Eq. (4.21) is equal to the average cavity photon number at time t. If the state of the system is known at time t one can then solve for the correlation function.

The entire procedure of finding the equations that govern a two-time correlation function and generating the code necessary to find a numerical solution is implemented in QuantumCumulants.jl with the `CorrelationFunction` type. Furthermore, spectra can be computed from correlation functions with the `Spectrum` functionality.

Mixing orders

In certain systems it might make sense to use different orders of the cumulant expansion in different context. For example, one could envision a situation where a laser model involving a cavity mode and many atoms should be treated such that the atoms are approximately independent of one another, but build up some correlations with the

cavity field. Thus, it makes sense to expand all expectation values involving atomic operators only to first order, whereas cavity mode expectation values as well as cavity-atom expectation values (such as $\langle a^\dagger \sigma^{ge} \rangle$) are kept up to the second order. This approach can be quite useful since then the number of equations scales only linearly with the atom number, whereas in second order it would already scale quadratically.

Mixed orders can be used within the framework simply by providing a vector instead of a single integer as the order parameter in the cumulant expansion. Each entry in that vector corresponds to the order of the subsystem of the product space. The order to be applied to an average is then determined by the action on the respective subspace. If an average acts on multiple subsystems, the order is chosen according to a function which by default picks the maximum (note that this can be changed by the user).

4.4 Examples

In this section we will showcase the framework's usefulness by implementing a few examples. Note that similar examples can also be found in the documentation [4.31]. Before we dive into more involved examples, let us briefly show the one used in Sec. 4.2. In code sample 2, we see how one can implement a single-atom laser model in the framework.

```
using QuantumCumulants

# Define hilbert space and fundamental operators
hf = FockSpace(:cavity)
ha = NLevelSpace(:atom,(:g,:e))
h = hf ⊗ ha
@qnumbers a::Destroy(h) σ::Transition(h)

# Hamiltonian and collpase operators
@cnumbers Δ g γ κ ν
H = Δ*a'*a + g*(a'*σ(:g,:e) + a*σ(:e,:g))
J = [a,σ(:g,:e),σ(:e,:g)]
rates = [κ,γ,ν]

# Derive a set of second-order equations
eqs = meanfield(a'*a,H,J;rates=rates,order=2)
eqs_completed = complete(eqs)

# Convert to an ODESystem and solve numerically
using OrdinaryDiffEq, ModelingToolkit
@named sys = ODESystem(eqs_completed)
u0 = zeros(ComplexF64,length(eqs_completed))
p = (Δ, g, γ, κ, ν)
p0 = (0.5, 1.5, 1.25, 1, 4)
prob = ODEProblem(sys,u0,(0.0,20.0),p.=>p0)
sol = solve(prob,RK4())

# Compute the spectrum
c = CorrelationFunction(a', a, eqs_completed; steady_state=true)
S = Spectrum(c,p)
ω = range(-π,π,length=301)
s = S(ω,sol.u[end],p0)
```

Code sample 2: *The single-atom laser example implemented with QuantumCumulants.jl.*

Let us stress here that the code shown in code sample 2 is actually more general than what has been discussed in Sec. 4.2. In particular, one could consider a higher-order approximation simply by editing one line in the script when completing the system of equations, e.g.

```
eqs_completed = complete(eqs;order=4)
```

will use a fourth-order cumulant expansion. The script will produce and solve the equations as well as compute the spectrum of the laser. In fact, the results computed in code sample 2 were used in the graphs shown in Fig. 4.1(b) and Fig. 4.1(c).

4.4.1 A laser with a three-level pump scheme

Here, we will show how one can implement systems with atoms that feature multiple energy levels. Consider therefore a slightly modified version of the single-atom laser,

that features an atom with three levels. This is inspired by the first laser ever built, which used Ruby as a gain medium [4.37]. There are three states, which we denote by $|1\rangle, |2\rangle$ and $|3\rangle$, respectively. The atoms are incoherently driven from the ground state $|1\rangle$ to the state $|2\rangle$, which is the highest in energy, at a rate ν. The state $|2\rangle$ then decays non-radiatively into the state $|3\rangle$ at a rate Γ. While the state $|3\rangle$ can also decay to the ground state $|1\rangle$ at a rate γ, population inversion can be achieved in $|3\rangle$ so long as $\Gamma, \nu \gg \gamma$. Coupling a cavity to the transition $|1\rangle$ to $|3\rangle$ allows stimulated emission and subsequent amplification thus leading to lasing action.

```
using QuantumCumulants

# Hilbert space
hf = FockSpace(:cavity)
ha = NLevelSpace(:atom, 3)
h = hf ⊗ ha

# Parameters and operators
@cnumbers Δ₃ g Γ γ κ ν
@qnumbers a::Destroy(h) σ::Transition(h)

# Hamiltonian and Decay
H = Δ₃*σ(3,3) + g*(a'*σ(1,3) + a*σ(3,1))
J = [a,σ(3,2),σ(1,3),σ(2,1)]
rates = [κ,Γ,γ,ν]

# Derive equations
eqs = meanfield([a'*a,σ(3,3),σ(2,2)],H,J;rates=rates,order=4)
eqs_completed = complete(eqs)

# Solve
using OrdinaryDiffEq, ModelingToolkit
@named sys = ODESystem(eqs_completed)
u0 = zeros(ComplexF64, length(eqs_completed))
p0 = (Δ₃=>0, g=>1.8, Γ=>20, γ=>1.5, κ=>1, ν=>10)
prob = ODEProblem(sys,u0,(0.0,6.0),p0)
sol = solve(prob,RK4())
```

Code sample 3: *Three-level pump scheme in a laser.*

The Hamiltonian of this system reads

$$H = \hbar\Delta_3\sigma^{33} + \hbar g\left(a^\dagger\sigma^{13} + a\sigma^{31}\right), \tag{4.22}$$

where $\Delta_3 = \omega_3 - \omega_c$ is the detuning between the cavity and the lasing transition, and g is the coupling strength between the cavity and the atom. The implementation of this model is shown in code sample 3.

The key difference to the previous laser model is that we added an additional energy level to the atom by specifying the underlying Hilbertspace as `NLevelSpace(:atom, 3)`. In general, any number of energy levels can be specified here. It would thus be simple to generalize the model further to describe, for example, a gain medium with four levels.

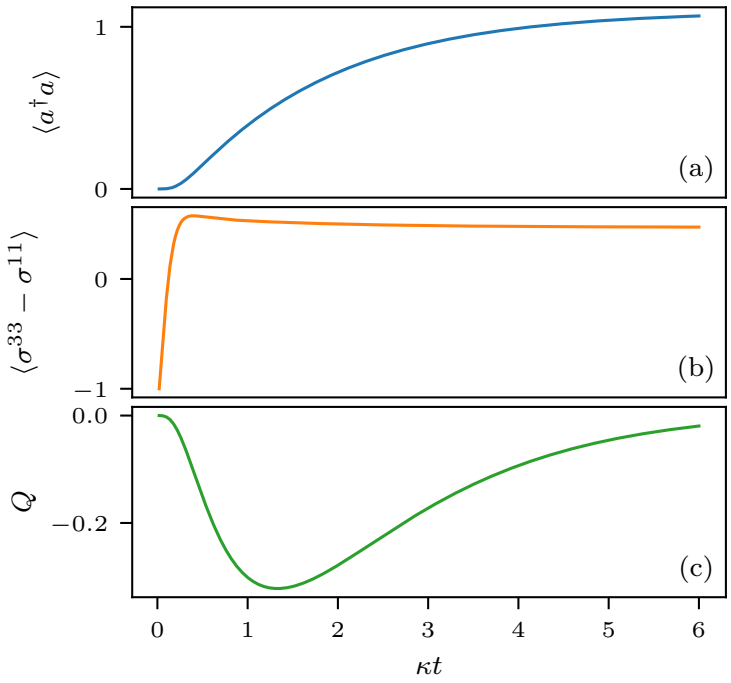

Figure 4.2: *Results of the three-level laser.* (a) The average photon number in the cavity and (b) the population inversion of the lasing transition and (c) the Mandel-Q parameter. The parameters are $\Delta_3 = 0$, $g = 1.8\kappa$, $\Gamma = 20\kappa$, $\gamma = 1.5\kappa$ and $\nu = 10\kappa$.

We plot the average cavity photon number in Fig. 4.2(a) as well as the population inversion of the lasing transition in Fig. 4.2(b). As we can see, the system indeed forms a minimal version of a laser. In addition, we also plot the so-called Mandel-Q parameter in Fig. 4.2(c), which is defined by

$$Q = \frac{\Delta n^2 - \langle n \rangle}{\langle n \rangle}, \tag{4.23}$$

where $n = a^\dagger a$ and $\Delta n^2 = \langle n^2 \rangle - \langle n \rangle^2$ is the variance of n. This parameter is a measure of non-classicality in that if $Q < 0$, the photon number variance is smaller than the average photon number, which corresponds to sub-Poissonian photon statistics. Clearly, in Fig. 4.2(c) Q is negative during the build-up phase of the laser and then tends towards 0. This signifies that a higher-order approximation (in this case moments up to fourth order are kept) suffices to capture nonclassical effects such as photon antibunching.

Let us stress here just how simple a fourth-order cumulant expansion becomes when using QuantumCumulants.jl. Deriving the 30 equations necessary for the fourth-order description would usually be challenging. With our framework, this can be achieved within a few lines of code and a runtime on the order of 10 seconds.

Note that the examples so far are relatively simple and (at least for low photon

numbers) could have been treated easily using a master equation as well. The aim of the next two examples will be to examine situations where this is no longer the case.

4.4.2 Pulsed superradiant laser

```julia
using QuantumCumulants

# Define parameters
N = 50
@cnumbers Δ g γ κ

# Define hilbert space
hf = FockSpace(:cavity)
ha = [NLevelSpace(Symbol(:atom,i),2) for i=1:N]
h = ⊗(hf, ha...)

# Define the fundamental operators
a = Destroy(h,:a)
σ(i,j,k) = Transition(h,Symbol(:σ, k),i,j,k+1)

# Hamiltonian
H = Δ*a'*a + g*sum(a'*σ(1,2,i) + a*σ(2,1,i) for i=1:N)

# Collapse operators
J = [a;[σ(1,2,i) for i=1:N]]
rates = [κ;[γ for i=1:N]]

# Derive equations for populations
ops = [σ(2,2,i) for i=1:N]
eqs = meanfield(ops,H,J;rates=rates,order=2)

# Complete but neglect phase-dependent terms
ϕ(x::Average) = ϕ(x.arguments[1])
ϕ(::Destroy) = -1
ϕ(::Create) = 1
ϕ(x::QTerm) = sum(map(ϕ, x.args_nc))
ϕ(x::Transition) = x.i - x.j
phase_invariant(x) = iszero(ϕ(x))
complete!(eqs;filter_func=phase_invariant)

using OrdinaryDiffEq, ModelingToolkit
@named sys = ODESystem(eqs)
u0 = zeros(ComplexF64, length(eqs))
u0[1:N] .= 1.0 # atoms are inverted initially
p0 = (Δ=>0.5, g=>0.5, γ=>0.25, κ=>1)
prob = ODEProblem(sys,u0,(0.0,10.0),p0)
sol = solve(prob,RK4())
```

Code sample 4: *Laser model with multiple atoms as gain medium.*

The previous examples showed comparably simple models of a laser where the gain

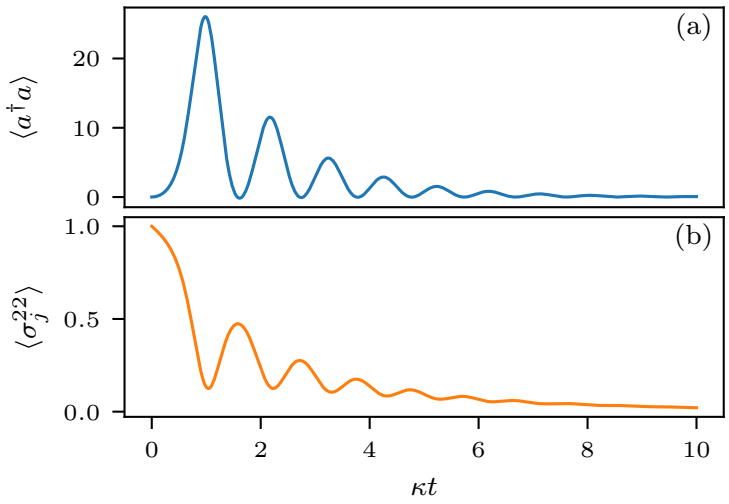

Figure 4.3: *Pulsed superradiant laser.* (a) The average photon number and (b) the excited state population of an atom inside the gain medium for a cavity mode coupled to $N = 50$ atoms that are initially in the excited state. The parameters are $\Delta = g = \kappa/2$, $\gamma = \kappa/4$ and $\nu = 4\kappa$.

medium consisted of only one atom. Here, we will consider a cavity mode which couples to a number of atoms N, which are initially inverted such that they provide gain. Note that we label the atomic ground state by $|1\rangle$ and the excited state by $|2\rangle$. The coherent dynamics is described by the Tavis-Cummings Hamiltonian,

$$H = \hbar\Delta a^\dagger a + \sum_{j=1}^{N} \hbar g_j \left(a^\dagger \sigma_j^{12} + a\sigma_j^{21} \right), \tag{4.24}$$

where g_j is the coupling rate of the jth atom. In addition, all atoms are subject to spontaneous emission at the rate γ. The implementation of this system in a second-order approximation for $N = 50$ is shown in code sample 4.

Note, that in the implementation we assumed equal couplings, i.e. $g \equiv g_j$. This is simply due to keeping the displayed code short and one can easily generalize code sample 4 to individual couplings. As can be seen in Fig. 4.3(a), a gain medium featuring $N = 50$ atoms leads to a substantial superradiant pulse. After an initial brief build-up of atomic coherences, collective stimulated emission leads to a steep increase of photons in the cavity mode. Following the initial pulse we observe oscillations in which the atoms reabsorb photons from the cavity [see Fig. 4.3(b)] and emit them again. The pulse size reduces over time as photons leak out of the cavity until finally no photons and atomic excitations are left. The results shown in Fig. 4.3 are in good qualitative agreement with the experimental demonstration of such a pulsed superradiant laser in Ref. [4.21].

Note that the key point of this example is that we are treating a number of atoms that

could not be investigated easily in a master equation approach as the size of the Hilbert space would already be huge. Deriving the necessary equations for a second-order approximation with our framework and a subsequent numerical solution takes only minutes on any modern computer and does not require a significant amount of memory. Increasing the atom number further to, say $N = 100$, code sample 4 would still finish in a time on the order of minutes, whereas a treatment with a master equation would be downright impossible at that point. The limiting factor for the cumulant expansion approach ultimately is the number of equations. Specifically, the number of equations in code sample 4 scales with the number of atoms as

$$n_{\text{eqs}} = \frac{N(N-1)}{2} + 2N + 1. \tag{4.25}$$

For $N = 50$, as used in code sample 4, this results in $n_{\text{eqs}} = 1326$ equations that need to be derived and solved.

As mentioned above, one could generalize the example to feature individual couplings of the atoms to the cavity or dissipation rates of the atomic ensemble. While we assumed ideal atomic positioning here, one could therefore also include fluctuations in the positions and hence the coupling rates. To do so, you would need to compute the time evolutions for many randomly generated atomic configurations and average over the results. So long as the time evolution itself remains deterministic, our toolbox is perfectly suitable for such simulations. It is important to note that in such a case the computationally intense symbolic derivation of equations still only has to be done once. Numerical variations of parameters can be done when setting the values for the time evolution.

4.4.3 Optomechanical cooling of a micromechanical oscillator

In this example, we show how to implement a cooling scheme based on radiation pressure coupling of light to a mechanical oscillator, such as a membrane. The oscillator is placed inside an optical cavity. The cavity is driven by a laser and the resulting radiation pressure of the cavity field effectively couples the photons in the cavity mode to the vibrational phonons of the mechanical oscillator mode. This model is based on the one studied in Ref. [4.38], and the Hamiltonian reads

$$H = -\hbar\Delta a^\dagger a + \hbar\omega_{\text{m}} b^\dagger b + \hbar G a^\dagger a \left(b + b^\dagger\right) + \hbar E \left(a + a^\dagger\right), \tag{4.26}$$

where $\Delta = \omega_\ell - \omega_c$ is the detuning between the laser (ω_ℓ) driving the cavity (ω_c). The amplitude of the laser is denoted by E, the resonance frequency of the mechanical oscillator by ω_m, and the radiation pressure coupling is given by G. The operators a and b are the photonic and phononic annihilation operators, respectively. Additionally, photons leak out of the cavity at a rate κ.

We will consider the membrane at room temperature. Its vibrational mode is in a

thermal state with an average number of phonons that can be estimated from

$$k_B T = n_{\text{vib}} \hbar \omega_m. \tag{4.27}$$

If the resonator has a resonance frequency of $\omega_m = 10\text{MHz}$, then the number of phonons at room temperature ($T \approx 300K$) is approximately $n_{\text{vib}} \approx 4 \times 10^6$. Let us stress here that treating such a large number of phonons in a master equation approach is problematic since this number determines the cut-off which can be chosen and thus the dimension of the Hilbert space. The averages treated in the cumulant expansion approach, however, are independent of this cut-off. Therefore, arbitrarily large numbers can be used (of course numerical floating-point errors may become substantial at some point). This makes QuantumCumulants.jl an ideal candidate to treat optomechanical problems in a high-temperature regime.

```
using QuantumCumulants
using OrdinaryDiffEq, ModelingToolkit

# Hilbert space
hc = FockSpace(:cavity)
hm = FockSpace(:motion)
h = hc ⊗ hm

# Operators
@qnumbers a::Destroy(h,1) b::Destroy(h,2)

# Parameters
@cnumbers Δ ωm E G κ

# Hamiltonian
H = -Δ*a'*a + ωm*b'*b + G*a'*a*(b + b') + E*(a + a')

# Derive equations
eqs = meanfield([b'*b,a'*a],H,[a];rates=[κ],order=2)
eqs_completed = complete(eqs)

# Numerical solution
@named sys = ODESystem(eqs_completed)
u0 = zeros(ComplexF64, length(eqs_completed))
u0[1] = 4*1e6 # Initial number of phonons
p0 = (Δ=>-10, ωm=>1, E=>200, G=>0.0125, κ=>20)
prob = ODEProblem(sys,u0,(0.0,60000),p0)
sol = solve(prob,RK4())
```

Code sample 5: *Cooling of a micromechanical oscillator at room temperature.*

The code implementing this model in a second-order approximation is shown in code sample 5. Note, that in order to accurately represent a thermal state, we cannot treat the problem in a first-order approximation since, in a thermal state, $\langle b \rangle = 0$, but the number of phonons is $\langle b^\dagger b \rangle \neq 0$ (with the initial value given by n_{vib}).

In Fig. 4.4 we show how the temperature of the membrane reduces while the photon

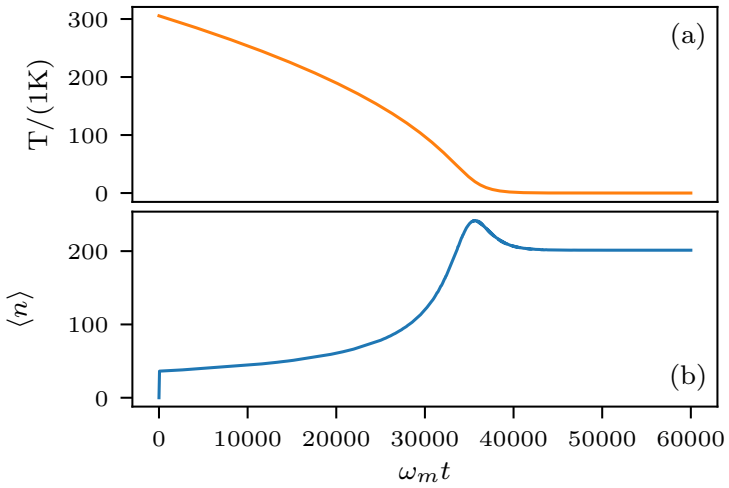

Figure 4.4: *Optomechanical cooling of a membrane.* (a) The temperature of the membrane reduces from room temperature over time. (b) At the same time, the field in the cavity builds up accumulating photons. The parameters were $\omega_m = 10\text{MHz}$, $\Delta = -10\omega_m$, $E = 200\omega_m$, $G = \omega_m/80$ and $\kappa = 20\omega_m$.

number inside the cavity builds up. The cooling works quite well, such that a final temperature below 1mK is reached.

4.5 Limitations and Outlook

As we have shown by now, the framework can be quite useful. However, there are some disadvantages, which we want to discuss in this section.

4.5.1 Principal limitations

First, we will provide an overview of the fundamental limits inherent to the approach. Mean-field descriptions based on the cumulant expansion are approximations that neglect a certain amount of quantum correlations. As such, they are not well suited to treat problems featuring large degrees of entanglement. In principle, one could go to ever higher orders to overcome this. However, this will polynomially increase the number of equations and quickly becomes unfeasible. Furthermore, there are cases where a full quantum treatment is simply necessary, and thus the mean-field approach cannot be used.

This brings us to a related issue: there is no generic way to know for certain if neglecting joint cumulants above a specific order is sufficiently accurate. The assumption that neglected cumulants are zero in principle has to be checked for each system and parameter set considered. This can only be done by actually computing the necessary cumulants or checking for convergence when going to higher orders. Note that this is

not always possible as a higher order means having to solve more equations.

When considering large composite systems, the number of equations increases polynomially, where the leading order of the polynomial is determined by the order. For example, N two-level atoms in second order lead to $\mathcal{O}(N^2)$ equations, in third order to $\mathcal{O}(N^3)$, etc. While this is a huge improvement over the exponential scaling with 2^N in a full quantum treatment, it can still limit the treatment of many atoms in higher orders.

4.5.2 Current limitations

There are some disadvantages to the framework that can possibly be addressed by changes in the future. One example is that QuantumCumulants.jl is currently not able to handle expressions involving exponentials of operators or similar functions. The exponential of an operator represents an infinite series involving all powers of its argument. As such, it is not straightforward to form the cumulant expansion. While it can be done for specific expressions, attempts at finding a generic way to do this for products involving multiple exponentials and other operators have not been successful so far.

Two more restrictions of QuantumCumulants.jl are not inherent, but the need to address them did not arise so far. The fact that we choose normal ordering of expressions is somewhat arbitrary and could be changed if, for example, one has a use-case that requires anti-normal ordering. Finally, there are currently only two Hilbert spaces implemented, namely `FockSpace`s and `NLevelSpace`s. Adding in different Hilbert spaces can be done, of course. We note, though, that a surprisingly large number of problems can be treated with only the two Hilbert spaces currently implemented.

4.5.3 Future changes

While QuantumCumulants.jl has already proven very useful, it is still in an early stage of development. Things may still change and new features will be added. Here we want to comment on the latter and mention a few possible directions.

At the very beginning when reviewing the theory, we presented the Quantum Langevin equation (QLE), Eq. (4.2), which features quantum noise. Throughout the entire paper, this noise was neglected as it does not contribute to averages. One possible future development is to actually consider this noise explicitly.

On the one hand, this would open the possibility to implement an approach based on the linearization of the operator equations around large average values. In steady state one can then compute the covariance matrix from a first-order (mean-field) solution of the system. This approach was used, for example, in Ref. [4.38].

On the other hand, one can convert the QLEs to c-number Langevin equations [4.39, 4.40], i.e. a set of stochastic differential equations. When the noise processes are chosen such that they reproduce the actual correlation functions of the quantum noise, one can obtain the second-order solutions by averaging over many trajectories. Additionally, one does not need to rely on white noise assumptions, but colored noise could be considered as well. Note that the ModelingToolkit.jl [4.34] framework and the

DifferentialEquations.jl [4.35, 4.41] library are already capable of handling stochastic differential equations.

Both the approaches based on the treatment of noise allow the reconstruction of second-order expectation values from a first-order solution. As such, they can be used in systems which are too large to be treated even in second order, but still exhibit some quantum phenomena.

Finally, another useful method exploits symmetry properties of multiple subsystem in order to significantly reduce the number of equations. This is done, for example, in the lasing model in Ref. [4.17] where atoms in the gain medium are assumed to be identical, which allows for an effective description with only a few equations for an arbitrarily large gain medium. An experimental automized version of this approach is already implemented in QuantumCumulants.jl (see Appendix 4.7.2).

4.6 Conclusions

We developed a novel open framework called QuantumCumulants.jl written in Julia, which automizes the analytical calculations and numerical implementation required for generalized mean-field approximations of the dynamics of open quantum systems. To this end we combined the symbolic handling of noncommutative variables for the automated cumulant expansion of moments to a specified order with other libraries offering automated code generation suitable for direct numerical solutions by standard differential equation solvers. After showing the general principle at the hand of the generic single atom laser model, we demonstrated the usefulness and versatility of our toolbox in several examples.

The framework already shows promising capabilities. Yet, the implications that it works at all go way beyond what can currently be done: the cumulant expansion approach is a powerful tool in its own right. Making the steps behind it easily accessible will allow a swift treatment of numerous problems that cannot be treated in a full quantum model. As development of QuantumCumulants.jl continues, the number of problems that can be addressed will continue to increase. Furthermore, even at points where the number of equations becomes too large to be handled by hand, the toolbox can still be successful. Potentially, the framework could be applied to problems not only in quantum optics, but also in quantum information, nanophotonics, and even condensed matter theory.

Acknowledgments

We would like to thank Anna Bychek and Georgy Kazakov for helpful discussions and testing of the software. We acknowledge funding from the European Union's Horizon 2020 research and innovation program under Grant Agreement No. 820404 iqClock. The graphs were produced with the open-source library Matplotlib [4.42].

4.7 Appendix

4.7.1 Correlation functions and power spectra

Correlation functions

Correlation functions can provide useful information about a system. The expectation values used to compute a correlation function are special in that they generally depend on two different times. Consider two operators A and B. Their two-time correlation function is given by

$$C(t,\tau) = \langle A(t+\tau)B(t)\rangle\,. \tag{4.28}$$

If the time difference $\tau = 0$, the correlation function is just the expectation value $\langle AB\rangle$ at time t. So in order to compute the correlation function, we can evolve a system of equations containing the expectation value at $\tau = 0$ up to a time t. The evolution with respect to the time delay is then determined by

$$\frac{d}{d\tau}C(t,\tau) = \langle\left(\frac{d}{d\tau}A(t+\tau)\right)B(t)\rangle\,. \tag{4.29}$$

Hence, we can derive the set of equations required to compute the correlation function from the equation of the operator A. Then, the same procedure as for a standard time evolution is used: the set of equations is expanded to a certain order and completed. Numerical code to solve the underlying differential equations is automatically generated.

As there is quite a bit of new theory involved here, let us go back to the example used throughout Sec. 4.2, namely the single-atom laser, to clarify the procedure explained above. The first-order coherence function of the cavity field is given by

$$C(t,\tau) = \langle a^\dagger(t+\tau)a(t)\rangle\,. \tag{4.30}$$

The equations of motion with respect to τ are readily constructed [cf. Eqs. (4.4)],

$$\frac{d}{d\tau}\langle a^\dagger(t+\tau)a(t)\rangle = \left(i\Delta - \frac{\kappa}{2}\right)\langle a^\dagger(t+\tau)a(t)\rangle + ig\,\langle\sigma^{eg}(t+\tau)a(t)\rangle \tag{4.31a}$$

$$\frac{d}{d\tau}\langle\sigma^{eg}(t+\tau)a(t)\rangle = -\frac{\gamma+\nu}{2}\langle\sigma^{eg}(t+\tau)a(t)\rangle - ig\,\langle a^\dagger(t+\tau)\sigma^{ee}(t+\tau)a(t)\rangle\,. \tag{4.31b}$$

Using the cumulant expansion to second order together with the phase invariance of the system, we obtain for the last term

$$\langle a^\dagger(t+\tau)\sigma^{ee}(t+\tau)a(t)\rangle = \langle a^\dagger(t+\tau)a(t)\rangle\,\langle\sigma^{ee}(t+\tau)\rangle\,. \tag{4.32}$$

In principle, we would have to compute the time evolution for $\langle\sigma^{ee}(t+\tau)\rangle$ with respect to τ together with the other equations. However, we will consider the system to be in steady state in order to avoid having to treat this additional equation.

Steady state

If the original system is evolved up to a time t such that it is in steady state, i.e. expectation values no longer change after that time, the set of equations determining the correlation function has a special property. Specifically, after the cumulant expansion has been performed, there can only be a single term in each product on the right-hand-side of the set of equations that depends on τ. All other terms depend on t alone, meaning that they are constant since they no longer change after the time t. Therefore, the system of equations from which the correlation function is computed is linear, in the sense that it can be written as

$$\frac{d}{d\tau}\mathbf{y}(\tau) = \mathbf{M}\mathbf{y}(\tau) + \mathbf{d}, \tag{4.33}$$

where $\mathbf{y}(\tau)$ is the vector of τ-dependent variables. The elements of the matrix $\mathbf{M}$ as well as the vector $\mathbf{d}$ are given by steady-state expectation values and parameters, i.e. they are independent of τ. In the case of the single-atom laser example, we have $\mathbf{y}(\tau) = \left(\langle a^\dagger(t+\tau)a(t)\rangle, \langle \sigma^{eg}(t+\tau)a(t)\rangle\right)^T$, $\mathbf{d} = \mathbf{0}$, and

$$\mathbf{M} = \begin{pmatrix} i\Delta - \frac{\kappa}{2} & ig \\ -ig\langle\sigma^{ee}\rangle & -\frac{\gamma+\nu}{2} \end{pmatrix}. \tag{4.34}$$

Power spectra

According to the Wiener-Khinchin theorem. the spectral density associated with a correlation function is given by its Fourier transform,

$$S(t,\omega) = 2\mathrm{Re}\left\{\int d\tau e^{-i\omega\tau} C(t,\tau)\right\}. \tag{4.35}$$

In order to compute this, we can solve the system of equations determining $C(t,\tau)$, subsequently taking the Fourier transform. However, if we are not interested in the temporal behavior of the correlation function, and if the system of which we want to compute the spectrum is in steady state, we can directly compute the spectrum from Eq. (4.33). To this end, we define

$$\mathbf{x}(s) = \mathcal{L}\left\{\mathbf{y}(\tau)\right\}, \tag{4.36}$$

where $\mathcal{L}$ denotes the Laplace transform with respect to τ. Taking the Laplace transform of Eq. (4.33), we have

$$(s\mathbb{1} - \mathbf{M})\,\mathbf{x}(s) = \mathbf{y}(0) + \frac{\mathbf{d}}{s}. \tag{4.37}$$

Note that the Laplace transform is equivalent to the Fourier transform at the point where $s = i\omega$, i.e $S(\omega) = 2\mathrm{Re}\left\{\mathbf{x}_1(i\omega)\right\}$. Hence, instead of computing the time evolution of the correlation function we can directly compute the spectrum by solving the linear

equation

$$\mathbf{x} = \mathbf{A}^{-1}\mathbf{b}, \tag{4.38}$$

where $\mathbf{A} = i\omega\mathbb{1} - \mathbf{M}$ and $\mathbf{b} = \mathbf{y}(0) + \mathbf{d}/(i\omega)$.

For the single-atom laser, solving Eq. (4.38) requires computing the inverse of a simple 2×2 matrix. For larger systems, the method using a Laplace transform is usually faster than integrating a system of equations of the same size. Additionally, it avoids numerical errors of the integration and the subsequent discrete Fourier transform.

4.7.2 Dealing with many identical subsystems

Consider a system consisting of multiple subsystems. If a subset of these subsystems is guaranteed to be identical at any point in time the number of equations needed to describe the whole system can be significantly reduced. In essence, instead of explicitly describing each subsystem, we may only describe a single one and place appropriate scaling factors at some points in the equations of motion.

For clarity, take the example from Sec. 4.4.2. The equation of motion for the average field amplitude is

$$\langle \dot{a} \rangle = -\left(i\Delta + \frac{\kappa}{2}\right)\langle a \rangle + \sum_{j=1}^{N} g_j \langle \sigma_j^{12} \rangle . \tag{4.39}$$

Now, given that all atoms are initially in the same state and their couplings to the cavity mode and the environment are all equal (i.e. $g_j \equiv g \;\forall\; j$ and similarly for γ_j and ν_j), then we know that $\langle \sigma_j^{k\ell} \rangle \equiv \langle \sigma_1^{k\ell} \rangle \;\forall\; j$. We may then rewrite the above equation and obtain

$$\langle \dot{a} \rangle = -\left(i\Delta + \frac{\kappa}{2}\right)\langle a \rangle + Ng \langle \sigma_1^{12} \rangle . \tag{4.40}$$

Thus, we only need to know $\langle \sigma_1^{12} \rangle$ in order to solve the above equation, instead of all the different $\langle \sigma_j^{12} \rangle$. Things are a bit more tricky, however, when looking at the equations of motion for atomic expectation values or mixed atom-field expectation values. One has to take care such that the equations reproduce the correct correlations between individual atoms. For example, the complete set of second-order equations of the laser

model involving many atoms reads

$$\frac{d}{dt}\langle {\sigma_1}^{22}\rangle = ig\langle a^\dagger {\sigma_1}^{12}\rangle - ig\langle a{\sigma_1}^{21}\rangle - \gamma\langle {\sigma_1}^{22}\rangle \tag{4.41a}$$

$$\begin{aligned}\frac{d}{dt}\langle a^\dagger {\sigma_1}^{12}\rangle &= ig\langle {\sigma_1}^{22}\rangle - ig\langle a^\dagger a\rangle + i\Delta\langle a^\dagger {\sigma_1}^{12}\rangle - 0.5\gamma\langle a^\dagger {\sigma_1}^{12}\rangle \\ &\quad - 0.5\kappa\langle a^\dagger {\sigma_1}^{12}\rangle + 2ig\langle {\sigma_1}^{22}\rangle\langle a^\dagger a\rangle + ig\langle {\sigma_1}^{21}{\sigma_2}^{12}\rangle\,(-1+N)\end{aligned} \tag{4.41b}$$

$$\frac{d}{dt}\langle a^\dagger a\rangle = -\kappa\langle a^\dagger a\rangle - iNg\langle a^\dagger {\sigma_1}^{12}\rangle + iNg\langle a{\sigma_1}^{21}\rangle \tag{4.41c}$$

$$\begin{aligned}\frac{d}{dt}\langle {\sigma_1}^{21}{\sigma_2}^{12}\rangle &= ig\langle a^\dagger {\sigma_1}^{12}\rangle - ig\langle a{\sigma_1}^{21}\rangle - \gamma\langle {\sigma_1}^{21}{\sigma_2}^{12}\rangle - 2ig\langle {\sigma_1}^{22}\rangle\langle a^\dagger {\sigma_1}^{12}\rangle \\ &\quad + 2ig\langle {\sigma_1}^{22}\rangle\langle a{\sigma_1}^{21}\rangle\end{aligned} \tag{4.41d, 4.41e}$$

As we can see, to fully capture the correlations we need to consider not a single atom, but two. Another noteworthy thing is that the mixed atom-field expectation value Eq. (4.41b) couples to all but one of the atomic ensemble. Therefore, the correlations are multiplied by $N-1$.

This approach is very useful to study atom numbers that would be otherwise inaccessible in even a first- or second-order description. The key point is that the number of equations is independent of the number of identical subsystems. The set of equations shown above is similar to the one studied in Ref. [4.17], where the symmetry property of the gain medium of a superradiant laser has been exploited to the same end as shown here.

QuantumCumulants.jl implements an experimental version that automizes the procedure of reducing equations and finding the correct scaling factors. To this end, we need to find the positions of the sums that occur when dealing with each subsystem explicitly. On top of that, sums may exclude certain indices which changes the scaling factor. Ultimately, we devised a set of rules that obtains this information based on the action of operators on the different Hilbert spaces. Similar rules are implemented to judge whether an expectation value can be eliminated by substitution. For example, whenever $\langle \sigma_2^{ij}\rangle$ occurs in the above equations, we can replace it by $\langle \sigma_1^{ij}\rangle$.

Currently, this functionality is tailored to Hamiltonians of the form similar to Eq. (4.24). To specify, we can currently treat systems comprised of many identical subsystems that are coupled by only one common Hilbert space. In the example shown here, the identical subsystems are the atoms inside the gain medium and they couple via the common cavity mode. Note that the approach is not restricted to this combination of Hilbert spaces, i.e. we could also treat a single atom coupling to many identical modes, or a single designated mode coupling to other modes. However, this automatic procedure is not applicable to more general problems and will be subject to changes in the future. Hence, we consider this part of the framework experimental.

The program which derives Eqs. (4.41) automatically and solves them is shown in code sample 6. This requires the use of a `ClusterSpace` which represents an arbitrary amount of identical copies of a single Hilbert space. Note that we also need to make the order of the problem known to the space in the beginning, as this is the actual number

of Hilbert spaces required to describe the system properly. Another advantage of this approach is that the equations only need to be derived once after which one can solve the system dynamics for arbitrary numbers of atoms as N is simply a parameter in code sample 6.

```
using QuantumCumulants

M = 2 #order
@cnumbers N Δ g κ γ
hf = FockSpace(:cavity)
ha1 = NLevelSpace(:atom, 2)
ha = ClusterSpace(ha1, N, M)
h = tensor(hf, ha)

@qnumbers a::Destroy(h)
# (i,j) -> levels, k -> atomic index
σ(i,j,k) = Transition(h, :σ, i, j)[k]

# Hamiltonian
H = Δ*a'*a + g*sum(a'*σ(1,2,i) + a*σ(2,1,i) for i=1:M)

# Collapse operators
J = [a;[σ(1,2,i) for i=1:M]]
rates = [κ;[γ for i=1:M]]

# Derive equation for atomic population
eqs = meanfield(σ(2,2,1),H,J;rates=rates,order=M)

# Complete but neglect phase-dependent terms
ϕ(x::Average) = ϕ(x.arguments[1])
ϕ(::Destroy) = -1
ϕ(::Create) = 1
ϕ(x::QTerm) = sum(map(ϕ, x.args_nc))
ϕ(x::Transition) = x.i - x.j
phase_invariant(x) = iszero(ϕ(x))
complete!(eqs;filter_func=phase_invariant)

using OrdinaryDiffEq, ModelingToolkit
@named sys = ODESystem(eqs)
u0 = zeros(ComplexF64, length(eqs))
u0[1] = 1.0 # atoms are inverted intially
p0 = (Δ=>0.5, g=>0.01, γ=>0.25, κ=>1, N=>500000)
prob = ODEProblem(sys,u0,(0.0,20.0),p0)
sol = solve(prob,RK4())
```

Code sample 6: *Automatic elimination of identical subsystems.* The above code derives and solves the equations for $N = 5 \times 10^5$ atoms in the gain medium.

5 Publication

Optics Express **30**(4), 5553 (2022)

Continuous multi-step pumping of the optical clock transition in alkaline-earth atoms with minimal perturbation†

C. Hotter[1], D. Plankensteiner[1], G. Kazakov[2] and H. Ritsch[1]

[1]*Institut für Theoretische Physik, Universität Innsbruck, Technikerstraße 21, A-6020 Innsbruck, Austria*
[2]*Atominstitut, TU Wien, Stadionallee 2, A-1020 Vienna, Austria*

A suitable scheme to continuously create inversion on an optical clock transition with negligible perturbation is a key missing ingredient required to build an active optical atomic clock. Repumping of the atoms on the narrow transition typically needs several pump lasers in a multi step process involving several auxiliary levels. In general this creates large effective level shifts and a line broadening, strongly limiting clock accuracy. Here we present an extensive theoretical study for a realistic multi-level implementation in search of parameter regimes where a sufficient inversion can be achieved with minimal perturbations. Fortunately we are able to identify a useful operating regime, where the frequency shifts remain small and controllable, only weakly perturbing the clock transition for useful pumping rates. For practical estimates of the corresponding clock performance we introduce a straightforward mapping of the multilevel pump scheme to an effective energy shift and broadening parameters for the reduced two-level laser model system. This allows to evaluate the resulting laser power and spectrum using well-known methods.

doi: 10.1364/OE.445976

†The author of the present thesis performed all calculations and simulations, except the analytic adiabatic elimination of the three-level atom, which was done by G. Kazakov. D. Plankensteiner and G. Kazakov contributed with helpful discussions and input.

5.1 Introduction

State of the art optical atomic lattice clocks achieve an excellent fractional stability of up to 6.6×10^{-19} after one hour of averaging [5.1]. In a typical atomic clock a stable local laser oscillator is compared to the reference transition frequency of trapped ultra-cold atoms. Technically the local laser oscillator is stabilized by an ultra-stable macroscopic cavity with a very good short time stability. Limitations of its stability originate from length fluctuations due to environmental and thermal perturbations [5.2]. Currently, these perturbations are the central limiting factor of the performance of passive atomic clocks on the short timescale. It has been proposed [5.3, 5.4] that active optical clocks, realized as so called superradiant lasers [5.3–5.31], can overcome this limitation. In such a laser an ensemble of atoms with a narrow and stable transition is used as gain medium inside an optical resonator. Since the cavity bandwidth is much broader than the gain profile, the frequency of such a bad-cavity laser is primarily determined by the stability of the resonance frequency of the gain medium which makes the system robust against cavity length fluctuations.

Maintaining population inversion on the atomic clock transition is, of course, a necessary ingredient required for continuous operation of an active optical clock laser. One possibility to achieve this is to prepare the atoms in the upper lasing state outside of the active lasing region and subsequently injecting them into the cavity. Such an approach is reminiscent of the hydrogen maser [5.32, 5.33]. In the optical regime this can be realized, for example, as an atomic beam laser [5.3, 5.18, 5.34, 5.35], where atoms in the upper lasing state traverse the cavity.

The most common approach to maintain inversion is to continuously repump the laser active atoms trapped within a magic wavelength optical lattice inside the cavity [5.4–5.6, 5.19, 5.21, 5.36, 5.37]. Hence each atom can emit several photons into the cavity and for a continuous operation, only a relatively small flux of atoms is needed to compensate the lost atoms. This could be e.g. achieved with an optical conveyor lattice through the cavity [5.13, 5.14, 5.35, 5.38, 5.39]. The central challenge of this approach are the perturbations of the clock atoms due to the presence of the repumping lasers. Typical theoretical models dedicated to superradiant clock lasers with continuous repumping simply assume an artificial transition rate modelled as inverse spontaneous decay from the ground to the excited lasing state [5.4, 5.11, 5.19–5.21]. This introduces an effective homogeneous broadening of the laser line but ignores all shifts and inhomogeneous broadening. To model this in a more realistic schemes, however, one needs to introduce laser-induced transitions to some auxiliary intermediate levels followed by a spontaneous decay to the upper lasing state. Naturally these lasers will introduce differential light shifts in addition to decoherence on the clock transition. For a non-uniform pump laser field distribution one, of course, gets inhomogeneous broadening. Besides broadening and shifting the laser line, it will eventually modify the threshold and even inhibit lasing. Frequency shifts lead to additional inaccuracy at least if they are not controllable and precisely measurable, as the resulting laser frequency then differs from the bare atomic transition. Luckily, as long as the inhomogeneous broadening is sufficiently small and symmetric, the atoms with different energies still synchronize [5.7, 5.15, 5.30] and a

narrow laser linewidth can be maintained. Therefore, the design of high-performance active optical clocks with a continuous repumping scheme requires the characterization, control and, if possible, minimization of the induced shifts and resulting decoherence.

The conceptually simplest realistic repumping scheme, the so-called three-level scheme, includes only a single intermediate level coherently coupled to the laser ground state, which ideally directly decays to the upper lasing level on a short time scale. Its theoretical study can be drastically simplified when the auxiliary level can be adiabatically eliminated, reducing the model to an effective two-level system subject to an effective incoherent pump, as e.g. in Lu^+ ions [5.16]. The Stark shift of the lasing transition can be effectively added to the model. However, in most metrology-relevant neutral atoms, as e.g. strontium or ytterbium, such an ideal intermediate level does not exist and thus any realistic repumping scheme requires at least two laser-induced transition steps to irreversibly excite the atoms from the lower to the upper clock state. This has the advantage that one has more possibilities to obtain a desired pump rate with minimal perturbation. However, it has also the disadvantage that, on the one hand, an analytic procedure of adiabatic elimination is cumbersome, especially for systems with a complex multilevel structure. On the other hand, a full numerical treatment, including all the relevant levels in the laser model, significantly increases the computational cost. Especially in time-domain simulations the characteristic time constants of the laser active and intermediate states often differ by many orders of magnitude, requiring a large number of time steps to be calculated.

Of course the numerical challenges become even more prominent for calculations beyond the mean-field approximation as needed for reliable predictions of linewidth and stability. As particularly useful models to tackle this, we will employ higher order cumulant expansion methods [5.40, 5.41]. Luckily we see that, as in the three level case, adiabatic elimination of the intermediate levels can reduce these multi-level systems to a simplified effective two-level system with sufficient accuracy.

In this paper we consider a quite general multi-level repumping scheme for neutral ^{88}Sr. We demonstrate that a proper choice of intensities and detunings of the pump lasers can lead to a sufficiently high effective repumping rate while at the same time frequency shifts and decoherence rates are kept small. To perform this analysis, we introduce a numerical method to reduce the complex multi-level system to an effective two-level system. This work is organized as follows: In Section 5.2 we review the simplified two-level model including incoherent repumping, and describe the generalized method used to reduce a multilevel system to a two-level one. In Section 5.3 we introduce a repumping scheme for trapped ^{88}Sr and calculate the effective parameters of the equivalent two-level system. The pumping scheme includes the two lasing states and four intermediate states. In Section 5.4 we compare the effective two-level laser model with the full six-level laser model.

5.2 A multistep excitation process as effective two-level system

In this section we describe the method to eliminate the intermediate states in a multi-level scheme with continuous repumping to an effective two-level system by using the eigenvalues of the non-hermitian Hamiltonian. The requirement on this procedure is that the intermediates states can be adiabatically eliminated. The motivation for this procedure is that the full laser system can be numerically very extensive for multilevel systems, and a "conventional" adiabatic elimination is often too cumbersome to be handled analytically. With our method we numerically calculate first the appropriate parameters of an equivalent two-level atom, to use them afterwards in an effective laser model. This has the additional advantage that this simplified model has already been studied extensively [5.4, 5.6, 5.7, 5.20, 5.21].

To establish the correspondence between the effective two-level and the multilevel system, we investigate first a two-level atom subjected to spontaneous decay, decoherence and incoherent pumping. In the Heisenberg representation the averaged value of an operator $\hat{O}$ for an open quantum system follows the equation

$$\frac{d\langle\hat{O}\rangle}{dt} = \frac{i}{\hbar}\langle[\hat{H},\hat{O}]\rangle + \langle\hat{\bar{\mathcal{L}}}[\hat{O}]\rangle \tag{5.1}$$

where $\hat{H}$ is the Hamiltonian and $\hat{\bar{\mathcal{L}}}$ is the super-operator describing the dissipative processes. Within the Born-Markov approximation $\hat{\bar{\mathcal{L}}}$ has the form

$$\hat{\bar{\mathcal{L}}}[\hat{O}] = \sum_j \frac{R_j}{2}\left(2\hat{J}_j^\dagger\hat{O}\hat{J}_j - \hat{J}_j^\dagger\hat{J}_j\hat{O} - \hat{O}\hat{J}_j^\dagger\hat{J}_j\right), \tag{5.2}$$

here $\hat{J}_j$ are the jump operators with the corresponding rates R_j. For our two-level atom in the rotating frame of the unperturbed atomic transition frequency the Hamiltonian can be written as $\hat{H} = \hbar(\delta_1\hat{\sigma}_{11} + \delta_2\hat{\sigma}_{22})$, where δ_1 and δ_2 are the shifts from the ground $|1\rangle$ and excited clock state $|2\rangle$, respectively and $\hat{\sigma}_{ij} = |i\rangle\langle j|$. The jump operators and corresponding rates of the dissipative processes are listed in Table 5.1. The equations of

#	jump	rate	description
1	$\hat{\sigma}_{12}$	Γ_{12}	decay from $\|2\rangle$ to $\|1\rangle$
2	$\hat{\sigma}_{21}$	R	incoherent pumping from $\|1\rangle$ to $\|2\rangle$
3	$\hat{\sigma}_{11}$	ν_1	dephasing on $\|1\rangle$
4	$\hat{\sigma}_{22}$	ν_2	dephasing on $\|2\rangle$

Table 5.1: *Dissipative processes of the two-level scheme.*

motion for the operator averages $\langle\hat{\sigma}_{ij}\rangle$ of such a two-level atom are

$$\partial_t \langle\hat{\sigma}_{22}\rangle = R\,\langle\hat{\sigma}_{11}\rangle - \Gamma_{12}\,\langle\hat{\sigma}_{22}\rangle \tag{5.3}$$

$$\partial_t \langle\hat{\sigma}_{12}\rangle = -\left(\frac{R+\Gamma_{12}+\nu}{2} + i\delta_{21}\right)\langle\hat{\sigma}_{12}\rangle\,, \tag{5.4}$$

where $\delta_{21} = \delta_2 - \delta_1$, and $\nu = \nu_1 + \nu_2$. From (5.3) one can easily express the incoherent repumping rate R via the ratio of the steady-state population as

$$R = \frac{\langle\hat{\sigma}_{22}\rangle}{\langle\hat{\sigma}_{11}\rangle}\Gamma_{12}. \tag{5.5}$$

To express the dephasing rates ν_1 and ν_2 we exploit the effective non-hermitian Hamiltonian

$$\hat{H}^{\mathrm{n}h}_{eff} = \hat{H} - \frac{i\hbar}{2}\sum_j R_j \hat{J}_j^\dagger \hat{J}_j, \tag{5.6}$$

as it is used e.g. in the Monte-Carlo wave function approach [5.42–5.44]. For our two-level system this non-hermitian Hamiltonian has the form

$$\hat{H}^{\mathrm{n}h}_{eff} = \hbar\delta_1\hat{\sigma}_{11} + \hbar\delta_2\hat{\sigma}_{22} - \frac{i\hbar}{2}\left[\Gamma_{12}\hat{\sigma}_{22} + R\hat{\sigma}_{11} + \nu_1\hat{\sigma}_{11} + \nu_2\hat{\sigma}_{22})\right], \tag{5.7}$$

which is already diagonal with the complex eigenvalues

$$E_1 = \hbar\left[\delta_1 - \frac{i}{2}\left(R+\nu_1\right)\right] \tag{5.8}$$

$$E_2 = \hbar\left[\delta_2 - \frac{i}{2}\left(\Gamma_{12}+\nu_2\right)\right]. \tag{5.9}$$

Using these relations and equation (5.5) for the incoherent pump rate R, we can express the shifts and decoherence rates via the eigenvalues of this effective Hamiltonian as:

$$\begin{aligned}
\delta_1 &= \mathrm{R}e\{E_1\}/\hbar \\
\delta_2 &= \mathrm{R}e\{E_2\}/\hbar \\
\nu_1 &= -2\mathrm{I}m\{E_1\}/\hbar - R \\
\nu_2 &= -2\mathrm{I}m\{E_2\}/\hbar - \Gamma_{12}
\end{aligned} \tag{5.10}$$

Therefore, to reduce a driven multilevel system to an effective two-level system with incoherent pumping, we perform the following steps: First, we calculate the steady-state values for $\langle\hat{\sigma}_{11}\rangle$ and $\langle\hat{\sigma}_{22}\rangle$, to obtain the effective repumping rate R from equation (5.5). Second, we diagonalize the effective non-hermitian Hamiltonian (5.6) to get the complex eigenvalues E_1 and E_2. These eigenvalues correspond to the eigenstates with the highest overlap with the unperturbed clock states $|1\rangle$ and $|2\rangle$. Using these eigenvalues we calculate the shifts δ_1 and δ_2 and the decoherence rates ν_1 and ν_2 according to equation (5.10). In appendix 5.6.1 we apply this method analytically to a three-level

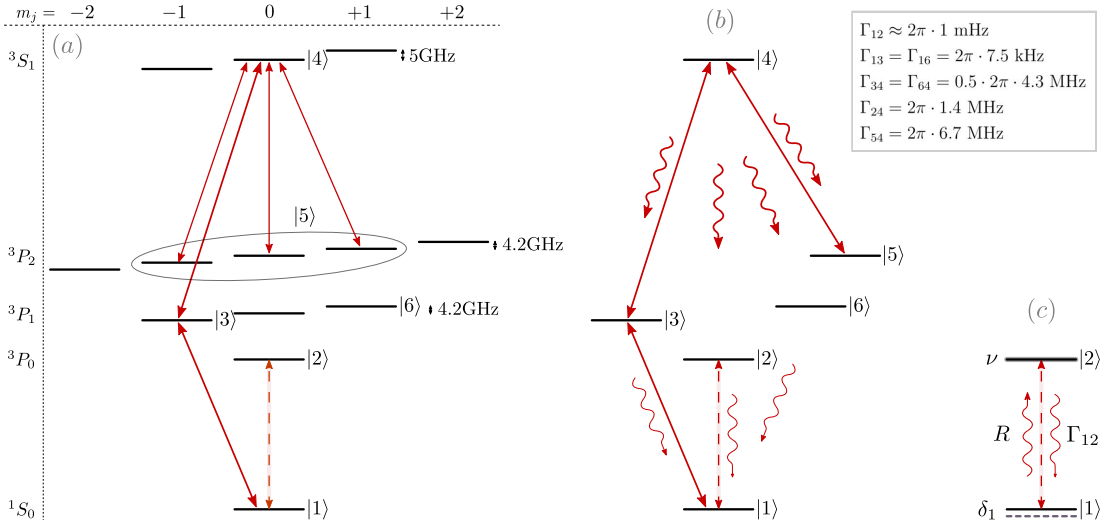

Figure 5.1: *Effective pump schemes:* Figure (a) shows all relevant atomic levels involved in CW pumping including the Zeeman sub-levels. Numbers show the level shifts for $B = 0.18$T. The directly involved transitions are indicated by the red solid lines. Figure (b) depicts a simplified six-level pump scheme with the relevant decay rates. (c) describes the resulting reduced two-level laser model including the effective emerging incoherent pump rate R and ground state Stark shift δ_1. We also include an effective dephasing with rate ν on the lasing transition. The cavity coupling is indicated by the dashed line between $|1\rangle$ and $|2\rangle$. The decay rates are from [5.45].

system, and compare it to the "conventional" adiabatic elimination procedure. Note that the atoms are coupled to the cavity only on the weak $|1\rangle \leftrightarrow |2\rangle$ transition, which will not be adiabatically eliminated. Therefore the atom-cavity coupling of the reduced system is anyway retained and we can, in a good approximation, neglect the cavity field and perform the adiabatic elimination on a single atom. This also assumes that we neglected direct interaction between the atoms as well as any collective coupling of the atoms to the bath modes.

5.3 Repumping scheme for bosonic strontium

In the following we present the concrete proposed repumping scheme based on the actual level structure of ^{88}Sr, see figure 5.1. In order to allow for superradiant lasing we assume a fairly strong and homogeneous magnetic field $B = 0.18$ T on the atoms, which induces an effective weak electric dipole coupling between the states $|1\rangle = {}^1\mathrm{S}_0$ and $|2\rangle = {}^3\mathrm{P}_0$ with spontaneous transition rate $\Gamma_{12} \approx 2\pi \cdot 1$ mHz [5.46]. Naturally such a strong magnetic field splits the Zeeman sub-levels quite far, such that they can be addressed independently. To obtain sufficient population in the upper clock state $|2\rangle = {}^3\mathrm{P}_0$ we consider the following processes: The atom is pumped coherently from the ground state $|1\rangle = {}^1\mathrm{S}_0$ to $|3\rangle = {}^3\mathrm{P}_{1,m=-1}$ and then further to $|4\rangle = {}^3S_{1,m=0}$. From there the atom can decay into the upper lasing state $|2\rangle$ as well as into the states $|5\rangle = {}^3\mathrm{P}_{2,m=\{-1,0+1\}}$

and $|6\rangle = {}^3\mathrm{P}_{1,m=-1}$. Note that the atoms can not decay from $|4\rangle$ to ${}^3\mathrm{P}_{1,m=0}$, since this transition is forbidden by angular momentum selection rules. Furthermore we combine here the three relevant Zeeman sub-levels of the state ${}^3\mathrm{P}_2$ to one state $|5\rangle$, this does not change the dynamics of the system, but one needs to be aware that in real experiments three individual lasers are needed to repump the atoms from these levels.

The decay $|4\rangle \rightarrow |2\rangle$ is the desired final step in the excitation process. Since the state $|5\rangle$ has a lifetime even longer than the upper clock state, we need to additionally depopulate $|5\rangle$ to avoid trapping of too much population in this state. If the atoms decay into the state $|6\rangle$, we can either repump it back to the state $|4\rangle$, or simply let it decay further to the ground state. Pumping from the state $|6\rangle$ would further increase the efficiency of the repumping process, but for simplicity we just consider spontaneous decay to the ground state. The Hamiltonian for the pumped six-level scheme (figure 5.1 (b)) in the rotating frame of the pump lasers then is

$$\hat{H}_\mathrm{p} = -\Delta_3\hat{\sigma}_{33} - \Delta_4\hat{\sigma}_{44} - \Delta_5\hat{\sigma}_{55} + \Omega_{13}(\hat{\sigma}_{13}+\hat{\sigma}_{31}) + \Omega_{34}(\hat{\sigma}_{34}+\hat{\sigma}_{43}) + \Omega_{54}(\hat{\sigma}_{45}+\hat{\sigma}_{54}) \quad (5.11)$$

with $\Delta_3 = \Delta_{13}$, $\Delta_4 = \Delta_3 + \Delta_{34}$ and $\Delta_5 = \Delta_4 - \Delta_{54}$. We define here $\Delta_{ij} = \omega_{ij}^l - \omega_{ij}$, ω_{ij} is the resonance frequency on the atomic transition $|i\rangle \leftrightarrow |j\rangle$, ω_{ij}^l is the frequency of the pump laser on this transition and Ω_{ij} the matrix element of the laser-induced transition. Dissipative processes for this pump scheme are described by the Liouvillian (5.2) with the parameters listed in table 5.2. These processes include all the relevant atomic decays, an effective phenomenological dephasing of the clock transition, as well as the dephasing induced by the pump lasers due to a finite linewidth.

5.3.1 Scanning over repumping parameters

Using the method described in section 5.2 we analyze our Strontium six-level repumping scheme. For high atom numbers $N \gg 1$ an effective incoherent repumping rate R

#	jump	rate	description
1	$\hat{\sigma}_{12}$	Γ_{12}	decay from $\|2\rangle$ to $\|1\rangle$
2	$\hat{\sigma}_{13}$	Γ_{13}	decay from $\|3\rangle$ to $\|1\rangle$
3	$\hat{\sigma}_{34}$	Γ_{34}	decay from $\|4\rangle$ to $\|3\rangle$
4	$\hat{\sigma}_{24}$	Γ_{24}	decay from $\|4\rangle$ to $\|2\rangle$
5	$\hat{\sigma}_{54}$	Γ_{54}	decay from $\|4\rangle$ to $\|5\rangle$
6	$\hat{\sigma}_{64}$	Γ_{64}	decay from $\|4\rangle$ to $\|6\rangle$
7	$\hat{\sigma}_{16}$	Γ_{16}	decay from $\|6\rangle$ to $\|1\rangle$
8	$\hat{\sigma}_{22}$	ν_{12}	general dephasing on $\|1\rangle \leftrightarrow \|2\rangle$
9	$\hat{\sigma}_{33} + \hat{\sigma}_{44} + \hat{\sigma}_{55}$	ν_{13}	pump laser linewidth on $\|1\rangle \leftrightarrow \|3\rangle$
10	$\hat{\sigma}_{44} + \hat{\sigma}_{55}$	ν_{34}	pump laser linewidth on $\|3\rangle \leftrightarrow \|4\rangle$
11	$\hat{\sigma}_{55}$	ν_{54}	pump laser linewidth on $\|4\rangle \leftrightarrow \|5\rangle$

Table 5.2: *Dissipative processes of the six-level pump scheme.*

above Γ_{12} would already be sufficient for superradiant lasing [5.4, 5.15]. A larger rate, however, leads to a higher output power and smaller linewidth, with an optimum at $R = 2Ng^2/\kappa$ [5.4]. Here g is the atom cavity coupling constant and κ the photon decay rate through the cavity mirrors. We will focus on incoherent repumping rates $R > 2\pi \cdot 1$ Hz, which is obviously much bigger than $\Gamma_{12} = 2\pi \cdot 1$ mHz but not the optimum for usual atom numbers and cavity parameters. The issue with too high repumping rates is, that they usually require stronger pump fields which lead to bigger level shifts on the clock transition. Shifts per se would not be a problem if they are constant and known. However, due to uncertainties and fluctuations in the pump process, atoms at different positions might experience different shifts, which leads to an effective inhomogeneous broadening of the ensemble. But as long as the frequency distribution is small enough, the atoms can still synchronize and emit light collectively on a single narrow line [5.7, 5.15, 5.30]. For an ensemble with an inhomogeneous frequency broadening less than the incoherent pump rate R the atoms synchronize in the superradiant regime.

Our aim is therefore to find parameters with an effective repumping rate $R > 2\pi \cdot 1$ Hz, but also sufficiently small frequency shift changes of the clock transition for realistic fluctuations and inaccuracies in the pump process. To this end we scan the effective repumping rate R and the ground state shift δ_1 on the relevant system parameters. Note that we only get shifts of the lower clock state in our model, since no pump laser couples to the upper clock state.

A parameter set to achieve the above goal is: $\Omega_{13} = 2\pi \cdot 1.5$ kHz, $\Omega_{34} = 2\pi \cdot 3.3$ MHz, $\Omega_{54} = 2\pi \cdot 100$ kHz, $\Delta_{13} = -2\pi \cdot 875$ kHz, $\Delta_{34} = -2\pi \cdot 5$ MHz and $\Delta_{54} = -2\pi \cdot 10$ MHz. The corresponding two-level system parameters are $R \approx 2\pi \cdot 1.91$ Hz, $\delta_1 \approx 2\pi \cdot 5.21$ mHz and $\nu \approx 2\pi \cdot 3.93$ Hz. These results are for pump laser linewidth of $\nu_{13} = \nu_{34} = \nu_{54} = 2\pi \cdot 0.75$ kHz and a dephasing rate on the clock transition of $\nu = 2\pi \cdot 1$ Hz. We will use these parameters as our "standard" parameters, i.e. whenever parameters are kept constant in scans we use these.

Figure 5.2 shows the dependence of the effective repumping rate R and the ground state shift δ_1 on the Rabi-frequencies Ω_{13} and Ω_{34} (upper row) as well as on the detunings Δ_{13} and Δ_{34} (lower row), when the other parameters are kept constant. We do not show here scans on Δ_{54} and Ω_{54}, since the dependences of R and δ_1 are very weak over a wide range of parameters, see one-dimensional scans in appendix 5.6.2. One can also see from these scans, that the dependence of both, R and δ_1, on Ω_{13} is quadratic. Therefore, the sensitivity of δ_1 to variations of Ω_{13} is proportional to δ_1, which means one should choose a working point with δ_1 close to zero (dark blue regions in Fig. 5.2 (b) and (e)), otherwise rather small fluctuations on Ω_{13} might lead to big variations of δ_1.

From the subplots (a) and (d) of Fig. 5.2 we can see, that there are wide regions with an effective repumping rate $R > 2\pi \cdot 1$ Hz. In the subplots (b) and (e) we plot the ground state shift and additionally indicate the relevant regions with the white line, which shows the repumping of $R > 2\pi \cdot 1$ Hz. In the panel (c) we zoom into an appropriate region for the Rabi-frequency scan. We see that for our parameters a deviation in Ω_{34} of $\pm 1.5\%$ still has tolerable shifts. For Ω_{13} the suitable range is much

bigger.

In the panel (f) we show a proper region for the detuing scan. We chose an area with a suitable range for Δ_{13} of $2\pi \cdot 50$ kHz and for Δ_{34} of $2\pi \cdot 1.5$ MHz. The reason to pick this region is the following: To avoid Doppler shifts a magic wavelength optical lattice is needed to trap the strontium atoms, but this lattice is in general only magic on the clock transition. This means for the other transitions the upper and lower state are not equally shifted and therefore non-clock transitions of atoms at different positions in the lattice have shifted resonance frequencies. However, the lattice can also be made magic on the $|1\rangle \leftrightarrow |3\rangle$ transition for a linearly polarized field, if one chooses the correct angle between the polarization axis and the quantization axis due to the static magnetic field [5.47]. Nonetheless, this does not work simultaneously on the $|3\rangle \leftrightarrow |4\rangle$ transition, which results in an effective inhomogeneous broadening of the transition frequency ω_{34} and hence in a Δ_{34} distribution. According to recent theoretical estimations [5.48], the scalar and tensor dynamic polarizabilities of the $(5s6s)^3S_1$ state at the 813 nm magic wavelength lattice are $\alpha_0(^3S_1) \approx -9 \times 10^2$ a.$u.$ (atomic units) and $\alpha_2(^3S_1) \approx 2$ a.$u.$, respectively. In turn, the scalar polarizabilities of the lasing states $|1\rangle$ and $|2\rangle$ at the magic wavelength are equal to $a_0(^1S_0) = a_0(^3P_0) \approx 2.8 \times 10^2$ a.$u.$ [5.49]. A thermal distribution of the atoms over different vibrational states and/or lattice sites with different potential depths will results into different shifts of the level $|4\rangle$. In particular, a temperature of $T = 5\ \mu K$ corresponds to a shift of level $|4\rangle$ in the range of approximately 0.4 MHz, which directly results in a Δ_{34} distribution. Therefore we need to choose parameters with a wide suitable range for Δ_{34}, but we can pick a point with a rather narrow range for Δ_{13}.

In summary, the main result in this section is that it occurs to be possible to achieve a significant repumping rate R together with a sufficient small and insensitive shift δ_1. The optimal set of parameters will be individual for each experimental setup, but they can be found fast with the above described method.

5.4 Effective linewidth and shift in the reduced laser model

In this section we calculate the spectrum of the superradiant laser, and demonstrate that our six-level laser model can be replaced by an effective two-level one. The laser model is given by N identical six-level atoms pumped inside an optical cavity. In the rotating frame of the pump lasers and the unperturbed clock transition the Hamiltonian can be written as

$$\begin{aligned} H_{\mathrm{L6}} = &- \Delta_{\mathrm{c}} a^\dagger a + \sum_{k=1}^{N} \big[- \Delta_3 \hat{\sigma}_{33}^k - \Delta_4 \hat{\sigma}_{44}^k - \Delta_5 \hat{\sigma}_{55}^k + g(a^\dagger \hat{\sigma}_{12}^k + a \hat{\sigma}_{21}^k) \\ &+ \Omega_{13}(\hat{\sigma}_{13}^k + \hat{\sigma}_{31}^k) + \Omega_{34}(\hat{\sigma}_{34}^k + \hat{\sigma}_{43}^k) + \Omega_{54}(\hat{\sigma}_{45}^k + \hat{\sigma}_{54}^k) \big]. \end{aligned} \tag{5.12}$$

Here $\Delta_{\mathrm{c}} = \omega_{12} - \omega_{\mathrm{c}}$ is the detuning between the clock transition frequency and the cavity resonance frequency, and g is the coupling coefficient between the cavity field and the clock transition. The dissipative processes for the atoms are listed in table

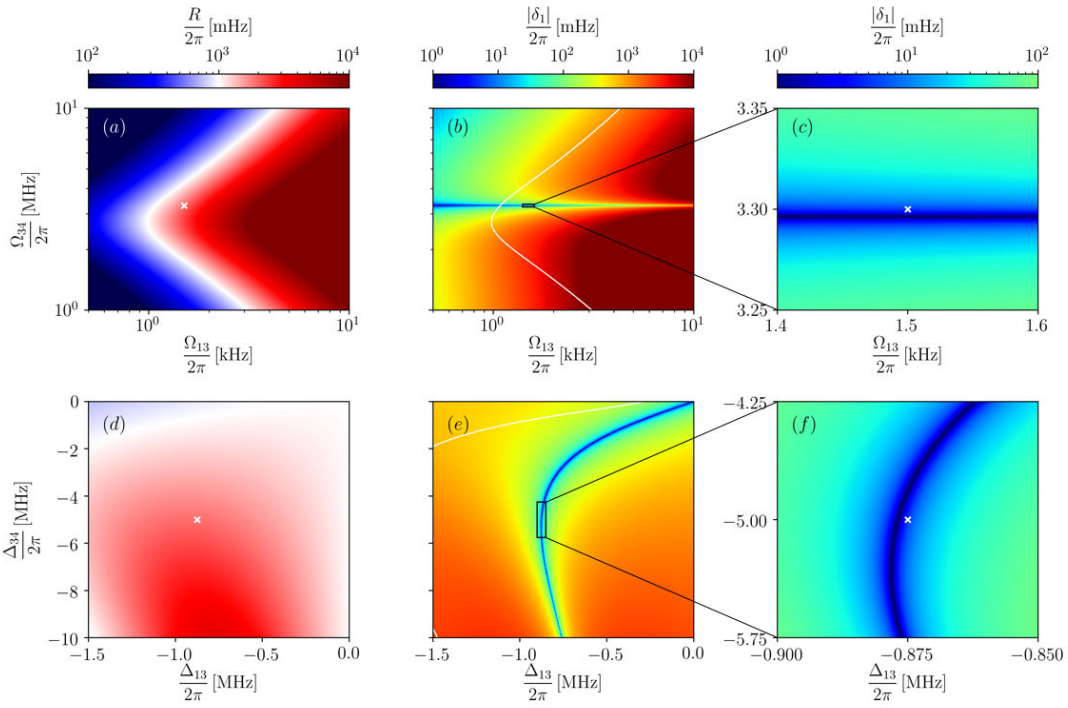

Figure 5.2: *Parameter scans of the effective pump rate R and the differential shift of the lasing transition δ_1.* In the upper row (a-c) we vary the amplitudes of the two pump lasers and in the lower row (d-f) their frequency detuning. We are targeting regions of sufficiently high pump rate and very low shift. The white contour line in the $|\delta_1|$-scans depicts $R = 2\pi \cdot 1$ Hz. Figure (c) and (f) show a zoom in a parameter region with small shifts $|\delta_1| < 2\pi \cdot 100$ mHz. The white crosses indicate the parameters fixed in the other plots.

5.2. The dissipative processes of the cavity are according to table 5.3. Using that all atoms behave identically we derive second order cumulant equations [5.40, 5.41] for the system variables and the correlation function [5.50]. However, we can use the adiabatic elimination from section 5.2 to numerically reduce the six-level atom lasing model into an effective two-level atom lasing model. This simplifies the model drastically and increases the computational efficiency significantly. The Hamiltonian of this two-level lasing model is

$$H_{\mathrm{L2}} = -\Delta_{\mathrm{c}} a^\dagger a + \sum_{k=1}^{N} \left[-\delta_1^k \hat{\sigma}_{22}^k + g_k (a^\dagger \hat{\sigma}_{12}^k + a \hat{\sigma}_{21}^k) \right] \tag{5.13}$$

and the dissipative processes are given by table 5.3 for the cavity and table 5.1 for each of the N atoms individually.

In Fig. 5.3 we see the excellent agreement of the laser properties calculated from the effective two-level lasing model and the six-level model for our standard parameters.

#	jump	rate	description
1	a	κ	cavity photon losses
2	$a^\dagger a$	η	fluctuations of the cavity resonance frequency

Table 5.3: *Dissipative processes of the cavity field.*

We compared these two models for many other relevant parameters, the laser properties (FWHM, δ_p, n) always agreed well.

Finally, let us discuss the effect of the pump laser induced dephasing. The main mechanism of such a dephasing is that the atoms pumped into the upper states $|3\rangle$ and $|4\rangle$ can decay into the state $|1\rangle$, instead of into the upper lasing state $|2\rangle$, see also appendix 5.6.1. Therefore, the dephasing rate ν needs to be proportional to the effective incoherent repumping rate R. Since the only way to get into the state $|2\rangle$ is to decay from $|4\rangle$ and since all other transitions are driven, the most prominent process to end up in $|1\rangle$ is via the decay into $|6\rangle$, therefore we can estimate

$$\nu \approx R\frac{\Gamma_{64}}{\Gamma_{24}} + \nu_{12} \approx 1.5R + \nu_{12}. \tag{5.14}$$

For the parameters used in Fig. 5.3 we get a FWHM of $\sim 2\pi \cdot 0.81$ mHz. In comparison the smallest linewidth we could theoretically get is $4g^2/\kappa \approx 2\pi \cdot 0.21$ mHz. With no dephasing at all ($\nu = 0$) this can, for these parameters, indeed be reached. Thus we see that the induced dephasing has an impact on the spectrum which is not to be neglected, but it is still reasonable. Note that the induced dephasing could e.g. be decreased in our case by additionally pumping the transition $|4\rangle \leftrightarrow |6\rangle$.

5.5 Conclusions

On the example of bosonic strontium trapped in a magic wavelength optical lattice we show that by choice of suitable pump laser parameters, it is possible to create significant population inversion on the clock transition with only a rather small shift and broadening of the lasing transition and the resulting active clock line. In particular we found a parameter regime where the induced level shifts on the clock transition are small enough, such that the atoms can still synchronize and thus emit light collectively in the superradiant regime, where cavity noise plays no role. To perform our scans of the many parameters characterizing the complex multilevel system, we have developed a fast numerical way to map the results to an effective two-level model, which can be well interpreted. For a range of generic test cases we have seen that the spectral and noise properties of these two models are in excellent agreement. The procedure can be adapted straight forward to find suitable repumping parameter for other alkaline-earth atoms.

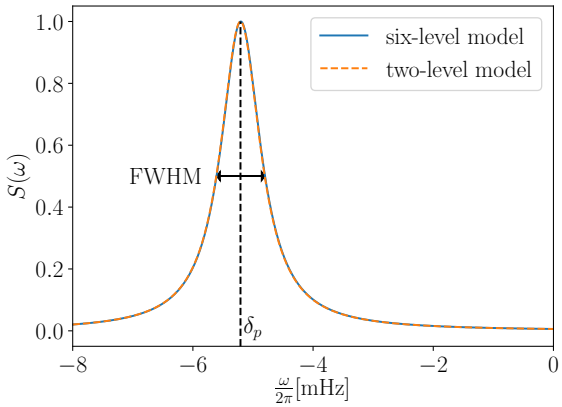

Figure 5.3: *Laser spectrum.* Comparison of the the effective two-level model with the full six-level model for a typical set of parameters. The laser properties are FWHM = $2\pi \cdot 0.806$ mHz ($2\pi \cdot 0.807$ mHz for the six-level model), $\delta_p = -2\pi \cdot 5.20$ mHz ($-2\pi \cdot 5.21$ mHz) and $n = 2.16$ (2.15), with an inaccuracy of the effective model below 1%. The atom number is $N = 2 \cdot 10^5$ and the cavity parameters are $\kappa = 2\pi \cdot 75$ kHz, $g = 2\pi \cdot 2$ Hz and $\eta = 2\pi \cdot 7.5$ kHz.

Acknowledgment

This work was supported by the European Union Horizon 2020 research and innovation programme, Quantum Flagship project No 820404 “iqClock” (C. H., D. P., G.K. and H. R.). Numerical simulations were performed with the open source frameworks QuantumOptics.jl [5.51] and QuantumCumulants.jl [5.41]. The graphs were produced using the open source plotting library Matplotlib [5.52]. The authors thank Marianna Safronova and Dmytro Filin for calculations of the dynamic polarizabilities on the $^3S_1$ state in neutral strontium atoms.

5.6 Appendix

5.6.1 Analytic adiabatic elimination on a three-level atom

Here we compare the ”conventional” adaibatic elimination with the adiabatic elimination using the eigenvalues of the non-hermitian Hamiltonian. We apply the two methods analytically on a pumped three-level atom to eliminate the auxiliary level $|3\rangle$.

The atom is coherently pumped on the transition $|1\rangle \leftrightarrow |3\rangle$ with a Rabi frequency Ω and laser detuning Δ_3, see Fig. 5.4. We suppose that the Rabi frequency Ω as well as the decay and decoherence rates associated with the state $|3\rangle$ (Γ_{13}, Γ_{23}, ν_3) are much larger than all the other rates in the system, and that the total decay rate of level $|3\rangle$ is much larger than Ω, therefore the population of the level $|3\rangle$ is much less than the populations of the levels $|1\rangle$ and $|2\rangle$. The Hamiltonian of a single atom can be written

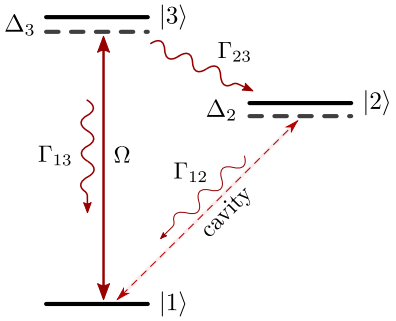

Figure 5.4: *Three-level scheme.* The considered three-level scheme for the adiabatic elimination of level $|3\rangle$ is depicted. The atoms are coherently pumped on the transition $|1\rangle \leftrightarrow |3\rangle$ and the cavity couples on the transition $|1\rangle \leftrightarrow |2\rangle$.

as

$$\hat{H} = \hbar(\Delta_2\hat{\sigma}_{22} + \Delta_3\hat{\sigma}_{33}) + \hbar\Omega(\hat{\sigma}_{13} + \hat{\sigma}_{31}), \tag{5.15}$$

where Δ_2 is some shift from the unperturbed atomic transition frequency. Jump operators and relaxation rates are listed in Table 5.4. Note that we neglect the interaction with the weak cavity field, see section 5.2.

#	jump	rate	description
1	$\hat{\sigma}_{12}$	Γ_{12}	decay from $\|2\rangle$ to $\|1\rangle$
2	$\hat{\sigma}_{13}$	Γ_{13}	decay from $\|3\rangle$ to $\|1\rangle$
3	$\hat{\sigma}_{23}$	Γ_{23}	decay from $\|3\rangle$ to $\|2\rangle$
4	$\hat{\sigma}_{11}$	ν_1^0	dephasing on $\|1\rangle$
5	$\hat{\sigma}_{22}$	ν_2^0	dephasing on $\|2\rangle$
6	$\hat{\sigma}_{33}$	ν_3^0	dephasing on $\|3\rangle$

Table 5.4: Dissipative processes of the three-level atom.

"Conventional" adiabatic elimination

First we perform an adiabatic elimination of the level $|3\rangle$, in the "conventional" way, similar to the one used in [5.16]. To this end we calculate the relevant equations for

operator averages $\langle\hat{\sigma}_{\alpha,\beta}\rangle$, where $\alpha,\beta \in \{1,2,3\}$:

$$\frac{d\langle\hat{\sigma}_{22}\rangle}{dt} = -\Gamma_{12}\langle\hat{\sigma}_{22}\rangle + \Gamma_{23}\langle\hat{\sigma}_{33}\rangle \tag{5.16}$$

$$\frac{d\langle\hat{\sigma}_{12}\rangle}{dt} = -\left(\frac{\Gamma_{12}+\nu_1^0+\nu_2^0}{2} + i\Delta_2\right)\langle\hat{\sigma}_{12}\rangle + i\Omega\langle\hat{\sigma}_{32}\rangle \tag{5.17}$$

$$\frac{d\langle\hat{\sigma}_{33}\rangle}{dt} = i\Omega\langle\hat{\sigma}_{13}-\hat{\sigma}_{31}\rangle - \Gamma_3\langle\hat{\sigma}_{33}\rangle \tag{5.18}$$

$$\frac{d\langle\hat{\sigma}_{13}\rangle}{dt} = -\left(\frac{\Gamma_3+\nu_1^0+\nu_3^0}{2} + i\Delta_3\right)\langle\hat{\sigma}_{13}\rangle - i\Omega\langle\hat{\sigma}_{11}-\hat{\sigma}_{33}\rangle \tag{5.19}$$

$$\frac{d\langle\hat{\sigma}_{23}\rangle}{dt} = -\left(\frac{\Gamma_3+\Gamma_{12}+\nu_2^0+\nu_3^0}{2} + i\Delta_3\right)\langle\hat{\sigma}_{23}\rangle - i\Omega\langle\hat{\sigma}_{21}\rangle \tag{5.20}$$

Here $\Gamma_3 = \Gamma_{13}+\Gamma_{23}$ is the total decay rate of the intermediate state $|3\rangle$. To perform the adiabatic elimination of $\langle\hat{\sigma}_{33}\rangle$, $\langle\hat{\sigma}_{23}\rangle$, $\langle\hat{\sigma}_{13}\rangle$ we use $\Gamma_{12} \ll \Gamma_3$ and $\nu_1^0, \nu_2^0 \ll \nu_3^0$ as well as $\langle\hat{\sigma}_{33}\rangle \ll \langle\hat{\sigma}_{11}\rangle$. Introducing

$$\Gamma' = \frac{\Gamma_3+\nu_3^0}{2} \approx \frac{\Gamma_3+\Gamma_{12}+\nu_2^0+\nu_3^0}{2} \approx \frac{\Gamma_3+\nu_1^0+\nu_3^0}{2} \tag{5.21}$$

we get

$$\langle\hat{\sigma}_{13}\rangle = \frac{-i\Omega}{\Gamma'+i\Delta_3}\langle\hat{\sigma}_{11}\rangle \tag{5.22}$$

$$\langle\hat{\sigma}_{23}\rangle = \frac{-i\Omega}{\Gamma'+i\Delta_3}\langle\hat{\sigma}_{21}\rangle \tag{5.23}$$

$$\langle\hat{\sigma}_{33}\rangle = \frac{2\Omega^2}{\Gamma_3}\frac{\Gamma'}{\Gamma'^2+{\Delta_3}^2}\langle\hat{\sigma}_{11}\rangle\,. \tag{5.24}$$

Substituting these expressions into (5.16) – (5.17), and introducing the repumping rate R, decoherence rate ν_{12} and effective shift Δ_{21} as

$$R = \frac{\Gamma_{23}}{\Gamma_3}\frac{2\Omega^2\Gamma'}{\Gamma'^2+{\Delta_3}^2} \tag{5.25}$$

$$\nu_{12} = \nu_1^0+\nu_2^0+\frac{\Gamma_{13}}{\Gamma_3}\frac{2\Omega^2\Gamma'}{\Gamma'^2+{\Delta_3}^2} \tag{5.26}$$

$$\Delta_{21} = \Delta_2 + \frac{\Omega^2\Delta_3}{\Gamma'^2+{\Delta_3}^2} \tag{5.27}$$

we can rewrite the equations Eq. (5.16) and Eq. (5.17) as

$$\frac{d\langle\hat{\sigma}_{22}\rangle}{dt} = -\Gamma_{12}\langle\hat{\sigma}_{22}\rangle + R\langle\hat{\sigma}_{11}\rangle \tag{5.28}$$

$$\frac{d\langle\hat{\sigma}_{12}\rangle}{dt} = -\left(\frac{R+\Gamma_{12}+\nu_{12}}{2} + i\Delta_{21}\right)\langle\hat{\sigma}_{12}\rangle\,, \tag{5.29}$$

similar to eqs. Eq. (5.3) and Eq. (5.4).

Adiabatic elimination using the eigenvalues of the non-hermitian Hamiltonian

Now we apply the procedure described in the end of Section 5.2. The simplicity of the considered 3-level scheme allows to follow this method analytically.

The expression for the repumping rate R, see eq. (5.5), can be obtained from the steady-state expression of $\langle\hat{\sigma}_{22}\rangle$ and $\langle\hat{\sigma}_{33}\rangle$,

$$\langle\hat{\sigma}_{22}\rangle = \frac{\Gamma_{23}}{\Gamma_{12}}\langle\hat{\sigma}_{33}\rangle = \frac{\Gamma_{23}}{\Gamma_{12}}\frac{2\Omega^2\Gamma'}{\Gamma(\Gamma'^2+{\Delta_3}^2)}\langle\hat{\sigma}_{11}\rangle\,. \tag{5.30}$$

The result is the same as in (5.25).

To determine the light shift and decoherence rate, one has to diagonalize the effective non-Hermitian Hamiltonian of our 3-level system in the absence of the cavity field. The Hamiltonian reads

$$\hat{H}_{\mathrm{eff}}^{\mathrm{n}h} = \hat{H} - \frac{i\hbar}{2}\sum_j R_j\hat{J}_j^\dagger\hat{J}_j = \hbar(\delta_2\hat{\sigma}_{22} + \Delta_3\hat{\sigma}_{33} + \Omega[\hat{\sigma}_{13}+\hat{\sigma}_{31}]) \tag{5.31}$$

$$-\frac{i\hbar}{2}\left[\Gamma_{12}\hat{\sigma}_{22} + \Gamma\hat{\sigma}_{33} + \nu_1^0\hat{\sigma}_{11} + \nu_2^0\hat{\sigma}_{22} + \nu_3^0\hat{\sigma}_{33})\right] \tag{5.32}$$

with the eigenvalues

$$\frac{E_2}{\hbar} = \Delta_2 - \frac{i}{2}(\Gamma_{12}+\nu_2^0) \tag{5.33}$$

$$\frac{E_{1,3}}{\hbar} = \frac{\Delta_3 - i\Gamma'}{2}\left\{1 \mp \sqrt{1 + \frac{4\Omega^2 + 2i\nu_1^0(\Delta_3 - i\Gamma')}{(\Delta_3 - i\Gamma')^2}}\right\}, \tag{5.34}$$

where Γ' is defined in (5.21), and we neglected Γ_{12}, ν_1^0 and ν_2^0 in comparison with Γ'. For $\nu_1^0, \Omega \ll \Gamma'$ we can perform a Taylor expansion on the term $[4\Omega^2 + 2i\nu_1^0(\Delta_3 - i\Gamma')]/(\Delta_3 - i\Gamma')^2 \ll 1$ and find

$$\frac{E_1}{\hbar} \approx -\frac{\Omega^2(\Delta_3 + i\Gamma')}{{\Delta_3}^2 + \Gamma'^2} - \frac{i\nu_1^0}{2}. \tag{5.35}$$

Using expressions (5.10), we get

$$\Delta_1 = -\frac{\Omega^2 \Delta_3}{\Gamma'^2 + {\Delta_3}^2} \tag{5.36}$$

$$\nu_1 = \nu_1^0 + \frac{2\Gamma'\Omega^2}{\Gamma'^2 + {\Delta_3}^2} - R = \nu_1^0 + \frac{\Gamma_{13}}{\Gamma}\frac{2\Omega^2\Gamma'}{\Gamma'^2 + {\Delta_3}^2}. \tag{5.37}$$

Similarly, from (5.33) follows $\nu_2 = \nu_2^0$. Therefore we obtain

$$\nu_{12} = \nu_1 + \nu_2 = \nu_1^0 + \nu_2^0 + \frac{\Gamma_{13}}{\Gamma}\frac{2\Omega^2\Gamma'}{\Gamma'^2 + {\Delta_3}^2} \tag{5.38}$$

$$\Delta_{21} = \Delta_2 - \Delta_1 = \Delta_2 + \frac{\Omega^2 \Delta_3}{\Gamma'^2 + {\Delta_3}^2}, \tag{5.39}$$

this coincides with (5.26) and (5.27). Thus, we can see that th adiabatic elimination in such a 3-level system performed with the help of the diagonalization of the effective non-Hermitian Hamiltonian gives the same result as a "conventional" adiabatic elimination.

5.6.2 One dimensional parameters scans

To get a better insight of the dependence on the different repumping parameters we show here one dimensional scans. Fig. 5.5 shows scans on the Rabi-frequencies and Fig. 5.6 on the detunings for R and δ_1.

The scans on Ω_{13}, Fig. 5.5 (a) and (d), show a quadratic dependence of R and δ_1 on the relevant regions of Ω_{13} with a constant prefactor depending on the other system parameters. A proper choice of parameters can reduce the prefactor of the ground state shift by orders of magnitudes, while the pump rate prefactor stays almost the same. For the Ω_{34}-scans, Fig. 5.5 (b) and (e), we find only a relative small area at approximately $\Omega_{34} \approx 2\pi \cdot 3.3$ MHz (see inset) where a repumping rate $R > 2\pi \cdot 1$ Hz can be achieved and the range of the shift $|\delta_1|$ is sufficiently small. For Ω_{54}, Fig. 5.5 (c) and (f), on the other hand, all values below $2\pi \cdot 1$ MHz have an almost constant R and δ_1. But note that for smaller values of Ω_{54} more population is trapped in $|5\rangle$, this is undesired since less population will contribute to lasing. However, for our parameters this gets only relevant for $\Omega_{54} < 2\pi \cdot 1$ kHz.

As we know from section 5.3.1 Δ_{13} can be controlled much more precisely than Δ_{34} due to the magic wavelength lattice, therefore we choose a parameter regime in which changes of Δ_{34} are far less important. Fig. 5.6 illustrates this very well. Differences in Δ_{13} of $\pm 2\pi \cdot 25$ kHz lead to shifts of $\pm 2\pi \cdot 50$ mHz, whereas changes of $\pm 2\pi \cdot 0.75$ MHz in Δ_{34} lead only to shifts in a range of approximately $2\pi \cdot 40$ mHz, see Fig. 5.6 (a) and (b) respectively. For the Δ_{54} dependency, Fig. 5.6 (c) and (f), we find that R and δ_1 do not significantly change for detunings between $-2\pi \cdot 15$ and $-2\pi \cdot 6$ MHz. Thus Δ_{54} does not need to be precisely controlled.

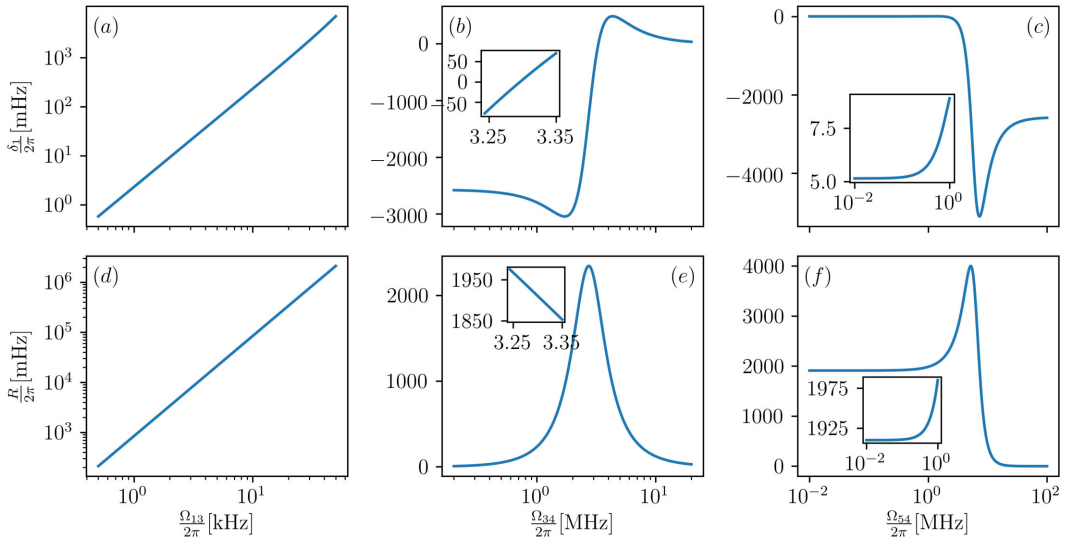

Figure 5.5: *Line shift (upper row) and pump rate (lower row) scans for varying pump amplitudes close to optimal operation conditions.* The dependence of the ground state shift and the repumping rate on the Rabi frequencies is shown with insets of interesting regions. The parameters when kept constant are our standard parameters from section 5.3.1.

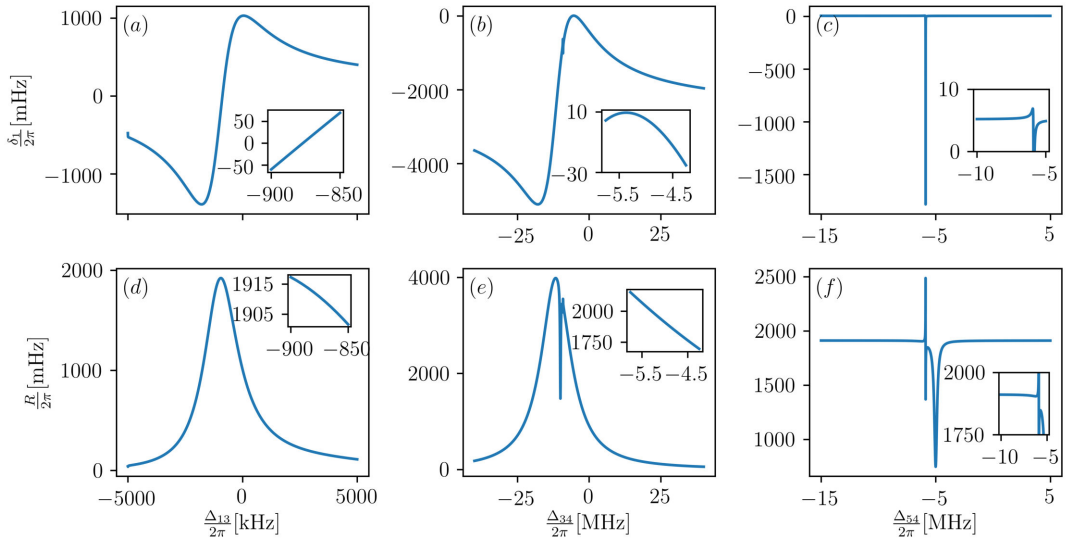

Figure 5.6: *Line shift (upper row) and pump rate (lower row) scans for varying pump detunings close to optimal operation conditions.* The dependence of the ground state shift and the repumping rate on the detuings is shown with insets of interesting regions. The parameters when kept constant are our standard parameters from section 5.3.1.

6 Publication

Physical Review Research **5**, 013056 (2023)

Cavity sub- and superradiance for transversely driven atomic ensembles[†]

C. Hotter[1], L. Ostermann[1] and H. Ritsch[1]

[1]*Institut für Theoretische Physik, Universität Innsbruck, Technikerstraße 21, A-6020 Innsbruck, Austria*

Large atomic ensembles coupled to a single optical resonator mode can be steered to strongly enhanced or suppressed collective emission via phase controlled excitation. Employing the Tavis-Cummings model we find so far unreported phenomena. Using a second order cumulant expansion we predict that a homogeneously excited ensemble equally distributed between odd and even sites along the cavity mode is extremely subradiant as long as the average excitation remains below 50%, but shows pulsed emission for inversion. The combination of these two properties enables the implementation of an efficient cavity enhanced Ramsey probing featuring a fast readout and minimal heating with particular advantages for atomic clock transitions. For continuous illumination the nonlinear atom-field interaction induces regular superradiant self-pulsing. Additionally, we observe an increased pulse delay time in comparison to an excitation through the cavity.

doi: 10.1103/PhysRevResearch.5.013056

[†]The author of this thesis performed all calculations and numerical simulations. L. Ostermann offered helpful discussions and input.

6.1 Introduction

The phenomena of super- and subradiance originating from constructive or destructive interference of the field radiated by an ensemble of dipoles has been studied for many decades [6.1–6.10]. The decisive quantity is the collective dipole moment of the emitters with respect to the system's electromagnetic radiation modes, which, apart from the ensemble's quantum state determining the internal phase relations, is strongly tied to their spatial distribution. For superradiance, phase coherence in one given emission mode is sufficient, yet, subradiance only appears when virtually all of the emission channels are blocked by destructive interference. While there are classical analogs of super- and subradiance, in quantum emitters the radiation is triggered by local vacuum fluctuations of the electromagnetic field, which are determined by the system's geometry [6.11–6.13]. These are isotropic and homogeneous in free space, but can be modified by, e.g., placing them in the evanescent field of a waveguide [6.9, 6.14, 6.15], inside a hollow core photonic crystal fiber [6.16], engineering interactions for superconducting qubits [6.17], or, as in our case putting them inside a (linear) resonator, which yields more precise control over their interference.

Pulsed superradiant output has been demonstrated for large atomic ensembles in optical cavities [6.8, 6.18–6.20]. Superradiant lasing [6.21–6.23] is one of the prime applications of cavity superradiance and even self-organization [6.24] can incorporate superradiant behavior. In contrast, subradiance is a lot harder to access experimentally [6.25] and treat theoretically [6.10, 6.26, 6.27].

In order to induce cavity mediated superradiant light emission from an atomic ensemble, it is favorable to excite the atoms through the cavity instead of from the side, since in this case all atoms obtain the same relative phase with respect to the cavity mode to constructively emit photons into the cavity [6.8, 6.28]. This raises the question about the behavior of an ensemble with arbitrary or vanishing relative phases, as it is, for example, naturally the case for a transversely driven large atomic ensemble, homogeneously distributed along the cavity axis covering odd and even sites of the cavity mode. On the one hand, one could intuitively think that an ensemble with vanishing relative phase features a subradiant behavior, since the light emitted into the cavity interferes destructively [6.24]. But, on the other hand, there is no phase information stored in a fully excited ensemble, hence, the dynamics of atoms inverted through the cavity or from the side must be identical in this case, i.e., the emission of a superradiant pulse [6.8, 6.17–6.20].

In this paper we show that there is a transition between cavity super- and subradiance for an atomic ensemble with vanishing relative phase. In particular, an inverted ensemble emits a superradiant pulse, whereas a non-inverted ensemble features a subradiant behavior. This can be crucial for the understanding and design of cavity QED experiments. Utilizing this transition from cavity sub- to superradiance enables the implementation of a cavity enhanced Ramsey spectroscopy. The central idea is that the non-inverted ensemble is decoupled from the cavity during the free evolution phase [6.29, 6.30], but the final readout of the inverted atoms is still performed via the superradiant manifold. This scheme allows for a fast and precise readout, without

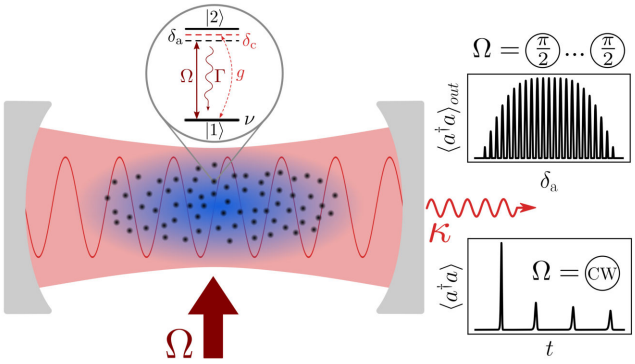

Figure 6.1: *Cavity Sub- and Superradiance Model.* We consider a homogeneous, dilute ensemble of narrow line two-level atoms at random but fixed positions in a standing wave optical resonator coherently driven by a transverse plane wave laser. We assume a weak single atom but strong collective coupling regime, i.e., κ, $\sum_j g_j^2/\kappa \gg \Gamma \gg g_j^2/\kappa$. The cavity Ramsey fringes and the photon number self-pulsing are indicated as cavity output signals for the respective drive laser operations.

destroying the measured ensemble. Beyond that, we find a yet unreported self-pulsing of the cavity output field upon continuously driving the ensemble, which can be explained by the system dynamics cyclically transitioning from cavity subradiance to superradiance. Lastly, our setup can be employed to more accessibly measure delay time statistics, when pumping the ensemble transversally instead of through the cavity as the cavity subradiance in this case will slow down the system's dynamics, making the output easier to detect.

6.2 Model

We consider N two-level atoms with a narrow transition at frequency ω_a coupled to a single mode cavity. The atoms are coherently driven with a detuning between the laser and the atomic transition of $\delta_\mathrm{a} = \omega_\mathrm{l} - \omega_\mathrm{a}$, the corresponding Rabi frequency is denoted by Ω. The cavity is detuned by $\delta_\mathrm{c} = \omega_\mathrm{l} - \omega_\mathrm{c}$ from the laser and we have an atom-cavity coupling of g_j for the j-th atom. The system is depicted in Fig. 6.1. Its Hamiltonian in the rotating frame of the pump laser reads

$$H = -\delta_\mathrm{c} a^\dagger a + \sum_{j=1}^{N} \Big[-\delta_\mathrm{a} \sigma_j^{22} + g_j (a^\dagger \sigma_j^{12} + a \sigma_j^{21}) + \frac{\Omega}{2} (\sigma_j^{21} + \sigma_j^{12}) \Big], \tag{6.1}$$

with the cavity photon creation (annihilation) operator $a^\dagger$ (a) and the atomic transition operator $\sigma_j^{kl} = |k\rangle_j \langle l|_j$ for the j-th atom. The coherent interaction is accompanied by dissipative processes accounted for by the Liouvillian $\mathcal{L}[\rho]$ in the master equation

$$\dot{\rho} = i[\rho, H] + \mathcal{L}[\rho]\,. \tag{6.2}$$

Table 6.1: *Dissipative Processes.* The system features a damped cavity mode as well as atomic decay and dephasing.

i	J_i	R_i	Description
1	a	κ	cavity photon losses
2	σ_j^{12}	Γ	decay from $\|2\rangle_j$ to $\|1\rangle_j$
3	σ_j^{22}	ν	dephasing of the j-th atom

In the Born-Markov approximation [6.31] we can write the Liouvillian in Lindblad form as

$$\mathcal{L}[\rho] = \sum_i R_i \left(2J_i\rho J_i^\dagger - J_i^\dagger J_i\rho - \rho J_i^\dagger J_i\right), \tag{6.3}$$

with the jump operators $\{J_i\}$ and their corresponding rates $\{R_i\}$ shown in Table 6.1, including cavity photon losses as well as individual decay and dephasing of the atoms.

As we are targeting narrow clock transitions the system is operated in the bad and large volume cavity regime $\kappa \gg \Gamma$ with only a small single atom cooperativity $C_j = g_j^2/(\kappa\Gamma) \ll 1$ but a sufficiently large ensemble to enter the strong collective coupling regime $NC = \sum_j C_j \gg 1$. Typically, this parameter regime implies a very large atom number, which does not allow for a full quantum simulation, but we can very well treat this problem in a second order cumulant expansion [6.32, 6.33]. A comparison with a full quantum simulation for a small atomic ensemble is shown in Appendix 6.7.1. Additionally, we neglect dipole-dipole interaction [6.4], as our atomic ensemble is sufficiently dilute. This also means that the individual free space decay rate of the atoms is not affected.

Throughout the paper we calculate the dynamics in a second order cumulant expansion [6.33, 6.34]. Nevertheless, the mean-field equations already contain the key physics and therefore we present these much simpler equations for a qualitative description of the system:

$$\frac{d}{dt}\langle a\rangle = -\left(i\delta_\mathrm{c} + \frac{\kappa}{2}\right)\langle a\rangle - i\sum_{j=1}^{N} g_j\langle\sigma_j^{12}\rangle \tag{6.4a}$$

$$\frac{d}{dt}\langle\sigma_j^{22}\rangle = -\Gamma\langle\sigma_j^{22}\rangle + i\frac{\Omega}{2}\left[\langle\sigma_j^{12}\rangle - \langle\sigma_j^{21}\rangle\right] + ig_j\left[\langle a^\dagger\rangle\langle\sigma_j^{12}\rangle - \langle a\rangle\langle\sigma_j^{21}\rangle\right] \tag{6.4b}$$

$$\frac{d}{dt}\langle\sigma_j^{12}\rangle = \left(i\delta_\mathrm{a} - \frac{\Gamma+\nu}{2}\right)\langle\sigma_j^{12}\rangle + i\left(\frac{\Omega}{2} + g_j\langle a\rangle\right)\left[2\langle\sigma_j^{22}\rangle - 1\right] \tag{6.4c}$$

6.3 Collective Cavity Mediated Super- and Subradiance

In the following, for simplicity, we assume the atoms located close to cavity mode antinodes with half of the atoms at the maxima and half at the minima of the mode function along the cavity axis. Hence their respective effective coupling is well approximated

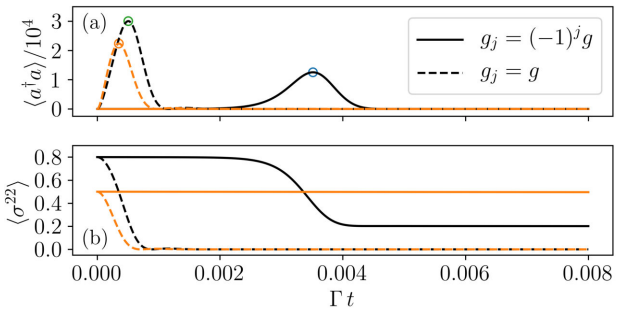

Figure 6.2: *Cavity Mediated Collective Decay.* Time evolution of the intra-cavity photon number (a) and the single atom excited state population (b) after a short pulse excitation preparing each atom in the same coherent superposition. The black line represents an inverted ensemble with $\langle \sigma^{22} \rangle = 80\%$ excited state fraction ($\approx 3\pi/4$-pulse) and the orange line depicts an ensemble after a $\pi/2$-pulse to create $\langle \sigma^{22} \rangle = 50\%$. For uniform cavity coupling (dashed line) we see an immediate superradiant population decay to the ground state creating a photon pulse in the cavity. Cavity coupling with alternating signs (solid line) leads to a weaker and time delayed pulse for an inverted ensemble, while the atomic excitation is almost perfectly protected from cavity decay without inversion (solid line in (b)). We have assumed $N = 2 \cdot 10^5$ atoms with $g = 10\Gamma$, $\kappa = 10^4\Gamma$ and $\delta_\mathrm{a} = \delta_\mathrm{c} = \nu = 0$.

by $+g$ and $-g$. As confirmed by more involved simulations, investigating a random distribution for the atom-field coupling, this simplification already captures the essential physics.

Inverting all atoms with a short π-pulse induces the emission of a delayed intense light pulse due to cavity enhanced superradiant decay [6.8, 6.17–6.20]. Synchronized stimulated emission in a cavity occurs even for a dilute ensemble, which does not exhibit free space superradiance. Figure 6.2(a) shows typical trajectories for the corresponding time evolution of the intra-cavity photon number $\left\langle a^\dagger a \right\rangle$. When all atoms are initially coherently prepared at $\langle \sigma^{22} \rangle = 80\%$ (black line), a superradiant pulse emerges. Figure 6.2(b) depicts the corresponding time evolution of the excited state population, showing the cavity mediated decay of the atoms. For comparison we display the behavior for all atoms equally coupled to the cavity (dashed line, $g_j = g$), similar to the case of excitation through the cavity [6.8, 6.28], showing a much faster and stronger pulse.

However, for the system we consider with alternating coupling ($g_j = (-1)^j g$), the dynamics depend drastically on the population of the atoms. Interestingly, we observe such pulsed emission for an ensemble of inverted atoms only. If the excited state population is below 50% the atoms do not emit a significant amount of photons into the cavity mode, see solid orange line in Fig. 6.2. Figure 6.3(a) shows the total number of emitted photons $\langle a^\dagger a \rangle_\mathrm{out}$ for different values of the initial excited state population. Almost no photons leak through the cavity mirrors until the atoms are inverted. Again, the dashed line represents the case of all atoms coupling equally ($g_j = g$), resembling a pulsed excitation of the atoms through the cavity. We see that also non-inverted

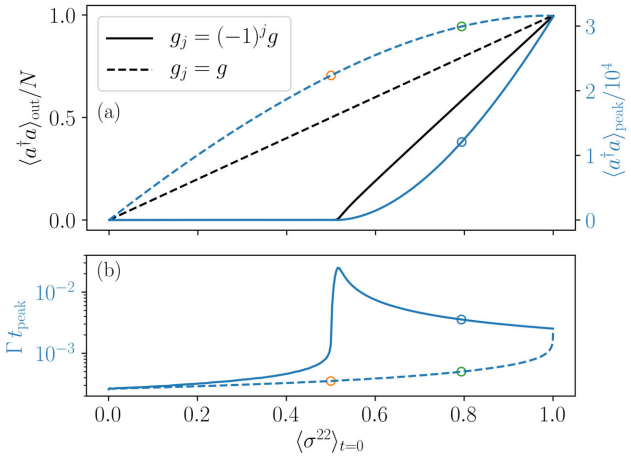

Figure 6.3: *Cavity Sub- and Superradiance.* (a) Comparison of the cavity-output photon number $\langle a^\dagger a \rangle_{\text{out}} = \kappa \int \langle a^\dagger a \rangle \, \mathrm{d}t$ (black) and peak intra-cavity photon number (blue) as a function of the single atom excitation probability for alternating coupling (solid line) and uniform coupling (dashed line). Note the strong suppression of superradiant emission in the alternating coupling case as long as no inversion is created initially. (b) Delay time of the peak photon number. For alternating coupling the pulse appears later in general and is more delayed for decreasing inversion, whereas for equally coupled atoms the pulse delay time increases with growing excited state population. The circles indicate the parameters chosen for Fig. 6.2(a).

atoms superradiantly emit photons into the cavity mode without retaining excitation. Additionally, we plot the peak intra-cavity photon number (blue) demonstrating the same behavior.

Figure 6.3b shows the average delay time of the peak photon number as a function of the atomic excitation. For uniformly coupled atoms (dashed line) a higher excitation leads to a later pulse. Whereas for alternating coupling (solid line) the delay time of the peak increases for lower inversion and is larger in general. For a perfect π-pulse excitation both cases lead to identical superradiant pulses in terms of delay time as well as photon number, since for fully inverted atoms the phase of the coupling does not matter. However, for only slightly imperfect π-pulses one already obtains much longer delay times for a transversely excited ensemble, than for an excitation through the cavity. Several experimental setups should allow for observing this result [6.8, 6.18–6.20, 6.28].

The origin of this subradiant suppression for a non-inverted ensemble is the destructive interference [6.5–6.7, 6.29] of photons emitted by the atoms coupled to the cavity with opposite g, in contrast to the widely studied synchronized superradiant emission due to constructive interference for a large inverted ensemble [6.8, 6.18–6.20, 6.28]. Analyzing the mean-field equations Eq. (6.4a) to Eq. (6.4c) explains the transition between cavity sub- and superradiance qualitatively. First, from eq. Eq. (6.4a) we notice the significance of the alternating coupling: the cumulative dipole moment of the atoms projected on

the cavity mode $\sum_j g_j \langle \sigma_j^{12} \rangle$ vanishes [6.29, 6.30] and hence the gain in the cavity field disappears. For simplicity we have chosen the same laser excitation phase for all atoms. Yet a varying excitation phase works equally well as long as the overall relative phase disappears. Typically, this is implicitly realized in a random spatial distribution of a sufficiently large and dilute ensemble. It is also true for a ring-cavity featuring a continuous atom-cavity coupling phase along the cavity axis [6.24] or for atoms coupled to waveguides or inside hollow core fibers with appropriate spacing [6.9, 6.14–6.16]. Furthermore, we see why an excitation through the cavity is effectively the same as all atoms equally coupled and excited from the side: with a drive through the cavity the phase of the coherence $\langle \sigma_j^{12} \rangle$ is determined by the phase of the coupling g_j, therefore the individual parts of the sum in eq. Eq. (6.4a) all carry the same phase and do not compensate.

By these arguments only there seems to be no difference in the behavior of inverted and non-inverted atoms, since the sum in eq. Eq. (6.4a) does not depend on the excited state population. Therefore we calculate the second time derivative of the cavity field to obtain a qualitative description. By inserting Eqs. Eq. (6.4c), with $\langle \sigma_j^z \rangle = 2\langle \sigma_j^{22} \rangle - 1$ we find

$$\frac{d^2}{dt^2}\langle a \rangle = \sum_j g_j^2 \langle \sigma_j^z \rangle \langle a \rangle + \underbrace{[...]}_{\text{decay}} . \tag{6.5}$$

For a clear view we set $\delta_\mathrm{a} = \delta_\mathrm{c} = 0$ and hint at the dissipative processes only. For short times, i.e. $\langle \sigma_j^z \rangle$ is constant, a non-zero initial field $\langle a \rangle_{t=0} \neq 0$ leads to the following possible solutions of eq. Eq. (6.5): for inverted atoms ($\langle \sigma_j^z \rangle > 0$) the field increases rapidly as a cosh function, which leads to the build up of the photon pulse, whereas for non-inverted atoms ($\langle \sigma_j^z \rangle < 0$) the field oscillates between zero and the initial value and is strongly damped due to the large cavity decay rate. Having to require a non-zero initial field is an artifact of the mean-field treatment in order to obtain a non-trivial solution and becomes unnecessary for higher order descriptions.

6.3.1 Dicke States Representation

In the mean field approximation the total number of output photons for a non-inverted atomic ensemble with vanishing cumulative dipole moment is exactly zero. However, a closer investigation in second order cumulant expansion shows that there actually is a small amount of photons released into the cavity. Another interesting aspect of the system is that an initial inversion with $\langle \sigma^{22} \rangle < 1$ leads to $N \cdot (2\langle \sigma^{22} \rangle - 1)$ photons only, as shown in Fig. 6.3(a). Consequently, the atoms retain an excited state population of $1 - \langle \sigma^{22} \rangle$ after the pulsed photon emission into the cavity, indicated by the solid line in Fig. 6.2(b). To explain these two features we use the Dicke states [6.1] of the atomic ensemble, which provide an intuitive picture for our considered system.

An ensemble of N identical two-level atoms can be expressed in the basis of Dicke

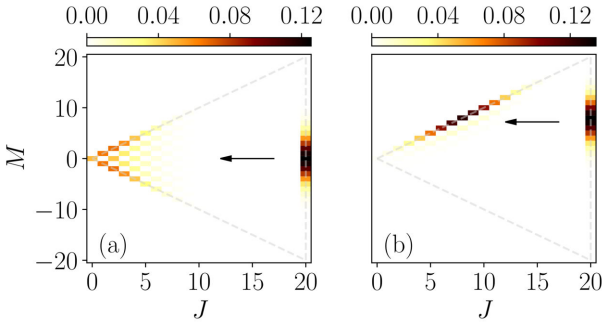

Figure 6.4: *Dicke States.* Population of the Dicke states for $N = 40$ atoms after an initial $\pi/2$-pulse in a) and $3\pi/4$-pulse in b). The states occupying the maximal J values correspond to the equally coupled case ($g_j = g$), whereas the states close to the boundary of minimal J represent the alternating coupling case ($g_j = (-1)^j g$). The arrow indicates the mapping between the two cases.

states $|J, M\rangle$, with

$$J^z |J, M\rangle = \frac{1}{2} \sum_j \sigma_j^z |J, M\rangle = M |J, M\rangle \tag{6.6a}$$

$$\vec{J}^2 |J, M\rangle = \frac{3N}{4} + \frac{1}{4} \sum_{j \neq k} \left[\sigma_j^{21} \sigma_k^{12} + \sigma_j^z \sigma_k^z \right] |J, M\rangle = J(J+1) |J, M\rangle \,, \tag{6.6b}$$

where $|M| \leq J$ and $0 \leq J \leq N/2$ [6.1, 6.26, 6.35, 6.36]. In this description collective decay has a particularly simple behavior, the J quantum number is unchanged, while M is reduced. In the triangle shaped Dicke state diagram in Fig. 6.4 this corresponds to a vertical line of decreasing M [6.26, 6.35, 6.36], where the change in M directly reflects the number of lost excitations (photons).

The collective emission in our system is induced by the cavity, with the crucial feature of alternating coupling. In the representation where the cavity mediated decay is described by a vertical line, this leads to a different distribution of the J quantum number due to the different relative phases between the atoms and the cavity field, see Appendix 6.7.2. Figure 6.4 compares the mapping of $N = 40$ identically coupled atoms, where states of maximal J are occupied exclusively, to the case of alternating cavity coupling, where states close to the boundary of minimal J are populated predominantly. Note that one finds very similar distributions for an incoherently pumped ensemble [6.26, 6.36]. In this representation we can explain the two features mentioned above in a straightforward way by recalling that the collective decay decreases M to its minimally possible value $M = -J$ only, without changing J and releasing $|J + M|$ photons. Under collective decay a state $|J, M = +J\rangle$ will thus go to $|J, M = -J\rangle$, explaining the remaining excited state population of $1 - \langle \sigma^{22} \rangle$ after the pulse. Furthermore, we obtain the total number of released photons by summing up the emitted excitations of each state weighted by the corresponding population. This explains the small losses after

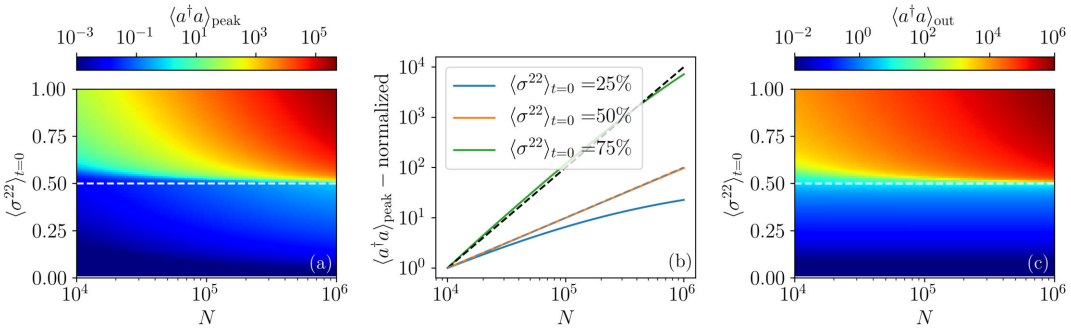

Figure 6.5: *Atom Number Scaling.* Scan of the atom number N and initial excitation $\langle\sigma^{22}\rangle_{t=0}$ for a) the peak photon number and c) the output photon number, to quantify and define the cavity sub- and superradiance regions. b) Shows the peak photon number for three different examples of initial excited state population. The photon number is normalized to the one at $N = 10^4$ for the respective value of $\langle\sigma^{22}\rangle_{t=0}$ to compare the different scalings.

a coherent $\pi/2$-pulse preparation, see Fig. 6.4(a). Note that the coherent excitation leads to a binomial distribution in M, regardless of the cavity coupling. Therefore, the width of the distribution per atom becomes narrower as $1/\sqrt{N}$ for an increasing number of atoms. Combined with the feature that the alternating coupling effectively occupies states close to the boundary of minimal J yields a shrinking percentage of lost excitations for a non-inverted ensemble for large atom numbers.

6.3.2 Atom Number Dependence

So far we have specified the cavity sub- and superradiance qualitatively only. A common way of defining sub- and superradiance quantitatively is the scaling of the emitted light with the atom number [6.1, 6.3, 6.26]. In our case there are two possibilities to do this: the usual approach is to look at the emitted peak photon number. In Fig. 6.5(a) and Fig. 6.5(b) we see that for an inverted ensemble we obtain a large peak photon number proportional to the atom number squared (black dashed line), and for a non-inverted ensemble the peak is orders of magnitude smaller and increases less than linearly with the atom number. At the threshold $\langle\sigma^{22}\rangle_{t=0} = 50\%$ it scales linearly with the number of atoms [Fig. 6.5(b) grey dashed line]. The other way of quantifying sub- and superradiance is the total number of emitted photons through the cavity. In Fig. 6.5(c) the output photon number scales linearly with the atom number in the superradiant domain and is independent of N in the subradiant regime. Therefore, the number of lost photons per atom reduces for increasing particle numbers in a non-inverted ensemble.

6.4 Cavity Enhanced Ramsey Probing

The suppression and delay of superradiance for a transverse excitation can be advantageous for storing excitations in an atomic ensemble, however, it might also be undesired if one is interested in fast emission of light. Thus, we can either use it to our advantage or try to avoid it, depending on the intended behavior of the system. For example, it can be convenient to store up to $N/2$ excitations in N two-level atoms in some type of quantum battery [6.37–6.39], however, releasing this energy on demand becomes more involved for a transverse excitation. On the other hand, if we strive for fast superradiant emission, as in superradiant lasing [6.18, 6.19, 6.23, 6.40], a coherent drive along the cavity axis should be preferred due to faster and stronger light emission. In any case, whether suppression of superradiance is desirable or not, it is crucial for the understanding, description and design of state of the art experiments [6.8, 6.18–6.20, 6.28, 6.41].

A particular application we would like to highlight in this section is a cavity enhanced Ramsey scheme, inspired by [6.29], where this idea was first presented for free space atoms. A transverse pump with an overall vanishing phase of the atom-cavity coupling allows for a $\pi/2$-pulse excitation of the atomic ensemble without an immediate rapid superradiant decay through the cavity. Combining this feature with fast direct measurements of the number of excited atoms via the superradiantly emitted cavity photons after the second Ramsey pulse allows for an implementation of a new cavity assisted Ramsey spectroscopy. The crucial advantage of this scheme is that it can be very fast with no additional manipulation of the atoms needed for the read out, hence the signal is less perturbed. Furthermore, the atoms are not significantly heated by this measurement and can therefore be reused, remarkably reducing the dead time between measurements. Another advantage to other non-destructive measurements for atomic clocks [6.42–6.44] is that the signal, i.e. the number of photons, scales linearly with the number of atoms. So, in principle, an arbitrarily large number of atoms can be employed, drastically increasing the signal to noise ratio.

Figure 6.6(a) shows the output signal, the total number of photons leaking through the cavity mirrors as a function of the laser-atom detuning δ_a. Similar to the conventional Ramsey method, fringes appear [6.45–6.47]. One striking difference, however, is that a non-inverted ensemble does not produce a signal, corresponding to the flat zero-photon regions. This narrows the FWHM of the cavity Ramsey fringes slightly compared to the conventional Ramsey fringes [see Fig. 6.6(b)]. Including an atomic dephasing with $\nu = 10\Gamma$ (dashed line) merely weakens the signal, yet, the shape of the curve is essentially the same. By choosing $\delta_\mathrm{c} = \delta_\mathrm{a}$ we have implicitly assumed that the cavity is perfectly on resonance with the atomic transition. Therefore, one might wonder if a detuned cavity impairs the signal. But, since we operate deeply in the bad cavity regime, only shifts of the cavity resonance frequency on the order of κ are important.

Overall, this means that enhancing the Ramsey spectroscopy by adding a cavity achieves the same (or even slightly improved) accuracy, but has the advantage of a convenient, fast, non-destructive measurement scaling linearly in the atom number, which can substantially reduce the measurement dead time. At this point we want to mention that the atoms initially need to be in the ground state for each subsequent

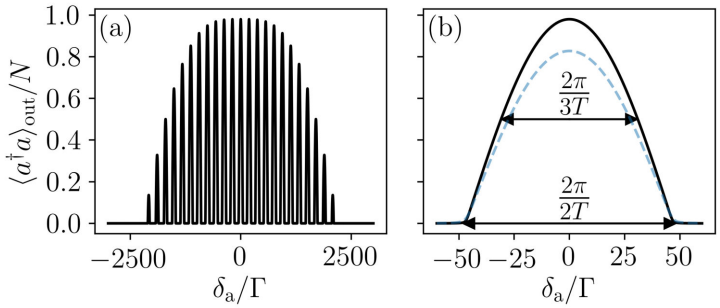

Figure 6.6: *Cavity Ramsey Method.* (a) Fringes in the photon number obtained via the cavity Ramsey method with characteristic flat zero-photon regions. (b) Zoom on the central fringe. The FWHM (π/T) of an optimal independent atom Ramsey sequence with waiting time T and the cavity Ramsey fringe ($\sim 2\pi/3T$) are highlighted. The parameters are $N = 2 \cdot 10^5$, $g = 10\Gamma$, $\kappa = 10^4\Gamma$, $\delta_c = \delta_a$, $\Omega = 1000\Gamma$ and $\nu = 0$ (solid) or $\nu = 10\Gamma$ (dashed). The free evolution time between the two $\pi/2$-pulses is $T = \pi/100\Gamma$. An example cavity Ramsey time evolution is shown in Appendix 6.7.3.

measurement. As we saw in Fig. 6.2(b) a not fully inverted ensemble will retain some population in the excited state. This means one needs to bring these atoms back to the ground state. Unfortunately, this is not possible in a straightforward way via a coherent drive on the clock transition only. However, there are other ways to achieve this, for example with an induced decay via another transition or by depleting the ground state population temporarily to some other level.

Obviously, this cavity assisted Ramsey procedure will not work for $\pi/2$-pulse excitations through the cavity mirrors as all atoms would exhibit the same relative atom-cavity phase and will therefore already decay superradiantly after the first $\pi/2$-pulse [6.8, 6.28], corresponding to the case of equal coupling ($g_j = g$) in Fig. 6.2 and Fig. 6.4.

6.5 Self-Pulsing under Continuous Illumination

Continuously driving the ensemble with a suitable Rabi frequency leads to striking self-pulsing of the system as shown in Fig. 6.7(a). Yet, the explanation for this initially surprising behavior is rather simple: as we have seen, the photon emission into the cavity for a non-inverted atomic ensemble with vanishing relative phase is strongly suppressed. Therefore, there is no significant cavity photon number at least until $t = \pi/2\Omega$ [see Fig. 6.7(b)]. But, as soon as a certain population inversion is achieved the ensemble emits a superradiant pulse into the cavity. Subsequently, the excited state population is depleted below 50% and the photon number quickly reduces to almost zero due to the very fast cavity decay. Since the laser is still on, the procedure starts over and we obtain another pulse, i.e. the system dynamically cycles from cavity sub- to superradiance. As we can see in Fig. 6.7(a) the peak photon number reduces from pulse to pulse. This can be explained in the Dicke state picture, where the not fully inverted ensemble retains some

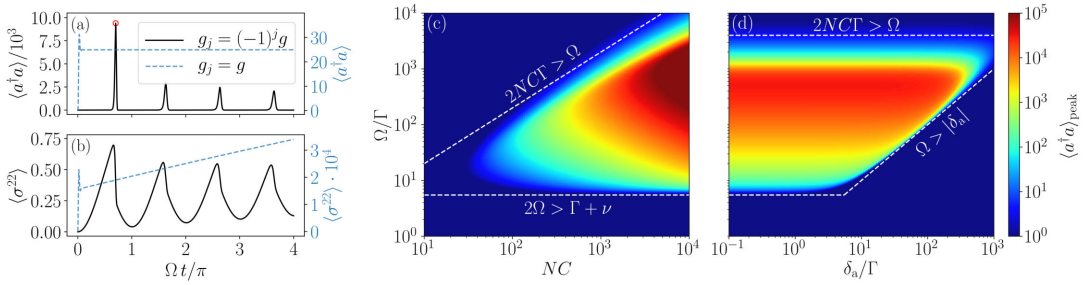

Figure 6.7: *Self-Pulsing.* Time evolution of the cavity photon number (a) and excited state population (b) for a continuous drive, resulting in photon number self-pulsing. (c) and (d) Scans over Ω, NC and δ_a for the peak photon number of the first pulse [red circle in (a)]. The dashed white lines represent the threshold $2NC\Gamma > \Omega > |\delta_a|, (\Gamma + \nu)/2$. The parameters when kept constant are $N = 2 \cdot 10^5$, $g = 10\Gamma$, $\kappa = 10^4\Gamma$, $\delta_c = \delta_a = 0$, $\Omega = 100\Gamma$ and $\nu = 10$.

excitation after the collective emission and hence starts over from this instead of the ground state, which leads to less inversion for the next pulse.

Additionally, the time evolution for equally coupled atoms (dashed blue line, $g_j = g$) is plotted in Fig. 6.7(a) and 6.7(b). In this case the self-pulsing does not occur and the cavity photon number reaches a steady state at $\langle a^\dagger a \rangle = \Omega^2/4g^2$ very quickly. The steady state value for the excited state population ($\langle \sigma^{22} \rangle \approx 1.7 \cdot 10^{-3}$) is reached much later. Note, that the system with vanishing relative phase also reaches a steady state with, surprisingly, the same photon number $\langle a^\dagger a \rangle = \Omega^2/4g^2$ but at a much higher excited state population ($\langle \sigma^{22} \rangle \approx 0.25$).

As we need an excited state population of at least 50% to observe the photon peaks, and the atoms perform Rabi oscillations to reach this, there should be a lower bound for the Rabi frequency Ω, depending on the laser-atom detuning δ_a, the atomic decay rate Γ and the dephasing rate ν. This is exactly what we see in Fig. 6.7(c) and Fig. 6.7(d). The condition $\Omega > |\delta_a|, (\Gamma + \nu)/2$ needs to be satisfied in order for the peak intra-cavity photon number of the first pulse to appear. Furthermore, the collective photon emission from the atoms into the cavity is determined by the frequency $NC\Gamma$. Thus, for the superradiant photon pulse to dominate over the coherent drive, we need to ensure that $NC\Gamma > \Omega/2$. This threshold is also shown in Fig. 6.7(c) and Fig. 6.7(d).

6.6 Conclusions

We have demonstrated and quantified the suppression of cavity superradiance of a non-inverted atomic ensemble with an overall vanishing collective cavity coupling. With the representation of the collective atomic states in the Dicke basis we have introduced an intuitive picture for the system, which explains the number of emitted photons and the retained population after the superradiant emission. Compared to a longitudinal pump through the cavity, the transverse drive leads to an increased pulse delay time. We have proposed a particular use case for the transition from cavity sub- to superradiance

in the form of a cavity enhanced Ramsey spectroscopy, which simplifies and accelerates the measurement procedure. We found that the chosen operating conditions with weak single atom coupling but strong collective coupling also induce an intriguing self-pulsing instability for continuous drive at suitable Rabi frequencies. Interestingly the necessary operating conditions are within reach of current experimental setups [6.18, 6.19, 6.28].

Some preliminary investigations on the influence of imperfections in the setup as variable coupling strengths, slow atomic motion, or fluctuations in the excitation procedure qualitatively yield very similar results for experimentally realistic assumptions. However, a more detailed study of these and other aspects such as heating and loss is required for a quantitative prediction of the practical system performance.

Acknowledgments

We thank Stefan Schäffer and Klaus Mølmer for helpful discussions and Jörg Helge Müller, Eliot Bohr and Sofus Kristensen for providing us with preliminary measurement data which strongly encouraged our work. We acknowledge funding from the European Union's Horizon 2020 research and innovation program under Grant Agreement No. 820404 iqClock. The numerical simulations were performed with the open-source frameworks QuantumCumulants.jl [6.33] and QuantumOptics.jl [6.48].

6.7 Appendix

6.7.1 Comparison with Full Quantum Model

To ensure the validity of our second order cumulant expansion we compare the results with a full quantum model. Of course this is only possible for a relatively small number of atoms. To push the number of atoms as far as possible we use the Monte Carlo wave-function method [6.48–6.50], and describe the atoms in the Dicke basis which means that only collective atomic effects are captured. Thus, we neglect individual atomic decay and dephasing. Figure 6.8 shows the comparison between the second order cumulant expansion and the full quantum model for the cavity subradiance [Fig. 6.8(a)-(c)], cavity Ramsey method [Fig. 6.8(d)] and self-pulsing [Fig. 6.8(e)-(f)]. Overall, we find a good qualitative agreement. A perfect quantitative correspondence is not to be expected for such small atom numbers. Note that the emitted photons we obtain in the time evolution of the full quantum treatment in Fig. 6.8(c) coincide with the ones calculated from the population distribution of the Dicke states as described in Section 6.3.1.

6.7.2 Dicke state mapping

If we represent the collective state of identical two-level atoms in the Dicke state basis, the cavity induced collective decay is only described by a vertical line, i.e. merely reducing M without changing J, if all atoms couple identically to the cavity. This is obviously not the case for our system. However, we can transform our system in to a

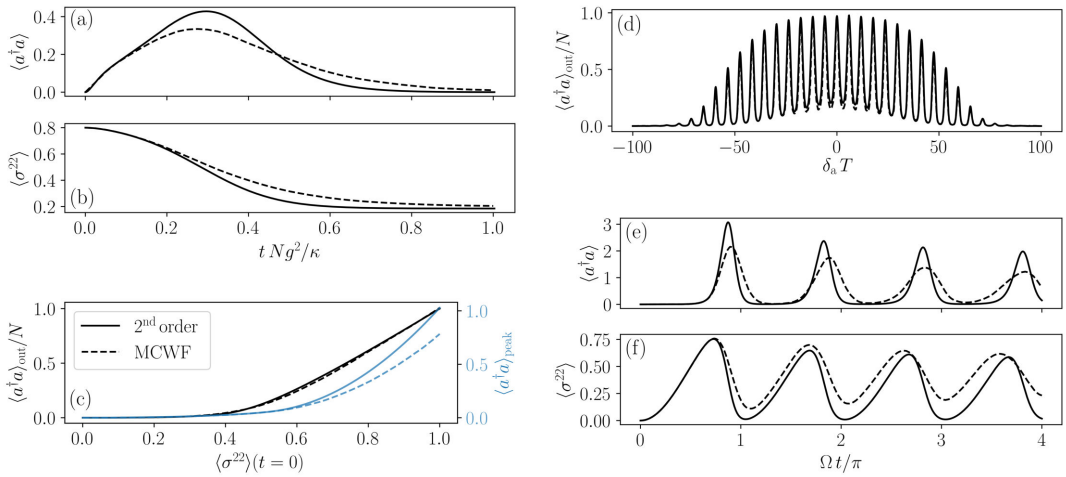

Figure 6.8: *Full Quantum Model.* The second order cumulant expansion (solid line) is compared with a full quantum model (dashed line) for the cavity subradiance in (a)-(c), the cavity Ramsey method in (d) and the self-pulsing in (e) and (f). In all plots we used $\kappa = 200, \Gamma = \nu = 0$ and $\delta_c = \delta_a$. For (a)-(c) the remaining parameters are $N = 20$, $g = 10$ and $\delta_a = 0$, for (d) $N = 20$, $g = 10$, $\Omega = 100$ and $T = \pi/10$ and for (e)-(f) $N = 2 \cdot 50$, $g = 4$, $\delta_a = 0$ and $\Omega = 4$.

reference frame where the atoms have an alternating phase. This leads to an effective system with equal cavity coupling for all atoms, but a relative phase between atoms. This means for the preparation of the atoms with the coherent drive, that the phase of the Rabi-frequency Ω is alternating, instead of the cavity coupling. To numerically calculate the correct state occupation for N atoms, as depicted in Fig. 6.4, we prepare two spin-$N/4$ particles with coherent drives of opposite phase, and combine these two spins by, e.g., using Clebsch-Gordan coefficients.

6.7.3 Cavity Ramsey Time Evolution

Figure 6.9 shows a typical time evolution of the cavity Ramsey method for two different detunings $\delta_a = 0$ and $\delta_a = 50\Gamma$. The measured signal corresponds to the area below the curve of the photon number $\langle a^\dagger a\rangle$ times κ. Additionally, we plot the same quantities for the case of equally coupled atoms ($g_j = g$). We observe that a detuning of $\delta_a = 50\Gamma$ does not significantly change the time evolution and therefore also the signal (the solid and dashed orange lines overlap).

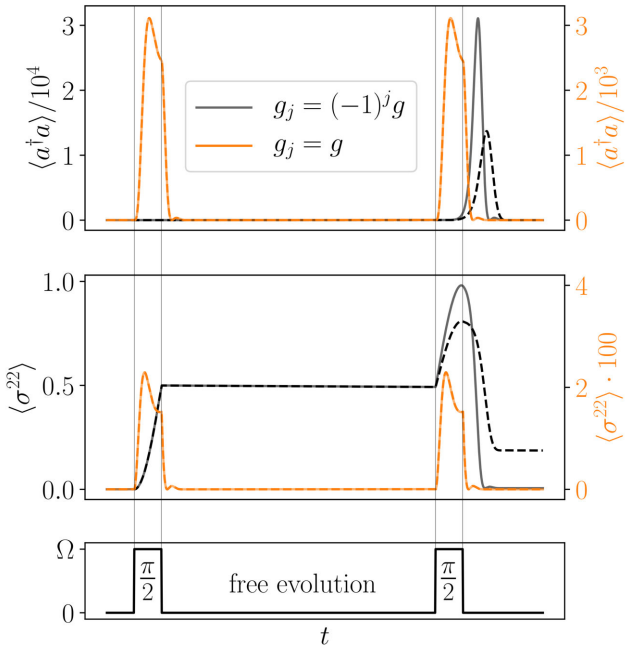

Figure 6.9: *Cavity Ramsey Sequence Time Evolution.* For opposite phase coupling of two sub-ensembles (black lines) the atomic population (middle graph) shows almost no decay between the two Ramsey $\pi/2$-pulses depicted in the lowest graph. A pulsed photon signal (upper graph) is obtained after the second pulse only. The maximum photon number appears in the resonant ($\delta_\mathrm{a} = 0$, solid) case and becomes smaller for the detuned case ($\delta_\mathrm{a} = 50\Gamma$, dashed). In contrast, for all atoms identically coupled (orange lines) cavity induced superradiant decay creates an almost identical photon signal after each pulse virtually transferring all atoms to the ground state independent of their detuning. The parameters are chosen as in Fig. 6.6 except for the free evolution time between the two $\pi/2$-pulses, which we set to $T = \pi/200\Gamma$. The solid lines show $\delta_\mathrm{c} = \delta_\mathrm{a} = 0\Gamma$ and the dashed lines depict $\delta_\mathrm{c} = \delta_\mathrm{a} = 50\Gamma$.

7 First experimental results on cavity sub- and superradiance for transversely driven atomic ensembles

In this chapter we present some yet unpublished results on the experimental implementation to study the transition from cavity sub- to superradiance. This includes a proof of principle run of the cavity enhanced Ramsey method, theoretically proposed and simulated in chapter 6. We find a convincing agreement between the experiment and theoretical results already in this first try.

The experiment is conducted by Eliot Bohr and Sofus Kristensen in the group of Jörg Helge Müller at the Niels Bohr Institute in Copenhagen, with help from Julian Robinson-Tait and Tanya Zelevinsky. The author of this thesis simulated the theoretical results and suggested some specific measurement procedures.

7.1 Experimental system and theoretical assumptions

In this section we introduce the relevant experimental parameters of the system using the notation as in chapter 6. Figure 6.1 depicts a model of the considered system. A cloud of up to fifty million ^{88}Sr atoms with a temperature of $2\,\mu$K is centered in an optical cavity. The cavity is tuned to resonance with the $^1\mathrm{S}_0 \leftrightarrow {}^3\mathrm{P}_1$ transition at a wavelength of $\lambda = 689\,\mathrm{nm}$. The cavity photon loss rate at this wavelength is around $\kappa = 2\pi \times 800\,\mathrm{kHz}$, which is much larger than the atomic decay rate $\Gamma = 2\pi \times 7.5\,\mathrm{kHz}$. With a vacuum Rabi frequency of $g \approx 2\pi \times 0.8\,\mathrm{kHz}$ and single atom cooperativity parameter $C = 4g^2/\kappa\Gamma \approx 4 \times 10^{-4}$, the system is in the weak single atom $C \ll 1$ but strong collective coupling regime $NC \gg 1$. The atomic ensemble, initially in the ground state $^1\mathrm{S}_0$, is excited on the $^1\mathrm{S}_0 \leftrightarrow {}^3\mathrm{P}_1$ transition by a narrowband laser injected perpendicular to the cavity axis, with Rabi frequency of around $\Omega = 2\pi \times 910\,\mathrm{kHz}$. The detuning δ_a between the laser and the atomic transition frequency is varied from shot to shot.

Due to the low kinetic temperature of the atoms, we can assume stationary positions during a measurement cycle. Furthermore, the atomic cloud, with a horizontal expansion (FWHM) of $200\,\mu$m and a vertical one of $100\,\mu$m, is well within the cavity waist radius of $450\,\mu$m. This means the only relevant position dependence for the atom-cavity coupling $g(x) = g\,\cos(2\pi x/\lambda)$ is along the cavity axis. All positions along the cosine cavity mode function are occupied almost equally for a large ensemble of atoms. However, it turns out that considering only a few different positions with an overall vanishing phase is already sufficient for a good theoretical modelling. This allows full numerical

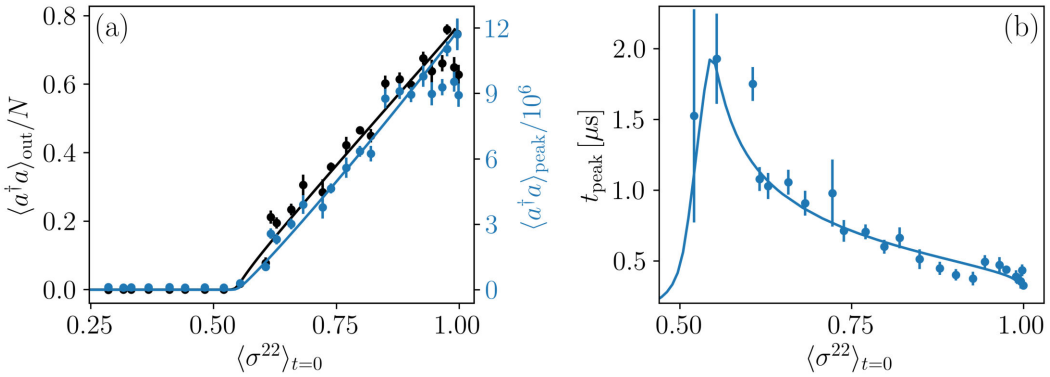

Figure 7.1: *Cavity sub- and superradiance.* (a) Cross-over between cavity sub- and superradiance at an upper state occupation fraction of $\langle\sigma^{22}\rangle_{t=0} \approx 55\%$. We show the integrated output photon number $\langle a^\dagger a\rangle_{\mathrm{out}}$ and the peak photon number $\langle a^\dagger a\rangle_{\mathrm{peak}}$. (b) Delay time of the superradiant pulse with respect to the excitation pulse. The solid lines are simulation results for the following parameters: $N = 20 \times 10^6$, $\kappa = 2\pi \times 800\,\mathrm{kHz}$, $\Gamma = 2\pi \times 7.5\,\mathrm{kHz}$, $g = 2\pi \times 0.815\,\mathrm{kHz}$, $\Omega = 2\pi \times 912.4\,\mathrm{kHz}$, $\delta_{\mathrm{a}} = 0$ and the atomic positions $x = [0, 1, 2, 3, 5, 6, 7, 8]\lambda/16$. The error bars represent the standard deviation from ten repeated measurements.

computation in a second order cumulant expansion as described in chapter 6.

For the excitation laser, we can assume that all atoms obtain the same power since its waist is much larger than the atomic cloud. Note that each atom acquires a different phase but this has the same effect as the overall vanishing phase for the cavity coupling. Hence, assuming the same excitation phase for all atoms essentially yields the same results. Moreover, the atoms will be excited with a laser pulse with almost rectangular shape, we simulate it with a Heaviside step function.

7.2 Transition from cavity sub- to superradiance

In chapter 6 it was predicted that a coherent transverse excitation of the atomic ensemble features a subsequent superradiant emission [7.1–7.3] only for inverted particles. Figure 7.1(a) shows this threshold behavior for the output (left-axis) and peak photon number (right-axis). The simulation results (solid lines) agree very well with the experimental data. Note that the only fit parameter is the amplitude of the experimental signal. We can clearly see the transition from cavity sub- to superradiance at $\langle\sigma^{22}\rangle_{t=0} \approx 55\%$. The onset of superradiance slightly above inversion is due to spontaneous decay of the atoms into free space. As predicted there is a delay time [figure 7.1(b)] for the superradiant pulse [7.2]. If the atoms decay too much in this duration, they will reach a subradiant state with respect to the collective cavity decay. Switching off the individual atomic decay in the simulations ($\Gamma = 0$, not shown) shifts the threshold to 50% as expected. The maximal output photon number is limited to about $0.8N$ due to the constant

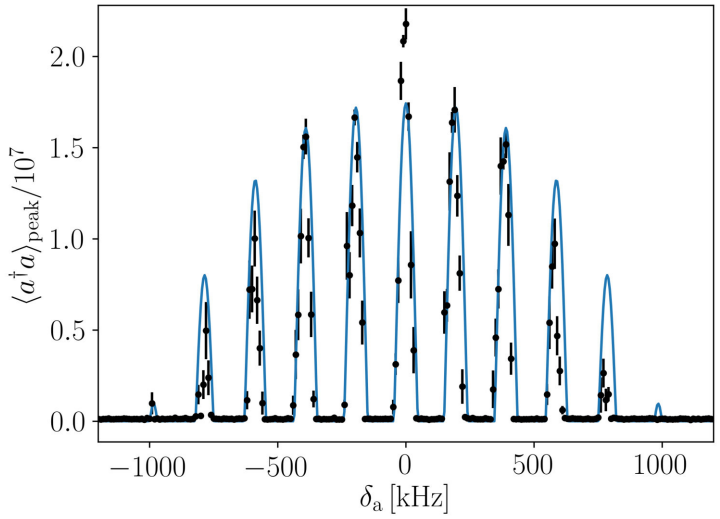

Figure 7.2: *Cavity Ramsey fringes.* Experimental and simulation data of the peak photon number signal for the cavity Ramsey method. The parameters are the same as in figure 7.1, except the atom number is $N = 30 \times 10^6$ and the positions are $x = [0, 1, 2, 4, 5, 6,]\lambda/12$. The error bars represent the standard deviation from ten repeated measurements.

atomic distribution along the cavity axis. A fraction of weakly coupled atoms around the cavity field nodes will not contribute to the superradiant emission. Moreover, we see a slightly larger deviation between the measurement and the simulation around total excitation. The reason for this is likely due to the excitation pulses being not perfect. On the x-axis we plot the theoretical population after a corresponding pulsed excitation. This does not always reliably reflect the actual excited state population of the atoms in the experiment. Note that the results do not average for repeated measurements for π-pulses since imperfections always lead to less inversion.

In figure 7.1(b) we plot the dependence of the superradiant pulse delay time on the initial excited state population, which is defined as the duration from the end of the excitation pulse to the peak of the superradiant pulse. Again, the simulation agrees well with the experiment. The only fit parameter here is a constant offset delay of 1.6 μs, subtracted from all experimental data points. A particularly interesting property is the increasing delay time for lower inversion. For an ensemble with an overall vanishing phase, the duration to synchronize for the superradiant emission reduces for higher inversion. In contrast, for an initial phase synchronized atomic ensemble, as in the case of a drive through the cavity [7.1, 7.4], the delay time increases for higher excitation.

7.3 Cavity enhanced Ramsey sequence

A first practical application of the population dependent transition from cavity sub- to superradiance is to enhance the readout of the excited state population after a Ramsey scheme [7.5]. Figure 7.2 shows the peak photon number signal for different atom-laser detunings in a Ramsey sequence. Fringes with the predicted characteristic flat zero-photon regions appear. The experimental data points agree qualitatively very well with the simulation (solid line). The amplitude of the experimental data points is scaled to fit the height of the theoretically obtained fringes.

7.4 Conclusions and outlook

We have shown preliminary experimental results demonstrating the predicted population dependent transition from cavity sub- to superradiance in a phase symmetric prepared clock atom ensemble and its use for a new type of a cavity enhanced Ramsey scheme. The results agree very well with the theoretical predictions. Further measurements on the atom number dependence and for the excited state population are planned in the near future. Developing an optimized cavity enhanced Ramsey scheme will be a subsequent project.

8 Conclusions & Outlook

We have theoretically studied CQED systems with large ensembles of clock atoms coupled to an optical cavity. In the first chapter, we have introduced all necessary building blocks, models and theoretical tools to understand the investigated systems, with a particular focus on the description and properties of the superradiant laser.

The first two projects in my thesis were devoted to introduce and study potential continuous atomic repumping processes for the superradiant laser. In one attempt we have considered a rather unknown and also unintuitive mechanism for a V-level atom, where proper coherent driving on both transitions can lead to inversion in the more long-lived upper state. We have shown that this process can be used to create gain for lasing, even with simultaneous cooling of the atoms. However, due to power broadening, this laser effectively operates in the conventional good cavity regime, making it unfortunately unsuitable as a repumping mechanism for a superradiant laser. In another approach we have studied a multi-step repumping scheme based on the level structure of strontium-88. We could show that an appropriate choice of the repumping laser parameters can yield a sufficient repumping rate together with minimal light shifts and acceptable heating rates. Furthermore, we introduced an efficient numerical method to reduce the complex multi-level system to an effective two-level atom, which can be utilized for other systems and atomic species.

Afterwards we have studied a system very similar to the superradiant laser, with the essential modification being a coherent transversal drive replacing the incoherent pump. It has turned out that it is crucial to take the alternating sign of the cavity coupling within an atomic cloud into account. Due to the overall vanishing phase in the atomic ensemble, a population dependent transition for the dynamics of the system emerges. In particular, a non-inverted ensemble is subradiant with respect to cavity mediated collective decay, whereas inverted atoms emit a superradiant pulse. For a continuous drive in a specific regime this results in photon number self-pulsing. Furthermore, we have proposed to utilize this transition between cavity sub- and superradiance to enhance the readout after the Ramsey sequence for an atomic clock. The population dependent transition as well as a proof of principle for the cavity enhanced Ramsey scheme have been verified experimentally on the inter-combination line of strontium-88.

All of the above mentioned projects feature large open quantum systems. In order to simulate them we have used a cumulant expansion, mostly in second order, which usually results in tens of equations. Dealing with them was only feasible due to the toolbox we have created, *QuantumCumulants.jl*, which automatically derives and implements those equations. In our projects we have merely simulated CQED systems with the package, however, it can be used for many other quantum systems.

In summary, we have investigated and characterized different repumping mechanism

for steady state superradiant lasing on a narrow atomic transitions. Furthermore, we have theoretically discovered and experimentally verified a population dependent transition from cavity sub- to superradiance. Additionally, we have created the framework *QuantumCumulants.jl*, which is already extensively used by many research groups.

The popularity of the toolbox motivates further development. A particularly useful extension would be to include stochastic processes e.g. to describe measurement back action or to derive quantum Langevin equations. But also implementations of additional Hilbert spaces would be convenient, e.g. for fermions or position and momentum.

An interesting consideration for the cavity sub- and superradiance is to include Zeeman sub-levels and light polarization. Including those leads to additional possibilities to create destructive and constructive interference for the cavity field. The same phenomena are also expected to emerge in waveguide systems. Furthermore, taking particle motion into account to study the influence of light forces on the atoms could be interesting.

9 Publication

Optics express **27**(22), 31193 (2019)

Superradiant cooling, trapping, and lasing of dipole-interacting clock atoms†

C. Hotter[1], D. Plankensteiner[1], L. Ostermann[1] and H. Ritsch[1]

[1]*Institut für Theoretische Physik, Universität Innsbruck, Technikerstraße 21a, A-6020 Innsbruck, Austria*

A cold atomic gas with an inverted population on a transition coupled to a field mode of an optical resonator constitutes a generic model of a laser. For quasi-continuous operation, external pumping, trapping and cooling of the atoms is required to confine them in order to achieve enough gain inside the resonator. As inverted atoms are high-field seekers in blue detuned light fields, tuning the cavity mode to the blue side of the atomic gain transition allows for combining lasing with stimulated cavity cooling and dipole trapping of the atoms at the antinodes of the laser field. We study such a configuration using a semiclassical description of particle motion along the cavity axis. In extension of earlier work we include free space atomic and cavity decay as well as atomic dipole-dipole interactions and their corresponding forces. We show that for a proper choice of parameters even in the bad cavity limit the atoms can create a sufficiently strong field inside the resonator such that they are trapped and cooled via the superradiant lasing action with less than one photon on average inside the cavity.

doi: 10.1364/OE.27.031193

†The author of the present thesis performed all calculations and numerical simulations. D. Plankensteiner and L. Ostermann contributed with guidance and helpful input.

9.1 Introduction

The idea of building a superradiant laser operating on an ultra-narrow optical clock transition in a cold gas has fostered the vision of implementing the optical analog of microwave clock masers [9.1] with a precision and accuracy improved by many orders of magnitude [9.2–9.5]. Today, a central limitation of the best optical clock implementations [9.6, 9.7] is noise within the mirrors of the reference oscillators [9.8] that act as the flywheels locked to the atomic transition frequency. When operated on the clock transition in the bad cavity regime and at low photon numbers, superradiant lasers have been predicted to be very insensitive to these fluctuations and create an accurate and precise frequency reference [9.3, 9.4, 9.9, 9.10].

In principle, operated at high photon numbers sufficiently above the lasing threshold, lasers do not exhibit a fundamental limit of their linewidth [9.11, 9.12]. In practice, however, the operational laser linewidth is determined by technical noise in the resonator and in the active medium. Technological advances have reduced this limit down to the order of Hz [9.13], which has lead to a growing interest in using long-lived clock states as the gain medium in a new generation of so-called superradiant lasers [9.3, 9.14–9.16]. However, the long lifetimes, i.e. the small linewidths, of those states entail a minute dipole moment of the involved transitions, thus making it necessary to work in the strong collective coupling regime. In this domain, by means of synchronization through the cavity field [9.17–9.19], a large collective dipole will build up, which can provide the necessary gain. Here, the atoms do not need to be confined in a small volume as is the case with Dicke superradiance [9.20], but they have to couple almost equally to the cavity.

In the present manuscript we investigate a model of a superradiant laser where the gain medium is self-trapped by the cavity field it creates via stimulated emission into the resonator. At a suitably chosen detuning of the cavity above the atomic transition frequency, the atoms will also slow down and experience a cooling within their prescribed trap positions while simultaneously acting as the gain medium for the laser [9.21, 9.22]. Recently, very efficient cooling has been predicted involving cavity mediated collective superradiant decay and atomic dipole-dipole interactions [9.23]. Since inverted atoms in a blue detuned cavity are high-field seekers they are drawn to mode antinodes and almost equal coupling can be achieved.

9.2 Model

Let us consider N identical two-level atoms confined to one-dimensional motion along the axis of a Fabry Perot cavity. At finite temperature we can assume a classical description of atomic motion along the cavity axis. All transition dipoles are assumed parallel and perpendicular to the cavity axis as in a $J = 0 \rightarrow J = 1$ transition. The atoms couple to the cavity mode via the well known Tavis-Cummings interaction with a strength given by the cavity mode function at the atomic position, $g(r_i)$. Given that the atomic ensemble is closely spaced, we need to take coherent dipole-dipole energy

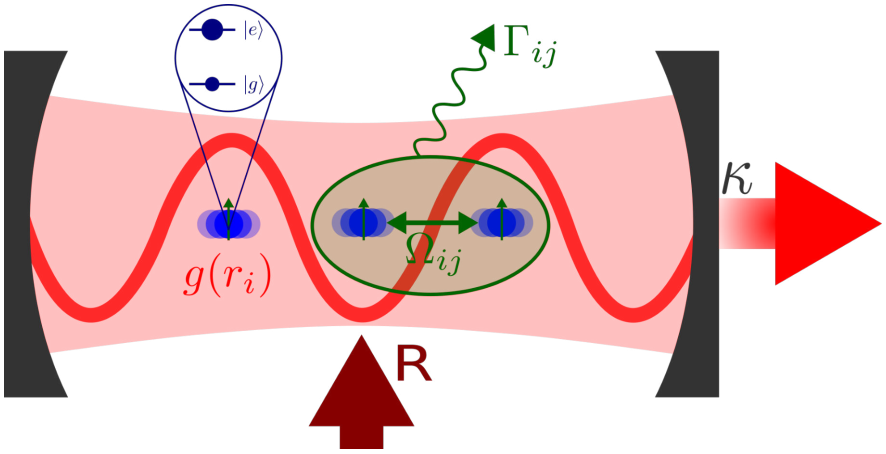

Figure 9.1: *Schematic of our model.* We consider a confined ensemble of two-level atoms moving along the axis of a cavity resonantly coupled to a single mode with amplitude $g(r_i)$. The atoms directly interact via resonant dipole-dipole coupling inducing pairwise energy exchange Ω_{ij} and collective decay with decay rates Γ_{ij}. A uniform transverse pump mechanism individually excites atoms at rate R, while the cavity loses photons at rate κ.

exchange (Ω_{ij}) and collective spontaneous emission (Γ_{ij}), which are both mediated by the surrounding vacuum, into account. Furthermore, we assume to create population inversion of the relevant two atomic levels via an individual transverse incoherent pump with the rate R. In practise this has to be implemented via a multistep process involving intermediate levels. Photons can leak through the cavity mirrors at a cavity loss rate κ (see Fig. 9.1).

The Hamiltonian of this system in the rotating wave approximation and in the reference frame of the atoms is

$$H = \hbar\Delta a^\dagger a + \sum_{i=1}^{N} \hbar g(r_i)[a\sigma_i^+ + a^\dagger\sigma_i^-] + \sum_{i,j:i\neq j} \hbar\Omega_{ij}\sigma_i^+\sigma_j^-, \tag{9.1}$$

where $a^\dagger$ (a) is the bosonic creation (annihilation) operator which creates (annihilates) a photon with frequency ω_c in the cavity. The operators σ_i^+ and σ_i^- are the atomic raising and lowering operators of the ith two-level atom with transition frequency ω_a. The ith dipole couples to the cavity mode with the position-dependent coupling strength $g(r_i) = g\cos(k_\mathrm{c} r_i)$. The coupling constant is denoted by g and $k_\mathrm{c} = 2\pi/\lambda_\mathrm{c}$ is the wave number of the cavity mode. The frequency Ω_{ij} quantifies the resonant dipole-dipole energy transfer between atoms i and j. The detuning between the cavity resonance frequency and the atomic transition frequency is given by $\Delta = \omega_\mathrm{c} - \omega_\mathrm{a}$.

Dissipative processes are accounted for by the Liouvillian $\mathcal{L}$ in the master equation

$$\dot{\rho} = -\frac{i}{\hbar}[H,\rho] + \mathcal{L}[\rho]. \tag{9.2}$$

Within the Markov approximation our Liouvillian consists of three parts, namely

$$\mathcal{L}[\rho] = \mathcal{L}_{\text{pump}}[\rho] + \mathcal{L}_{\text{cav}}[\rho] + \mathcal{L}_{\text{cd}}[\rho], \tag{9.3}$$

where the individual incoherent transversal pump is characterized by the pump rate R,

$$\mathcal{L}_{\text{pump}}[\rho] = \frac{R}{2}\sum_i (2\sigma_i^+\rho\sigma_i^- - \sigma_i^-\sigma_i^+\rho - \rho\sigma_i^-\sigma_i^+), \tag{9.4}$$

the cavity losses occur at the cavity decay rate κ,

$$\mathcal{L}_{\text{cav}}[\rho] = \kappa(2a\rho a^\dagger - a^\dagger a\rho - \rho a^\dagger a), \tag{9.5}$$

and the collective atomic decay is determined by the generalized spontaneous emission rates Γ_{ij},

$$\mathcal{L}_{\text{cd}}[\rho] = \frac{1}{2}\sum_{ij}\Gamma_{ij}(2\sigma_i^-\rho\sigma_j^+ - \sigma_i^+\sigma_j^-\rho - \rho\sigma_i^+\sigma_j^-). \tag{9.6}$$

The resonant dipole-dipole couplings Ω_{ij} and the collective decay rates Γ_{ij} depend on the interatomic distances [9.24, 9.25] and are given by

$$\Omega_{ij} = -\frac{3\Gamma}{4}\Big[(1-\cos^2\Theta)\frac{\cos(k_a r_{ij})}{k_a r_{ij}} - (1-3\cos^2\Theta)\left(\frac{\sin(k_a r_{ij})}{(k_a r_{ij})^2} + \frac{\cos(k_a r_{ij})}{(k_a r_{ij})^3}\right)\Big], \tag{9.7}$$

and

$$\Gamma_{ij} = \frac{3\Gamma}{2}\Big[(1-\cos^2\Theta)\frac{\sin(k_a r_{ij})}{k_a r_{ij}} + (1-3\cos^2\Theta)\left(\frac{\cos(k_a r_{ij})}{(k_a r_{ij})^2} - \frac{\sin(k_a r_{ij})}{(k_a r_{ij})^3}\right)\Big]. \tag{9.8}$$

Here, $k_{\text{a}} = \omega_{\text{a}}/c$ is the wavenumber corresponding to the atomic transition frequency and Θ denotes the angle between the atomic dipoles and the distance vector between atom i and atom j.

For the time evolution of the classical variables we have for the velocity of the ith particle

$$\dot{r}_i = \frac{p_i}{m} = 2\omega_{\text{r}}\frac{p_i}{\hbar k_{\text{a}}^2}, \tag{9.9}$$

and the force acting on a particle is (see Appendix 9.6.1 for details)

$$\dot{p}_i = -\hbar\partial_{r_i}\Big[g(r_i)\,\langle a\sigma_i^+ + a^\dagger\sigma_i^-\rangle + \sum_{j:j\neq i} 2\Omega_{ij}\text{Re}\langle\sigma_i^+\sigma_j^-\rangle\Big]. \tag{9.10}$$

Here, we defined $\omega_{\text{r}} := \hbar k_{\text{a}}^2/(2m)$ as the recoil frequency, with m the mass of an atom.

Note that the above equations are only valid for sufficiently slow particles. This is because we include the time dependence of the collective dipole-dipole interactions via the time-dependent atomic positions only. Thus, Doppler shifts and other effects depending on the velocity, or higher-order derivatives of the position, are neglected

in the dipole-dipole coupling. Furthermore, we note that forces stemming from the collective decay are neglected here (see Appendix 9.6.1). Additionally, since we assume classical motion, the recoil from spontaneous emission is neglected in the kinetic energy. This is probably the most drastic approximation made here.

9.3 Cooling and trapping properties

We investigate the stability of the system described above in the lasing regime by showing that the atoms are cooled and trapped within the cavity field potential created by the photons scattered from the inverted atoms. Due to the exponential scaling of the Hilbert space dimension with the number of atoms numerical methods are limited. Thus, we restrict ourselves to treating a sufficiently small system that still exhibits collective effects.

We study a system with three atoms inside the cavity. The initial state is as follows. The atoms are placed $\lambda_c/2$ apart at the cavity field antinodes. Furthermore, the atoms are in the ground state and there are no photons inside the cavity. The set of initial momenta is picked from a normal distribution that depends on the recoil frequency. Namely, we always choose a normal distribution for the atomic momentum such that the average kinetic energy is constant in respect to ω_r. In general, the kinetic energy of the ith particle is $p_i^2/(2m)$. Thus, if the recoil frequency is multiplied by an arbitrary constant c (i.e. the mass is divided by c), we need to scale the momentum with $1/\sqrt{c}$ in order to keep the kinetic energy constant. The standard deviation $\bar{p}_0$ of the initial momentum distribution of the atoms is chosen depending on the choice of ω_r according to this relation.

To analyze the trapping and cooling properties of the system we study the time evolution of the particle positions. In Fig. 9.2(a) we show a case where the particles are cooled until they are cold enough to get trapped in the potential created by the cavity field. The particles distribute themselves relatively far from each other, which means that collective effects hardly play a role. As we aim to investigate collective effects as well, we restrict our calculations to particle trajectories that remain in their initially prescribed trap for the entire time evolution. We call them completely stable trajectories, see for example Fig. 9.2(b). We refer to Appendix 9.6.3 for more details on the stability. The momentum transfer from particle 2 to particle 3, depicted in Fig. 9.2(a), stems from the collective dipole-dipole effects.

In order to quantitatively capture the cooling process, we study the time evolution of the particles' kinetic energy

$$E_{\mathrm{kin}}(t) = \sum_i \frac{p_i(t)^2}{2m}, \tag{9.11}$$

and average over 100 thermally distributed initial momenta. However, we consider the completely stable trajectories only. As evident from Fig. 9.2(c) (blue line) this kinetic energy of the stable trajectories oscillates very rapidly on the time scale of the cooling process and thus does not yield comparable results. Therefore, we introduce

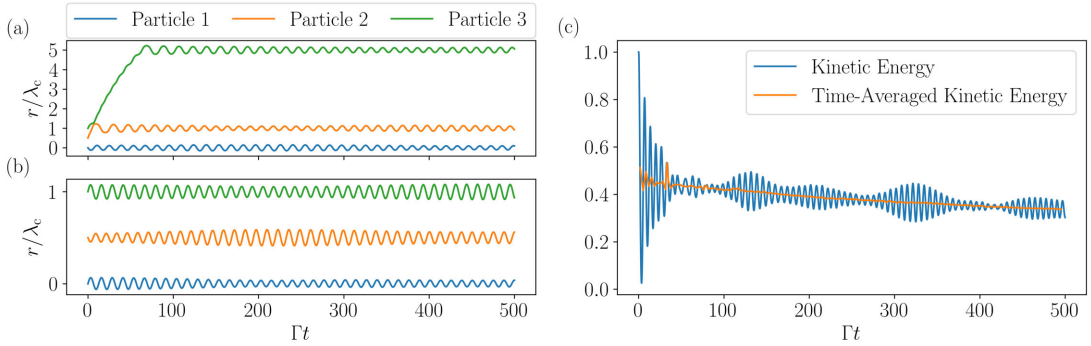

Figure 9.2: *Exemplary trajectories of three particles and their time-averaged kinetic energy loss.* In figure (a) an initially untrapped particle (green and orange line) is slowed down by cavity cooling until it is trapped, whereas all other particles in the examples remain close to their initial trapping position near a field antinode. The set of initial momenta is $p_0 \simeq [-1.78, 3.92, 2.83]\hbar k_a$ in (a) and $p_0 \simeq [1.00, -0.73, 1.18]\hbar k_a$ in (b). In (c), we see that the time-averaged relative kinetic energy does not vary that much in time as opposed to the momentary kinetic energy exhibiting trapped oscillatory motion. For better visibility we normalize the kinetic energy to its initial value. The parameters are $N = 3$, $\omega_r = 0.1\Gamma$, $\Delta = 10\Gamma$, $g = 5\Gamma$, $\kappa = 10\Gamma$ and $R = 8\Gamma$ for all three figures.

the time-averaged kinetic energy $\bar{E}_{\mathrm{kin}}(t)$, which is obtained by taking the midpoints between two adjacent extrema of the kinetic energy as seen in Fig. 9.2(c) (orange line). The parameter we use in order to characterize cooling or heating is

$$\bar{E}^{\mathrm{rel}}_{\mathrm{kin}}(t) = \frac{\bar{E}_{\mathrm{kin}}(t)}{\bar{E}_{\mathrm{kin}}(0)}, \tag{9.12}$$

which we call time-averaged relative kinetic energy.

We scan over the experimentally most accessible parameters using the procedure described above for three different ω_r. The thermally distributed initial kinetic energy corresponds to a normal distribution of the initial momenta. As discussed above, in order to ensure that the particles start with the same average kinetic energy for all values of ω_r we scale the standard deviation $\bar{p}_0$ of the momentum distribution. We choose $\bar{p}_0 = 2\hbar k_a$ for $\omega_r = 0.1\Gamma$, $\bar{p}_0 = 2/\sqrt{10}\hbar k_a$ for $\omega_r = 1\Gamma$ and $\bar{p}_0 = 2/10\hbar k_a$ for $\omega_r = 10\Gamma$. Fig. 9.3 shows the scan over Δ and R as well as over g and R for all three values of ω_r. Every value of $\bar{E}^{\mathrm{rel}}_{\mathrm{kin}}(t)$ above 1.0 corresponds to heating and is artificially fixed to 1.0, as these are points of little interest.

We observe that only trajectories with $\Delta > 0$ realize cooling, which corresponds to the expected blue detuning of the cavity mode with respect to the atoms. This is due to the fact that atoms inside a cavity favour the emission of photons near the cavity resonance frequency [9.26]. An atom in a blue detuned cavity emits photons at a frequency higher than its transition frequency. Therefore, the atom has to exert energy in order to lose a photon into the cavity, which it does by losing kinetic energy. The

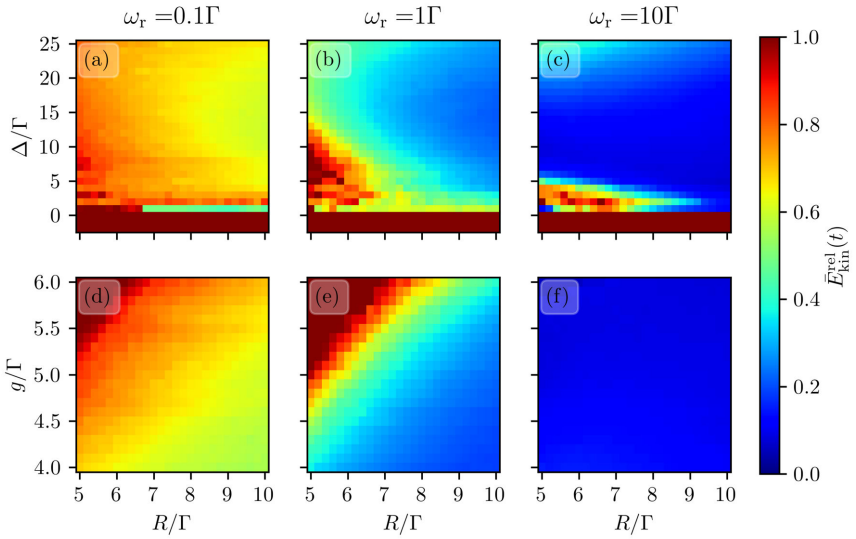

Figure 9.3: *Cycle-averaged relative kinetic energy change after an evolution time of 500 atomic lifetimes as function of various operating parameters.* We show scans over Δ and R in (a),(b) and (c) and vary g and R, respectively, in (d),(e) and (f) for different ω_r. The parameters when kept constant are $N = 3$, $\Delta = 5\Gamma$, $g = 5\Gamma$, and $\kappa = 10\Gamma$ and $t = 500/\Gamma$.

atoms feel an effective friction force that is largest at the points where the cavity field is maximal (high-field seeking). As can be seen from the scans, there is an optimum for the detuning where the cooling is maximal. This is similar to the maximal force in the process of Doppler cooling. The force is also proportional to the excited state population of the atoms. The cooling is thus best when the pump is sufficiently strong to keep the atoms inverted at almost all times.

Furthermore, we can see that atoms with a larger ω_r reach a lower relative kinetic energy during a fixed cooling time. On the one hand, this means that lighter particles are cooled down faster. On the other hand, their initially larger velocities make them more difficult to trap, i.e. more trajectories are unstable (see Appendix 9.6.3). Heavier atoms (smaller ω_r) are easier to trap for the same initial kinetic energy (see Fig. 9.8), even though they do not cool as much during the observed time interval. Note the difference between cooling and trapping here: heavier atoms can still be trapped if they cool poorly, since even a larger kinetic energy in this case oftentimes corresponds to a relatively small velocity insufficient for the particles to climb the potential walls of the trapping potential created by the cavity field. Since they start with a lower initial velocity, however, the cooling is much slower. The inverse line of argument holds for lighter atoms: they are more difficult to trap, but if they are trapped the cooling is more efficient.

Finally, as can be seen in Figs. 9.3(d)-9.3(f), the coupling to the cavity mode should not be too large in order for the system to cool the atoms. This can be explained by the growing probability of the atoms absorbing photons from the cavity, which

causes heating. Hence, the coupling strength should always be well below the cavity loss rate, such that it is much more probable for a photon to leave the cavity than to be reabsorbed. Higher pump strengths can also counteract the heating. If the atoms are pumped strongly they are inverted at almost all times and thus cannot absorb an incident cavity photon. Note that the red areas in Fig. 9.3 with $\Delta > 0$ are mainly caused by extremely slow initial atoms. In these cases the atoms do remain trapped, even though they are heated (note again the difference between cooling and trapping). They are initially so slow that the noise stemming from the cavity field causes heating inside their trap. If the atoms here started with a larger kinetic energy (temperature), they would indeed be cooled. However, they would then also be fast enough to leave their initial traps.

At this point we would like to emphasize again that we describe the system in a semiclassical treatment and we neglect the recoil arising from spontaneous emission. Since the absolute values of the particles' momenta are around $\hbar k_\mathrm{a}$ we need to view the cooling and trapping results critically, especially for $\omega_\mathrm{r} = 1\Gamma$ and $\omega_\mathrm{r} = 10\Gamma$. Note, though, that the recoil heating would only have an effect here since we formulate the superradiant laser regime in terms of a toy model. Specifically, the spontaneous emission rate is taken to be in the limit where $\Gamma \ll \kappa$. However, it is still chosen much larger than it would be for realistic clock atoms in order to avoid numerical difficulties due to different timescales. While we choose $\Gamma \sim 10^{-1}\kappa$, a more realistic choice would be $\Gamma \sim 10^{-6}\kappa$. In that case, a spontaneous emission event is so rare that the recoil can be safely neglected. Still, the fact that we do not include recoil effects for our choice of parameters may be viewed as a rather drastic simplification in our model.

9.3.1 Collective cooling effects

Let us now investigate the relevance of the collective effects for the cooling process. Therefore, we set $\Omega_{ij} = 0$ and $\Gamma_{ij} = \delta_{ij}\Gamma$, and compare this independent cooling to the collective cooling from above. In order to acquire collective effects we find that we need to extend the cooling time by orders of magnitude. In Fig. 9.4 we see the time evolution of $\bar{E}_\mathrm{kin}^\mathrm{rel}$ for collectively interacting atoms in comparison to independent ones.

The main result from Fig. 9.4 is that independent atoms will always reach a lower final kinetic energy for long cooling times. In the collective case the atoms push or pull each other away from the cavity field antinodes and thus their displacement amplitude is larger. Therefore, their kinetic energy is bigger on average. Until approximately $\Gamma t = 5000$ the collective line is slightly below the independent line, for $\omega_\mathrm{r} = 0.1\Gamma$. The reason for this is that parts of the kinetic energy are absorbed into the dipole-dipole interaction potential. The fact that there is a minimum below the final value in the collective case stems also from the dipole-dipole interaction. The minimal temperatures in the two collective cases shown in Fig. 9.4 are reached at approximately the same time in units of ω_r.

As we mentioned in the beginning, we restrict our considerations to $N = 3$ due to the exponential growth of the Hilbert space. Let us still comment on what one might expect for a larger number of atoms in terms of cooling. In [9.23], it has been shown

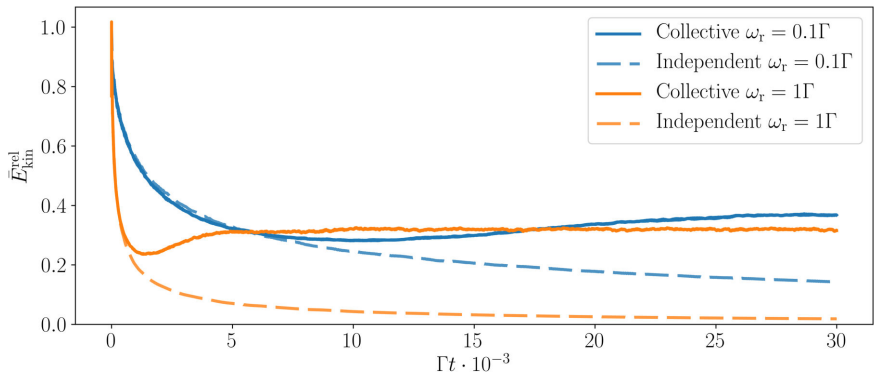

Figure 9.4: *Comparison of motional cooling in time with and without direct dipole interaction.* We compare the motional energy loss for collectively interacting (solid lines) and independent atoms (dashed lines) showing $\bar{E}_{\mathrm{kin}}^{\mathrm{rel}}$ for both cases. The independent case describes atoms far apart from each other. The parameters are $N = 3$, $\Delta = 5\Gamma$, $g = 5\Gamma$, $\kappa = 10\Gamma$ and $R = 8\Gamma$ for both, $\omega_r = 0.1\Gamma$ and $\omega_r = 1\Gamma$.

that efficient cavity cooling can be achieved without direct dipole-dipole interactions between the atoms. Rather, the interactions there stem from the cavity mediated dipole coupling. These findings in combination with the result shown in Fig. 9.4 suggest that the limit imposed on the final kinetic energy by direct dipole-dipole coupling will be more pronounced for larger atom numbers. More precisely, the cooling without direct dipole-dipole interactions yields lower final kinetic energies with growing atom number [9.23]. The larger energy due to the displacement caused by direct dipole-dipole interactions should thus cause an increasing difference to non-interacting atoms.

9.4 Laser properties

After having established that the system is stable for a given set of parameters, we proceed by analyzing its lasing properties. To this end we study the cavity spectrum, the average photon number as well as the second-order correlation function. Furthermore, we look at the atomic inversion. We use the density matrices at $\Gamma t = 500$, which describe a quasi-stationary final state, in order to calculate the properties mentioned above.

9.4.1 Laser spectrum

The laser spectrum can be calculated as the Fourier transform of the first order correlation function $g^{(1)}(\tau) = \langle a^\dagger(t+\tau)a(t)\rangle$. According to the Wiener-Khinchin theorem [9.27], we have

$$S(\omega) = 2\mathrm{Re}\int_0^\infty \mathrm{d}\tau e^{-i\omega\tau} g^{(1)}(\tau). \tag{9.13}$$

Appendix 9.6.2 provides details on how the spectrum is calculated in our semiclassical approximation. Most of the spectra are well described by a Lorentzian distribution (see

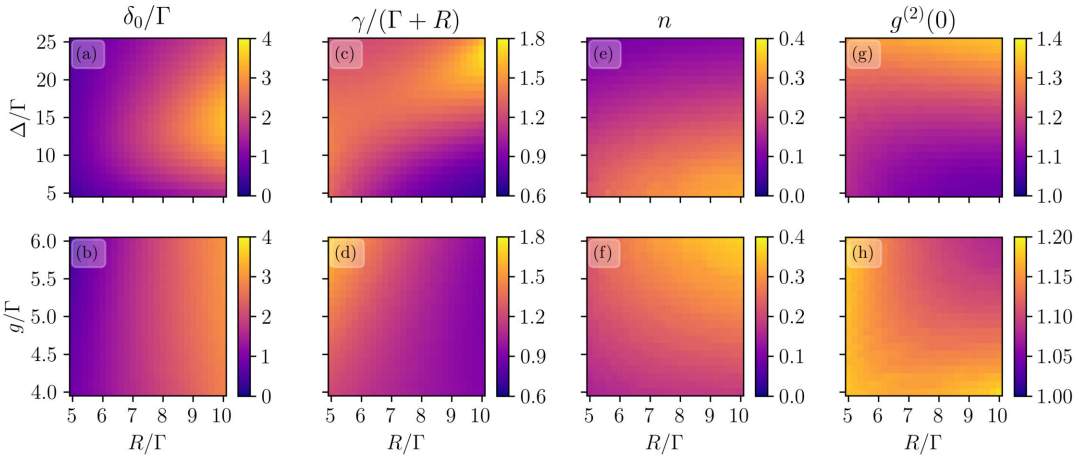

Figure 9.5: *Properties of the emitted laser light as a function of different system parameters.* We depict scans for the peak frequency shift δ_0 from the atomic resonance in (a) and (b), the laser linewidth γ in (c) and (d), the average photon number n in (e) and (f), and the bunching parameter $g^{(2)}(0)$ in (g) and (h). We focus on values of $\Delta \geq 5\Gamma$, since below this threshold the particle motion shows few stable trajectories only (see Fig. 9.8). The remaining parameters are the same as in Fig. 9.3.

Fig. 9.7). Thus, we determine the full width at half maximum (FWHM) γ and the offset to the atomic resonance frequency δ_0. The dependency of the linewidth γ and the offset δ_0 on our scan parameters is depicted in Figs. 9.5(a)-9.5(d). We show these plots for one choice of the recoil frequency only, namely $\omega_\mathrm{r} = 1\Gamma$, since they are qualitatively identical for the other two choices of ω_r. The central observation from Figs. 9.5(a)-9.5(d) is that the laser offset δ_0 is much smaller than the corresponding detuning Δ for all parameters. Mathematically, this means that the slope of the offset's dependency on the detuning (cavity pulling coefficient) is smaller than one. For a conventional laser in the good cavity regime the cavity pulling coefficient is approximately one. In our case it is roughly between 0.1 and 0.2, depending on the pump rate R. In addition, the linewidth γ does not vary much with the detuning. The significance of these two features is that the spectrum of the superradiant laser depends less on cavity fluctuations than the spectrum of a normal laser, which is the expected behaviour. Between $\Delta = 5\Gamma$ and $\Delta = 15\Gamma$ the frequency offset grows as expected, but for larger detunings it seems to reduce. The reason for this is that too large detunings lead to the formation of a distinct second peak approximately at the cavity resonance frequency, as shown in Fig. 9.6. Therefore, in these cases we determine the frequency close to the atomic resonance only, which almost vanishes.

The incoherent drive effectively broadens the atomic transition, resulting in an actual linewidth of $R + \Gamma$. We hence plot the FWHM in units of this effective atomic linewidth in Fig. 9.5(c) and Fig. 9.5(d). One can see that there are areas where the laser linewidth is even lower than the effective atomic linewidth. This is the case for high pump strengths and small detunings. The smallest laser linewidth, however, is achieved

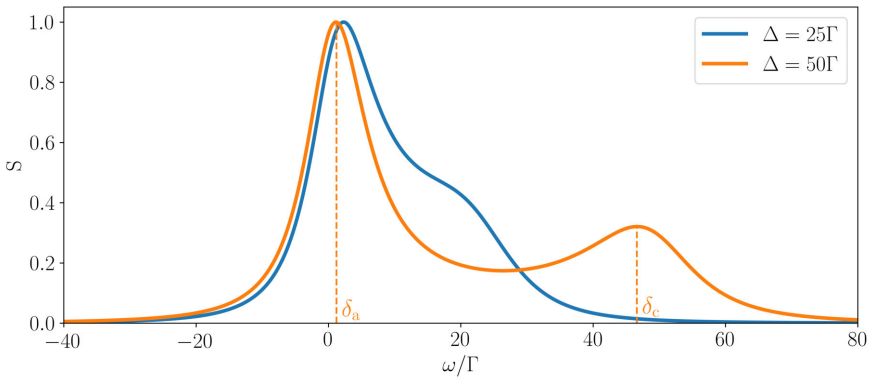

Figure 9.6: *Appearance of a second maximum in the spectrum for large atom cavity detuning.* For detunings larger than $\Delta = 25\Gamma$ a second peak emerges at the cavity resonance to the right-hand side of the atomic peak. For $\Delta = 50\Gamma$ this peak is almost completely separated. This shifts the average of the emitted intensity towards the cavity resonance. We call the offset from the atomic transition frequency δ_a and the one from the cavity resonance δ_c. The parameters are $N = 3$, $\omega_\mathrm{r} = 0.1\Gamma$, $g = 5\Gamma$, $\kappa = 10\Gamma$ and $R = 10\Gamma$ for both, $\Delta = 25\Gamma$ and $\Delta = 50\Gamma$.

for small pump rates. We can also see that, for all stable parameters, the laser linewidth is well below the cavity linewidth, $\gamma < 2\kappa$. The linewidth and the offset grow with increasing pump strength, which implies that the narrowest laser spectrum featuring a low frequency shift is achieved at small pump rates just above the lasing threshold. The atom-field coupling does not affect the offset, but the linewidth grows with it.

We note that the lasing properties shown in Fig. 9.5 are almost identical for the three different ω_r, which indicates that the laser properties do not change dramatically compared to a laser with fixed particle positions as described in [9.4]. To further support this statement we calculate the spectrum in the same manner as before, but for fixed atomic positions ($r_1 = 0$, $r_2 = \lambda_c/2$ and $r_3 = \lambda_c$). Comparing the resulting spectrum to the one with moving atoms, we find an almost perfect overlap. Therefore, the atomic motion appears to merely change the effective atom-field coupling, which does not significantly alter the spectrum.

9.4.2 Photon number, second-order correlation and population inversion

Besides the spectrum we also calculate other characteristic quantities of a laser. Specifically, we compute the average intra-cavity photon number,

$$n = \langle a^\dagger a \rangle \,, \tag{9.14}$$

and the second-order correlation function at zero time delay,

$$g^{(2)}(0) = \frac{\langle a^\dagger a^\dagger a a \rangle}{\langle a^\dagger a \rangle^2}. \tag{9.15}$$

Finally, the population inversion of the atoms is relevant as well. The overall excitation is given by

$$p_{\mathrm{e}} = \sum_{i=1}^{N} \langle \sigma_i^+ \sigma_i^- \rangle \tag{9.16}$$

where inversion is achieved if $p_{\mathrm{e}} > N/2$.

Figs. 9.5(e)-9.5(h) depict n and $g^{(2)}(0)$ as functions of the scan parameters for $\omega_{\mathrm{r}} = 1\Gamma$. The most significant feature is that we always have less than half a photon on average inside the cavity. The figure also shows that the most photons are created and the field is most coherent ($g^{(2)}(0) = 1$) for small detunings, large pump strengths and large atom-field coupling. This behaviour coincides with that of a conventional (good-cavity) laser. The excited state population is always above 1.5, and we note that the overall scan of the atomic excitation is similar to that obtained for a conventional laser.

Comparing the cooling and the lasing scan, we find that the optimal lasing point does not coincide with the best cooling, specifically for the pump strength dependency. We therefore conclude that there is a certain trade-off between the optimal cooling and lasing regimes.

9.5 Conclusions

We have seen that even less than one average intra-cavity photon can be sufficient in order to accumulate excited state atoms dynamically at positions of maximal light coupling, i.e. at field mode antinodes, in the blue-detuned regime. For a sufficient pumping one can thus achieve population inversion and gain which subsequently leads to superradiant lasing. This behaviour is stable with respect to forces and heating induced by dipole-dipole interaction. The output spectrum of such a laser exhibits a very low sensitivity to cavity length fluctuations with a linewidth determined by the atomic linewidth broadened by the pump rate. We have obtained these results by means of a semiclassical model, in which we have treated the atomic states as well as the cavity field mode quantum mechanically, whereas the atomic motion has been described classically.

Overall, for sufficiently slow atoms, the atomic motion only marginally affects the operating conditions and output characteristics of such a laser. In particular, its spectral and coherence properties remain almost unchanged as long as the photon numer is low. This is a promising result for the construction of a superradiant laser, where inverted atoms are moved through the cavity by an optical lattice conveyer belt. It seems that using as many atoms as possible with a weak pump and a large bandwidth cavity is the optimal way to operate such a device. Note, that we have used a rather generic rate based spatially uniform pumping scheme. This should be refined and modeled in more detail for future considerations.

Acknowledgments

We acknowledge funding by the European Union's Horizon 2020 research and innovation programme under grant agreement No 820404 (C. H. and H. R.) and by the Austrian Science Fund (FWF) through projects DK-ALM W1259-N27 (D. P.) and P29318-N27 (L. O.). The numerical simulations were performed with the open source framework QuantumOptics.jl [9.28].

9.6 Appendix

9.6.1 Semiclassical master equation for dipole-dipole interacting atoms

In the following we develop the semiclassical description of our model. The internal atomic degrees of freedom as well as the cavity mode will be described in a quantum mechanical sense, whereas the atomic motion will be written in terms of classical variables only. We start from a full quantum model describing the coupling of moving two-level atoms to a cavity mode as well as to a continuum of free space vacuum modes. The Hamiltonian reads

$$\begin{aligned} H_{\mathrm{tot}} = H_0 + \sum_i \hbar g(\hat{r}_i^{\mathrm{c}}) \left(a^\dagger \sigma_i^- + \sigma_i^+ a\right) + \sum_{\mathbf{k},\lambda} \hbar\omega_k b_{\mathbf{k},\lambda}^\dagger b_{\mathbf{k},\lambda} \\ + \sum_i \sum_{\mathbf{k},\lambda} \hbar g_{\mathbf{k},\lambda} \left(b_{\mathbf{k},\lambda}^\dagger \sigma_i^- e^{-i\mathbf{k}\cdot\hat{\mathbf{r}}_i} + \mathrm{H.c.}\right) + \sum_i \frac{\hat{\mathbf{p}}_i^2}{2m}, \end{aligned} \tag{9.17}$$

where the modes of the free space vacuum are described by the bosonic creation and annihilation operators, $b_{\mathbf{k},\lambda}^\dagger$ and $b_{\mathbf{k},\lambda}$, respectively. Each wavevector $\mathbf{k}$ features two polarizations $\lambda = 1, 2$. The (generally 3D) motion of the atoms is accounted for by the position and momentum operators $\hat{\mathbf{r}}_i$ and $\hat{\mathbf{p}}_i$. The coupling to the cavity mode is determined by the component of the position along the cavity axis $\hat{r}_i^{\mathrm{c}} = \mathbf{k}_{\mathrm{c}} \cdot \hat{\mathbf{r}}_i / k_{\mathrm{c}}$. The free energy part of the cavity and the atoms is given by

$$H_0 := \hbar\omega_{\mathrm{c}} a^\dagger a + \hbar\omega_{\mathrm{a}} \sum_i \sigma_i^+ \sigma_i^- \tag{9.18}$$

Note, that we perform the so-called independent bath assumption for the atoms and the cavity, i.e., the cavity decay does not affect the coupling of the atoms to the environment. Since the cavity damping does not affect the motion of the atoms directly either, we will neglect it for now.

The density operator describing the internal atomic dynamics as well as the motional degrees of freedom, the cavity mode and the 3D vacuum modes ρ_{tot} is then governed by the von Neumann equation,

$$\dot{\rho}_{\mathrm{tot}} = -\frac{i}{\hbar}[H_{\mathrm{tot}}, \rho_{\mathrm{tot}}]. \tag{9.19}$$

Essentially, the semiclassical approximation consists of two assumptions. First, we

assume that there are no correlations (entanglement) between the motion and the remaining degrees of freedom. Secondly, we will assume that the motion is classical such that all expectation values factorize. The assumption that there are no correlations between the motion and the remaining degrees of freedom amounts to setting

$$\rho_{\mathrm{tot}}(t) \approx \rho_{\mathrm{acf}}(t) \otimes \rho_{\mathrm{m}}(t). \tag{9.20}$$

On the one hand, the density operator ρ_{acf} describes the state of the atomic excitation, the cavity, as well as the free-space vacuum modes. On the other hand, the motional degrees of freedom are given by $\rho_{\mathrm{m}}(t)$. We now aim at finding an equation for the reduced system density operator ρ_{acf}. To this end, we take the partial trace,

$$\dot{\rho}_{\mathrm{acf}} = -\frac{i}{\hbar}\mathrm{tr}_{\mathrm{m}}\left([H_{\mathrm{tot}}, \rho_{\mathrm{tot}}]\right) = -\frac{i}{\hbar}[H_{\mathrm{acf}}, \rho_{\mathrm{acf}}]. \tag{9.21}$$

Here, we have defined the reduced Hamiltonian

$$\begin{aligned} H_{\mathrm{acf}} := H_0 &+ \sum_i g(r_i^c(t))\left(a^\dagger \sigma_i^- + \sigma_i^+ a\right) + \sum_{\mathbf{k},\lambda} \hbar\omega_k b_{\mathbf{k},\lambda}^\dagger b_{\mathbf{k},\lambda} \\ &+ \sum_i \sum_{\mathbf{k},\lambda} \hbar g_{\mathbf{k},\lambda}\left(b_{\mathbf{k},\lambda}^\dagger \sigma_i^- e^{-i\mathbf{k}\cdot\mathbf{r}_i(t)} + \mathrm{H.c.}\right), \end{aligned} \tag{9.22}$$

where we wrote

$$\mathbf{r}_i(t) = \langle \hat{\mathbf{r}}_i \rangle (t) = \mathrm{tr}\left(\hat{\mathbf{r}}_i \rho_{\mathrm{m}}(t)\right). \tag{9.23}$$

Additionally, we made our second assumption of treating the motion clasically, such that $\langle f(\hat{\mathbf{r}})\rangle \approx f(\mathbf{r})$ for any function f.

The assumptions from above constitute our semiclassical approximation. We can now proceed by eliminating the field modes. This leads to the dipole-dipole interactions among the atoms in the form of coherent energy exchange as well as collective decay. The only additional assumption one has to make to arrive at this is the Markov approximation for the atomic positions. The remaining procedure remains the same and yields [9.24],

$$\dot{\rho} = \mathrm{tr}_{\mathrm{f}}\left(\dot{\rho}_{\mathrm{acf}}\right) = -\frac{i}{\hbar}[H, \rho] + \mathcal{L}_{\mathrm{cd}}[\rho], \tag{9.24}$$

with H the Hamiltonian from Eq. (9.1).

The motion of the atoms, however, is still determined by H_{tot} via

$$\dot{\mathbf{p}}_i = \mathrm{tr}(\hat{\mathbf{p}}_i \dot{\rho}_{\mathrm{tot}}) = -\frac{i}{\hbar}\mathrm{tr}(\hat{\mathbf{p}}_i [H_{\mathrm{tot}}, \rho_{\mathrm{tot}}]) \tag{9.25}$$

and equivalently for $\dot{\mathbf{r}}_i$. While the velocity is given in Eq. (9.9), for the average force on

the ith particle we have (in 1D)

$$\dot{p}_i = -\hbar\partial_{r_i} \sum_{j:j\neq i} \left(2\Omega_{ij}\mathrm{Re}\langle\sigma_i^+\sigma_j^-\rangle + \Gamma_{ij}\mathrm{Im}\langle\sigma_i^+\sigma_j^-\rangle\right). \tag{9.26}$$

Note that the term proportional to the collective decay does not significantly contribute since in our system $\mathrm{Im}\langle\sigma_i^+\sigma_j^-\rangle \approx 0\ \forall\ i,j$ due to almost perfect phase invariance [9.14].

9.6.2 Calculation of the spectrum

The spectrum is given by the Fourier transform of the correlation function

$$g(\tau) = \langle a^\dagger(t+\tau)a(t)\rangle\,. \tag{9.27}$$

A common method to calculate this is to define a new density operator at time t which is then evolved up to a time $t+\tau$. This is also known as the optical regression theorem and the essential steps are as follows. Let H_{tot} be a Hamiltonian which describes the entire system and bath dynamics. The evolution of the system is then reversible and given by the unitary operator $U(t) = \exp(-iH_{\mathrm{tot}}t/\hbar)$. Thus, we can write the correlation function as

$$g(\tau) = \mathrm{tr}\left(U^\dagger(t)U^\dagger(\tau)a^\dagger U(\tau)aU(t)\rho_{\mathrm{tot}}(0)\right) = \mathrm{tr}\left(a^\dagger U(\tau)a\rho_{\mathrm{tot}}U^\dagger(\tau)\right), \tag{9.28}$$

where ρ_{tot} is the total density operator. Upon defining a new density operator $\bar{\rho}_{\mathrm{tot}}(0) := a\rho_{\mathrm{tot}}(t)$, we may write

$$g(\tau) = \mathrm{tr}\left(a^\dagger\bar{\rho}_{\mathrm{tot}}(\tau)\right). \tag{9.29}$$

The time evolution of $\bar{\rho}_{\mathrm{tot}}$ is given by the same unitary operator as before. Therefore, eliminating the bath leads to the same master equation, but for a new operator $\bar{\rho} = a\rho$. In this way it is possible to compute $g(\tau)$ from the reduced system density operator via the master equation.

One has to be careful when deriving the semiclassical master equation for $\bar{\rho}$, though. In particular, the force on the atoms is proportional to average values of system variables such as $\langle a^\dagger\sigma_j\rangle$. These have to be computed from the actual density operator ρ, rather than from $\bar{\rho}$. Assuming, as before, that there is no entanglement between the atomic motion and the remaining degrees of freedom [Eq. (9.20)] is equivalent to writing $U(t) \approx U_{\mathrm{acf}}(t)\otimes U_{\mathrm{m}}(t)$. We can hence write

$$\bar{\rho}_{\mathrm{tot}}(\tau) = U_{\mathrm{acf}}(\tau)a\rho_{\mathrm{acf}}(t)U_{\mathrm{acf}}^\dagger(\tau)\otimes U_{\mathrm{m}}(\tau)\rho_{\mathrm{m}}(t)U_{\mathrm{m}}^\dagger(\tau) = \bar{\rho}_{\mathrm{acf}}(\tau)\otimes\rho_{\mathrm{m}}(t+\tau), \tag{9.30}$$

where in the second step we have implicitly defined $\bar{\rho}_{\mathrm{acf}}(0) := a\rho_{\mathrm{acf}}(t)$ and have used the fact that a does not act on the motional degrees of freedom. It is then possible to obtain a semiclassical master equation for $\bar{\rho}$ by tracing out the motion as well as the vacuum modes. However, as can be seen from Eq. (9.30), the motional degrees of

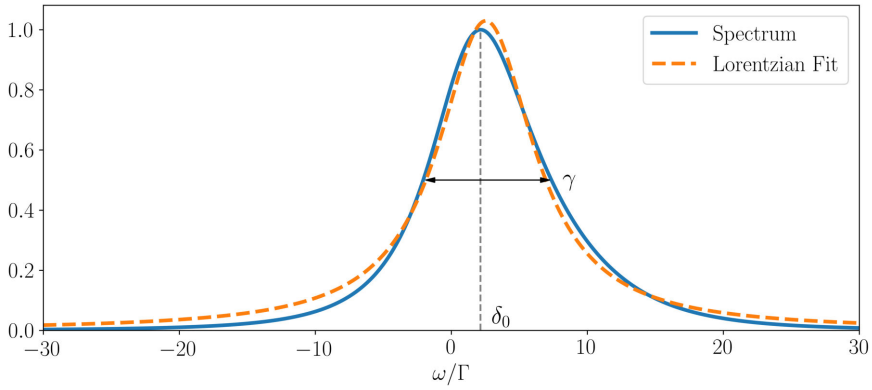

Figure 9.7: *Lorentzian fit of the normalized spectrum.* The calculated spectrum is fitted with a three-parameter Lorentzian function. We call the FWHM γ and the offset to the atomic resonance frequency δ_0. The parameters are the same as in Fig. 9.2(b).

freedom are still determined by $\rho_{\mathrm{m}}(t+\tau)$. Thus, we need to compute the motion up to a time $t+\tau$ in a time evolution with the density operator ρ. Only then can we calculate the proper time evolution of $\bar{\rho}$ by using the previously calculated particle positions and obtain the correlation function $g(\tau)$.

If the detuning between the cavity and the atoms is not too large, the cavity output spectrum can be well described by a Lorentzian distribution, see Fig. 9.7.

9.6.3 Stability

In Fig. 9.8 we provide a scan of the number of completely stable trajectories, i.e. trajectories where the atoms stay in their initial trap for the whole time evolution. As mentioned in Sec. 9.3 we see that lighter particles with the same kinetic energy are more difficult to trap. This is simply because they have a higher initial velocity and therefore it is harder for the cavity field to keep them trapped. Also, it takes a certain amount of time for the cavity to build up a sufficiently strong field which can confine the atoms. If the atomic velocity is too large, an atom may leave its initial trap during this build-up time.

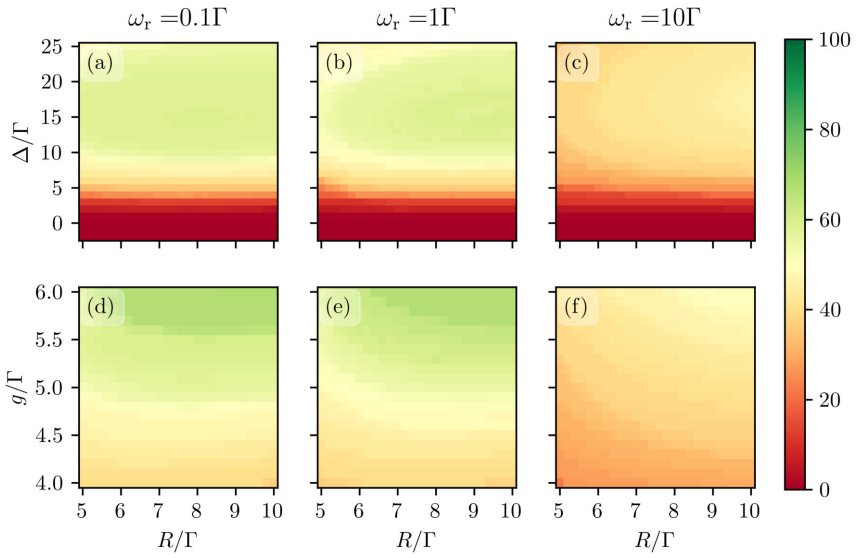

Figure 9.8: *Percentage of completely stable trajectories.* For $\Delta \leq 0$ there are no stable trajectories, because the atoms are heated and leave their initial trap. The fixed parameters are the same as in Fig. 9.3.

10 Publication

Open Research Europe **1**, 73 (2021)

Superradiant lasing in inhomogeneously broadened ensembles with spatially varying coupling†

A. Bychek[1], C. Hotter[1], D. Plankensteiner[1] and H. Ritsch[1]

[1]*Institut für Theoretische Physik, Universität Innsbruck, Technikerstraße 21, A-6020 Innsbruck, Austria*

Background: Theoretical studies of superradiant lasing on optical clock transitions predict a superb frequency accuracy and precision closely tied to the bare atomic linewidth. Such a superradiant laser is also robust against cavity fluctuations when the spectral width of the lasing mode is much larger than that of the atomic medium. Recent predictions suggest that this unique feature persists even for a hot and thus strongly broadened ensemble, provided the effective atom number is large enough.
Methods: Here we use a second-order cumulant expansion approach to study the power, linewidth and lineshifts of such a superradiant laser as a function of the inhomogeneous width of the ensemble including variations of the spatial atom-field coupling within the resonator.
Results: We present conditions on the atom numbers, the pump and coupling strengths required to reach the buildup of collective atomic coherence as well as scaling and limitations for the achievable laser linewidth.
Conclusions: We show how sufficiently large numbers of atoms subject to strong optical pumping can induce synchronization of the atomic dipoles over a large bandwidth. This generates collective stimulated emission of light into the cavity mode leading to narrow-band laser emission at the average of the atomic frequency distribution. The linewidth is orders of magnitudes smaller than that of the cavity as well as the inhomogeneous gain broadening and exhibits reduced sensitivity to cavity frequency noise.

doi: 10.12688/openreseurope.13781.2

†The main contribution from the author of this thesis and D. Plankensteiner were discussions, support and minor calculations. Most calculations and simulations have been performed by A. Bychek.

10.1 Introduction

Collective stimulated emission of coherent light by atoms inside an optical cavity is a fundamental phenomenon studied for decades in quantum optics [10.1–10.7]. Even very recently a large number of theoretical and experimental studies focused on continuous superradiance [10.6–10.15], aiming at the development of a superradiant laser [10.16–10.22]. Such a superradiant laser typically operates in a bad-cavity regime, where the cavity mode is much broader than the natural linewidth of the atoms providing the gain. In the limit of low photon number operation the coherence necessary for frequency stability is stored in the atoms rather than the cavity field. This makes the laser frequency insensitive to thermal and mechanical fluctuations of the cavity, which is the main limitation for conventional good-cavity lasers [10.23, 10.24]. In recent years pulsed superradiance has been experimentally demonstrated [10.16, 10.20–10.22] and a number of new theoretical ideas have been proposed [10.25–10.27]. However, the experimental realization of a continuous wave superradiant laser has not yet been achieved.

Effects such as frequency broadening in the gain medium are an inherent part of any experiment. Such processes are capable of disrupting the collective interaction between the atoms and the cavity field. In this work, we aim to offer a comprehensive study of these potentially detrimental effects. To this end, we study a model of a superradiant laser and focus on inhomogeneity among the atomic ensemble. The inhomogeneity is primarily associated with a distribution of the atomic resonance frequencies leading to stimulated emission into the cavity at a range of different frequencies. Similar differences in the atom-field coupling due to variation in the atomic positioning are also included in the system.

We numerically investigate the dynamics of an atomic medium with a wide range of resonance frequencies and show how the intensity of the pumping rate can lead to cooperative effects among the atoms such that superradiant lasing is achieved. Furthermore, we consider atoms to have different coupling strengths to the cavity. We also study the laser sensitivity to cavity noise.

10.2 Model

We consider an ensemble of N incoherently pumped two-level atoms inside a single mode optical cavity as shown in Figure 10.1. In a bad-cavity regime, where the cavity relaxation rate exceeds the natural linewidth of the atomic transition by many orders of magnitude ($\kappa \gg \Gamma$), the system constitutes a generic model of a superradiant laser. The i-th atom couples to the cavity field with the coupling strength g_i and has a resonance frequency ω_i which might be shifted from the unperturbed atomic transition frequency ω_a. Assuming that the cavity is on resonance with the unperturbed atomic transition frequency, we describe the coherent dynamics of the system by the Tavis-Cummings

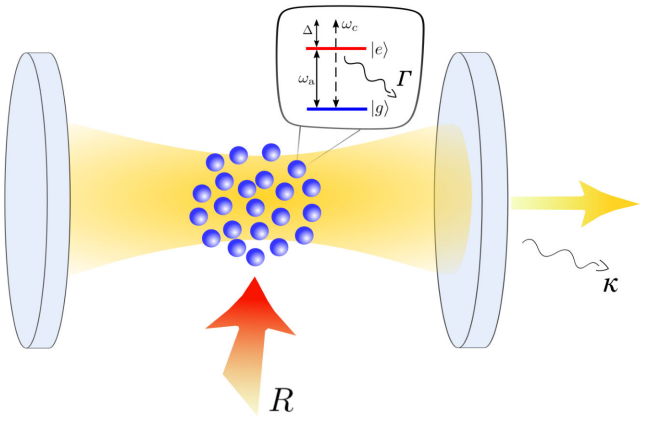

Figure 10.1: Schematic illustration of the system. The atomic medium is placed inside the optical resonator which has a resonance frequency ω_c. Each atom features a ground and an excited state separated by the transition energy $\hbar\omega_a$. The transition couples to the cavity mode (g) as well as the environment (Γ). Additionally, the atoms are incoherently driven from the side (R) such that they can provide gain to the cavity mode.

Hamiltonian in the rotating frame of the cavity,

$$H = -\sum_{i=1}^{N} \Delta_i \sigma_i^+ \sigma_i^- + \sum_{i=1}^{N} g_i (a\sigma_i^+ + a^\dagger \sigma_i^-). \tag{10.1}$$

Here, $\Delta_i = \omega_c - \omega_i$, $\sigma_i^+ = (\sigma_i^-)^\dagger = |e\rangle_i\langle g|_i$ denote the raising and lowering operators of the i-th atom, where $|g\rangle$ and $|e\rangle$ are the atomic ground and excited states, respectively, and $a^\dagger$ (a) is the photon creation (annihilation) operator of the cavity mode. The dissipative processes of this system are described by the Liouvillian terms

$$\begin{aligned}
\mathcal{L}_\kappa[\rho] &= \frac{\kappa}{2}(2a\rho a^\dagger - a^\dagger a\rho - \rho a^\dagger a) \\
\mathcal{L}_\Gamma[\rho] &= \frac{\Gamma}{2}\sum_i (2\sigma_i^-\rho\sigma_i^+ - \sigma_i^+\sigma_i^-\rho - \rho\sigma_i^+\sigma_i^-) \\
\mathcal{L}_R[\rho] &= \frac{R}{2}\sum_i (2\sigma_i^+\rho\sigma_i^- - \sigma_i^-\sigma_i^+\rho - \rho\sigma_i^-\sigma_i^+),
\end{aligned} \tag{10.2}$$

representing the loss of photons through the cavity at the rate κ, the spontaneous atomic decay with the single-atom spontaneous emission rate Γ, and the individual incoherent pumping with the pump strength R. Thus, the full dynamics of the system is determined by the master equation for the density matrix ρ in standard Lindblad form

$$\dot{\rho} = -i[H, \rho] + \mathcal{L}_\kappa[\rho] + \mathcal{L}_\Gamma[\rho] + \mathcal{L}_R[\rho]. \tag{10.3}$$

Since the exponential growth of the Hilbert space with the number of atoms renders

the solution of the master equation 10.3 intractable for $N \gg 1$, we use a cumulant expansion method [10.7, 10.28]. First, we write down the equations for operator averages describing our system, which for a given operator $\mathcal{O}$ reads

$$\frac{d}{dt}\langle\mathcal{O}\rangle = i\langle[H,\mathcal{O}]\rangle + \kappa\langle\mathcal{D}[a]\mathcal{O}\rangle + \Gamma\sum_i\langle\mathcal{D}[\sigma_i^-]\mathcal{O}\rangle + R\sum_i\langle\mathcal{D}[\sigma_i^+]\mathcal{O}\rangle, \tag{10.4}$$

where $\mathcal{D}[c]\mathcal{O} = \left(2c^\dagger\mathcal{O}c - c^\dagger c\mathcal{O} - \mathcal{O}c^\dagger c\right)/2$. We note that in some cases (mentioned in the description of the results) we additionally include cavity dephasing and atomic dephasing described by the terms $\xi\langle\mathcal{D}[a^\dagger a]\mathcal{O}\rangle$ and $\nu\sum_i\langle\mathcal{D}[\sigma_i^+\sigma_i^-]\mathcal{O}\rangle$, respectively. The cavity dephasing accounts for the effective noise imposed on the system by thermal fluctuations of the cavity mirrors, whereas the atomic dephasing models perturbations on the lasing transition.

To obtain a closed set of differential equations we use the cumulant expansion method [10.28] up to second order:

$$\begin{aligned}
&\frac{d}{dt}\langle a^\dagger a\rangle = -\kappa\langle a^\dagger a\rangle + i\sum_{m=1}^{N} g_m\langle a\sigma_m^+\rangle - i\sum_{m=1}^{N} g_m\langle a^\dagger\sigma_m^-\rangle\\
&\frac{d}{dt}\langle a\sigma_m^+\rangle = -\big((\kappa+\Gamma+R+\xi+\nu)/2 + i\Delta_m\big)\langle a\sigma_m^+\rangle + ig_m\langle a^\dagger a\rangle - 2ig_m\langle a^\dagger a\rangle\langle\sigma_m^+\sigma_m^-\rangle\\
&- ig_m\langle\sigma_m^+\sigma_m^-\rangle - i\sum_{j;m\neq j}^{N} g_j\langle\sigma_m^+\sigma_j^-\rangle\\
&\frac{d}{dt}\langle\sigma_m^+\sigma_m^-\rangle = ig_m\langle a^\dagger\sigma_m^-\rangle - ig_m\langle a\sigma_m^+\rangle - (\Gamma+R)\langle\sigma_m^+\sigma_m^-\rangle + R\\
&\frac{d}{dt}\langle\sigma_m^+\sigma_j^-\rangle = ig_m\langle a^\dagger\sigma_j^-\rangle - ig_j\langle a\sigma_m^+\rangle - 2ig_m\langle a^\dagger\sigma_j^-\rangle\langle\sigma_m^+\sigma_m^-\rangle + 2ig_j\langle a\sigma_m^+\rangle\langle\sigma_j^+\sigma_j^-\rangle\\
&- (\Gamma+R+\nu)\langle\sigma_m^+\sigma_j^-\rangle.
\end{aligned} \tag{10.5}$$

In order to calculate the spectrum of the cavity light field we make use of the Wiener–Khinchin theorem [10.29], which states that the spectrum can be computed as the Fourier transform of the first-order correlation function $g^{(1)}(\tau) = \left\langle a^\dagger(\tau)a(0)\right\rangle$,

$$S(\omega) = 2\mathrm{R}e\left\{\int_0^\infty d\tau e^{-i\omega\tau}g^{(1)}(\tau)\right\}. \tag{10.6}$$

We use the quantum regression theorem [10.30] to write down the set of differential

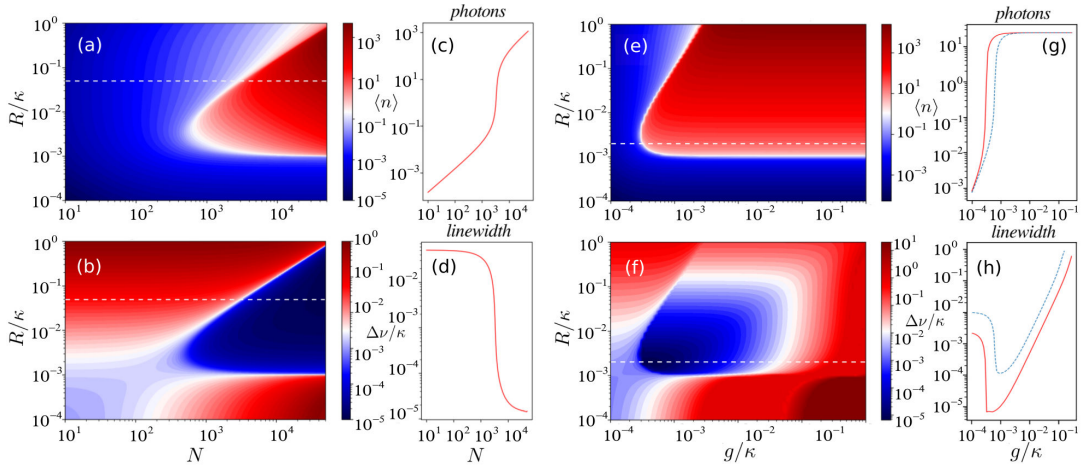

Figure 10.2: (a) The mean photon number and (b) the linewidth (in units of κ) as functions of the number of atoms N and pumping rate R for the parameter set $(\Delta, g, \Gamma, \xi, \nu) = (0, 0.002\kappa, 0.001\kappa, 0, 0)$. (c-d) The cut through the white dashed line in (a-b) for $R = 0.05\kappa$. (e-f) The mean photon number and the linewidth as functions of the atom-cavity coupling strength g and pumping rate R. Additional cavity dephasing occurs at the rate $\xi = \kappa$. Parameters: $\Delta = 0, \Gamma = 0.001\kappa, N = 5 \times 10^4$. (g-h) The cut through the white dashed line in (e-f): the ultra-narrow linewidth is robust to cavity dephasing $\xi = \kappa$ (red solid line) in the regime where the photon number is low. For the blue dashed line atomic dephasing was added to the system with the rate $\nu = 10\Gamma$.

equations for the two-time correlation function, which in matrix form reads,

$$\frac{d}{d\tau}\begin{pmatrix} \langle a^\dagger(\tau)a(0)\rangle \\ \langle \sigma_1^+(\tau)a(0)\rangle \\ \vdots \\ \langle \sigma_N^+(\tau)a(0)\rangle \end{pmatrix} = \mathbf{A}\begin{pmatrix} \langle a^\dagger(\tau)a(0)\rangle \\ \langle \sigma_1^+(\tau)a(0)\rangle \\ \vdots \\ \langle \sigma_N^+(\tau)a(0)\rangle \end{pmatrix}, \tag{10.7}$$

where

$$\mathbf{A} = -\begin{pmatrix} \frac{\kappa+\xi}{2} & -ig_1 & \dots & -ig_N \\ 2ig_1(\langle \sigma_1^+\sigma_1^-\rangle^{st} - \frac{1}{2}) & \frac{\Gamma+R+\nu}{2} + i\Delta_1 & \dots & 0 \\ \vdots & \vdots & \ddots & \vdots \\ 2ig_N(\langle \sigma_N^+\sigma_N^-\rangle^{st} - \frac{1}{2}) & 0 & \dots & \frac{\Gamma+R+\nu}{2} + i\Delta_N \end{pmatrix}. \tag{10.8}$$

We obtain the laser emission spectrum by taking the Laplace transform of Eq. 10.7, where the initial conditions are the steady-state solutions of Eqs. 10.5, for example $\langle a^\dagger(\tau = 0)a(0)\rangle = \langle a^\dagger a\rangle^{st}$.

In this section, we suppose that all atoms in the ensemble are identical with the same detunings $\{\Delta_i\} = \Delta$ and couplings $\{g_i\} = g$ to the cavity mode. This reduces the problem to a set of four differential equations in Eqs. 10.5. The mean intra-cavity photon number and the laser linewidth $\Delta\nu$ (the FWHM of the spectrum) are depicted

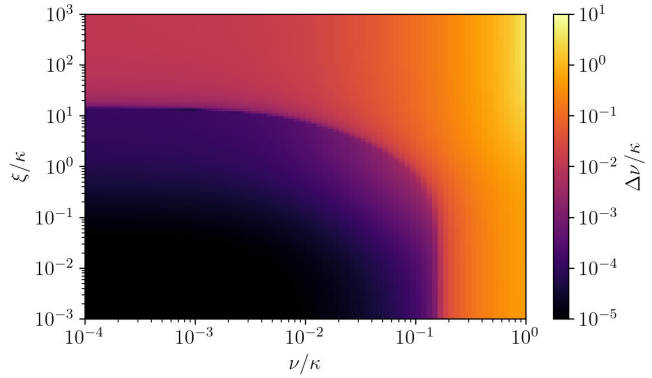

Figure 10.3: The linewidth of the emission spectrum of $N = 5 \times 10^4$ atoms as a scan over cavity dephasing (ξ) and atomic dephasing (ν). The optimal parameters are taken from Fig. 10.2(f), where the system is in the superradiant regime for $(\Delta, g, \Gamma, R) = (0, 0.001\kappa, 0.001\kappa, 0.01\kappa)$.

in Figure 10.2 as functions of the number of atoms, pumping rate, and atom-cavity coupling strength. Superradiance is expected in the parameter regime where the single-atom cooperativity parameter $C = 4g^2/(\kappa\Gamma) < 1$, but the system is in the collective strong coupling regime [10.7], where $CN \gg 1$. Figures 10.2(a-d) show the emergence of the superradiant regime as the number of atoms increases. Above the lasing threshold the collective emission of light with an ultra-narrow linewidth is observed. In this collective regime the phases of the atomic dipoles are synchronized via photon exchange through the cavity which leads to the buildup of a collective dipole among the atoms.

A key feature of such a laser is its insensitivity to thermal and mechanical fluctuations of the cavity length, since the coherence is primarily stored in the atoms rather than in the cavity field. To show the robustness against cavity noise we include cavity dephasing with the rate ξ in the equations. In Figure 10.2(f) we scan the linewidth over the coupling strength g and pumping rate R for an ensemble of $N = 5 \times 10^4$ atoms. In the superradiant regime, the laser linewidth is less than the natural linewidth of the atomic transition and approaches the value $\Delta\nu \sim C\Gamma$, which can be well below 1 mHz for the $^1S_0 \rightarrow {}^3P_0$ transition in ^{87}Sr, as has been pointed out in Ref. [10.7]. Furthermore, we study the influence of noise on the laser linewidth in more detail. In Figure 10.3 we scan the linewidth over both cavity and atomic dephasing, where the other parameters of the system correspond to the superradiant regime. One can see that the linewidth of the superradiant laser can be extremely robust to noise sources within a wide range.

So far the results are based on the idea of absolutely identical atoms. In the next sections, we focus on inhomogeneity within the atomic medium. In particular, we will consider the atoms to be subject to distinct frequency shifts and different couplings to

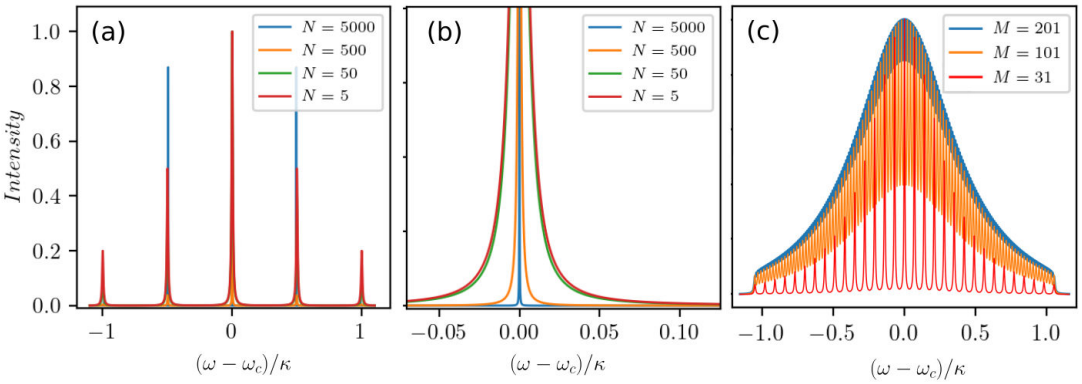

Figure 10.4: Cavity output spectra for weakly driven atomic ensembles composed of several discrete clusters with varying atomic frequencies. (a) $M = 5$ clusters of atoms with the detunings $\Delta_m = [-\kappa; -\kappa/2; 0; \kappa/2; \kappa]$ for different total numbers of atoms $N = 5, ..., 5000$. (b) A zoom-in showing the narrowing of the central peak in the spectrum from (a) around the resonance frequency. (c) Transition of the spectral distribution from discrete to quasi-continuous for an increasing number of clusters. Parameters: $(g, \Gamma, R) = (0.002\kappa, 0.001\kappa, 0.01\kappa)$.

the resonator mode.

10.3 Atomic ensembles with inhomogeneous broadening

While the individual atoms in free space are identical and have the same transition frequencies in principle, in practise they are often subject to individual perturbations introducing local lineshifts, e.g. from trapping within the cavity, motion, or optical pumping. Specifically, it can be an inhomogeneous trapping lattice or pump lasers with a Gaussian profile. Doppler shifts would have similar broadening effects in ring cavities, whereas in a standing-wave cavity they would generate a time-dependent atom-field coupling which we do not consider here. In this section we study the overall effects of inhomogeneous broadening of the gain medium on the laser properties.

In contrast to the case of identical atoms, where the atom number in Eqs. 10.5 and 10.7 only enters as a constant factor, the inhomogeneity among atomic frequencies requires keeping track of the time evolution of each atom separately. For the solution of the collective dynamics one then needs to solve $\mathcal{O}(N^2)$ equations. This is only possible for a limited atom number and we thus have to resort to further approximation methods in order to treat larger ensembles. As a possible approach to approximate a large ensemble with a continuous frequency distribution we combine several atoms in subgroups representing their average atomic frequencies, which we call clusters, see also Refs. [10.14, 10.15, 10.31]. Each atom in a cluster is assumed to be completely identical to all other atoms in the same frequency cluster. This preserves the central physics of the inhomogeneous broadening, but at the same time substantially reduces the number

of equations.

First, we simulate $N = 5$ atoms in five clusters centered at $\Delta_m = \omega_c - \omega_m$, where $\Delta_m \in [-\kappa : \kappa]$. Note that this is equivalent to $M = 5$ frequency clusters each containing a single atom. At low excitation the resulting cavity output spectrum then consists of precisely five spectral lines at the frequency of each cluster. Basically, these are five independent lasers using the same cavity mode simultaneously. If we increase N and set the number of atoms per cluster according to a Gaussian normal distribution with the standard deviation $\sigma = \kappa$, the structure of the spectrum in Figure 10.4(a) will remain unchanged, with each peak becoming more pronounced. In particular, in Figure 10.4(b) we observe growing collective emission among atoms of the same cluster so that the linewidth of each peak becomes smaller as the atom number in the corresponding cluster increases. In Figure 10.4(c) we show how more and more lines appear as we increase the number of clusters up to $M = 201$ until the output merges into a single broad emission line. Note that an increase of the collective coupling to $g\sqrt{N} \sim \kappa$ or a randomization of the individual cluster detunings do not lead to any substantial difference in the spectral profile of the laser. Hence, one can expect a single broadened peak in the emission spectrum in the more realistic case of a large ensemble of atoms with a continuous frequency distribution.

So far we limited investigations to weak incoherent pumping in order to avoid significant additional broadening of the atomic linewidth due to pumping. However, this broadening effect can actually aid the buildup of coherences between the clusters. When the pumping is strong enough such that the distinct spectral lines overlap, the discrete spectral lines of the clusters merge into a single central peak (see Figure 10.5). In other words, more intra-cavity photons and broader individual atomic gain lines ultimately lead to a dramatic narrowing of the laser line. We attribute this effect to a dynamical phase transition from the unsynchronized phase of the dipoles to the synchronized one. Note that an analogous phenomenon has previously been studied in Ref. [10.32] for two mesoscopic ensembles of atoms collectively coupled to a cavity with opposite detunings. Furthermore, we show how an atom number imbalance at a particular frequency in Figure 10.5(b) and overall atom number fluctuations modeled by slight random deviations from a Gaussian distribution in Figure 10.5(c) lead to a shift of the spectral lines. However, in the synchronized regime the lineshift of the central peak is much smaller than its linewidth.

The collapse of the emission spectrum into a single central line occurs at a critical pump strength R_c. This critical value strongly depends on the overall width of the frequency distribution, but shows almost no dependence on the number of subensembles M and the total number of atoms N. The critical transition pump strength is shown for different standard deviations σ of the atomic frequency distribution in Figure 10.6. The data points show the numerical results for an ensemble of $N = 10^2$ (red dots) and $N = 10^4$ (blue circles) atoms sampled by $M = 31$ clusters. For comparison, we also plot the linear (solid line) function $R_c = 0.4\sigma$. We calculate the critical pumping

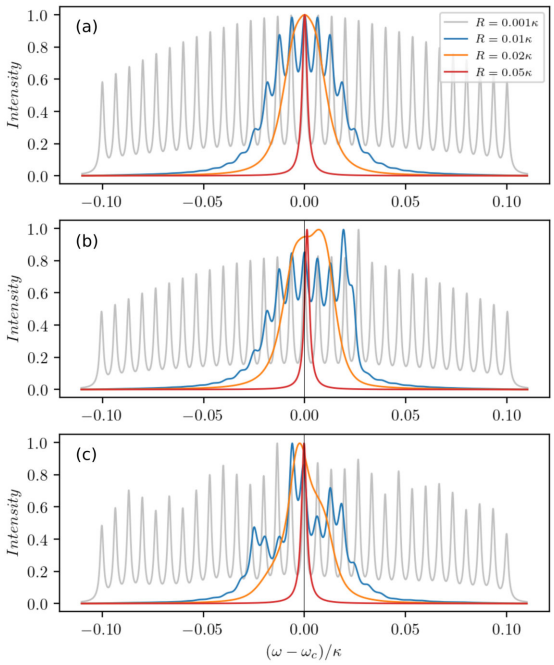

Figure 10.5: Cavity output spectra of a large inhomogeneously broadened ensemble of $N = 10^4$ atoms for different pumping rates $R = 0.001\kappa$ (grey), 0.01κ (blue), 0.02κ (orange), 0.05κ (red). The ensemble is represented by $M = 31$ clusters with the number of atoms per cluster chosen according to a Gaussian normal distribution (a) with the standard deviation $\sigma = 0.1\kappa$, (b) when adding particle imbalance at $\Delta = 0.027\kappa$, (c) with overall atom number fluctuations. The emission intensity is normalized and the other parameters are chosen as $\Delta \in [-\sigma : \sigma]$, $g = 0.002\kappa$, $\Gamma = 0.001\kappa$.

by computing the spectrum for different R. We then determine the critical value of the pump strength as the value at which the spectrum has only a single local maximum, i.e. all separate peaks have merged into a single spectral line. We find a linear dependence for large inhomogeneously broadened ensembles while for narrow ensembles a significantly lower pump strength is required.

Once the laser is operating at a single distinct emission frequency, we can characterize the properties of the output light by the linewidth and the average photon number. The results for different distributions of atomic frequencies are shown in Figure 10.7, where $\Delta \in [-3\sigma : 3\sigma]$ and $\Gamma \leq 3\sigma \leq \kappa$. Figure 10.7(a) illustrates how a narrow linewidth appears for different σ as the number of atoms increases. Note that we chose a pumping strength well above the critical value for a wide atomic frequency distribution (red line). The sharp decrease of the linewidth is accompanied by an increase in the average photon number as can be seen in Figure 10.7(b). This is indicative of a lasing threshold being crossed at a certain number of atoms.

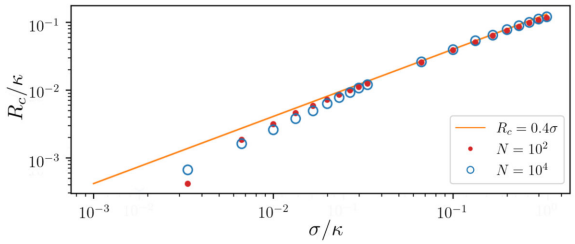

Figure 10.6: Critical value of pumping above which the collective superradiant regime is established depending on the standard deviation σ of the atomic frequency distribution. The data points show the numerical results for an ensemble of $N = 10^2$ (red dots) and $N = 10^4$ (blue circles) atoms sampled by $M = 31$ clusters. For comparison we plot the linear (solid line) function $R_c = 0.4\sigma$ as a linear approximation to the data points. Parameters: $\Delta \in [-3\sigma : 3\sigma], g = 0.001\kappa, \Gamma = 0.001\kappa$.

10.4 Inhomogeneously broadened ensembles with variable coupling strength

Up to now we have assumed that the atoms are perfectly positioned inside the cavity such that they couple equally to the cavity mode. Let us now include spatial variations of the atom-field coupling within the resonator. We consider the ensemble of atoms with the position-dependent coupling strength $g(x) = g_0 \cos(kx)$, where g_0 is the coupling constant, $k = 2\pi/\lambda$ is the cavity mode wave number and x represents the position of an atom. In order to describe the atom-field dynamics we use a similar cluster approach as before. We assume equidistant positions for different clusters $x_m \in [0, ..., \lambda/4)$ and corresponding couplings $g_m(x) = g_0 \cos(kx_m) = \{g_1, g_2, ..., g_K\}$, where K is the total number of clusters. Note, that the sign of the coupling is irrelevant in our system, therefore we only consider couplings with $g_m > 0$.

The dashed lines in Figure 10.7 show the results for $M = 11$ frequency clusters and $K = 5$ clusters of different couplings. As can be seen in Figure 10.7(a), for atoms with different couplings to the cavity mode the dependence of the linewidth on the number of atoms remains roughly the same as for atoms equally coupled to the cavity. This holds as long as the effective overall coupling strength $g_{\text{eff}} = \sqrt{(\sum g_m^2)/K}$ is constant. Thus, the linewidth is essentially unaffected by atoms having different couplings to the cavity.

Finally, let us include cavity dephasing in order to describe lasing in a large inhomogeneously broadened ensemble in the presence of cavity noise. The spectral linewidth and mean photon number under strong cavity dephasing at the rate $\xi = \kappa$ are depicted in Figure 10.8 (blue dashed line). Note that establishing coherence in such a largely broadened ensemble requires sufficiently strong pumping. This subsequently leads to a large number of photons in the cavity mode making the setup sensitive to cavity fluctuations, see Figure 10.2(f). However, additional atomic dephasing can actually relax the constraint on the pumping, since both incoherent pumping

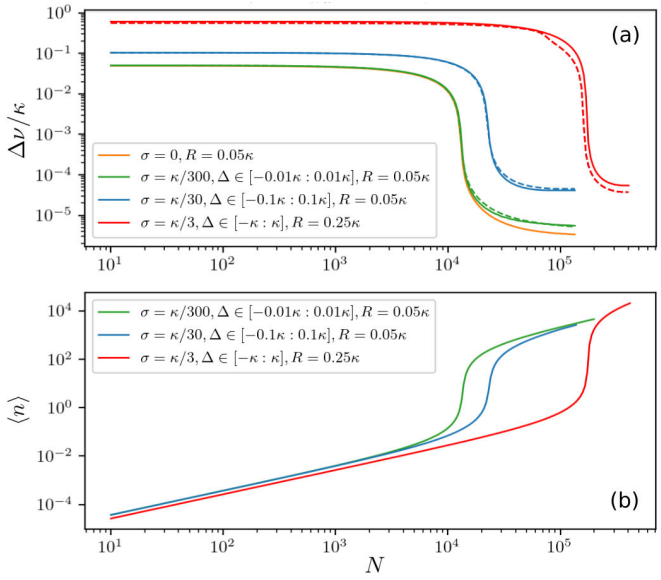

Figure 10.7: (a) Laser spectral linewidth and (b) mean photon number for inhomogeneously broadened ensembles with different standard deviations σ and spectral widths of atomic frequencies $\Delta \in [-3\sigma : 3\sigma]$, where $\sigma = \kappa/300$ (green line), $\sigma = \kappa/30$ (blue line), $\sigma = \kappa/3$ (red line) as a function of the total number of atoms. The number of clusters is $M = 31$ with the number of atoms per cluster chosen according to a Gaussian normal distribution. The dashed lines represent the results including an additional spatial variation of the atom-field coupling $g(x) = g_0 \cos(kx)$. The ensemble is comprised of $M = 11$ frequency clusters and $K = 5$ clusters of different couplings. The couplings are chosen such that the effective coupling strength $g_{\text{eff}} = \sqrt{(\sum_m g_m^2)/K} \equiv g$. Parameters: $g = 0.001\kappa$, $g_0 = 0.0013\kappa$, $\Gamma = 0.001\kappa$.

and atomic dephasing are closely tied to the same physical effect of broadening the atomic emission line. Thus individual atomic dephasing induce additional atom-atom coupling by enlarging the overlap of distinct spectral lines, which finally leads to better synchronization. Adding atomic dephasing to the system at the rate $\nu = 0.01\kappa$ allows for maintaining collective interactions in the ensemble and at the same time enables a reduction of the pump strength by one order of magnitude to $R = 0.005\kappa$. In the low photon number regime, a linewidth on the order of the natural atomic linewidth Γ can be achieved in the presence of strong atomic and cavity dephasing (dash-dotted grey line).

The presented results can be reproduced by using the source code *N_atoms_M_clusters_Delta.jl* (see *Software availability*) [10.33]. The file contains an example of the cluster approach written in Julia version 1.5.0 using the parameters in Figure 10.5. Numerical simulations were performed with the open-source framework Differentialequations.jl [10.34]. The toolbox QuantumCumulants.jl [10.35] has been used to check the equations and verify the second-order cumulant expansion. The graphs were produced using the Matplotlib library [10.36].

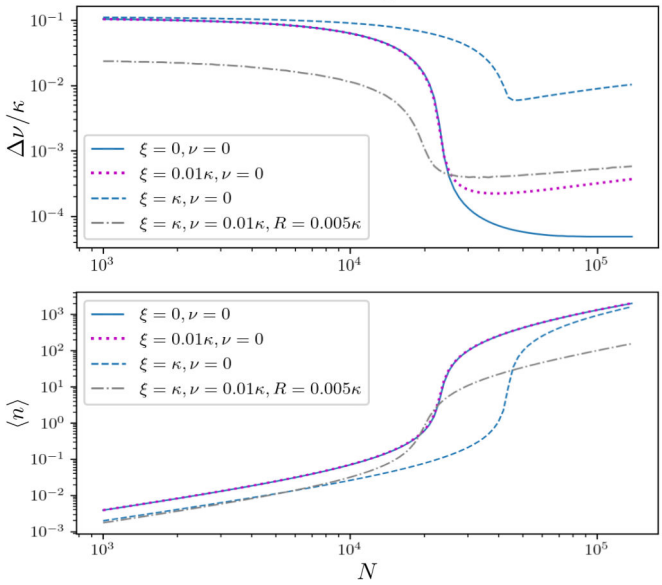

Figure 10.8: Laser linewidth (upper panel) and mean photon number (lower panel) for an inhomogeneously broadened ensemble with spatially varying coupling for $\sigma = \kappa/30$, $\Delta \in [-0.1\kappa : 0.1\kappa]$ and $R = 0.05\kappa$ (solid line). Adding various cavity dephasing at the rate $\xi = \kappa$ (dashed blue line) and $\xi = 0.01\kappa$ (dotted magenta line) we can identify an optimal atom number, above which the cavity noise overwhelms the linewidth narrowing due to large photon numbers. The dash-dotted grey line shows the results when adding additional atomic dephasing at the rate $\nu = 0.01\kappa$. This additional broadening allows synchronization of the individual clusters in the weak pumping regime $R = 0.005\kappa$ ultimately leading to a smaller linewidth.

10.5 Conclusions

We studied superradiant lasing when the gain medium is subject to substantial inhomogeneous frequency broadening and variable coupling. In extensive numerical simulations based on a second-order cumulant expansion we were able to confirm previous predictions that sufficiently large numbers of atoms subject to strong optical pumping can induce synchronization of the atomic dipoles over a large bandwidth. This generates collective stimulated emission of light into the cavity mode leading to narrow-band laser emission at the average of the atomic frequency distribution. The linewidth is orders of magnitudes smaller than that of the cavity as well as the inhomogeneous gain broadening and exhibits reduced sensitivity to cavity frequency noise. We determine the operational conditions and, in particular, the best pump rate to choose for achieving the smallest linewidth for a given atom number and cavity. The minimum occurs not at very low photon numbers but at intra-cavity photon numbers reaching a significant fraction of the atom number.

Typically, full synchronization requires fairly strong pumping, which increases the

effective atomic linewidth. We determined the minimum pump strength to achieve collective phase-locked oscillation of all atomic dipoles. Interestingly, some individual line-broadening effects such as atomic dephasing can actually induce synchronization at significantly lower pump rates. Furthermore, our simulations also show that variations in the atom-field coupling strength induced by the cavity mode structure play only a minor role for the laser stability and noise. In fact, they can be compensated by an increase of the effective overall coupling using a larger atom number or stronger pump.

In the present work, we did not take into account collisions or dipole-dipole interactions between atoms. The effect of dipole-dipole interactions have been studied in a small-scale full quantum model in Ref. [10.9] and do not appear too detrimental. Moreover, collisions could even have a positive effect on synchronization [10.37] but a quantitative prediction is complicated. So far our model is still based on a very simplistic effective pump description via an individual, independent and equal pump rate for each atom. More detailed studies of optical pumping schemes including the shifts induced by the pump light will be at the center of future studies.

10.6 Appendix. Cross-correlations between atoms in different clusters.

As we refer to in the main text, we model a continuous atomic frequency distribution with the standard deviation σ by choosing equidistant cluster detunings Δ_m with the number of atoms per cluster N_m given by a Gaussian distribution with the standard deviation σ. The Heisenberg equations for an ensemble of N atoms sampled by M clusters can be written as

$$
\begin{aligned}
\frac{d}{dt}\langle a^\dagger a\rangle &= -\kappa\langle a^\dagger a\rangle + ig\sum_{m=1}^{M} N_m\langle a\sigma_m^+\rangle - ig\sum_{m=1}^{M} N_m\langle a^\dagger\sigma_m^-\rangle \\
\frac{d}{dt}\langle a\sigma_m^+\rangle &= -\big((\kappa+\Gamma+R)/2 + i\Delta_m\big)\langle a\sigma_m^+\rangle + ig\langle a^\dagger a\rangle - 2ig\langle a^\dagger a\rangle\langle\sigma_{am}^+\sigma_{am}^-\rangle \\
&\quad - ig\langle\sigma_{am}^+\sigma_{am}^-\rangle - ig(N_m-1)\langle\sigma_{am}^+\sigma_{bm}^-\rangle - ig\sum_{j;m\neq j}^{M} N_j\langle\sigma_m^+\sigma_j^-\rangle \\
\frac{d}{dt}\langle\sigma_{am}^+\sigma_{am}^-\rangle &= ig\langle a^\dagger\sigma_m^-\rangle - ig\langle a\sigma_m^+\rangle - (\Gamma+R)\langle\sigma_{am}^+\sigma_{am}^-\rangle + R \\
\frac{d}{dt}\langle\sigma_{am}^+\sigma_{bm}^-\rangle|_{a\neq b} &= ig\langle a^\dagger\sigma_m^-\rangle - ig\langle a\sigma_m^+\rangle - 2ig\langle a^\dagger\sigma_m^-\rangle\langle\sigma_{am}^+\sigma_{am}^-\rangle \\
&\quad + 2ig\langle a\sigma_m^+\rangle\langle\sigma_{am}^+\sigma_{am}^-\rangle - (\Gamma+R)\langle\sigma_{am}^+\sigma_{bm}^-\rangle. \\
\frac{d}{dt}\langle\sigma_m^+\sigma_j^-\rangle|_{m\neq j} &= -i(\Delta_m-\Delta_j)\langle\sigma_m^+\sigma_j^-\rangle + ig\langle a^\dagger\sigma_j^-\rangle(1-2\langle\sigma_{am}^+\sigma_{am}^-\rangle) \\
&\quad - ig\langle a\sigma_m^+\rangle(1-2\langle\sigma_{aj}^+\sigma_{aj}^-\rangle) - (\Gamma+R)\langle\sigma_m^+\sigma_j^-\rangle,
\end{aligned}
\tag{A1}
$$

where indices a, b refer to an atom, and m, j are cluster indices. The last equation describes the cross-correlations between atoms in different clusters. Next, we study the phase and the amplitude of these correlations as the system reaches the steady-state. In the weak pumping regime, the correlations are zero and therefore there is no coherence between the distinct spectral lines of the output spectra in Figure 10.4. However, in the synchronized regime shown in Figure 10.5(a) for $R = 0.05\kappa$, the existing cross-correlations of the m-th cluster with the other clusters $j = m..M$ are presented in Figure 10.9(a).

Let us follow these correlations as the system goes from the unsynchronized phase to the synchronized one. We study the magnitude of cross-correlations between the first (outer) cluster and the central cluster in Figure 10.5(a) as a function of the pumping strength. The correlations are zero in the weak pumping regime and grow with the pumping strength as shown in Figure 10.9(b). The function reaches its maximal value when the ensemble is fully synchronized. However, as pumping continues to grow the correlations decrease due-to growing dephasing imposed by pumping.

10.7 Data availability

Underlying data

Figshare: Superradiant_laser_Figures. https://doi.org/10.6084/m9.figshare.15321819 [10.38].
This project contains the following underlying data:

- Data used in Figures 2-8. All data have .jld2 file extension using JLD2.jl data

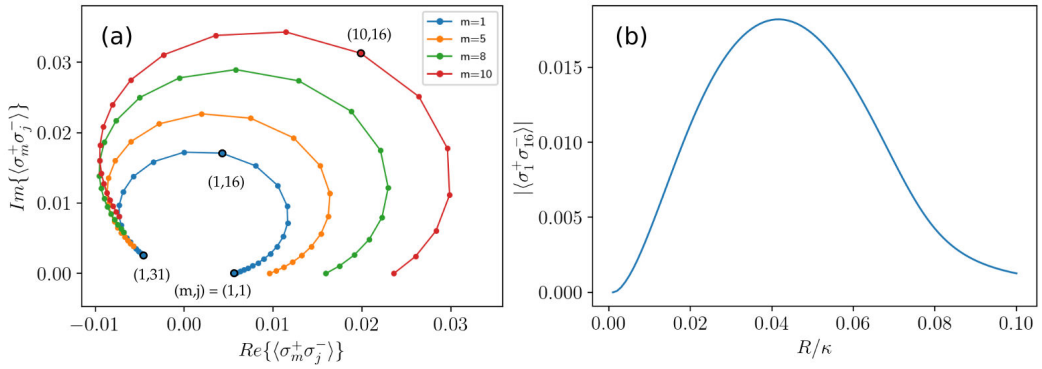

Figure 10.9: Cross-correlations between the 31 clusters presented in Figure 10.5(a). (a) Real and imaginary part of $\langle\sigma_m^+\sigma_j^-\rangle$ correlations between atoms in the m-th and j-th clusters on the complex plane for $R = 0.05\kappa$. (b) The magnitude of the cross-correlations between atoms in the first and the central clusters as a function of the pumping strength.

package in Julia.

10.8 Software availability

- Source code available from: https://github.com/by-anna/Clusters
- Archived source code at time of publication: https://doi.org/10.5281/zenodo.4916393 [10.33]
- License: MIT License

Bibliography

References for Chapter 1

[1.1] A. Einstein, "Zur Quantentheorie der Strahlung," *Phys. Z.*, vol. 18, pp. 121–128, 1917.

[1.2] A. Kastler, "Quelques suggestions concernant la production optique et la détection optique d'une inégalité de population des niveaux de quantifigation spatiale des atomes. Application à l'expérience de Stern et Gerlach et à la résonance magnétique," *J. Phys. Radium*, vol. 11, no. 6, pp. 255–265, 1950.

[1.3] J. P. Gordon, H. J. Zeiger, and C. H. Townes, "Molecular microwave oscillator and new hyperfine structure in the microwave spectrum of nh_3," *Phys. Rev.*, vol. 95, pp. 282–284, Jul 1954.

[1.4] A. L. Schawlow and C. H. Townes, "Infrared and optical masers," *Phys. Rev.*, vol. 112, pp. 1940–1949, Dec 1958.

[1.5] T. H. Maiman, "Stimulated optical radiation in ruby," *Nature*, vol. 187, pp. 1476–4687, Aug 1960.

[1.6] A. E. Siegman, *Lasers*. University science books, 1986.

[1.7] W. T. Silfvast, *Laser fundamentals*. Cambridge university press, 2004.

[1.8] A. D. Ludlow, M. M. Boyd, J. Ye, E. Peik, and P. O. Schmidt, "Optical atomic clocks," *Rev. Mod. Phys.*, vol. 87, pp. 637–701, Jun 2015.

[1.9] D. B. Newell, E. Tiesinga, *et al.*, "The international system of units (si)," *NIST Special Publication*, vol. 330, pp. 1–138, 2019.

[1.10] T. P. Heavner, E. A. Donley, F. Levi, G. Costanzo, T. E. Parker, J. H. Shirley, N. Ashby, S. Barlow, and S. R. Jefferts, "First accuracy evaluation of nist-f2," *Metrologia*, vol. 51, p. 174, may 2014.

[1.11] M. Takamoto, F.-L. Hong, R. Higashi, and H. Katori, "An optical lattice clock," *Nature*, vol. 435, no. 7040, pp. 321–324, 2005.

[1.12] H. Katori, M. Takamoto, V. Pal'Chikov, and V. Ovsiannikov, "Ultrastable optical clock with neutral atoms in an engineered light shift trap," *Physical Review Letters*, vol. 91, no. 17, p. 173005, 2003.

[1.13] S. L. Campbell, R. Hutson, G. Marti, A. Goban, N. Darkwah Oppong, R. McNally, L. Sonderhouse, J. Robinson, W. Zhang, B. Bloom, *et al.*, "A fermi-degenerate three-dimensional optical lattice clock," *Science*, vol. 358, no. 6359, pp. 90–94, 2017.

[1.14] E. Oelker, R. Hutson, C. Kennedy, L. Sonderhouse, T. Bothwell, A. Goban, D. Kedar, C. Sanner, J. Robinson, G. Marti, *et al.*, "Demonstration of 4.8× 10-17 stability at 1 s for two independent optical clocks," *Nature Photonics*, vol. 13, no. 10, pp. 714–719, 2019.

[1.15] T. Bothwell, C. J. Kennedy, A. Aeppli, D. Kedar, J. M. Robinson, E. Oelker, A. Staron, and J. Ye, "Resolving the gravitational redshift across a millimetre-scale atomic sample," *Nature*, vol. 602, no. 7897, pp. 420–424, 2022.

[1.16] Y. Wang, X. Lu, B. Lu, D. Kong, and H. Chang, "Recent advances concerning the 87sr optical lattice clock at the national time service center," *Applied Sciences*, vol. 8, no. 11, p. 2194, 2018.

[1.17] E. D. Black, "An introduction to pound–drever–hall laser frequency stabilization," *American journal of physics*, vol. 69, no. 1, pp. 79–87, 2001.

[1.18] N. Picqué and T. W. Hänsch, "Frequency comb spectroscopy," *Nature Photonics*, vol. 13, no. 3, pp. 146–157, 2019.

[1.19] H. J. Metcalf and P. Van der Straten, "Laser cooling and trapping of neutral atoms," *The Optics Encyclopedia: Basic Foundations and Practical Applications*, 2007.

[1.20] N. F. Ramsey, "A molecular beam resonance method with separated oscillating fields," *Phys. Rev.*, vol. 78, pp. 695–699, Jun 1950.

[1.21] R. Kaubruegger, D. V. Vasilyev, M. Schulte, K. Hammerer, and P. Zoller, "Quantum variational optimization of ramsey interferometry and atomic clocks," *Phys. Rev. X*, vol. 11, p. 041045, Dec 2021.

[1.22] H. G. Dehmelt, "Monoion oscillator as potential ultimate laser frequency standard," *IEEE transactions on instrumentation and measurement*, no. 2, pp. 83–87, 1982.

[1.23] G. J. Dick, J. D. Prestage, C. A. Greenhall, and L. Maleki, "Local oscillator induced degradation of medium-term stability in passive atomic frequency standards," in *Proceedings of the 22th Annual Precise Time and Time Interval Systems and Applications Meeting*, pp. 487–508, 1990.

[1.24] K. Numata, A. Kemery, and J. Camp, "Thermal-noise limit in the frequency stabilization of lasers with rigid cavities," *Phys. Rev. Lett.*, vol. 93, p. 250602, Dec 2004.

[1.25] D. Meiser, J. Ye, D. Carlson, and M. Holland, "Prospects for a millihertz-linewidth laser," *Physical review letters*, vol. 102, no. 16, p. 163601, 2009.

[1.26] J. G. Bohnet, Z. Chen, J. M. Weiner, D. Meiser, M. J. Holland, and J. K. Thompson, "A steady-state superradiant laser with less than one intracavity photon," *Nature*, vol. 484, no. 7392, pp. 78–81, 2012.

[1.27] H. M. Goldenberg, D. Kleppner, and N. F. Ramsey, "Atomic hydrogen maser," *Phys. Rev. Lett.*, vol. 5, pp. 361–362, Oct 1960.

[1.28] R. H. Dicke, "Coherence in spontaneous radiation processes," *Phys. Rev.*, vol. 93, pp. 99–110, 1954.

[1.29] M. A. Norcia, M. N. Winchester, J. R. Cline, and J. K. Thompson, "Superradiance on the millihertz linewidth strontium clock transition," *Science advances*, vol. 2, no. 10, p. e1601231, 2016.

[1.30] T. Laske, H. Winter, and A. Hemmerich, "Pulse delay time statistics in a superradiant laser with calcium atoms," *Physical Review Letters*, vol. 123, no. 10, p. 103601, 2019.

[1.31] S. A. Schäffer, M. Tang, M. R. Henriksen, A. A. Jørgensen, B. T. Christensen, and J. W. Thomsen, "Lasing on a narrow transition in a cold thermal strontium ensemble," *Physical Review A*, vol. 101, no. 1, p. 013819, 2020.

[1.32] H. Liu, S. B. Jäger, X. Yu, S. Touzard, A. Shankar, M. J. Holland, and T. L. Nicholson, "Rugged mhz-linewidth superradiant laser driven by a hot atomic beam," *Physical Review Letters*, vol. 125, no. 25, p. 253602, 2020.

[1.33] C.-C. Chen, S. Bennetts, R. G. Escudero, B. Pasquiou, and F. Schreck, "Continuous guided strontium beam with high phase-space density," *Phys. Rev. Appl.*, vol. 12, p. 044014, Oct 2019.

References for Chapter 2

[2.1] C. Gardiner and P. Zoller, *The Quantum World of Ultra-Cold Atoms and Light Book I: Foundations of Quantum Optics*. ICP, 2014.

[2.2] S. Haroche and J.-M. Raimond, *Exploring the quantum: atoms, cavities, and photons*. Oxford university press, 2006.

[2.3] C. Gerry, P. Knight, and P. L. Knight, *Introductory quantum optics*. CUP, 2005.

[2.4] R. Loudon, *The quantum theory of light*. OUP, 2000.

[2.5] H. Ritsch, P. Domokos, F. Brennecke, and T. Esslinger, "Cold atoms in cavity-generated dynamical optical potentials," *Rev. Mod. Phys.*, vol. 85, pp. 553–601, Apr 2013.

[2.6] I. I. Rabi, "Space quantization in a gyrating magnetic field," *Physical Review*, vol. 51, no. 8, p. 652, 1937.

[2.7] C. Cohen-Tannoudji and D. Guéry-Odelin, "Advances in atomic physics: an overview," 2011.

[2.8] E. T. Jaynes and F. W. Cummings, "Comparison of quantum and semiclassical radiation theories with application to the beam maser," *Proc. IEEE*, vol. 51, no. 1, pp. 89–109, 1963.

[2.9] M. Tavis and F. W. Cummings, "Exact Solution for an N-Molecule—Radiation-Field Hamiltonian," *Phys. Rev.*, vol. 170, pp. 379–384, 1968.

[2.10] R. J. Glauber, "The quantum theory of optical coherence," *Physical Review*, vol. 130, no. 6, p. 2529, 1963.

[2.11] D. Walls and G. J. Milburn, *Quantum Optics*. Springer Berlin, Heidelberg, 2007.

[2.12] H.-P. Breuer, F. Petruccione, *et al.*, *The theory of open quantum systems*. Oxford University Press on Demand, 2002.

[2.13] C. Gardiner and P. Zoller, *Quantum noise: a handbook of Markovian and non-Markovian quantum stochastic methods with applications to quantum optics*. SSBM, 2004.

[2.14] V. Weisskopf and E. Wigner, "Berechnung der natürlichen linienbreite auf grund der diracschen lichttheorie," in *Part I: Particles and Fields. Part II: Foundations of Quantum Mechanics*, pp. 30–49, Springer, 1997.

[2.15] H. Tanji-Suzuki, I. D. Leroux, M. H. Schleier-Smith, M. Cetina, A. T. Grier, J. Simon, and V. Vuletić, "Interaction between atomic ensembles and optical resonators: Classical description," in *Advances in atomic, molecular, and optical physics*, vol. 60, pp. 201–237, Elsevier, 2011.

[2.16] S. H. Autler and C. H. Townes, "Stark effect in rapidly varying fields," *Phys. Rev.*, vol. 100, pp. 703–722, Oct 1955.

[2.17] D. Plankensteiner, C. Hotter, and H. Ritsch, "QuantumCumulants.jl: A Julia framework for generalized mean-field equations in open quantum systems," *Quantum*, vol. 6, p. 617, Jan. 2022.

[2.18] R. Kubo, "Generalized cumulant expansion method," *Journal of the Physical Society of Japan*, vol. 17, no. 7, pp. 1100–1120, 1962.

[2.19] K. Henschel, J. Majer, J. Schmiedmayer, and H. Ritsch, "Cavity qed with an ultracold ensemble on a chip: Prospects for strong magnetic coupling at finite temperatures," *Physical Review A*, vol. 82, no. 3, p. 033810, 2010.

[2.20] D. Meiser, J. Ye, D. R. Carlson, and M. J. Holland, "Prospects for a millihertz-linewidth laser," *Phys. Rev. Lett.*, vol. 102, p. 163601, Apr 2009.

[2.21] M. Aspelmeyer, T. J. Kippenberg, and F. Marquardt, "Cavity optomechanics," *Reviews of Modern Physics*, vol. 86, no. 4, p. 1391, 2014.

[2.22] F. Robicheaux and D. A. Suresh, "Beyond lowest order mean-field theory for light interacting with atom arrays," *Phys. Rev. A*, vol. 104, p. 023702, Aug 2021.

[2.23] O. Rubies-Bigorda, S. Ostermann, and S. F. Yelin, "Characterizing superradiant dynamics in atomic arrays via a cumulant expansion approach," *arXiv preprint arXiv:2211.11895*, 2022.

[2.24] R. Schack and A. Schenzle, "Moment hierarchies and cumulants in quantum optics," *Physical Review A*, vol. 41, no. 7, p. 3847, 1990.

[2.25] "GitHub repository of QuantumCumulants.jl." https://github.com/qojulia/QuantumCumulants.jl, Accessed: Accessed: January 10, 2023.

[2.26] "Documentation of QuantumCumulants.jl." https://qojulia.github.io/QuantumCumulants.jl/stable/, Accessed: January 10, 2023.

[2.27] B. Young, F. Cruz, W. Itano, and J. Bergquist, "Visible lasers with subhertz linewidths," *Physical Review Letters*, vol. 82, no. 19, p. 3799, 1999.

[2.28] R. R. Puri *et al.*, *Mathematical methods of quantum optics*, vol. 79. Springer, 2001.

[2.29] H. Carmichael, *Statistical methods in quantum optics 1: master equations and Fokker-Planck equations*, vol. 1. Springer Science & Business Media, 1999.

[2.30] P. Avan and C. Cohen-Tannoudji, "Two-level atom saturated by a fluctuating resonant laser beam. calculation of the fluorescence spectrum," *Journal of Physics B: Atomic and Molecular Physics*, vol. 10, p. 155, feb 1977.

[2.31] K. Debnath, Y. Zhang, and K. Mølmer, "Lasing in the superradiant crossover regime," *Phys. Rev. A*, vol. 98, p. 063837, Dec 2018.

[2.32] M. Tang, S. A. Schäffer, and J. H. Müller, "Prospects of a superradiant laser based on a thermal or guided beam of ^{88}Sr," *Phys. Rev. A*, vol. 106, p. 063704, Dec 2022.

[2.33] C. Hotter, D. Plankensteiner, and H. Ritsch, "Continuous narrowband lasing with coherently driven v-level atoms," *New Journal of Physics*, vol. 22, p. 113021, nov 2020.

[2.34] R. H. Dicke, "Coherence in spontaneous radiation processes," *Phys. Rev.*, vol. 93, pp. 99–110, 1954.

[2.35] R. Lehmberg, "Radiation from an N-atom system. I. General formalism," *Phys. Rev. A*, vol. 2, no. 3, p. 883, 1970.

[2.36] A. Shankar, J. T. Reilly, S. B. Jäger, and M. J. Holland, "Subradiant-to-subradiant phase transition in the bad cavity laser," *Phys. Rev. Lett.*, vol. 127, p. 073603, Aug 2021.

[2.37] Y. Zhang, Y.-X. Zhang, and K. Mølmer, "Monte-carlo simulations of superradiant lasing," *New Journal of Physics*, vol. 20, p. 112001, nov 2018.

[2.38] D. Meiser and M. J. Holland, "Steady-state superradiance with alkaline-earth-metal atoms," *Phys. Rev. A*, vol. 81, p. 033847, Mar 2010.

[2.39] N. Shammah, S. Ahmed, N. Lambert, S. De Liberato, and F. Nori, "Open quantum systems with local and collective incoherent processes: Efficient numerical simulations using permutational invariance," *Phys. Rev. A*, vol. 98, p. 063815, Dec 2018.

[2.40] F. Haake, M. I. Kolobov, C. Fabre, E. Giacobino, and S. Reynaud, "Superradiant laser," *Physical review letters*, vol. 71, no. 7, p. 995, 1993.

[2.41] J. G. Bohnet, Z. Chen, J. M. Weiner, D. Meiser, M. J. Holland, and J. K. Thompson, "A steady-state superradiant laser with less than one intracavity photon," *Nature*, vol. 484, no. 7392, pp. 78–81, 2012.

References for Chapter 3

[3.1] A. L. Schawlow and C. H. Townes, "Infrared and optical masers," *Physical Review*, vol. 112, no. 6, p. 1940, 1958.

[3.2] V. S. Strelnitski, V. O. Ponomarev, and H. A. Smith, "Hydrogen masers. i: Theory and prospects," *arXiv preprint astro-ph/9511118*, 1995.

[3.3] H. M. Goldenberg, D. Kleppner, and N. F. Ramsey, "Atomic hydrogen maser," *Phys. Rev. Lett.*, vol. 5, pp. 361–362, Oct 1960.

[3.4] F. Haake, M. I. Kolobov, C. Fabre, E. Giacobino, and S. Reynaud, "Superradiant laser," *Phys. Rev. Lett.*, vol. 71, pp. 995–998, Aug 1993.

[3.5] D. Meiser, J. Ye, D. Carlson, and M. Holland, "Prospects for a millihertz-linewidth laser," *Physical review letters*, vol. 102, no. 16, p. 163601, 2009.

[3.6] M. A. Norcia and J. K. Thompson, "Cold-strontium laser in the superradiant crossover regime," *Physical Review X*, vol. 6, no. 1, p. 011025, 2016.

[3.7] M. A. Norcia, J. R. Cline, J. A. Muniz, J. M. Robinson, R. B. Hutson, A. Goban, G. E. Marti, J. Ye, and J. K. Thompson, "Frequency measurements of superradiance from the strontium clock transition," *Physical Review X*, vol. 8, no. 2, p. 021036, 2018.

[3.8] T. Laske, H. Winter, and A. Hemmerich, "Pulse delay time statistics in a superradiant laser with calcium atoms," *Physical Review Letters*, vol. 123, no. 10, p. 103601, 2019.

[3.9] S. A. Schäffer, M. Tang, M. R. Henriksen, A. A. Jørgensen, B. T. Christensen, and J. W. Thomsen, "Lasing on a narrow transition in a cold thermal strontium ensemble," *Physical Review a*, vol. 101, no. 1, p. 013819, 2020.

[3.10] A. Gogyan, G. Kazakov, M. Bober, and M. Zawada, "Characterisation and feasibility study for superradiant lasing in 40ca atoms," *Opt. Express*, vol. 28, pp. 6881–6892, Mar 2020.

[3.11] J. G. Bohnet, Z. Chen, J. M. Weiner, D. Meiser, M. J. Holland, and J. K. Thompson, "A steady-state superradiant laser with less than one intracavity photon," *Nature*, vol. 484, no. 7392, pp. 78–81, 2012.

[3.12] T. Maier, S. Kraemer, L. Ostermann, and H. Ritsch, "A superradiant clock laser on a magic wavelength optical lattice," *Optics express*, vol. 22, no. 11, pp. 13269–13279, 2014.

[3.13] M. A. Norcia, M. N. Winchester, J. R. Cline, and J. K. Thompson, "Superradiance on the millihertz linewidth strontium clock transition," *Science advances*, vol. 2, no. 10, p. e1601231, 2016.

[3.14] K. Numata, A. Kemery, and J. Camp, "Thermal-noise limit in the frequency stabilization of lasers with rigid cavities," *Physical review letters*, vol. 93, no. 25, p. 250602, 2004.

[3.15] J. Chen, "Active optical clock," *Chinese Science Bulletin*, vol. 54, pp. 348–352, Feb 2009.

[3.16] G. A. Kazakov and T. Schumm, "Active optical frequency standards using cold atoms: perspectives and challenges," in *2014 European Frequency and Time Forum (EFTF)*, pp. 411–414, IEEE, 2014.

[3.17] C.-C. Chen, S. Bennetts, R. G. Escudero, B. Pasquiou, and F. Schreck, "Continuous guided strontium beam with high phase-space density," *Phys. Rev. Applied*, vol. 12, p. 044014, Oct 2019.

[3.18] K. K. Meduri, G. A. Wilson, P. B. Sellin, and T. W. Mossberg, "Dynamically induced irreversibility in coherently driven systems," *Phys. Rev. Lett.*, vol. 71, pp. 4311–4314, Dec 1993.

[3.19] H. Gothe, D. Sholokhov, A. Breunig, M. Steinel, and J. Eschner, "Continuous-wave virtual-state lasing from cold ytterbium atoms," *Phys. Rev. A*, vol. 99, p. 013415, Jan 2019.

[3.20] D. Plankensteiner, J. Schachenmayer, H. Ritsch, and C. Genes, "Laser noise imposed limitations of ensemble quantum metrology," *Journal of Physics B: Atomic, Molecular and Optical Physics*, vol. 49, p. 245501, nov 2016.

[3.21] U. Dorner, "Quantum frequency estimation with trapped ions and atoms," *New Journal of Physics*, vol. 14, p. 043011, apr 2012.

[3.22] R. Kubo, "Generalized cumulant expansion method," *Journal of the Physical Society of Japan*, vol. 17, no. 7, pp. 1100–1120, 1962.

[3.23] R. R. Puri, *Mathematical methods of quantum optics*. Springer Berlin Heidelberg, 2001.

[3.24] H. J. Carmichael, *Statistical methods in quantum optics 1: master equations and Fokker-Planck equations*. Springer Science & Business Media, 2013.

[3.25] P. Avan and C. Cohen-Tannoudji, "Two-level atom saturated by a fluctuating resonant laser beam. calculation of the fluorescence spectrum," *Journal of Physics B: Atomic and Molecular Physics*, vol. 10, no. 2, p. 155, 1977.

[3.26] K. Henschel, J. Majer, J. Schmiedmayer, and H. Ritsch, "Cavity qed with an ultracold ensemble on a chip: Prospects for strong magnetic coupling at finite temperatures," *Physical Review A*, vol. 82, no. 3, p. 033810, 2010.

[3.27] R. Dum, P. Zoller, and H. Ritsch, "Monte carlo simulation of the atomic master equation for spontaneous emission," *Phys. Rev. A*, vol. 45, pp. 4879–4887, Apr 1992.

[3.28] K. Mølmer, Y. Castin, and J. Dalibard, "Monte carlo wave-function method in quantum optics," *J. Opt. Soc. Am. B*, vol. 10, pp. 524–538, Mar 1993.

[3.29] T. Salzburger and H. Ritsch, "Atomic self-trapping induced by single-atom lasing," *Physical review letters*, vol. 93, no. 6, p. 063002, 2004.

[3.30] C. Hotter, D. Plankensteiner, L. Ostermann, and H. Ritsch, "Superradiant cooling, trapping, and lasing of dipole-interacting clock atoms," *Optics express*, vol. 27, no. 22, pp. 31193–31206, 2019.

[3.31] H. Ritsch, P. Domokos, F. Brennecke, and T. Esslinger, "Cold atoms in cavity-generated dynamical optical potentials," *Rev. Mod. Phys.*, vol. 85, pp. 553–601, Apr 2013.

[3.32] C. Cohen-Tannoudji and D. Guéry-Odelin, *Advances in Atomic Physics: An Overview*. World Scientific, 2011.

[3.33] G. Vrijsen, O. Hosten, J. Lee, S. Bernon, and M. A. Kasevich, "Raman lasing with a cold atom gain medium in a high-finesse optical cavity," *Physical review letters*, vol. 107, no. 6, p. 063904, 2011.

[3.34] S. Krämer, D. Plankensteiner, L. Ostermann, and H. Ritsch, "Quantumoptics.jl: A Julia framework for simulating open quantum systems," *Comput. Phys. Commun.*, vol. 227, pp. 109–116, 2018.

[3.35] C. Rackauckas and Q. Nie, "Differentialequations. jl–a performant and feature-rich ecosystem for solving differential equations in julia," *Journal of open research software*, vol. 5, no. 1, 2017.

[3.36] J. D. Hunter, "Matplotlib: A 2d graphics environment," *Computing in science & engineering*, vol. 9, no. 3, pp. 90–95, 2007.

[3.37] C. W. Gardiner *et al.*, *Handbook of stochastic methods*, vol. 3. springer Berlin, 1985.

[3.38] "GitHub repository for the QuantumCumulants.jl package." https://github.com/qojulia/QuantumCumulants.jl. Accessed: May 31, 2023.

References for Chapter 4

[4.1] S. M. Tan, "A computational toolbox for quantum and atomic optics," *J. Opt. B: Quantum Semiclassical Optics*, vol. 1, no. 4, p. 424, 1999.

[4.2] J. Johansson, P. Nation, and F. Nori, "Qutip: An open-source Python framework for the dynamics of open quantum systems," *Comput. Phys. Commun.*, vol. 184, no. 4, p. 1234, 2013.

[4.3] J. R. Johansson, P. D. Nation, and F. Nori, "QuTiP 2: A Python framework for the dynamics of open quantum systems," *Comp. Phys. Comm.*, vol. 184, no. 4, pp. 1234–1240, 2013.

[4.4] A. Vukics and H. Ritsch, "C++ QED: an object-oriented framework for wave-function simulations of cavity QED systems," *The European Physical Journal D*, vol. 44, no. 3, pp. 585–599, 2007.

[4.5] X.-Z. Luo, J.-G. Liu, P. Zhang, and L. Wang, "Yao.jl: Extensible, efficient framework for quantum algorithm design," *Quantum*, vol. 4, p. 341, 2020.

[4.6] B. Bauer, L. Carr, H. G. Evertz, A. Feiguin, J. Freire, S. Fuchs, L. Gamper, J. Gukelberger, E. Gull, S. Guertler, *et al.*, "The ALPS project release 2.0: open source software for strongly correlated systems," *Journal of Statistical Mechanics: Theory and Experiment*, vol. 2011, no. 05, p. P05001, 2011.

[4.7] D. S. Steiger, T. Häner, and M. Troyer, "ProjectQ: an open source software framework for quantum computing," *Quantum*, vol. 2, p. 49, 2018.

[4.8] J. Javanainen, "The software atom," *Comput. Phys. Commun.*, vol. 212, pp. 1–7, 2017.

[4.9] J. Bezanson, A. Edelman, S. Karpinski, and V. B. Shah, "Julia: A fresh approach to numerical computing," *SIAM Rev.*, vol. 59, no. 1, pp. 65–98, 2017.

[4.10] S. Krämer, D. Plankensteiner, L. Ostermann, and H. Ritsch, "Quantumoptics.jl: A Julia framework for simulating open quantum systems," *Comput. Phys. Commun.*, vol. 227, pp. 109–116, 2018.

[4.11] S. V. Isakov, I. N. Zintchenko, T. F. Rønnow, and M. Troyer, "Optimised simulated annealing for Ising spin glasses," *Comput. Phys. Commun.*, vol. 192, pp. 265–271, 2015.

[4.12] S. R. White, "Density matrix formulation for quantum renormalization groups," *Phys. Rev. Lett.*, vol. 69, pp. 2863–2866, Nov 1992.

[4.13] U. Schollwöck, "The density-matrix renormalization group in the age of matrix product states," *Ann. Phys.*, vol. 326, no. 1, pp. 96–192, 2011.

[4.14] R. Kubo, "Generalized cumulant expansion method," *J. Phys. Soc. Jpn.*, vol. 17, no. 7, pp. 1100–1120, 1962.

[4.15] R. F. Chang, V. Korenman, C. O. Alley, and R. W. Detenbeck, "Correlations in light from a laser at threshold," *Phys. Rev.*, vol. 178, no. 2, p. 612, 1969.

[4.16] M. Fleischhauer, "Relation between the n-atom laser and the one-atom laser," *Phys. Rev. A*, vol. 50, no. 3, p. 2773, 1994.

[4.17] D. Meiser, Y. Jun, D. R. Carlson, and M. J. Holland, "Prospects for a millihertz-linewidth laser," *Phys. Rev. Lett.*, vol. 102, no. 16, p. 163601, 2009.

[4.18] D. Meiser and M. Holland, "Steady-state superradiance with alkaline-earth-metal atoms," *Phys. Rev. A*, vol. 81, no. 3, p. 033847, 2010.

[4.19] K. Sandner, H. Ritsch, R. Amsüss, C. Koller, T. Nöbauer, S. Putz, J. Schmiedmayer, and J. Majer, "Strong magnetic coupling of an inhomogeneous nitrogen-vacancy ensemble to a cavity," *Phys. Rev. A*, vol. 85, no. 5, p. 053806, 2012.

[4.20] K. Debnath, Y. Zhang, and K. Mølmer, "Lasing in the superradiant crossover regime," *Phys. Rev. A*, vol. 98, no. 6, p. 063837, 2018.

[4.21] S. A. Schäffer, M. Tang, M. R. Henriksen, A. A. Jørgensen, B. T. Christensen, and J. W. Thomsen, "Lasing on a narrow transition in a cold thermal strontium ensemble," *Phys. Rev. A*, vol. 101, no. 1, p. 013819, 2020.

[4.22] C. Hotter, D. Plankensteiner, and H. Ritsch, "Continuous narrowband lasing with coherently driven v-level atoms," *New J. Phys.*, vol. 22, no. 11, p. 113021, 2020.

[4.23] P. Kirton and J. Keeling, "Suppressing and restoring the Dicke superradiance transition by dephasing and decay," *Phys. Rev. Lett.*, vol. 118, no. 12, p. 123602, 2017.

[4.24] P. Kirton and J. Keeling, "Superradiant and lasing states in driven-dissipative Dicke models," *New J. Phys.*, vol. 20, no. 1, p. 015009, 2018.

[4.25] F. Reiter, T. L. Nguyen, J. P. Home, and S. F. Yelin, "Cooperative breakdown of the oscillator blockade in the dicke model," *Phys. Rev. Lett.*, vol. 125, p. 233602, Nov 2020.

[4.26] M. Tang, S. A. Schäffer, A. A. Jørgensen, M. R. Henriksen, B. T. Christensen, J. H. Müller, and J. W. Thomsen, "Cavity-immune spectral features in the pulsed superradiant crossover regime," *Physical Review Research*, vol. 3, no. 3, p. 033258, 2021.

[4.27] S. Krämer and H. Ritsch, "Generalized mean-field approach to simulate the dynamics of large open spin ensembles with long range interactions," *EPJ D*, vol. 69, no. 12, pp. 1–11, 2015.

[4.28] F. Robicheaux and D. A. Suresh, "Beyond lowest order mean-field theory for light interacting with atom arrays," *Phys. Rev. A*, vol. 104, p. 023702, Aug 2021.

[4.29] M. D. Lee, S. D. Jenkins, and J. Ruostekoski, "Stochastic methods for light propagation and recurrent scattering in saturated and nonsaturated atomic ensembles," *Phys. Rev. A*, vol. 93, p. 063803, Jun 2016.

[4.30] C. Gardiner, P. Zoller, and P. Zoller, *Quantum noise: a handbook of Markovian and non-Markovian quantum stochastic methods with applications to quantum optics*. Springer Science & Business Media, 2004.

[4.31] "Documentation of QuantumCumulants.jl." https://qojulia.github.io/QuantumCumulants.jl/stable/, Accessed: December 20, 2021.

[4.32] "GitHub repository of QuantumCumulants.jl." https://github.com/qojulia/QuantumCumulants.jl, Accessed: December 20, 2021.

[4.33] S. Gowda, Y. Ma, A. Cheli, M. Gwozdz, V. B. Shah, A. Edelman, and C. Rackauckas, "High-performance symbolic-numerics via multiple dispatch," *arXiv preprint arXiv:2105.03949*, 2021.

[4.34] Y. Ma, S. Gowda, R. Anantharaman, C. Laughman, V. Shah, and C. Rackauckas, "Modelingtoolkit: A composable graph transformation system for equation-based modeling," 2021.

[4.35] C. Rackauckas and Q. Nie, "Differentialequations.jl–a performant and feature-rich ecosystem for solving differential equations in julia," *Journal of Open Research Software*, vol. 5, no. 1, 2017.

[4.36] "GitHub repository of Combinatorics.jl." https://github.com/JuliaMath/Combinatorics.jl. Accessed: December 20, 2021.

[4.37] T. H. Maiman, "Stimulated optical radiation in ruby," *nature*, vol. 187, no. 4736, pp. 493–494, 1960.

[4.38] C. Genes, D. Vitali, P. Tombesi, S. Gigan, and M. Aspelmeyer, "Ground-state cooling of a micromechanical oscillator: Comparing cold damping and cavity-assisted cooling schemes," *Phys. Rev. A*, vol. 77, no. 3, p. 033804, 2008.

[4.39] C. Benkert, M. . Scully, J. Bergou, L. Davidovich, M. Hillery, and M. Orszag, "Role of pumping statistics in laser dynamics: Quantum Langevin approach," *Phys. Rev. A*, vol. 41, no. 5, p. 2756, 1990.

[4.40] M. Orszag, *Quantum optics: including noise reduction, trapped ions, quantum trajectories, and decoherence*. Springer, 2016.

[4.41] C. Rackauckas and Q. Nie, "Adaptive methods for stochastic differential equations via natural embeddings and rejection sampling with memory," *Discrete Cont. Dyn.-B*, vol. 22, no. 7, p. 2731, 2017.

[4.42] J. D. Hunter, "Matplotlib: A 2D graphics environment," *Computing in Science & Engineering*, vol. 9, no. 3, pp. 90–95, 2007.

References for Chapter 5

[5.1] E. Oelker, R. Hutson, C. Kennedy, L. Sonderhouse, T. Bothwell, A. Goban, D. Kedar, C. Sanner, J. Robinson, G. Marti, D. Matei, T. Legero, M. Giunta, R. Holzwarth, F. Riehle, U. Sterr, and J. Ye, "Demonstration of 4.8× 10- 17 stability at 1 s for two independent optical clocks," *Nature Photonics*, vol. 13, no. 10, pp. 714–719, 2019.

[5.2] K. Numata, A. Kemery, and J. Camp, "Thermal-noise limit in the frequency stabilization of lasers with rigid cavities," *Physical review letters*, vol. 93, no. 25, p. 250602, 2004.

[5.3] J. Chen, "Active optical clock," *Chinese Science Bulletin*, vol. 54, no. 3, pp. 348–352, 2009.

[5.4] D. Meiser, J. Ye, D. Carlson, and M. Holland, "Prospects for a millihertz-linewidth laser," *Physical review letters*, vol. 102, no. 16, p. 163601, 2009.

[5.5] J. G. Bohnet, Z. Chen, J. M. Weiner, D. Meiser, M. J. Holland, and J. K. Thompson, "A steady-state superradiant laser with less than one intracavity photon," *Nature*, vol. 484, no. 7392, pp. 78–81, 2012.

[5.6] J. G. Bohnet, Z. Chen, J. M. Weiner, K. C. Cox, and J. K. Thompson, "Linear-response theory for superradiant lasers," *Phys. Rev. A*, vol. 89, p. 013806, Jan 2014.

[5.7] A. Bychek, C. Hotter, D. Plankensteiner, and H. Ritsch, "Superradiant lasing in inhomogeneously broadened ensembles with spatially varying coupling," *Open Research Europe 2021, 1:73*, 2021.

[5.8] K. Debnath, Y. Zhang, and K. Mølmer, "Lasing in the superradiant crossover regime," *Physical Review A*, vol. 98, no. 6, p. 063837, 2018.

[5.9] A. Gogyan, G. Kazakov, M. Bober, and M. Zawada, "Characterisation and feasibility study for superradiant lasing in 40ca atoms," *Opt. Express*, vol. 28, pp. 6881–6892, Mar 2020.

[5.10] F. Haake, M. I. Kolobov, C. Fabre, E. Giacobino, and S. Reynaud, "Superradiant laser," *Phys. Rev. Lett.*, vol. 71, pp. 995–998, Aug 1993.

[5.11] C. Hotter, D. Plankensteiner, L. Ostermann, and H. Ritsch, "Superradiant cooling, trapping, and lasing of dipole-interacting clock atoms," *Optics express*, vol. 27, no. 22, pp. 31193–31206, 2019.

[5.12] S. B. Jäger, H. Liu, A. Shankar, J. Cooper, and M. J. Holland, "Regular and bistable steady-state superradiant phases of an atomic beam traversing an optical cavity," *Phys. Rev. A*, vol. 103, p. 013720, Jan 2021.

[5.13] G. A. Kazakov and T. Schumm, "Active optical frequency standard using sequential coupling of atomic ensembles," *Physical Review A*, vol. 87, no. 1, p. 013821, 2013.

[5.14] G. A. Kazakov and T. Schumm, "Active optical frequency standards using cold atoms: perspectives and challenges," in *2014 European Frequency and Time Forum (EFTF)*, pp. 411–414, IEEE, 2014.

[5.15] G. A. Kazakov and T. Schumm, "Stability analysis for bad cavity lasers using inhomogeneously broadened spin-1/2 atoms as a gain medium," *Phys. Rev. A*, vol. 95, p. 023839, Feb 2017.

[5.16] G. A. Kazakov, J. Bohnet, and T. Schumm, "Prospects for a bad-cavity laser using a large ion crystal," *Phys. Rev. A*, vol. 96, p. 023412, Aug 2017.

[5.17] T. Laske, H. Winter, and A. Hemmerich, "Pulse delay time statistics in a superradiant laser with calcium atoms," *Physical Review Letters*, vol. 123, no. 10, p. 103601, 2019.

[5.18] H. Liu, S. B. Jäger, X. Yu, S. Touzard, A. Shankar, M. J. Holland, and T. L. Nicholson, "Rugged mhz-linewidth superradiant laser driven by a hot atomic beam," *Physical Review Letters*, vol. 125, no. 25, p. 253602, 2020.

[5.19] T. Maier, S. Kraemer, L. Ostermann, and H. Ritsch, "A superradiant clock laser on a magic wavelength optical lattice," *Optics express*, vol. 22, no. 11, pp. 13269–13279, 2014.

[5.20] D. Meiser and M. Holland, "Intensity fluctuations in steady-state superradiance," *Physical Review A*, vol. 81, no. 6, p. 063827, 2010.

[5.21] D. Meiser and M. Holland, "Steady-state superradiance with alkaline-earth-metal atoms," *Physical Review A*, vol. 81, no. 3, p. 033847, 2010.

[5.22] M. A. Norcia and J. K. Thompson, "Cold-strontium laser in the superradiant crossover regime," *Physical Review X*, vol. 6, no. 1, p. 011025, 2016.

[5.23] M. A. Norcia, M. N. Winchester, J. R. Cline, and J. K. Thompson, "Superradiance on the millihertz linewidth strontium clock transition," *Science advances*, vol. 2, no. 10, p. e1601231, 2016.

[5.24] M. A. Norcia, R. J. Lewis-Swan, J. R. Cline, B. Zhu, A. M. Rey, and J. K. Thompson, "Cavity-mediated collective spin-exchange interactions in a strontium superradiant laser," *Science*, vol. 361, no. 6399, pp. 259–262, 2018.

[5.25] M. A. Norcia, J. R. Cline, J. A. Muniz, J. M. Robinson, R. B. Hutson, A. Goban, G. E. Marti, J. Ye, and J. K. Thompson, "Frequency measurements of superradiance from the strontium clock transition," *Physical Review X*, vol. 8, no. 2, p. 021036, 2018.

[5.26] S. A. Schäffer, M. Tang, M. R. Henriksen, A. A. Jørgensen, B. T. Christensen, and J. W. Thomsen, "Lasing on a narrow transition in a cold thermal strontium ensemble," *Physical Review a*, vol. 101, no. 1, p. 013819, 2020.

[5.27] M. Tang, S. A. Schäffer, A. A. Jørgensen, M. R. Henriksen, B. T. Christensen, J. H. Müller, and J. W. Thomsen, "Cavity-immune spectral features in the pulsed superradiant crossover regime," *Physical Review Research*, vol. 3, no. 3, p. 033258, 2021.

[5.28] A. Shankar, J. T. Reilly, S. B. Jäger, and M. J. Holland, "Subradiant-to-subradiant phase transition in the bad cavity laser," *Phys. Rev. Lett.*, vol. 127, p. 073603, Aug 2021.

[5.29] J. M. Weiner, K. C. Cox, J. G. Bohnet, and J. K. Thompson, "Phase synchronization inside a superradiant laser," *Physical Review A*, vol. 95, no. 3, p. 033808, 2017.

[5.30] M. Xu, D. A. Tieri, E. Fine, J. K. Thompson, and M. J. Holland, "Synchronization of two ensembles of atoms," *Physical review letters*, vol. 113, no. 15, p. 154101, 2014.

[5.31] Y. Zhang, C. Shan, and K. Mølmer, "Ultranarrow superradiant lasing by dark atom-photon dressed states," *Physical Review Letters*, vol. 126, no. 12, p. 123602, 2021.

[5.32] H. M. Goldenberg, D. Kleppner, and N. F. Ramsey, "Atomic hydrogen maser," *Phys. Rev. Lett.*, vol. 5, pp. 361–362, Oct 1960.

[5.33] V. S. Strelnitski, V. O. Ponomarev, and H. A. Smith, "Hydrogen masers. i: Theory and prospects," *arXiv preprint astro-ph/9511118*, 1995.

[5.34] T. Salzburger and H. Ritsch, "Atom-photon pair laser," *Phys. Rev. A*, vol. 75, p. 061601, Jun 2007.

[5.35] C.-C. Chen, S. Bennetts, R. G. Escudero, B. Pasquiou, and F. Schreck, "Continuous guided strontium beam with high phase-space density," *Phys. Rev. Applied*, vol. 12, p. 044014, Oct 2019.

[5.36] H. Katori, M. Takamoto, V. Pal'Chikov, and V. Ovsiannikov, "Ultrastable optical clock with neutral atoms in an engineered light shift trap," *Physical Review Letters*, vol. 91, no. 17, p. 173005, 2003.

[5.37] J. Ye, H. Kimble, and H. Katori, "Quantum state engineering and precision metrology using state-insensitive light traps," *science*, vol. 320, no. 5884, pp. 1734–1738, 2008.

[5.38] R. G. Escudero, C.-C. Chen, S. Bennetts, B. Pasquiou, and F. Schreck, "A steady-state magneto-optical trap of fermionic strontium on a narrow-line transition," *arXiv preprint arXiv:2104.06814*, 2021.

[5.39] S. Bennetts, C.-C. Chen, B. Pasquiou, and F. Schreck, "Steady-state magneto-optical trap with 100-fold improved phase-space density," *Phys. Rev. Lett.*, vol. 119, p. 223202, Dec 2017.

[5.40] R. Kubo, "Generalized cumulant expansion method," *Journal of the Physical Society of Japan*, vol. 17, no. 7, pp. 1100–1120, 1962.

[5.41] D. Plankensteiner, C. Hotter, and H. Ritsch, "QuantumCumulants.jl: A Julia framework for generalized mean-field equations in open quantum systems," *Quantum*, vol. 6, p. 617, Jan. 2022.

[5.42] R. Dum, P. Zoller, and H. Ritsch, "Monte carlo simulation of the atomic master equation for spontaneous emission," *Phys. Rev. A*, vol. 45, pp. 4879–4887, Apr 1992.

[5.43] K. Mølmer, Y. Castin, and J. Dalibard, "Monte carlo wave-function method in quantum optics," *J. Opt. Soc. Am. B*, vol. 10, pp. 524–538, Mar 1993.

[5.44] M. B. Plenio and P. L. Knight, "The quantum-jump approach to dissipative dynamics in quantum optics," *Rev. Mod. Phys.*, vol. 70, pp. 101–144, Jan 1998.

[5.45] A. Kramida, Yu. Ralchenko, J. Reader, and and NIST ASD Team. NIST Atomic Spectra Database (ver. 5.8), [Online]. Available: https://physics.nist.gov/asd [2021, September 1]. National Institute of Standards and Technology, Gaithersburg, MD., 2020.

[5.46] A. Taichenachev, V. Yudin, C. Oates, C. Hoyt, Z. Barber, and L. Hollberg, "Magnetic field-induced spectroscopy of forbidden optical transitions with application to lattice-based optical atomic clocks," *Physical review letters*, vol. 96, no. 8, p. 083001, 2006.

[5.47] D. S. Barker, N. C. Pisenti, B. J. Reschovsky, and G. K. Campbell, "Three-photon process for producing a degenerate gas of metastable alkaline-earth-metal atoms," *Phys. Rev. A*, vol. 93, p. 053417, May 2016.

[5.48] D. Filin and M. Safronova, "private communication," 2021.

[5.49] M. J. Martin, *Quantum Metrology and Many-Body Physics: Pushing the Frontier of the Optical Lattice Clock*. PhD thesis, University of Colorado, 2013.

[5.50] Program examples using the Julia package QuantumCumulants.jl, which analytically derive the system and correlation function equations for the six-level and two-level laser model are given in the supplementary material. Additionaly we show an example to calculate the two-level system parameters from the pumped six-level atom, using the Julia package QuantumOptics.jl. The equations in these examples are solved numerically for our standard parameters.

[5.51] S. Krämer, D. Plankensteiner, L. Ostermann, and H. Ritsch, "QuantumOptics.jl: A Julia framework for simulating open quantum systems," *Comput. Phys. Commun.*, vol. 227, pp. 109–116, 2018.

[5.52] J. D. Hunter, "Matplotlib: A 2d graphics environment," *Computing in science & engineering*, vol. 9, no. 3, pp. 90–95, 2007.

References for Chapter 6

[6.1] R. H. Dicke, "Coherence in spontaneous radiation processes," *Phys. Rev.*, vol. 93, pp. 99–110, Jan 1954.

[6.2] R. H. Lehmberg, "Radiation from an n-atom system. i. general formalism," *Phys. Rev. A*, vol. 2, pp. 883–888, Sep 1970.

[6.3] M. Gross and S. Haroche, "Superradiance: An essay on the theory of collective spontaneous emission," *Physics Reports*, vol. 93, no. 5, pp. 301–396, 1982.

[6.4] Z. Ficek and R. Tanaś, "Entangled states and collective nonclassical effects in two-atom systems," *Physics Reports*, vol. 372, no. 5, pp. 369–443, 2002.

[6.5] S. Filipp, A. F. van Loo, M. Baur, L. Steffen, and A. Wallraff, "Preparation of subradiant states using local qubit control in circuit qed," *Phys. Rev. A*, vol. 84, p. 061805, Dec 2011.

[6.6] R. Reimann, W. Alt, T. Kampschulte, T. Macha, L. Ratschbacher, N. Thau, S. Yoon, and D. Meschede, "Cavity-modified collective rayleigh scattering of two atoms," *Phys. Rev. Lett.*, vol. 114, p. 023601, Jan 2015.

[6.7] B. Casabone, K. Friebe, B. Brandstätter, K. Schüppert, R. Blatt, and T. E. Northup, "Enhanced quantum interface with collective ion-cavity coupling," *Phys. Rev. Lett.*, vol. 114, p. 023602, Jan 2015.

[6.8] M. A. Norcia, M. N. Winchester, J. R. Cline, and J. K. Thompson, "Superradiance on the millihertz linewidth strontium clock transition," *Science advances*, vol. 2, no. 10, p. e1601231, 2016.

[6.9] L. Ostermann, C. Meignant, C. Genes, and H. Ritsch, "Super-and subradiance of clock atoms in multimode optical waveguides," *New Journal of Physics*, vol. 21, no. 2, p. 025004, 2019.

[6.10] A. Piñeiro Orioli, J. K. Thompson, and A. M. Rey, "Emergent dark states from superradiant dynamics in multilevel atoms in a cavity," *Phys. Rev. X*, vol. 12, p. 011054, Mar 2022.

[6.11] D. Kornovan, N. Corzo, J. Laurat, and A. Sheremet, "Extremely subradiant states in a periodic one-dimensional atomic array," *Physical Review A*, vol. 100, no. 6, p. 063832, 2019.

[6.12] M. Moreno-Cardoner, R. Holzinger, and H. Ritsch, "Efficient nano-photonic antennas based on dark states in quantum emitter rings," *Optics Express*, vol. 30, no. 7, pp. 10779–10791, 2022.

[6.13] S. J. Masson, I. Ferrier-Barbut, L. A. Orozco, A. Browaeys, and A. Asenjo-Garcia, "Many-body signatures of collective decay in atomic chains," *Physical review letters*, vol. 125, no. 26, p. 263601, 2020.

[6.14] A. Tiranov, V. Angelopoulou, C. J. van Diepen, B. Schrinski, O. A. D. Sandberg, Y. Wang, L. Midolo, S. Scholz, A. D. Wieck, A. Ludwig, *et al.*, "Coherent super-and subradiant dynamics between distant optical quantum emitters," *arXiv preprint arXiv:2210.02439*, 2022.

[6.15] M. Zanner, T. Orell, C. M. Schneider, R. Albert, S. Oleschko, M. L. Juan, M. Silveri, and G. Kirchmair, "Coherent control of a multi-qubit dark state in waveguide quantum electrodynamics," *Nature Physics*, vol. 18, no. 5, pp. 538–543, 2022.

[6.16] S. Okaba, D. Yu, L. Vincetti, F. Benabid, and H. Katori, "Superradiance from lattice-confined atoms inside hollow core fibre," *Communications Physics*, vol. 2, no. 1, pp. 1–10, 2019.

[6.17] J. A. Mlynek, A. A. Abdumalikov, C. Eichler, and A. Wallraff, "Observation of dicke superradiance for two artificial atoms in a cavity with high decay rate," *Nature communications*, vol. 5, no. 1, pp. 1–6, 2014.

[6.18] T. Laske, H. Winter, and A. Hemmerich, "Pulse delay time statistics in a superradiant laser with calcium atoms," *Physical Review Letters*, vol. 123, no. 10, p. 103601, 2019.

[6.19] S. A. Schäffer, M. Tang, M. R. Henriksen, A. A. Jørgensen, B. T. Christensen, and J. W. Thomsen, "Lasing on a narrow transition in a cold thermal strontium ensemble," *Physical Review A*, vol. 101, no. 1, p. 013819, 2020.

[6.20] M. Tang, S. A. Schäffer, A. A. Jørgensen, M. R. Henriksen, B. T. Christensen, J. H. Müller, and J. W. Thomsen, "Cavity-immune spectral features in the pulsed superradiant crossover regime," *Physical Review Research*, vol. 3, no. 3, p. 033258, 2021.

[6.21] F. Haake, M. I. Kolobov, C. Fabre, E. Giacobino, and S. Reynaud, "Superradiant laser," *Phys. Rev. Lett.*, vol. 71, pp. 995–998, Aug 1993.

[6.22] D. Meiser, J. Ye, D. Carlson, and M. Holland, "Prospects for a millihertz-linewidth laser," *Physical review letters*, vol. 102, no. 16, p. 163601, 2009.

[6.23] J. G. Bohnet, Z. Chen, J. M. Weiner, D. Meiser, M. J. Holland, and J. K. Thompson, "A steady-state superradiant laser with less than one intracavity photon," *Nature*, vol. 484, no. 7392, pp. 78–81, 2012.

[6.24] H. Ritsch, P. Domokos, F. Brennecke, and T. Esslinger, "Cold atoms in cavity-generated dynamical optical potentials," *Rev. Mod. Phys.*, vol. 85, pp. 553–601, 2013.

[6.25] W. Guerin, M. O. Araújo, and R. Kaiser, "Subradiance in a large cloud of cold atoms," *Phys. Rev. Lett.*, vol. 116, p. 083601, Feb 2016.

[6.26] A. Shankar, J. T. Reilly, S. B. Jäger, and M. J. Holland, "Subradiant-to-subradiant phase transition in the bad cavity laser," *Phys. Rev. Lett.*, vol. 127, p. 073603, Aug 2021.

[6.27] M. Gegg, A. Carmele, A. Knorr, and M. Richter, "Superradiant to subradiant phase transition in the open system dicke model: dark state cascades," *New Journal of Physics*, vol. 20, p. 013006, jan 2018.

[6.28] M. A. Norcia, J. R. Cline, J. A. Muniz, J. M. Robinson, R. B. Hutson, A. Goban, G. E. Marti, J. Ye, and J. K. Thompson, "Frequency measurements of superradiance from the strontium clock transition," *Physical Review X*, vol. 8, no. 2, p. 021036, 2018.

[6.29] L. Ostermann, H. Ritsch, and C. Genes, "Protected state enhanced quantum metrology with interacting two-level ensembles," *Physical review letters*, vol. 111, no. 12, p. 123601, 2013.

[6.30] L. Ostermann, D. Plankensteiner, H. Ritsch, and C. Genes, "Protected subspace ramsey spectroscopy," *Phys. Rev. A*, vol. 90, p. 053823, Nov 2014.

[6.31] C. Gardiner, P. Zoller, and P. Zoller, *Quantum noise: a handbook of Markovian and non-Markovian quantum stochastic methods with applications to quantum optics*. Springer Science & Business Media, 2004.

[6.32] R. Kubo, "Generalized cumulant expansion method," *Journal of the Physical Society of Japan*, vol. 17, no. 7, pp. 1100–1120, 1962.

[6.33] D. Plankensteiner, C. Hotter, and H. Ritsch, "QuantumCumulants.jl: A Julia framework for generalized mean-field equations in open quantum systems," *Quantum*, vol. 6, p. 617, Jan. 2022.

[6.34] The Supplemental Material includes a Julia code example to derive and numerically solve the equations for our system.

[6.35] N. Shammah, S. Ahmed, N. Lambert, S. De Liberato, and F. Nori, "Open quantum systems with local and collective incoherent processes: Efficient numerical simulations using permutational invariance," *Phys. Rev. A*, vol. 98, p. 063815, Dec 2018.

[6.36] Y. Zhang, Y.-X. Zhang, and K. Mølmer, "Monte-carlo simulations of superradiant lasing," *New Journal of Physics*, vol. 20, p. 112001, nov 2018.

[6.37] D. Ferraro, M. Campisi, G. M. Andolina, V. Pellegrini, and M. Polini, "High-power collective charging of a solid-state quantum battery," *Phys. Rev. Lett.*, vol. 120, p. 117702, Mar 2018.

[6.38] F. Pirmoradian and K. Mølmer, "Aging of a quantum battery," *Phys. Rev. A*, vol. 100, p. 043833, Oct 2019.

[6.39] G. Ferioli, A. Glicenstein, L. Henriet, I. Ferrier-Barbut, and A. Browaeys, "Storage and release of subradiant excitations in a dense atomic cloud," *Phys. Rev. X*, vol. 11, p. 021031, May 2021.

[6.40] H. Liu, S. B. Jäger, X. Yu, S. Touzard, A. Shankar, M. J. Holland, and T. L. Nicholson, "Rugged mhz-linewidth superradiant laser driven by a hot atomic beam," *Physical Review Letters*, vol. 125, no. 25, p. 253602, 2020.

[6.41] J. Kim, S.-h. Oh, D. Yang, J. Kim, M. Lee, and K. An, "A photonic quantum engine driven by superradiance," *Nature Photonics*, vol. 16, no. 10, pp. 707–711, 2022.

[6.42] J. Lodewyck, P. G. Westergaard, and P. Lemonde, "Nondestructive measurement of the transition probability in a sr optical lattice clock," *Physical Review A*, vol. 79, no. 6, p. 061401, 2009.

[6.43] G. Vallet, E. Bookjans, U. Eismann, S. Bilicki, R. Le Targat, and J. Lodewyck, "A noise-immune cavity-assisted non-destructive detection for an optical lattice clock in the quantum regime," *New Journal of Physics*, vol. 19, no. 8, p. 083002, 2017.

[6.44] R. Hobson, W. Bowden, A. Vianello, I. R. Hill, and P. Gill, "Cavity-enhanced non-destructive detection of atoms for an optical lattice clock," *Optics express*, vol. 27, no. 26, pp. 37099–37110, 2019.

[6.45] N. F. Ramsey, "A molecular beam resonance method with separated oscillating fields," *Physical Review*, vol. 78, no. 6, p. 695, 1950.

[6.46] Y. Sortais, S. Bize, M. Abgrall, S. Zhang, C. Nicolas, C. Mandache, P. Lemonde, P. Laurent, G. Santarelli, N. Dimarcq, *et al.*, "Cold atom clocks," *Physica Scripta*, vol. 2001, no. T95, p. 50, 2001.

[6.47] S. Bize, P. Laurent, M. Abgrall, H. Marion, I. Maksimovic, L. Cacciapuoti, J. Grünert, C. Vian, F. P. Dos Santos, P. Rosenbusch, *et al.*, "Cold atom clocks and applications," *Journal of Physics B: Atomic, molecular and optical physics*, vol. 38, no. 9, p. S449, 2005.

[6.48] S. Krämer, D. Plankensteiner, L. Ostermann, and H. Ritsch, "Quantumoptics.jl: A Julia framework for simulating open quantum systems," *Comput. Phys. Commun.*, vol. 227, pp. 109–116, 2018.

[6.49] R. Dum, P. Zoller, and H. Ritsch, "Monte carlo simulation of the atomic master equation for spontaneous emission," *Physical Review A*, vol. 45, no. 7, p. 4879, 1992.

[6.50] K. Mølmer, Y. Castin, and J. Dalibard, "Monte carlo wave-function method in quantum optics," *JOSA B*, vol. 10, no. 3, pp. 524–538, 1993.

References for Chapter 7

[7.1] M. A. Norcia, M. N. Winchester, J. R. Cline, and J. K. Thompson, "Superradiance on the millihertz linewidth strontium clock transition," *Science advances*, vol. 2, no. 10, p. e1601231, 2016.

[7.2] T. Laske, H. Winter, and A. Hemmerich, "Pulse delay time statistics in a superradiant laser with calcium atoms," *Physical Review Letters*, vol. 123, no. 10, p. 103601, 2019.

[7.3] S. A. Schäffer, M. Tang, M. R. Henriksen, A. A. Jørgensen, B. T. Christensen, and J. W. Thomsen, "Lasing on a narrow transition in a cold thermal strontium ensemble," *Physical Review A*, vol. 101, no. 1, p. 013819, 2020.

[7.4] M. A. Norcia, J. R. Cline, J. A. Muniz, J. M. Robinson, R. B. Hutson, A. Goban, G. E. Marti, J. Ye, and J. K. Thompson, "Frequency measurements of superradiance from the strontium clock transition," *Physical Review X*, vol. 8, no. 2, p. 021036, 2018.

[7.5] N. F. Ramsey, "A molecular beam resonance method with separated oscillating fields," *Physical Review*, vol. 78, no. 6, p. 695, 1950.

References for Chapter 9

[9.1] J. Vanier and C. Audoin, *The quantum physics of atomic frequency standards*. CRC, 1989.

[9.2] F. Haake, M. I. Kolobov, C. Fabre, E. Giacobino, and S. Reynaud, "Superradiant laser," *Phys. Rev. Lett.*, vol. 71, pp. 995–998, Aug 1993.

[9.3] J. G. Bohnet, Z. Chen, J. M. Weiner, D. Meiser, M. J. Holland, and J. K. Thompson, "A steady-state superradiant laser with less than one intracavity photon," *Nature*, vol. 484, pp. 78–81, 2012.

[9.4] T. Maier, S. Kraemer, L. Ostermann, and H. Ritsch, "A superradiant clock laser on a magic wavelength optical lattice," *Optics express*, vol. 22, no. 11, pp. 13269–13279, 2014.

[9.5] M. A. Norcia, R. J. Lewis-Swan, J. R. Cline, B. Zhu, A. M. Rey, and J. K. Thompson, "Cavity-mediated collective spin-exchange interactions in a strontium superradiant laser," *Science*, vol. 361, no. 6399, pp. 259–262, 2018.

[9.6] S. L. Campbell, R. Hutson, G. Marti, A. Goban, N. D. Oppong, R. McNally, L. Sonderhouse, J. Robinson, W. Zhang, B. Bloom, and J. Ye, "A fermi-degenerate three-dimensional optical lattice clock," *Science*, vol. 358, no. 6359, pp. 90–94, 2017.

[9.7] H. Leopardi, J. Davila-Rodriguez, J. Sherman, F. Quinlan, S. Diddams, and T. Fortier, "Absolute frequency comb comparisons and the measurement of optical atomic clock transitions," in *CLEO: Science and Innovations*, pp. SM1L–4, Optical Society of America, 2018.

[9.8] A. D. Ludlow, X. Huang, M. Notcutt, T. Zanon-Willette, S. M. Foreman, M. M. Boyd, S. Blatt, and J. Ye, "Compact, thermal-noise-limited optical cavity for diode laser stabilization at 1×10^{-15}," *Opt. Lett.*, vol. 32, no. 6, pp. 641–643, 2007.

[9.9] D. Meiser and M. Holland, "Steady-state superradiance with alkaline-earth-metal atoms," *Phys. Rev. A*, vol. 81, no. 3, p. 033847, 2010.

[9.10] M. A. Norcia, M. N. Winchester, J. R. Cline, and J. K. Thompson, "Superradiance on the millihertz linewidth strontium clock transition," *Science advances*, vol. 2, no. 10, p. e1601231, 2016.

[9.11] A. L. Schawlow and C. H. Townes, "Infrared and optical masers," *Phys. Rev.*, vol. 112, no. 6, p. 1940, 1958.

[9.12] S. Kuppens, M. Van Exter, and J. Woerdman, "Quantum-limited linewidth of a bad-cavity laser," *Phys. Rev. Lett.*, vol. 72, no. 24, p. 3815, 1994.

[9.13] T. Kessler, C. Hagemann, C. Grebing, T. Legero, U. Sterr, F. Riehle, M. J. Martin, L. Chen, and J. Ye, "A sub-40-mhz-linewidth laser based on a silicon single-crystal optical cavity," *Nature Photonics*, vol. 6, pp. 687–692, 2012.

[9.14] D. Meiser, J. Ye, D. R. Carlson, and M. J. Holland, "Prospects for a millihertz-linewidth laser," *Phys. Rev. Lett.*, vol. 102, p. 163601, 2009.

[9.15] J. G. Bohnet, Z. Chen, J. M. Weiner, K. C. Cox, and J. K. Thompson, "Active and passive sensing of collective atomic coherence in a superradiant laser," *Phys. Rev. A*, vol. 88, p. 013826, Jul 2013.

[9.16] V. Vuletic, "An almost lightless laser," *Nature*, vol. 484, pp. 43–44, 2012.

[9.17] J. M. Weiner, K. C. Cox, J. G. Bohnet, and J. K. Thompson, "Phase synchronization inside a superradiant laser," *Phys. Rev. A*, vol. 95, no. 3, p. 033808, 2017.

[9.18] M. Xu, D. A. Tieri, and M. J. Holland, "Simulating open quantum systems by applying su(4) to quantum master equations," *Phys. Rev. A*, vol. 87, p. 062101, Jun 2013.

[9.19] K. Henschel, J. Majer, J. Schmiedmayer, and H. Ritsch, "Cavity qed with an ultracold ensemble on a chip: Prospects for strong magnetic coupling at finite temperatures," *Phys. Rev. A*, vol. 82, p. 033810, Sep 2010.

[9.20] R. H. Dicke, "Coherence in spontaneous radiation processes," *Phys. Rev.*, vol. 93, pp. 99–110, 1954.

[9.21] T. Salzburger and H. Ritsch, "Atomic self-trapping induced by single-atom lasing," *Phys. Rev. Lett.*, vol. 93, p. 063002, 2004.

[9.22] T. Salzburger and H. Ritsch, "Lasing and cooling in a finite-temperature cavity," *Phys. Rev. A*, vol. 74, p. 033806, 2006.

[9.23] M. Xu, S. B. Jäger, S. Schütz, J. Cooper, G. Morigi, and M. J. Holland, "Supercooling of atoms in an optical resonator," *Phys. Rev. Lett.*, vol. 116, p. 153002, Apr 2016.

[9.24] R. Lehmberg, "Radiation from an N-atom system. I. General formalism," *Phys. Rev. A*, vol. 2, no. 3, p. 883, 1970.

[9.25] Z. Ficek and R. Tanaś, "Entangled states and collective nonclassical effects in two-atom systems," *Phys. Rep.*, vol. 372, no. 5, pp. 369 – 443, 2002.

[9.26] H. Ritsch, P. Domokos, F. Brennecke, and T. Esslinger, "Cold atoms in cavity-generated dynamical optical potentials," *Rev. Mod. Phys.*, vol. 85, pp. 553–601, 2013.

[9.27] R. R. Puri, *Mathematical methods of quantum optics*. Springer Berlin Heidelberg, 2001.

[9.28] S. Krämer, D. Plankensteiner, L. Ostermann, and H. Ritsch, "Quantumoptics. jl: A julia framework for simulating open quantum systems," *Comp. Phys. Comm.*, vol. 227, pp. 109–116, 2018.

References for Chapter 10

[10.1] R. H. Dicke, "Coherence in spontaneous radiation processes," *Physical review*, vol. 93, no. 1, p. 99, 1954.

[10.2] R. Bonifacio, P. Schwendimann, and F. Haake, "Quantum statistical theory of superradiance. i," *Physical Review A*, vol. 4, no. 1, p. 302, 1971.

[10.3] F. Haake, M. I. Kolobov, C. Fabre, E. Giacobino, and S. Reynaud, "Superradiant laser," *Physical review letters*, vol. 71, no. 7, p. 995, 1993.

[10.4] M. G. Benedict, *Super-radiance: Multiatomic coherent emission*. CRC Press, 1996.

[10.5] M. O. Scully and A. A. Svidzinsky, "The super of superradiance," *Science*, vol. 325, no. 5947, pp. 1510–1511, 2009.

[10.6] J. Chen, "Active optical clock," *Chinese Science Bulletin*, vol. 54, no. 3, pp. 348–352, 2009.

[10.7] D. Meiser, J. Ye, D. Carlson, and M. Holland, "Prospects for a millihertz-linewidth laser," *Physical review letters*, vol. 102, no. 16, p. 163601, 2009.

[10.8] D. Meiser and M. Holland, "Steady-state superradiance with alkaline-earth-metal atoms," *Physical Review A*, vol. 81, no. 3, p. 033847, 2010.

[10.9] T. Maier, S. Kraemer, L. Ostermann, and H. Ritsch, "A superradiant clock laser on a magic wavelength optical lattice," *Optics express*, vol. 22, no. 11, pp. 13269–13279, 2014.

[10.10] Y. Zhang, Y.-X. Zhang, and K. Mølmer, "Monte-carlo simulations of superradiant lasing," *New Journal of Physics*, vol. 20, no. 11, p. 112001, 2018.

[10.11] K. Debnath, Y. Zhang, and K. Mølmer, "Lasing in the superradiant crossover regime," *Physical Review A*, vol. 98, no. 6, p. 063837, 2018.

[10.12] C. Hotter, D. Plankensteiner, L. Ostermann, and H. Ritsch, "Superradiant cooling, trapping, and lasing of dipole-interacting clock atoms," *Optics express*, vol. 27, no. 22, pp. 31193–31206, 2019.

[10.13] A. Gogyan, G. Kazakov, M. Bober, and M. Zawada, "Characterisation and feasibility study for superradiant lasing in 40 ca atoms," *Optics express*, vol. 28, no. 5, pp. 6881–6892, 2020.

[10.14] A. Shankar, J. T. Reilly, S. B. Jäger, and M. J. Holland, "Subradiant-to-subradiant phase transition in the bad cavity laser," *arXiv preprint arXiv:2103.07402*, 2021.

[10.15] Q. Wu, Y. Zhang, X. Yang, S.-L. Su, C. Shan, and K. Mølmer, "A superradiant maser with nitrogen-vacancy center spins," *arXiv preprint arXiv:2105.12350*, 2021.

[10.16] J. G. Bohnet, Z. Chen, J. M. Weiner, D. Meiser, M. J. Holland, and J. K. Thompson, "A steady-state superradiant laser with less than one intracavity photon," *Nature*, vol. 484, no. 7392, pp. 78–81, 2012.

[10.17] M. A. Norcia and J. K. Thompson, "Cold-strontium laser in the superradiant crossover regime," *Physical Review X*, vol. 6, no. 1, p. 011025, 2016.

[10.18] M. A. Norcia, M. N. Winchester, J. R. Cline, and J. K. Thompson, "Superradiance on the millihertz linewidth strontium clock transition," *Science advances*, vol. 2, no. 10, p. e1601231, 2016.

[10.19] C.-C. Chen, S. Bennetts, R. G. Escudero, B. Pasquiou, F. Schreck, *et al.*, "Continuous guided strontium beam with high phase-space density," *Physical Review Applied*, vol. 12, no. 4, p. 044014, 2019.

[10.20] T. Laske, H. Winter, and A. Hemmerich, "Pulse delay time statistics in a superradiant laser with calcium atoms," *Physical review letters*, vol. 123, no. 10, p. 103601, 2019.

[10.21] S. A. Schäffer, M. Tang, M. R. Henriksen, A. A. Jørgensen, B. T. Christensen, and J. W. Thomsen, "Lasing on a narrow transition in a cold thermal strontium ensemble," *Physical Review A*, vol. 101, no. 1, p. 013819, 2020.

[10.22] M. Tang, S. A. Schäffer, A. A. Jørgensen, M. R. Henriksen, B. T. Christensen, J. H. Müller, and J. W. Thomsen, "Cavity-immune features in the spectra of superradiant crossover laser pulses," *arXiv preprint arXiv:2104.13305*, 2021.

[10.23] K. Numata, A. Kemery, and J. Camp, "Thermal-noise limit in the frequency stabilization of lasers with rigid cavities," *Physical review letters*, vol. 93, no. 25, p. 250602, 2004.

[10.24] M. Notcutt, L.-S. Ma, A. D. Ludlow, S. M. Foreman, J. Ye, and J. L. Hall, "Contribution of thermal noise to frequency stability of rigid optical cavity via hertz-linewidth lasers," *Physical Review A*, vol. 73, no. 3, p. 031804, 2006.

[10.25] H. Liu, S. B. Jäger, X. Yu, S. Touzard, A. Shankar, M. J. Holland, and T. L. Nicholson, "Rugged mhz-linewidth superradiant laser driven by a hot atomic beam," *Physical Review Letters*, vol. 125, no. 25, p. 253602, 2020.

[10.26] S. B. Jäger, H. Liu, A. Shankar, J. Cooper, and M. J. Holland, "Regular and bistable steady-state superradiant phases of an atomic beam traversing an optical cavity," *Physical Review A*, vol. 103, no. 1, p. 013720, 2021.

[10.27] M. A. Norcia, A. W. Young, W. J. Eckner, E. Oelker, J. Ye, and A. M. Kaufman, "Seconds-scale coherence in a tweezer-array optical clock," *arXiv preprint arXiv:1904.10934*, 2019.

[10.28] R. Kubo, "Generalized cumulant expansion method," *Journal of the Physical Society of Japan*, vol. 17, no. 7, pp. 1100–1120, 1962.

[10.29] R. R. Puri, *Mathematical methods of quantum optics*, vol. 79. Springer Science & Business Media, 2001.

[10.30] H. J. Carmichael, *Statistical methods in quantum optics 1: master equations and Fokker-Planck equations*. Springer Science & Business Media, 2013.

[10.31] K. Debnath, Y. Zhang, and K. Mølmer, "Collective dynamics of inhomogeneously broadened emitters coupled to an optical cavity with narrow linewidth," *Physical Review A*, vol. 100, no. 5, p. 053821, 2019.

[10.32] M. Xu, D. A. Tieri, E. Fine, J. K. Thompson, and M. J. Holland, "Synchronization of two ensembles of atoms," *Physical review letters*, vol. 113, no. 15, p. 154101, 2014.

[10.33] A. Bychek, "Clusters," *Zenodo*, https://doi.org/10.5281/zenodo.4916393, 2021.

[10.34] C. Rackauckas and Q. Nie, "Differentialequations. jl–a performant and feature-rich ecosystem for solving differential equations in julia," *Journal of Open Research Software*, vol. 5, no. 1, 2017.

[10.35] D. Plankensteiner, C. Hotter, and H. Ritsch, "Quantumcumulants. jl: A julia framework for generalized mean-field equations in open quantum systems," *arXiv preprint arXiv:2105.01657*, 2021.

[10.36] J. D. Hunter, "Matplotlib: A 2D graphics environment," *Computing in Science & Engineering*, vol. 9, no. 3, pp. 90–95, 2007.

[10.37] B. Zhu, J. Schachenmayer, M. Xu, F. Herrera, J. G. Restrepo, M. J. Holland, and A. M. Rey, "Synchronization of interacting quantum dipoles," *New Journal of Physics*, vol. 17, no. 8, p. 083063, 2015.

[10.38] A. Bychek, "Superradiant_laser_figures," *Figshare*, https://doi.org/10.6084/m9.figshare.15321819.v1, 2021.

List of publications

- C. Hotter, D. Plankensteiner, H. Ritsch. Continuous narrowband lasing with coherently driven V-level atoms. *New Journal of Physics*, **22**(11), 113021 (2020).

- D. Plankensteiner, C. Hotter, H. Ritsch. QuantumCumulants.jl: A Julia framework for generalized mean-field equations in open quantum systems. *Quantum* **6**, 617 (2022).

- C. Hotter, D. Plankensteiner, G. Kazakov, H. Ritsch. Continuous multi-step pumping of the optical clock transition in alkaline-earth atoms with minimal perturbation. *Optics Express*, **30**(4), 5553 (2022).

- C. Hotter, L. Ostermann, H. Ritsch. Cavity sub- and superradiance for transversely driven atomic ensembles. *Physical Review Research*, **5**(1), 013056 (2023).

- C. Hotter, D. Plankensteiner, L. Ostermann, H. Ritsch. Superradiant cooling, trapping, and lasing of dipole-interacting clock atoms. *Optics Express*, **27**(22), 31193 (2019).

- A. Bychek, C. Hotter, D. Plankensteiner, H. Ritsch. Superradiant lasing in inhomogeneously broadened ensembles with spatially varying coupling [version 2; peer review: 2 approved]. *Open Research Europe*, **1**:75 (2021).